DEM-based triangulation pore network model for particle aggregates: Drying and capillary forces

Dissertation
zur Erlangung des akademischen Grades
Doktoringenieur
(Dr.-Ing.)

von M.Sc. **Son Thai Pham**
geb. am 09. August 1987 in Hanoi, Vietnam
genehmigt durch die Fakultät für Verfahrens- und Systemtechnik
der Otto-von-Guericke-Universität Magdeburg

Promotionskommission:

Prof. Dr.-Ing. habil. Eckehard Specht	(Vorsitz)
PD. Dr.-Ing. habil. Abdolreza Kharaghani	(Gutachter)
Prof. Dr.-Ing. habil. Evangelos Tsotsas	(Gutachter)
Prof. Dr.-Ing. habil. Bruno Chareyre	(Gutachter)

eingereicht am: 02. März 2021
Promotionskolloquium am: 12. November 2021

Kurzzusammenfassung

Feststoffe werden in einer Vielzahl von Industrien verarbeitet. Die meisten Produkte haben partikuläre Form. Auslegung und Optimierung der jeweiligen Prozesse erfordern Verständnis über die zugrundeliegenden physikalischen Vorgänge und die sich entwickelnden Produkteigenschaften. Das Entfernen von Flüssigkeit aus nassen granularen Produkten durch konvektives Trocknen ist ein wesentlicher und entscheidender Schritt in vielen Fertigungsverfahren. Dynamische Veränderungen an der räumlichen Verteilung der flüssigen Phase sind jedoch einer der Hauptgründe für die Schädigung von Partikelaggregaten während der Konvektionstrocknung, was sich auf die Qualität der Endprodukte auswirkt.

Es wird ein dreidimensionales Triangulationsporennetzwerkmodell (TPNM) entwickelt, welches die zeitliche Verteilung der Flüssigphase im Hohlraum von Aggregaten aus kugelförmigen Primärpartikeln unter den Grenzbedingungen eines kapillardominierten Regimes gut simulieren kann. Die Aggregate werden mittels der diskrete Elemente Methode (DEM) numerisch erzeugt, wobei der komplementäre Hohlraum unter Verwendung der regulären Delaunay-Triangulation und ihrer dualen Voronoi-Tessellation in Poren und Hälse zerlegt wird. Eine modifizierte Version des klassischen Invasions-Perkolationsalgorithmus wird eingerichtet, um die bevorzugte Verdunstung der in den Poren eingeschlossenen Flüssigkeit zu beschreiben. Die aus TPNM-Trocknungssimulationen erhaltene Flüssigkeitsverteilung erfasst die Entwicklung gemessener Phasenmuster besser als es frühere Porennetzwerkmodelle vermögen. Lokale Kapillarkräfte, die sowohl durch den Flüssigkeitsdruck als auch durch die Oberflächenspannung entstehen, werden über die Zeit aus dem Füllzustand der Poren berechnet. Diese Kapillarkräfte sind die Eingabe für die Kopplungssimulation, die die Entwicklung der Flüssigkeitsverteilung mit daraus resultierenden trocknungsinduzierten Mikrorissen der festen Struktur verbindet. Solche Mikrorisse werden als Bruch von Bindungen zwischen festen Partikeln erfasst.

Das vielseitige TPNM wird verwendet, um drei Sätze synthetischer Aggregate unterschiedlicher Partikelgrößendispersität (monodispers, bidispers, polydispers) bei zwei unterschiedlichen Aggregatgrößen systematisch zu untersuchen. Der Einfluss der Grenzwände auf die Flüssigphasenverteilung nimmt mit zunehmendem Aggregat-

Partikel Größenverhältnis ab. Es gibt keine signifikanten Unterschiede in der Trocknungskinetik gleich großer Aggregate. Stets wird ein langer erster Trocknungsabschnitt beobachtet, welcher auf eine aggregatübergreifende Flüssigkeitskonnektivität zurückzuführen ist, die sich aus einer sehr breiten Verteilung des Kapillareintrittsradius der Porenhälse ergibt. Der Einfluss der Partikelgrößendispersität auf die Flüssigkeitsverteilung und die Trocknungskinetik ist für große Aggregate vernachlässigbar.

Was die auf Primärpartikel ausgeübte Kapillarkraft betrifft, so hängt diese von drei Faktoren ab: Partikelgröße, Kapillardruck und Flüssigkeitsverteilung im lokalen Partikelmaßstab. Kleine monodisperse und bidisperse Aggregate unterscheiden sich in der Kapillarkraft stärker als große monodisperse und polydisperse Aggregate. Die Kapillarkraft in monodispersen Aggregaten skaliert nahezu direkt proportional mit der Partikelgröße. Unterschiedliche Feststoffgerüste ergeben zwar keine signifikanten Unterschiede in der Trocknungskinetik, verursachen aber bemerkenswerte Differenzen in der Kapillarkraft und der durch Trocknung verursachten Schädigung. Größere Partikel führen bei monodispersen Aggregaten zu weniger Schäden, Heterogenität in der Partikelgröße verursacht hingegen vermehrt Mikrorisse.

Abstract

Solids processing is encountered across a wide range of industries, where the majority of manufactured products involve particulate forms. The design and optimization of respective industrial processes require the understanding of underlying physical phenomena and evolving product properties. Removing the liquid out of wet granular products by convective drying is an essential and crucial step in many manufacturing lines. Evolution of the spatial distribution of the liquid phase is, though, one of the main reasons for the damage of particle aggregates during convective drying, which affects the quality of final products.

A three-dimensional triangulation pore network model (TPNM) is developed that can readily simulate liquid phase distribution over time in the void space of aggregates made of spherical primary particles in the limiting condition of capillary-dominated regime. The discrete element method (DEM) is used to numerically generate the aggregates, whereby the complementary void space is decomposed into pores and throats using the regular Delaunay triangulation and its dual Voronoi tessellation. A modified version of the classical invasion percolation algorithm is set up to describe the preferential evaporation of the liquid confined in the pores. The liquid phase distribution obtained from drying TPNM simulations captures the evolution of phase patterns measured experimentally better than the predictions of other pore network models. Local capillary forces caused by both fluid pressure and surface tension are computed over time from the filling state of pores. These capillary forces are the input for the coupling simulation that relates the evolution of liquid phase distribution with drying-induced micro-cracks of the solid structure, latter represented by the breakage of the bond between solid particles.

The versatile TPNM is utilized to systematically investigate three sets of synthetic aggregates with different types of size distribution of the constituent particles (monodisperse, bidisperse and polydisperse) at two aggregate dimensions. The influence of the boundary walls on the liquid phase distribution decreases with increasing aggregate-to-particle size ratio. There is no significant difference in terms of drying kinetics for aggregates having the same aggregate dimension. Extended first drying period is observed for all investigated aggregates, which is interpreted by an

aggregate-spanning liquid connectivity resulting from a broad distribution of throat entry capillary radius. The influence of particle size dispersity on liquid distribution and drying kinetics is found to be negligible at higher aggregate dimension.

As to the capillary force exerted on solid primary particles, there are three factors having an influence on it: particle size, capillary pressure and local particle-scale liquid distribution. The difference in capillary force is higher between small mondisperse and bidisperse aggregates than between large mondisperse and polydisperse aggregates. Capillary force is found to scale up almost direct proportionally to particle size in monodisperse aggregates. Different solid skeletons do not result in significant difference in drying kinetics, but they do give rise to remarkable difference in capillary force and drying-induced damage. Bigger particles lead to less damage for the case of monodisperse aggregates. Higher heterogeneity in particle size results in more micro-cracks.

Nomenclature

Roman symbols

A_{ij}	mass exchange area	m^2
d_c/d_f	diameter ratio of coarse and fine particles	-
$\vec{F}_{cap,k}$	capillary force	N
$\vec{F}_{sl,k}$	force contribution induced by capillary pressure	N
$\vec{F}_{slg,k}$	force contribution induced by surface tension	N
$\vec{F}_{tot,i}$	total force acting on particle i	N
L_{ij}	distance between the centers (Voronoi vertices) of two adjacent tetrahedral cells i and j	m
$\dot{M}_{v,ij}$	vapor mass flow rate	kg s^{-1}
$\widetilde{M}_v$	molar vapor mass	kg $kmol^{-1}$
p	pressure	Pa
$p_{v,i}$	unknown vapor pressure of pore i	Pa
$p_{v,i}$ *	equilibrium vapor pressure	Pa
$p_{v,\infty}$	vapor pressure in the gas ambient	Pa
Q_f	volume fraction of fine particles	-
Q_c	volume fraction of coarse particles	-
$r_{c,e}$	entry capillary radius	m
$\tilde{R}$	universal gas constant	J $kmol^{-1}$ K^{-1}
S	network saturation	-
T	absolute temperature	K

Greek symbols

δ	diffusion coefficient (vapor in air)	m^2 s^{-1}
ε	porosity	
ε_∞	porosity of unconfined packing	-
ζ	particle size dispersity parameter	-
σ	surface tension	N m^{-1}

Superscripts and subscripts

c,e	entry capillary
c	capillary
g	gas
l	liquid

Abbreviations

CFD	computational fluid dynamics
COV	coefficient of variation
CPNM	classical pore network model
CRP	constant rate period
DDPM	dense discrete phase method
DEM	discrete element method
DPM	discrete phase method
FRP	falling rate period
FVM	finite volume method
LBM	lattice Boltzmann method
MLC	main liquid cluster
MRI	magnetic resonance imaging
MS-P	Mayer and Stowe–Princen
PDF	probability distribution function
PNM	pore network model
PSZ	partially saturated zone
RPNM	ring pore network model

SD	Standard deviation
TPNM	triangulation pore network model
vdW	van der Waals

Contents

Contents

Chapter 1

Introduction

1.1 Background

Removing the liquid solvent out of capillary porous materials by (convective) drying is an essential and crucial step in several engineering processes, e.g. preparation of supported catalysts [1-3] or fabrication of building materials [4]. When the liquid is removed by evaporation from the pores confined by the solid matrix, a liquid-gas interface (meniscus) appears at the constrictions between pores, which induces capillary forces acting on the solid matrix. The heterogeneity in capillary force field induced by gradients in the liquid phase distribution (or moisture distribution) gives rise to mechanical stresses that eventually lead to structural problems (cracks formation, shrinkage, deformations, etc.) in porous materials. Thus, it is of paramount importance to understand and describe the evolution of liquid phase distribution during the drying process of porous materials.

Granular materials, composed of solid particles, play a crucial role in a wide range of industries, particularly in engineering processes that deal with powders and grains. Industries in which the transportation, storage and processing of materials in granular form are frequently involved in production processes are, e.g., the agricultural, food, pharmaceutical, cosmetics and constructions industries. The design and operation of respective technological processes require advanced research that needs to be based on the determination of the properties of granular matter. Granular packings (i.e. particle assemblies or aggregates of particles) may differ from one another owing to

differences, for example, in properties of composing particles, i.e. they may differ in particle size as a fundamental particle property. Particles produced by fragmentation and aggregation processes have a broad size distribution for most of the soils, powders and natural composites [5, 6]. The significant influence of particle size distribution on the material hydraulic and strength properties has been discussed and investigated [7, 8]. Particle size polydispersity is one of the most important factors in the performance optimization in various industrial applications. Concrete is one of the most typical examples for this. A broad size distribution reduces porosity and thus enhances the strength of the final products in this [9], as well as in other cases. Besides, particle size distribution also has an influence on the pore space characteristics, an important factor in several chemical engineering applications that involve liquid flow, such as water retention, the adsorbent action of particles, and filtering [10-13]. In the present work, the influence of particle size dispersity on the drying behavior of assemblies of particles will be studied, including thermo-mechanical aspects, such as induced capillary forces and the damage of interparticle bonds.

1.2 Pore-scale modeling for the drying of porous media

To accurately assess drying kinetics and stresses, it is important to understand and describe the evolution of liquid distribution inside of drying porous materials at the pore-scale level [14-16]. This is generally achieved using different modeling routes. A simple but fundamental and illustrative approach represents the pore structure of a capillary porous medium as a bundle of parallel capillary tubes with radii selected randomly from a normal distribution [17]. With the capillaries ending at the surface, this model assumes liquid hydraulic connectivity from the interior to the porous medium surface and thus successfully captures the constant rate period of drying, that is, the drying period characterized by a relatively high drying rate [18, 19]. However, the pore size distribution is the only pore-scale information that this model can take into account. Other characteristic structural properties of a real three-dimensional pore structure, such as pore coordination number, cannot be studied. The consequence of this limitation is that the liquid phase essentially remains in a single liquid cluster during drying – an unrealistic situation.

A more sophisticated approach describes the void structure as a network of pores interconnected through constrictions (throats). In early works, the network is a regular lattice of pore nodes (volume-less pores) interconnected through throats with uniform length and radii that are mathematically generated following a probability density function. Later on, irregular networks and pores with volume have also been considered [20]. In this way, structural and morphological properties characterizing a real three-dimensional pore space (such as pore size distribution, pore coordination number as well as spatial correlation of pore sizes) can be taken into account in pore network models. Taking this opportunity, Metzger et al. [21] investigated by means of pore network models how such properties can control and impact the liquid phase distribution in drying porous media. These pore networks are, however, generated without a complementary pore-scale consideration of the solid matrix. They are often used for situations where the solid matrix remains rigid and passive during the simulated process.

In fact, the void space and the solid matrix in a porous medium are complementary to each other. In recent studies, therefore, efforts are made to directly extract the void space structure from the solid matrix. Examples include the study carried out by Borgman et al. [22], where the constructed pore structure mimics to some extent the actual void space of a quasi-two-dimensional transparent microfluidic cell, in which an array of cylindrical solid pillars is placed on a regular grid. In another study grids of cylindrical pillars are tailored to specific patterns [23]. Results obtained from these investigations clearly indicate that the phase distribution depends on the placement of solid pillars relative to one another. Studies with more or less similar objectives have also been conducted with spherical glass beads either sandwiched between transplant glass plates [24] or packed in three-dimensional cylindrical containers [25, 26]. In general, the reconstruction of porous space under conditions that enable to preserve and reflect the local features of a given solid structure is a still open and challenging issue.

1.3 Capillary forces in granular porous media and the influence of particle size

The macroscopic behavior of granular porous media composed of particles can be predicted by including physical phenomena at the particle scale in numerical studies

by application of discrete modeling methods, such as the discrete element method (DEM). One of the most typical locally induced phenomena is cohesion, which may result from several interparticle physicochemical forces: van der Waals forces (vdW) [27], electrostatic forces [28] and capillary forces [29]. However, the relative impact of these forces depends on the applications to be modelled. Simplifications in the models may be necessary to make the complex physical phenomena computable or to reduce the total numerical cost. Figure 1.1 shows the importance of several fundamental forces with respect to particle diameter D [30]. The dependence in very simplified way of forces on particle size ranks in decreasing order as follows: Body forces (weight) $\propto D^3$; surface-area-based forces (electrostatic) $\propto D^2$; interfacial forces (capillary and vdW) $\propto D$. In wet granular materials, the capillary force is usually assumed to dominate the other cohesive forces. Hence, the cohesion in wet granular materials is mostly assumed to originate from capillary forces between the constituting particles [31-35].

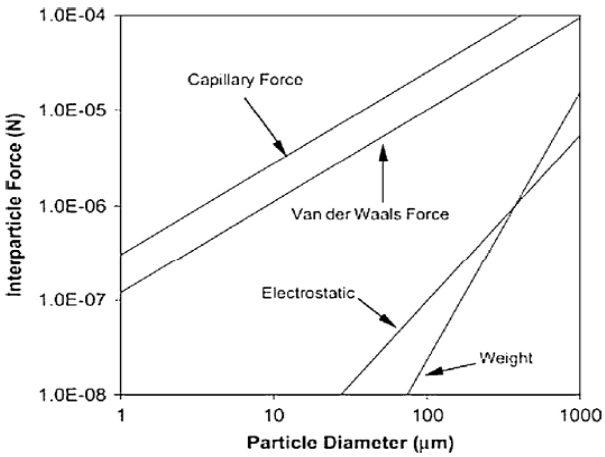

Figure 1.1 Relative importance of inter-particulate forces with regards to particle diameter for contacting smooth spheres (figure taken from [30]).

The influence of capillary forces on the macroscopic cohesion of granular media has been numerically investigated in, for example, [31, 36]. The results underline two points: First, the number of liquid bridges per grain is a key parameter to ensure macroscopic strength [36]; second, the liquid bridge volume has no remarkable influence on macroscopic strength. Besides, there are many studies on the relation between the capillary force and the geometry of the liquid bridge for the case of

monodisperse materials (composed of uniformly sized particles). Whereas there are fewer similar studies for the case of polydisperse materials (composed of particles having different sizes). Increment in particle polydispersity leads to increment in the macroscopic cohesion of a wet granular material [37]. The evolution of an evaporating capillary bridge between two glass spheres at fixed separations has been investigated by means of isothermal experiments in [38]. The analyzed variables included the total evaporated mass, the average evaporation flux, geometric characteristics (such as the radius of bridge gorge, central external radius, angles and radii of contact), and the capillary force [38]. A further analysis and discussion on this experimental data set is reported in [39]. Other studies on capillary bridge evaporation have addressed nano-scale separations (< 100 nm) [40, 41], spheres in direct contact [42], or the drying of colloidal crystals [43]. Although a two-grain liquid bridge represents the last stage of the evolution of evaporating multi-particle bridges in a way that provides tractable access to fundamental phenomena, its behavior may not necessarily be generalized to the behavior of a wet granular medium. Consequently, further research is needed at this end.

1.4 Drying-induced cracks of granular porous media and the influence of particle size

During the drying process, the formation of menisci between the particles induces capillary forces. Capillary forces are exerted on the particles and pull them together. In real systems, broad distributions of pore sizes lead to pronounced heterogeneity in the resulting drying stress [44-47]. As this capillary force overcomes other forces, such as the compressive stress, cracks occur in consolidated granular materials or in drying particle films. Understanding crack formation and developing strategies to suppress the initiation of local breakage is an important field of research in the industrial development of new materials and processing routes, as product qualities generally decline with the appearance of cracks [48, 49]. The avoidance of cracks is crucial in many applications involving hard particle coatings, for example: Nanoparticles-coated polyethylene separator in lithium-ion batteries [50], photonic crystal structures consisting of silica particles [51], anti-reflective coatings of silica nanoparticles on the rough surfaces of polycrystalline silicon solar cells [52], antimicrobial and

superhydrophilic (for low resistance to liquid flow) layer of borosilicate glass particles in high performance membrane filters [53].

The drying-induced cracks that may appear during the evaporation of solvent from colloidal suspensions, gels, or pastes give rise to tremendous technological and scientific concerns. These cracks can weaken or even damage the structure of concrete [54]; films composed of ceramic particles [55], muddy sediments [56], paste made of clay and sand [57]; or the functionalities of coating layers [58]. Many different strategies have been developed in order to avoid or reduce the drying-induced fractures of porous materials [59]. Some examples are increasing pore size to increase permeability (which is inversely proportional to the stress); addition of surfactants to the liquid to reduce the interfacial energy leading to the reduction in capillary stress, etc. An experimental study on cracking behavior during drying of binder-free granular ceramic films is reported in [60]. The films were produced from aqueous dispersions of alumina. The influence of particle size on the cracking behavior was investigated in this study using a statistical design methodology. Critical cracking thickness (CCT, a drying film would crack at thickness higher than CCT) was used to evaluate the tendency toward cracking. It was found that CCT increases linearly with the average particle size.

An interesting strategy has been applied in [61] to suppress crack formation during the drying of thin films made from hard particle suspensions. The addition of small amount of a secondary liquid (immiscible with the primary liquid of the suspensions) results in a ternary particle-liquid-liquid system (termed capillary suspension) [62, 63]. Capillary force induced by this secondary liquid preserves the cohesion between particles, which can create a particulate gel comprising a sample-spanning particle network, regardless of the wettability of the secondary liquid compared to the primary liquid [64]. Capillary suspensions have been utilized in different technical applications on various materials and products: Food industry, e.g. corn starch, chocolate spreads with low caloric value [64, 65]; electronic applications, e.g. new slurry concept for lithium-ion battery electrodes [66] or conductive pastes for front side metallization of solar cells [67]; capillary foams [68]; macroporous ceramic materials [69].

The previously mentioned study from [61] focuses on the pendular regime and demonstrates how to prevent crack formation using a secondary fluid in capillary

suspension systems. The influence of particle polydispersity (solid phase) on the stress developed during the drying of a colloidal drop of silica nanoparticles is reported in [70]. For the case of a bidisperse suspension (size ratio of about 10), the addition of about 1% (number of particles) of large particles remarkably reduces the measured stress value, compared to the value observed for the suspension of small particles only. This result is interpreted by the formation of larger pore sizes due to the presence of large particles, which is assumed to reduce the stress induced by the pressure gradient of the Darcy flow. It is noticed that the small and large nanoparticle suspensions of this investigation are not strictly monodisperse, but rather polydisperse. Particle of the large type are, nevertheless, larger than the largest particles of the small type. The Darcy stress that has been computed based on the average particle size of the 30% largest particles is significantly different to the stress that has been calculated using the average particle size of the whole suspension.

1.5 Motivation

The fact that liquid distribution in drying porous media can be predicted by pore network models triggers the idea of investigating whether these models can be coupled with a mechanical model (e.g. discrete element method) to describe the fluid-solid interaction in porous materials. This idea has already been implemented to investigate the influence of pore-scale effects on the solid phase during drying of monodisperse particle aggregates either with regular [71] or irregular [72] packing structures. However, the classical Voronoi tessellation [73] utilized in these studies is not applicable for the case of aggregates composed of primary particles with a size distribution. Since most of the aggregates encountered in many natural or technical porous systems are composed of a broad range of particle sizes, it is necessary to overcome this limitation. The regular Delaunay triangulation [74] is a good candidate to this purpose. It has already been utilized to generate a graph to the centroid of spherical particles of dense polydisperse packings [75] in order to study the fluid-solid interactions during the oedometer test [76]. This approach has then been further improved and implemented for several other applications. For instance, it has been used to study the hydro-mechanical response of particle packings during drainage [77] or the swelling of super absorbent polymers [78]. The reconstruction of pore networks

which are in close correspondence with given particle assemblies by Delaunay triangulation will be a central aspect of the present work. Further discussion of literature will be presented in Chapter 2. Then, Chapters 3 to 7 will refer to the main contributions of this thesis, as outlined in the following section.

1.6 Contributions of this thesis

In this work, a drying pore network model is developed that appears to be more versatile compared to existing pore network models. It can describe both phase distribution and evolving capillary forces in solid aggregates made of spherical primary particles with size distributions. The void space of aggregates is represented by networks of pores and throats, which are obtained by applying the regular Delaunay triangulation and its dual Voronoi tessellation to the centroid of primary particles (Chapter 3). Transport phenomena are described by non-viscous capillary flow in liquid-filled regions and vapor diffusion in gas-filled network regions and boundary layer. Simulation results obtained from our drying pore network model are compared to experimental results (Chapter 3) in terms of evolution of liquid distribution (represented by saturation profile) as well as drying kinetics (calculated based on X-ray tomography images). Predictions obtained from previous drying pore network models (classical and ring pore network models) are compared to the predictions obtained from the novel pore network model, with reference to the experimental results (Chapter 3).

The novel and validated pore network model is further applied to synthetic aggregates numerically generated by using the discrete element method (Chapter 4). There are three sets of aggregates, at two different aggregate dimensions. The first set consists of five monodisperse aggregates having different primary particle sizes. The second set contains bidisperse aggregates having the same aggregate dimensions as in the first set. There are three aggregates in the third and last set, one monodisperse and two polydisperse aggregates. These three aggregates have bigger aggregate dimensions than in the first two sets. The influence of particle size as well as particle size distribution on the evolution of liquid distribution and drying kinetics during isothermal capillary-dominated drying are, in this manner, systematically investigated in Chapter 4. The influence of particle size on drying kinetics and liquid phase

distribution is investigated by varying the particle radius of different monodisperse aggregates. Then, taking the monodisperse aggregate as a reference, the impact of particle size distribution is investigated by comparing the results obtained for monodisperse aggregates with the ones obtained for bidisperse and polydisperse aggregates.

Capillary forces with contributions from both capillary pressure and surface tension are formulated in a discrete way in Chapter 5. Taking the evolution of liquid distribution from the drying simulations as an input, the evolution of capillary forces during the drying of all aggregates investigated in Chapter 4 is presented in Chapter 5. The influence of particle size as well as particle size distribution on capillary force of these aggregates is evaluated using statistical analysis.

The capillary force calculated in Chapter 5, in its turn, is the input for the evaluation of the drying-induced damage (represented by the breakage of the bond between particles in contact to each other) in Chapter 6. By employing the discrete element method capillary forces are loaded on the primary particles, which are interlinked by bonds with predefined strengths. In a one-way coupling approach (assuming negligible particle displacement, thus, neglecting the influence of the change in solid structure on the fluid phase), micro cracks (bond breakage) of all aggregates investigated in Chapter 4 and 5 are simulated. By consequent use of this approach, the impact of the internal structure of the porous media on the mechanical behavior of the aggregates, for the case of three-dimensional particle aggregates with various degrees of particle size heterogeneity, is presented in Chapter 6.

Concluding remarks and future research suggestions are outlined in Chapter 7.

Chapter 2

Literature review

2.1 Descriptions of the void space structure of porous media

Pore network models have been extensively employed for the investigation of many physical and chemical processes [14-16]. The importance of incorporating pore scale kinetics, rather than depending on macroscopic averages, has been shown in various contexts, for example regarding the transport of solute in wet porous media [79]. Compared to other pore-scale modeling methods, e.g. lattice Boltzmann method, pore network models require much less computational resources (i.e. computational time, memory capacity) due to the simplifications used in the construction of the network representing the investigated media. The probably earliest pore network model was introduced by Fatt [80] in an investigation on the analogy between flow in porous media and a network of resistors. The pore network used in this study was a two-dimensional network of tubes having fixed coordination number. The pores were located at the intersection of the tubes. These tubes were arranged on square or hexagonal lattices. The pore network represented the experimentally obtained pore size distributions by the random assignment of tube diameters according to those size distributions. After this pioneer work, the pore network models have grown in sophistication and have been used to study a variety of different physical processes, including different sequences of displacement (liquid by gas, gas by liquid, etc.), two and three-phase flow, as well as networks having irregular lattices. [16, 81-84].

However, the correspondence between the void space of the investigated porous media and their representation in the simulations (the pore networks) has a significant

influence on the credibility and accuracy of predictions obtained from the models. It is difficult to prescribe precise rules for the definition of pores and throats for the case of irregularly shaped void spaces composed of interconnected converging–diverging channels. This problem is further aggravated by the demand of describing real pore structures, based on characterization methods which contain both experimental error and limitations in resolution.

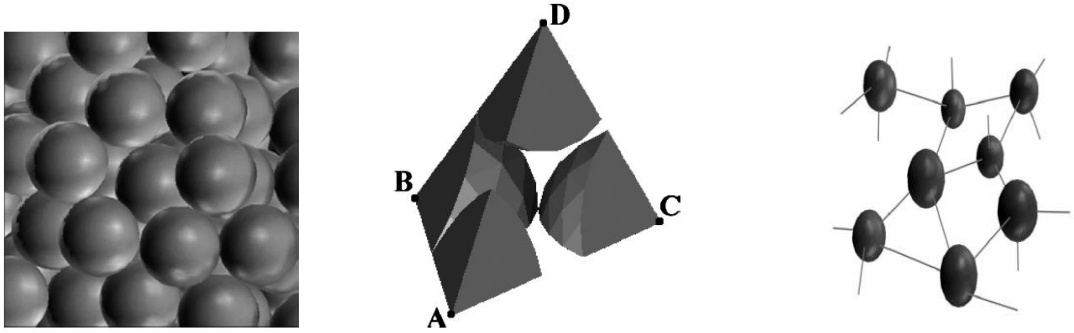

Figure 2.1. (a) Random close packing of uniformly sized spheres. (b) A tetrahedral cell resulting from Delaunay tessellation. The vertices of the tetrahedron (points A, B, C, D) are the centers of four neighbor spheres. Only the sections of the solid spheres contained within the tetrahedron are shown. (c) Schematic representation of a pore network topology. The spheres in (c) correspond to the internal regions of tetrahedral cells shown in (b) and should not be confused with solid spheres shown in (a). The throats (the line connecting spheres) correspond to tetrahedral cell faces. Each pore has four neighboring pores, each pair of adjacent pores is connected through one throat. These three figures are taken from [107].

So early as in 1899, the random packing of equal spheres was suggested by Slichter as an “ideal soil” [85]. This oversimplified approach, nevertheless, captures many essential features of the void space of real sediments. Its most important features are the randomness in the locations of spheres and the fact that the geometry of void space is determined by the geometry of the spheres making up the porous medium. This approach offered useful qualitative insights in the decades after its introduction [86-93], and many experimental works have been conducted to accurately measure the position coordinates of solid particles in random close packing (RCP) of spheres. One of the most well-known and widely used set of RCP data was published in 1970, namely for the so-called Finney pack [94] (Fig. 2.1a). This highly precise measured

packing consists of 7994 equal steel particles, being much larger than other packs with published position data (around 1000 particles) [95]. In 1971, Mason [96] proposed an approach for extracting a network model corresponding to the void space in a random packing of spheres having predetermined geometry. The idea in this as well as in many other subsequent investigations is to extract a reliable representation of the actual void space geometry from a simple but physically representative model of the porous medium [96-101]. This approach paved the way for the second generation of pore network models. Instead of creating a statistically equivalent pore network on a lattice structure as it had been done in the first generation (without taking into account any clear correspondence between the void and solid phase of the porous medium), the pore network is mapped directly from the void structure in a three-dimensional packing [100, 102]. This approach can be used on numerically generated materials [103-105] or with actual materials if the detailed structure of the solid phase is available [100]. The advantage of such physically representative networks is that real pore-scale spatial correlations and the allocation of pore structures in space are directly incorporated into the network.

Delaunay tessellation of the sphere center coordinates is a natural way of constructing a pore network model from the geometric data of the random close packing of equal spheres [106]. Applied to points in n-dimensional space, Delaunay tessellation groups n+1 nearest neighboring points together. The volume of the solid sphere packing (Fig. 2.1a) is subdivided into tetrahedra (Fig. 2.1b). Then, a simple pore network is defined as being visualized in Fig. 2.1c. Pores (sites) represented by spheres in Fig. 2.1c correspond to the internal regions of tetrahedral Delaunay cells, and throats (bonds) represented by lines in Fig. 2.1c correspond to the faces of those tetrahedral cells. It is noted that spheres in Fig. 2.1c do not depict the real geometry of the pores. The sketch of spheres and lines in Fig. 2.1c is just for the convenience of illustrating pore network topology. The actual shapes of the pores are the void spaces of Delaunay tetrahedra, shown in Fig. 2.1b. The spheres in Fig. 2.1c should also not be confused with the actual spherical solid particles of the sphere packing. All geometrical properties of pores and throats follow directly from the predetermined center coordinates of spheres, which naturally defines the topology of the pore network. Each tetrahedral cell has common faces with four neighbors. This results in a lattice of connectivity four (equal to the number of four faces of the tetrahedron). For example,

3367 spheres in the central region of the Finney pack result in a network having about 15,000 pores and 30,000 throats [107]. The network is, though, completely irregular. A more detailed description of the Finney pack and the corresponding pore network obtained from it by Delaunay tessellation can be found in [95, 96, 101]. Despite the simplicity of representing a model porous medium as a packing of equal spheres, such representation provides a powerful tool to study processes occurring in porous media. For example, respective a priori predictions of macroscopic properties, e.g. permeability or percolation threshold of the porous medium, have been successfully validated by experimental data in [98, 99, 108].

The third generation of pore network model construction approaches was inspired by the improvement in the ability to capture high resolution images of porous media. The pore properties are defined directly from the tomography data, thus, this approach is termed image-based network modeling. The effect of network structure on characterization and flow modeling for the case of single phase permeability and two-phase quasi-static drainage has been investigated in [109] using data from X-ray micro-tomography. Tomography images of three different porous media (made of irregular packings of glass spheres, irregular shape sand particles, and cylinders, respectively) have been used to create a series of four pore networks for each porous medium. Despite of being constructed from the same tomography image data, the generated pore networks vary over two orders of magnitude in pore density (number of pores per unit volume), which in turn affects network properties such as pore size distribution and pore coordination. There are two reasons for the large variations in pore density: different methods for conducting the search for pores (defined by means of maximal inscribed spheres), and differently set merging criteria (rules for the merging of overlapping inscribed spheres to create single pores). The total number of pores of the sphere packing obtained from four different pore network construction methods was found to vary from 3243 to 262665, while the values for the sand packing and the cylinder packing are 4494 to 319500 and 908 to 34208, respectively. The throats in all four network construction schemes had no volume, with number of throats that showed similar differences as the number of pores. Despite the mentioned differences in pore density, predictions of single-phase permeability of the packings (calculated using the one-dimensional form of Darcy's law) remain remarkably consistent for a given porous medium (largest variation is by a factor of two), even for

the simplest throat conductance formulas. However, the capillary pressure curves generated from quasi-static drainage are more sensitive, though not dramatically, to network structure than permeability is. The liquid phase distribution in the higher pore density networks is more even than the one in lower pore density networks. As interface-controlled processes like drainage are sensitive upon pore structure, this result is expected. These results suggest that different pore network structures of porous media which are more complex than regular packing of spheres do not necessarily result in significant difference in terms of single phase or multiphase flow physics.

2.2 Studies on the liquid phase distribution during the drying of porous media

There are two main processes associated with the liquid during the drying of porous materials: (a) migration, the movement of liquid inside the porous media; and (b) desorption, the escape of liquid from the porous media to the surrounding environments [110]. On the porous medium surface desorption occurs by evaporation. Evaporation is a process whereby a liquid is transformed to the vapor phase and removed from the evaporating surface. Typically, the drying process is described as having two consecutive stages [19, 25, 59, 111-114]. The first stage, characterized by an initially high and often presumed constant evaporation rate (constant rate period, CRP), is controlled primarily by atmospheric conditions. The evaporative demand is supplied by capillary liquid flow connecting the liquid bulk inside the medium with an evaporative external surface of the medium, where the phase transformation occurs [59, 113, 115, 116]. The interruption of the continuous liquid pathways to the surface marks the onset of the second drying stage with lower evaporation rate, the so-called falling rate period (FRP) [19, 117]. During the second drying stage, the phase transition occurs inside the medium, causing an extending unsaturated subsurface region (partially saturated zone (PSZ) [118] or vadose zone), and the evaporation rate depends on porous medium properties such as pore size distribution. The existence of this PSZ has been demonstrated by the use of three-dimensional imaging techniques such as magnetic resonance imaging (MRI) [119-122].

There have been several approaches to study the liquid flow through pores in the PSZ. In one approach, the mechanism of this liquid transport is based on the heterogeneity

of pore sizes. The pressure gradient induced by the pore size distribution provides the drying force for liquid flow from larger pores to smaller ones [113, 123]. In another approach, the transport of liquid is controlled by the pore shape [124-127]. The sharp corner edges of the pores influence evaporation rates. Experimental and simulated results show that corners within the pore walls help maintain hydraulic pathways for the transport of liquid from the interior of the porous medium to the surface [121, 124-126]. Recent results have demonstrated that the hydraulic connectivity provided by small quantities of fluid (chains of liquid bridges) can significantly influence the transport properties of granular materials [128-130]. The influence on drying kinetics of the hydraulic connections induced by chains of spherical particles is investigated in [131]. Packing configurations of the particles, from ‘‘straight packing’’ to ‘‘close-packing’’, contribute to the transition from capillary-supported (fast) to diffusion-controlled (slow) drying period. Close-packed systems have more stable hydraulic connections, which results in higher evaporation rates. Straight packing (more loosely packed systems) leads to unstable liquid connections and, consequently, lower evaporation rates.

Advances in imaging techniques have provided the possibility of directly visualizing the liquid phase distributions in three-dimensional (3D) porous media during evaporation [120, 121, 132]. Synchrotron X-ray tomography was utilized to demonstrate the important role of the capillary-driven liquid flow from large to small pores in supplying the liquid to the evaporation front [121]. Similar flow pattern is observed by using confocal microscopy to study drying dynamics of 3D granular porous media [122]. Beside homogeneous porous media, studies on the drying of so-called composite systems, namely of porous media made of layers of different characteristics, have been reported. Capillary effects are found to play a major role in such cases, and tend to impose specific liquid distributions corresponding to the different pore sizes in the different regions of the system [133]. Similar effect is also observed during the drying of porous media made of two or three layers of bead packings with different bead sizes [134]. The top surface of such packings is exposed to an air flow, but the water is removed from the layer made of the largest beads, regardless of its position with respect to the sample top surface. Another experimental study on a composite system is reported in [135]. Magnetic resonance imaging (MRI) is utilized to investigate the convective drying of a porous medium covered with a

paste. The porous medium is composed of glass beads packed in a cylindrical glass container up to a height of 2.3 cm, while the paste is a mixture of water with a colloidal phase and is coated over the top surface of the beads packing to form a layer of a uniform thickness of 1.7 cm. Initially, the granular medium remains saturated while the paste shrinks to finally form a rigid porous structure (which will not shrink any more) [135]. Then the desaturation occurs in the medium with the largest pores first. When capillary effects are similar in both media they desaturate simultaneously. The drying process is governed by this capillary effect down to very low saturation. Both media desaturate homogeneously (i.e moisture is uniformly distributed within each medium) at different rates, depending on the porous structure of the media to maintain capillary equilibrium throughout the specimen. The drying rate of the whole system remains constant until a low but still sufficient saturation of the paste. Then, a drying front develops in the paste and the drying rate decreases.

The evolution of the liquid distribution in different parts of a sample also provides important information for the prediction on the transport and accumulation of ions or particles in different parts of a composite system. In general, liquid distributions are strong indicators of how porous materials dry, depending on the structural characteristics of the porous space.

2.3 Capillary force calculation methods

The liquid distribution in granular media can strongly affect their mechanical behavior, e.g. tensile strength [136] or crushing strength [137]. With the decrement of the liquid volume from the initial state of a medium fully saturated with liquid, various regimes are encountered in the porous media [138, 139] (Fig. 2.2). The capillary regime is defined as the particles are deeply immersed in liquid, giving rise to tetrahedral structures. The funicular regime is when there are coalesced liquid bridges, i.e. there are liquid clusters which are simultaneously in contact with at least three particles creating trimers, pentamers and heptamers that consist of three, five and seven interconnected liquid bridges, respectively. And the pendular regime is when liquid bridges between particles do not coalesce but exist as isolated liquid bridges.

After the early pioneer works of Haines [89] and Fisher [29], pendular liquid bridges have been extensively investigated [31, 140-151]. This kind of liquid bridge produces a capillary force originating from the capillary pressure (the pressure difference across the phase interface of fluids) and from the surface tension of the liquid acting at the three-phase contact line. The Laplace-Young equation can provide an exact solution for the force component induced by the capillary pressure [142, 152]. This equation,

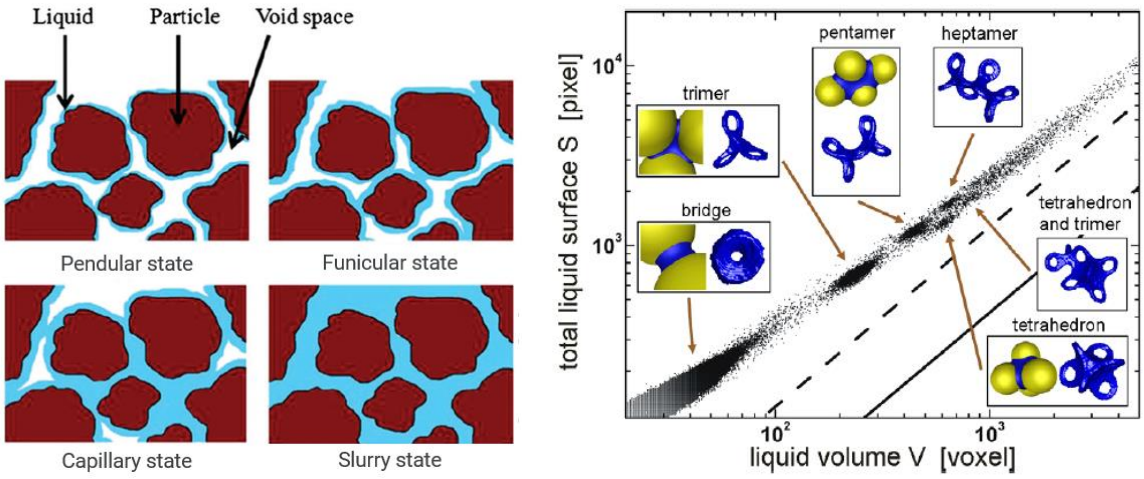

(a) (b)

Figure 2.2. (a) Different liquid saturation regimes (taken from [138]); (b) Correlation between surface area and volume of liquid clusters based on three-dimensional X-ray microtomography image data. Insets: Comparison of occurring liquid cluster morphologies (taken from [139]).

however, can only be analytically solved in few special cases. Consequently, approximate solution procedures have been proposed. The simplest approximation, denoted by “toroidal approximation”, is to describe the meridional profile of a pendular bridge as a segment of a circle, as originally introduced by Haines [89]. The application of the toroidal approximation to unequally sized spherical particles involves more complex terms compared to the case for uniformly sized spheres [153]. Derjaguin approximation [154] is introduced to calculate the capillary forces for this case. The radius of the particle in the equation for two equal spheres is replaced by the harmonic mean sphere radius in this case.

The errors associated with estimating the capillary forces using the toroidal approximation have been examined in [150] and [153]. These errors are less than 10% for small values of separation distances and bridge volumes. A simple toroidal

approximation is derived for a sphere in contact with a flat surface in [155]. Marmur [156] showed, however, that the applicability of this equation was limited. Furthermore, Hotta et al. [141] introduced the “gorge method”, another approximation method for computing the capillary force based on the neck of a liquid bridge. Hotta proved that this method improves the accuracy of capillary force prediction and this has been verified by Lian et al. [142].

The calculation of capillary forces in wet granular materials remained an active field of study since the already mentioned pioneer works of Haines [89] and Fisher [29]. The majority of models calculating capillary forces refers, however, to the case of isolated pendular liquid bridges [141-143, 149-151], which restricts the applicability to the region of low liquid content of the media [36, 157]. At higher liquid content, the pendular liquid bridges coalesce and transformation into a funicular structure takes place. Despite the recent developments in three-dimensional imaging techniques, such as fast confocal microscopy [158] and X-ray tomography [159], there are only few studies on the calculation of capillary forces between spherical particles in the funicular regime [159-161]. The magnitude of capillary cohesion evolves smoothly during the increment of the liquid content from the pendular regime into the funicular regime [159]. Measurements of capillary cohesion employing the fluidization threshold or the tensile strength [36, 159] reveal a plateau in the range of liquid content lower than 25%. At higher liquid contents, capillary cohesion gradually decreases with increasing liquid content and vanishes at full saturation of the pore space. Besides, the liquid transfer from one capillary bridge to another is not taken into account in many studies [29, 142, 144, 145, 152, 154, 162-165]. This is justifiable for the case of isolated pendular liquid bridges but not for higher saturation regimes, like the funicular and the capillary regime, because the liquid bridges can coalesce in these cases.

Former DEM-based studies on capillary forces in granular media emphasized the effect of capillary interactions on the macroscopic cohesion [31, 36]. It is stressed that the number of liquid bridges per grain plays an important role in the behavior of macroscopic strength [31], whereas the volume of liquid bridge does not have a remarkable influence on macroscopic strength. In the context of a drying process, the evolution of the liquid bridge between two spherical particles has been investigated for the cases of fixed distance in [38] and extended distance in [39]. Capillary force is

determined from the measured bridge curvatures along the evaporation process and compared to the experimentally measured data [39]. Simulation results on the evolution of capillary force for the case of irregular two-dimensional and regular three-dimensional packings of equal-sized particles during drying process have been reported in [71] and [72], respectively. The calculation of capillary force acting on each solid particle is based on the saturation of the pores associated to the considered particle. The force contribution from the three-phase contact line is not considered in either of these two studies. The drying simulations have been conducted at two conditions, with and without liquid viscosity.

2.4 Modeling of fluid-solid interaction

The heterogeneity in the spatial distribution of pore size leads to heterogeneity in the spatial distribution of capillary forces inside the porous media. This governs the liquid (usually water) transport within the pore space. Understanding the interaction between pore-scale water movements and the behavior of associated solid skeleton in the context of drying is important to control the mechanical behavior (e.g., crack formation, shrinkage) and increase the quality of the final products.

The coupling between pore-scale water movement and microstructure formation in cement-based materials during drying has been experimentally investigated using X-ray dark-field contrast imaging in [166]. Water menisci inside the pore space are formed due to the evaporation. The evaporation typically starts from the surface(s) exposed to the surrounding ambient, then slowly propagates towards the interior of the specimen. The heterogeneity in the spatial-temporal distribution of such menisci results in the development of gradients in the capillary force field, which is responsible for plastic deformation and drying shrinkage. Thus, it is important to understand the interrelation between microstructure formation (the appearance of shrinkage-induced micro-cracks) and the drying progress inside the specimen. This contributes to the development of crack/shrinkage reduction approaches based, e.g., upon shrinkage reducing admixtures [167] or internal curing water-saturated particles [168].

Equations governing the interaction between liquid and solid phase are challenging to be solved analytically due to the nonlinear and complex boundary conditions

encountered in practical problems. Therefore, numerical approach is conventionally used to solve the system of governing equations. In the context of drying investigations, the Lattice Boltzmann Method (LBM) has been utilized recently to investigate the capillary instabilities and film-effects for the case of a bundle of capillaries [169]. This model was extended to study the fluctuations in drying rate curves of porous media [170] and to take into account thermal gradients [171]. The porous media investigated in these studies are of limited size, due to the high

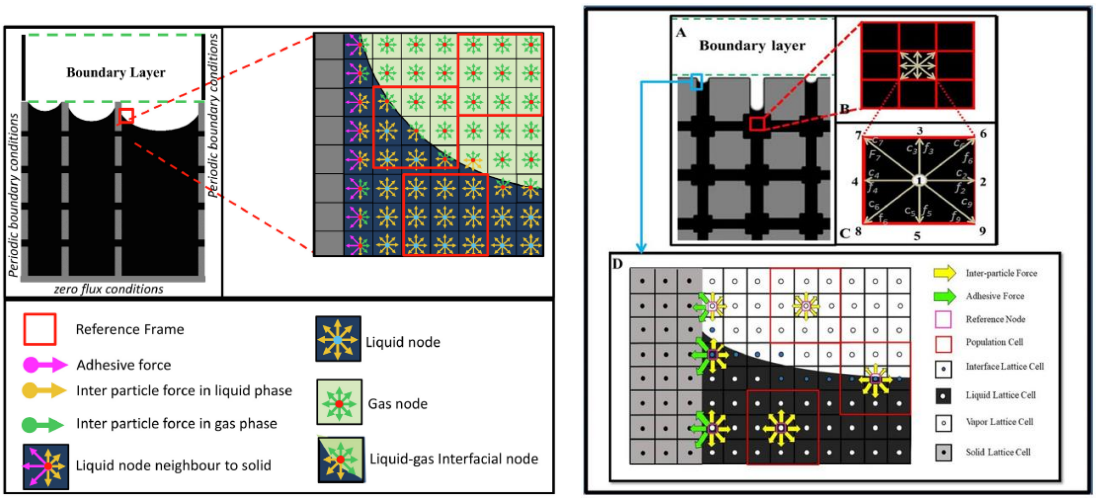

(a) (b)

Figure 2.3. Illustration of the solid–liquid-vapour interaction in Lattice Boltzmann model for the study on the drying problem of (a) a bundle of capillaries [169] and (b) two-dimensional regular pore network [170]. Figures have been taken from [169] and [170].

computational cost of LBM. The capillary channel shown in Fig. 2.3a had a depth of 7.2 mm and a width of 0.72 mm, while irregular porous media were assumed to be two-dimensional (Fig. 2.3b). Regarding the fluid-particle interaction modeling, computational fluid dynamics (CFD) has been coupled with the discrete element method (DEM) to investigate the drying of droplets on particle surfaces in a Wurster fluidized bed [172]. In this frame, the influence of the capillary force resulting from the liquid bridges between particles on the coating and agglomeration behavior can be investigated using DEM. An investigation at the microscopic scale of three-dimensional highly porous particle aggregates during convective drying is reported in [173]. The solid phase is numerically generated using DEM. The liquid‑gas interface is tracked over time using the volume of fluid (VOF) method (Fig. 2.4). The high

porosity of the aggregate results in significant displacement of the particles, which requires a proper update of the void space in the deformed solid matrix as well as of pore saturation (liquid redistribution) in each drying simulation step. The investigated aggregate consisted of 395 primary monodisperse particles having diameter of 10^{-8} m.

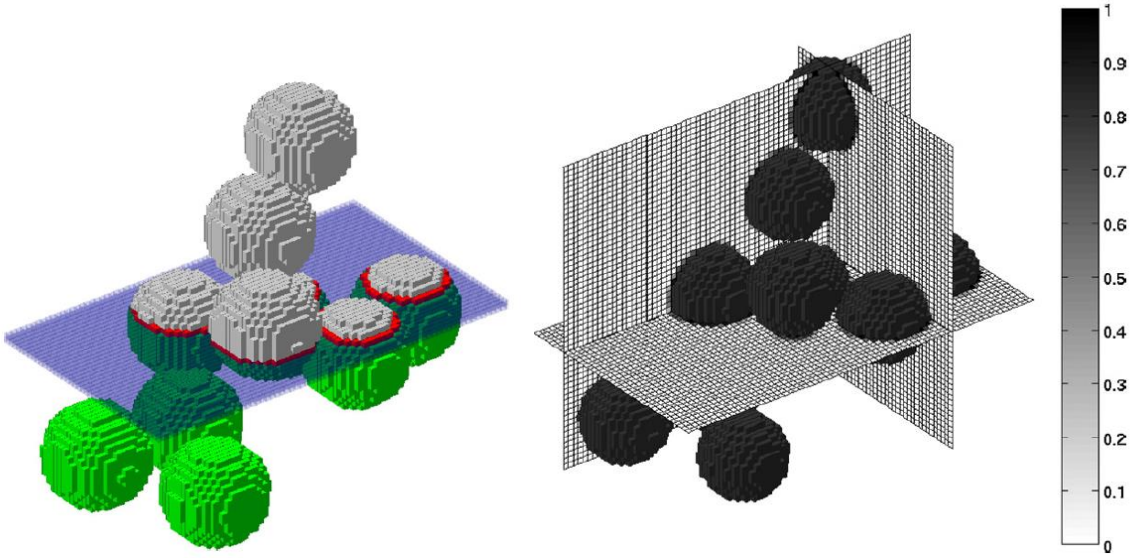

(a) (b)

Figure 2.4. Illustration of (a) the uniform spatial discretization of the solid and fluid phases in a study of the drying of a highly porous aggregate using the VOF method; (b) The resulting solid volume fraction. Figures have been taken from [173].

To avoid the high computational cost of the CFD or LBM, pore network models (PNM) are a very promising compromise for combination with DEM. In these models, the spatial discretization of the void space leads to a fluid computational mesh that has a size similar to the size of solid particles. Moreover, proper assignment of properties to pores and throats can capture the effect of local void geometry on the flow. PNM has been extensively used for studying single phase and multiphase flow in rigid porous materials, e.g. in two dimensions for granular materials [174, 175] and in three dimensions for fractured rocks [176] or sphere packings [75]. As already mentioned, PNM can reflect the effects of the local geometry of the pore space on the flow and gives predictive estimation of the permeability [177].

In the context of drying aggregates, a coupled PNM-DEM scheme has been implemented to study the micro-mechanical behavior of three-dimensional densely packed monodisperse aggregates in [71]. This fluid-particle coupling is executed in two separated passes. In the first pass, the evolution of liquid distribution obtained from the drying PNM is the input for the calculation of capillary forces exerted on solid particles (Fig. 2.5). These calculated capillary forces are stored over time for the whole drying simulation. Then, in the second pass, the saved capillary force protocol is the

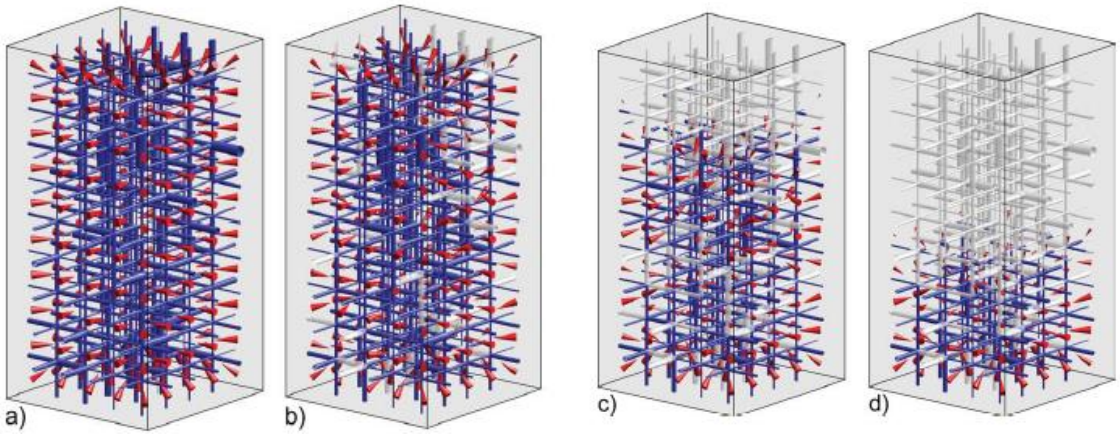

Figure 2.5. Illustration of capillary forces at different network saturations during the drying of three-dimensional regular monodisperse aggregate for the case of negligible liquid viscosity: (a) fully saturated network, (b) network saturation of 0.9, (c) 0.6, and (d) 0.3. Figures are taken from [71].

input for the DEM-based simulation to evaluate the mechanical behavior of the particle aggregates. The investigated aggregates had two sizes: 5 × 5 × 10 particles and 10 × 10 × 20 particles, and the particle diameter was 500 nm. To apply a capillary effect in the void space of this regular particle packing, the radii of the cylindrical pores were assumed to be mathematically distributed following a normal distribution having a mean of 103 nm and standard deviation of 1 nm. Simulated results for the case of an aggregate made of stiff material suggest that the difference in spatial liquid distributions and the corresponding capillary forces cannot explain the fact of more damage under fast drying conditions.

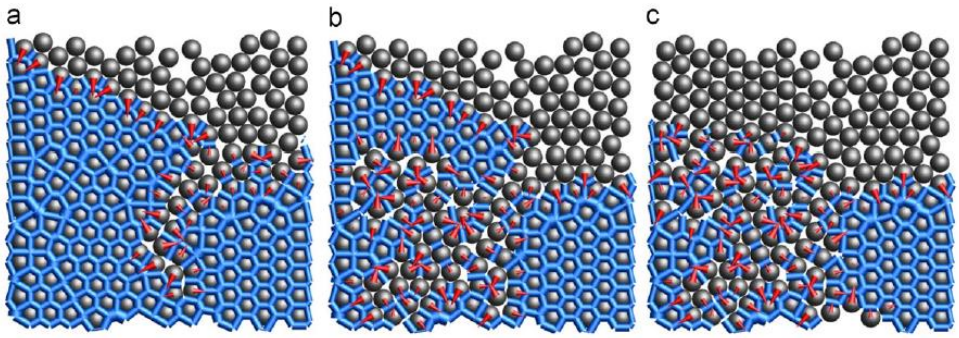

Figure 2.6. Illustration of capillary force at different network saturation during the drying of two-dimensional irregular monodisperse aggregate for the case of negligible liquid viscosity: (a) network saturation of 0.85, (b) 0.55, and (c) 0.3. Figures are taken from [72].

The PNM-DEM coupling scheme that has been introduced for the case of regularly packed aggregates in [71] was extended to be applicable for the case of irregularly packed aggregates in [72]. The pore network representing the void space was generated using Voronoi tessellation [73]. Cylindrical pores were based on Voronoi edges, and the pore radii were calculated from the distances between Voronoi edges and their associated particles. This pore network construction results in a more physical geometry than the one in [71], in terms of pore location and pore radius distribution, as well as pore coordination. The PNM-DEM coupling is executed in two passes, similarly to [71], which neglects the influence of the change in the solid matrix on the liquid flow simulation, corresponding to a one-way coupling approach. The investigation of drying kinetics was conducted for a two-dimensional aggregate consisting of 4142 particles. The particle radius was 250 nm, resulting in a network size of 30 μm^2. The radius distribution of the associated pore network had a mean value of 103 nm and standard deviation of 15 nm. However, for the investigation of liquid-particle interaction, simulations were implemented on smaller aggregates, 216 particles having diameter of 80 µm (Fig. 2.6) and 1490 particles (on average) having the same diameter. Simulation results show that higher local force gradient (for the case of negligible viscosity) results in more damage induced by capillary forces compared to more uniform force distribution patterns (for the case of high liquid viscosity, i.e. immobile water). Simulation results also suggest the potential influence of liquid phase distribution on the damage, in terms of number and distribution of

cracks. However, the results from this study still cannot explain the fact that conditions of fast drying are empirically known to create more damage.

Chapter 3

Pore network models for given 3D aggregates of randomly packed particles

The porous media are represented by dense, randomly arranged packings of spherical particles (called aggregates) in this study. The information on the radius and the center coordinates of the particles can be obtained directly from the post-processed data of X-ray images of the aggregate used in reality (as will be presented in this chapter) or be numerically generated using the discrete element method (DEM) (presented in the next chapter). The void space complementary to the given solid aggregate is discretized using Delaunay triangulation and its dual Voronoi tessellation. The output of Delaunay-Voronoi discretization is the pore morphology data used as the input of the newly developed drying pore network model (called triangulation pore network model (TPNM) in this study). These pore morphology data are obtained by using Yade-DEM. This derivation and the way in which the morphology of the void space in particle assemblies can be represented is first outlined. Then the drying PNM algorithm that has been developed in a manner that enables to make use of the structural information provided by Yade-DEM and implement the specific pore morphology data is presented. The resulting TPNM is assessed by comparing the outcome of simulation by this pore network model with experimental results gained in a previous investigation by drying a small packed bed of spherical particles inside the X-ray μ-CT scanner. Moreover, comparisons are made with simulated results obtained

from other pore network models. Latter are more conventional in their design as well as much more indirect in respect to and remote from real morphology than TPNM.

3.1 Void space discretization: Delaunay triangulation – Voronoi tessellation

After the solid skeleton has been defined, either by imaging the real particles in 3D or by algorithmic generation of a synthetic particle packing, the corresponding void space is decomposed into an interconnected network of tetrahedral cells having their vertices located at the centroids of particles (Fig. 3.1a). This is achieved by applying the regular Delaunay triangulation (grouping the four nearest center points in 3D or the three nearest center points in 2D). The resulting tetrahedra fill the space completely. Each of them contains parts of four particles and a void space in the middle. The wide void volumes inside tetrahedral cells represent pores which are interconnected to other adjacent pores via four truncated triangular facets (Fig. 3.1b). Each facet is in the middle of one of the faces of the tetrahedron and its adjoining neighbor, and it is called a throat. So throats do not have volume in this model, just their cross-sectional area.

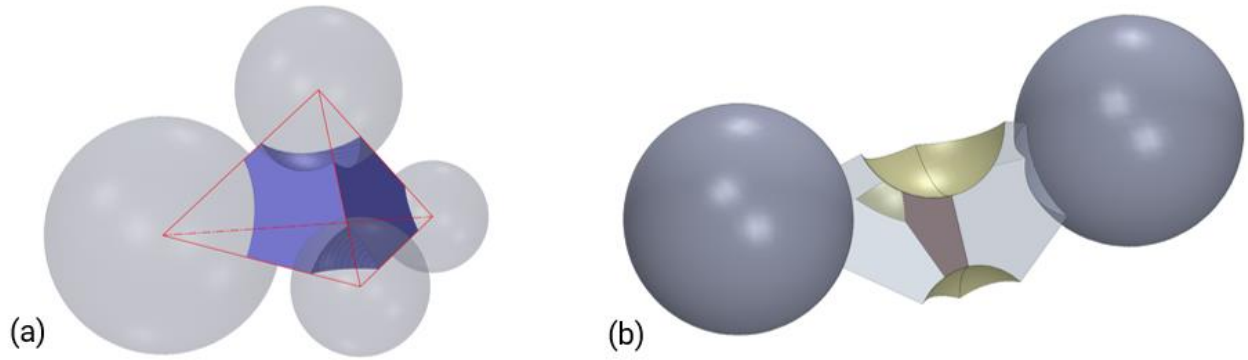

Figure 3.1. (a) Illustration of a pore (in blue) enclosed in a tetrahedral cell (red edges) among four neighboring spherical particles (transparent grey spheres). Parts of faces of the tetrahedron which are not occupied by the solid phase represent throats. (b) A throat (brown, truncated triangle) located at the common facet between two adjacent pores. These two pores are transparent to make this common throat visible. The common particles of these two pores are hidden. The contact area between these common particles and the two pores is shown in gold. Solid particles which are not in common for these two pores are shown as grey spheres.

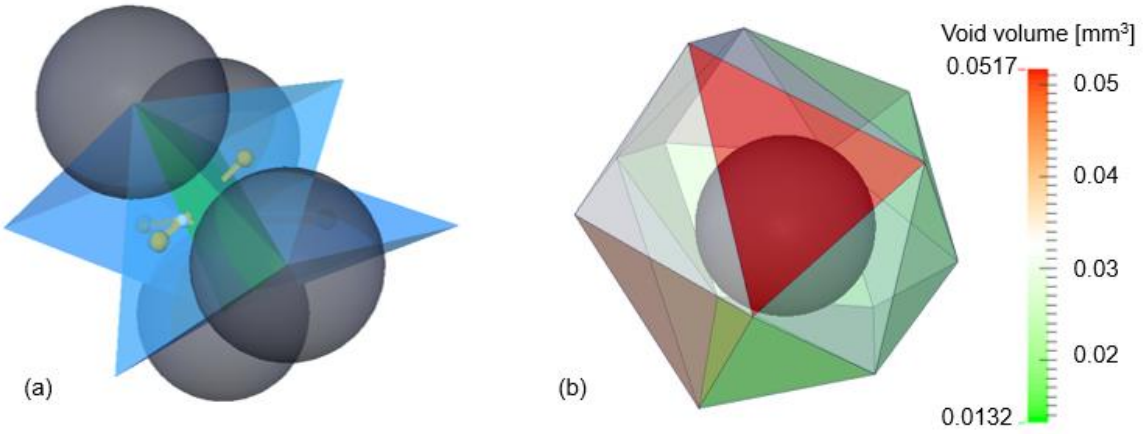

Figure 3.2. (a) Illustration of a tetrahedral cell (green) and its four neighboring tetrahedral cells (blue). Only four solid particles, serving as vertices of the green tetrahedral cell, are shown as transparent spheres, all other vertex particles of the four neighboring tetrahedral cells are not shown. The Voronoi center of the green tetrahedral cell is indicated by a small sphere (white) and the Voronoi centers of the four neighboring cells are indicated by further four small spheres (yellow). (b) The local void space surrounding a solid particle is shared among many tetrahedral cells; in this case twenty-six cells. The color map shows the volume of the tetrahedral cells.

Contrary, the pores have volume. The volume of a pore is determined by subtracting from the total volume of the corresponding tetrahedral cell its respective solid volume, which is the sum of the four solid particle portions confined within this tetrahedral cell. The positions of pores are defined as the vertices of the Voronoi tessellation dual to the Delaunay triangulation that has resulted in the pores (Fig. 3.2a). The Delaunay edge is the line connecting two particle centers and its associated Voronoi edge is a collection of points having equal distance to these two particle centers (Fig. 3.3). Each facet of the truncated tetrahedral pore (Fig. 3.1a) is one throat. One pore has four throats, through which this pore connects to its four neighboring pores. Volume, position as well as coordination information of pores (i.e. data structure of the pore network, ID of four neighboring pores of each pore as well as ID of the associated throats between these adjacent pores) are used as input for the drying model described in Sec. 3.3.

Exemplary tetrahedral cells surrounding a solid particle are shown in Fig. 3.2b. The number of pores associated to one particle (i.e. the number of pores that have a certain particle as their vertex) depends on the spatial distribution of the particles in the packing (dense or loose packing) as well as the size ratio between particles (one big

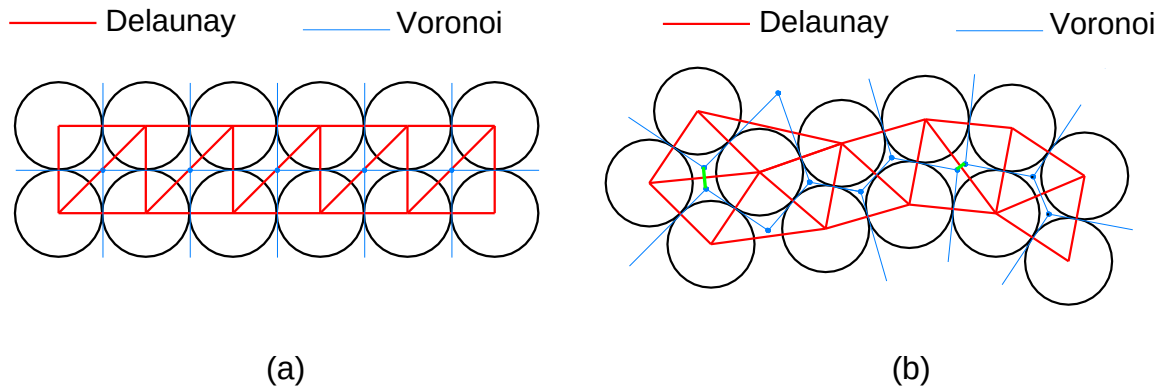

Figure 3.3. Illustration of the Delaunay triangulation and its dual Voronoi tessellation in 2D: (a) Regular packing and (b) irregular packing of monodisperse disks. The blue dots represent Voronoi vertices. Contrary to the regular packing, some distances between Voronoi vertices (marked green) are much smaller than particle size in the irregular packing.

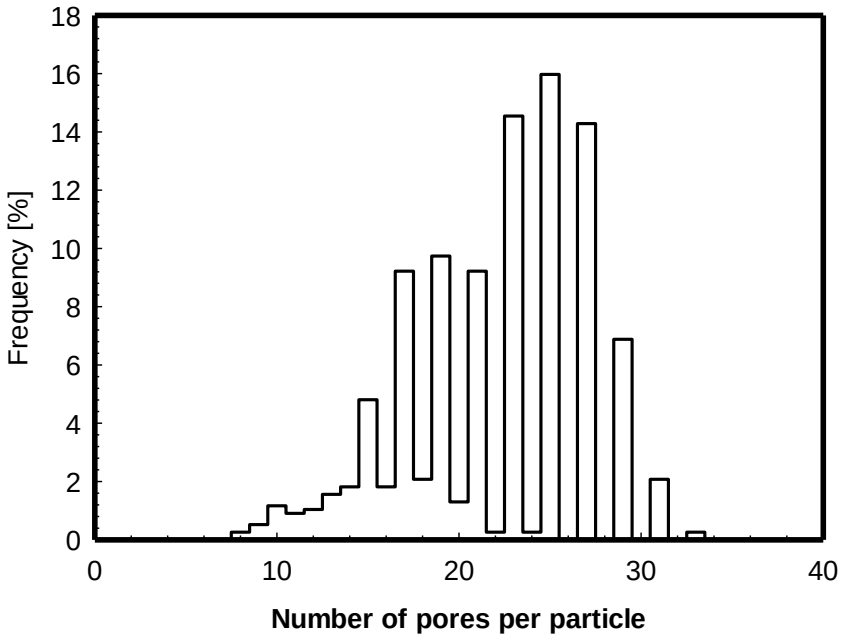

Figure 3.4. The distribution of the number of pores per particle of the network used in TPNM simulation, based on the post-processed X-ray data of the aggregate used in the experiment of [199].

particle surrounded by many small particles results in higher number of associated pores than the same particle surrounded by bigger neighboring particles). The distribution of the number of pores per particle of the network used in TPNM simulation, based on the post-processed X-ray data of the aggregate used in the experiment that has been described in [178], is illustrated in Fig. 3.4. An illustration of

particles having different number of pores per particle in this aggregate is shown in Fig. 3.5. The average number of pores per particle is 20.7 and the respective standard deviation is 5.3. These numbers are shifted to 23.3 (average) and 4.3 (standard deviation) for particles located in the interior of the aggregate. For particles at the margin of the aggregate the average and the standard deviation of the distribution of the number of pores per particle are 16.9 and 3.4, respectively.

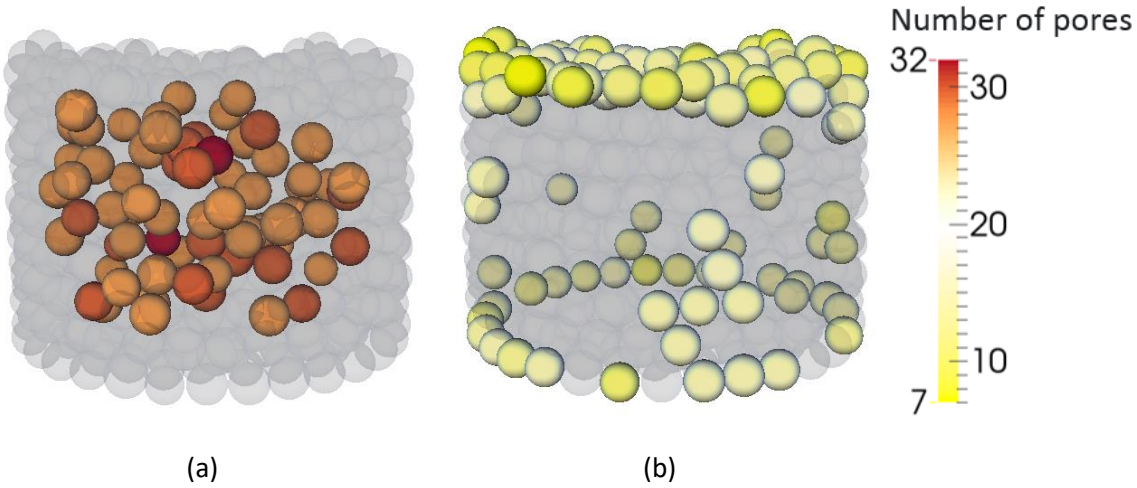

Figure 3.5. Illustration of the particles having different number of pores per particle of the network used in TPNM simulation, based on the post-processed X-ray data of the aggregate used in the experiment from [178]: (a) Particles having number of pores per particle from 28 to 32; (b) from 7 to 15. Particles located in the interior of the aggregate have higher number of pores per particle than particles located at the outer region of the aggregate.

3.2 Morphology data of the void space

Delaunay triangulation results in a network of truncated tetrahedral pores (Fig. 3.1a) interconnected through irregularly shaped throats (Fig 3.1b). As already stressed, the throats are merely cross-sectional areas, without volume. The volumes of the tetrahedral cells as well as the volumes of the associated pores are obtained from the open-source software Yade-DEM [179]. During the drying process, a meniscus (liquid-gas phase interface) appears at one of the four throats of a pore once the adjacent pore interconnected to this pore through that throat is occupied totally by the gas phase. The liquid is then gradually drained from this pore, but the meniscus remains pinned at the specific throat until the capillary pressure across this meniscus exceeds

the entry capillary threshold value associated with the throat. Then the pore becomes fully invaded and totally occupied by gas phase, and a new meniscus appears at another throat between this pore and its adjacent saturated (fully or partially) pores. The determination of capillary pressure at a throat is presented in the subsequent drying algorithm section. Regarding the capillary threshold value, its determination, in this study, is based on the MS-P (Mayer and Stowe-Princen) method as proposed in [77, 180] and implemented in Yade-DEM. The determination results for every throat in an entry capillary pressure $p_{c,e}$, which is obtained from an entry capillary radius $r_{c,e}$ as

$$p_{c,e} = \frac{\sigma}{r_{c,e}} , \tag{3.1}$$

where σ is the surface tension. The meniscus recedes through the throat into the corresponding pore once the capillary pressure p_c at that meniscus exceeds $p_{c,e}$. This entry value of the capillary radius $r_{c,e}$ depends on the geometry of the throat, which, in turn, is determined based on the spatial correlation as well as the sizes of the solid particles confining the associated pore. Specifically, following the implementation of the MS-P method [181, 182] proposed by [183, 184] $r_{c,e}$ is the common radius of three menisci in the throat facet (Fig. 3.6a) which fulfills the balance between capillary pressure and surface tension applied on the three-phase contact line associated with the meniscus. Under perfectly wetting conditions of the solid surface by the liquid (i.e. contact angle of θ = 0°) the equations presented by [77, 184] can be used for computing the value of $r_{c,e}$. The respective derivation is presented with some more detail in Appendix A1 and has been used through the present work, assuming θ = 0°. The real value of $r_{c,e}$ usually lies between an upper bound, which is the radius of the circle inscribed in the throat, and a lower bound, which is the maximal half-distance between circular particle cross-sections associated to the considered throat, Fig. 3.6b. Then, the value of $r_{c,e}$ can be computed by dichotomy in this interval. Out-of-range values are though possible in exceptional situations of, e.g., very flat Delaunay triangles [185]. In any case, the entry capillary radius $r_{c,e}$ must be computed iteratively, but at constant and given contact angle this can be done in advance (i.e. before PNM simulation of drying), because $r_{c,e}$ is a purely geometrical property of the respective throat.

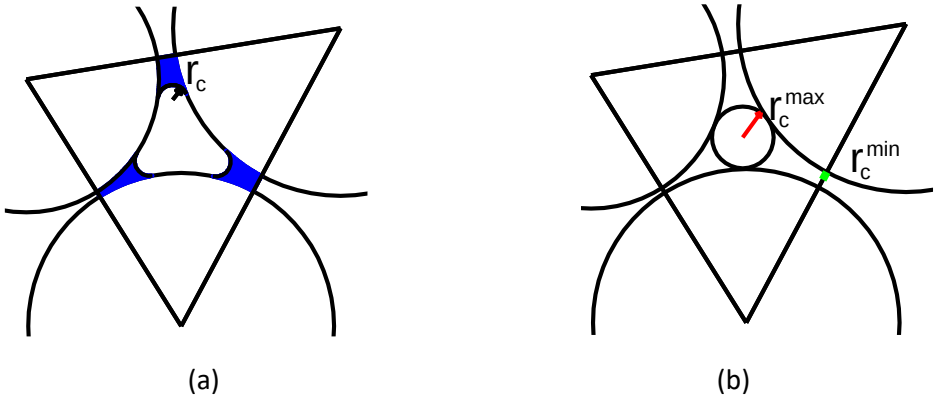

Figure 3.6. Illustration of (a) the entry capillary radius and (b) the usual upper and lower bounds of it.

The morphology data on the void space of the given solid aggregate to be used as the input of the drying model consists of the following information:

(i) The locations of Voronoi vertices, which are assumed to define the centers of the pores (location of pores in space).

(ii) The void volume of each pore, as a measure of pore size.

(iii) The data structure regarding the coordination between pores in the network (which pore connects to which other pore, through which throat).

(iv) The entry capillary threshold value of the four throats associated to each pore (to decide whether this pore is invaded when the invasion front (or the gas phase) reaches it at these throats) (Fig. 3.6).

(v) The area of the irregularly shaped (a triangle truncated by the solid sectors) throat between two adjacent pores.

The application of morphological features of the void space, especially the pore volume and throat entry capillary threshold, in the TPNM will be presented in the next section.

3.3 Drying algorithm

In many pore network model (PNM) algorithms, the drying process is interpreted as an invasion percolation phenomenon driven by the transformation of liquid into vapor. At the current state of model development, the algorithm used in TPNM is limited to the capillary dominated regime, i.e. the effects of liquid viscosity or gravity are neglected [186]. The pore network is initially saturated with volatile liquid (here, water). Menisci are assigned to all throats with at least one neighboring pore located in the gas-filled region. This region is initially just the boundary layer (BL) outside of the drying material (a diffusive layer on the network's top surface), but it develops further into the pore network once more and more pores are occupied by the gas phase. Corresponding to air (convective) drying, the gas phase is considered to be a binary mixture of air and water vapor. The evaporation occurs at active menisci, which decreases the liquid pressure in the corresponding pores. The gradient in liquid pressure thus leads to liquid capillary flow within the liquid phase. As mentioned, liquid flow is here considered to be frictionless.

In this study, conditions of slow drying (or low heat supply from the surrounding atmosphere) are assumed. Under such simplified conditions, liquid supply from the interior of the pore network can more easily satisfy the evaporation demand at the pore network surface. This implies that the liquid capillary flow is much faster than the local evaporation at menisci as well as the vapor diffusion from the menisci towards the gas-filled region. Consequently, it is justified to neglect the effect of liquid viscosity. The amount of evaporated liquid is contributed from all pores having menisci at their throats to maintain a uniform liquid pressure field. It is also assumed that only one pore empties in each drying time step. The meniscus associated to this pore is called moving meniscus, whereas all other menisci located in saturated pores are called stationary menisci. The pore with a moving meniscus has the highest liquid pressure. By definition, the capillary pressure at the meniscus p_c is the pressure difference between the gas phase p_g and the liquid phase p_l:

$$p_c = p_g - p_l. \tag{3.2}$$

Due to the slow drying condition, the gas pressure is the same everywhere within the gas-filled region of the network. Consequently, the liquid pressure of a pore with

meniscus at its throat depends only on the capillary pressure at the corresponding throat meniscus:

$$p_l = p_g - p_c. \tag{3.3}$$

The liquid pressure is calculated based on the threshold capillary value of the throat at which the meniscus is pinned (or equivalently the meniscus curvature, where the two are related via the Young-Laplace law):

$$p_l = p_g - p_{c,e} = p_g - \frac{\sigma}{r_{c,e}}. \tag{3.4}$$

The pore associated with a throat having highest $r_{c,e}$ is the one having highest liquid pressure and empties in this time step. This time step is calculated based on the volume of liquid in this pore and the total evaporation rate of all menisci during this invasion. Besides, there is initially one liquid cluster, but when drying proceeds, due to the size distribution of pore volumes and throat entry capillary radii, the initial liquid cluster splits into separate liquid clusters of different sizes. Each liquid cluster with a moving meniscus requires a certain period of time to empty its pores. The time step is chosen as the shortest time among all liquid clusters. This choice results in formation of partially liquid-filled pores which require longer time to be completely drained by gas. The liquid clusters are labelled using the modified form of the Hoshen-Kopelman algorithm [187]. This drying algorithm is graphically shown in Fig. 3.7.

What makes TPNM different to previous drying PNM is the application of the pore volume and throat entry capillary radius $r_{c,e}$ to the pore invasion rule. When a pore (called pore A) is reached by the gas phase for the first time at one of its four throats (this throat is called throat 1), only the $r_{c,e}$ of this throat 1 is used to decide the invasion of this pore A and is the representative $r_{c,e}$ of pore A. The $r_{c,e}$ of the other three throats of pore A will not be used at this moment. If the representative $r_{c,e}$ of this throat 1 is not the largest one among all representative $r_{c,e}$ of other pores also reached by the gas phase and belonging to the same liquid cluster with the considered pore A, the pore A will not be invaded at this simulation step (the meniscus at this throat 1 is a stationary meniscus). Later on, the gas phase reaches the pore A at another throat of it, called throat 2. Now, the representative $r_{c,e}$ to be chosen to decide the invasion of pore A will be the highest value among the $r_{c,e}$ values of throat 1 and of throat 2. If this

representative $r_{c,e}$ of pore A is the largest one among all representative $r_{c,e}$ of other pores also reached by the gas phase and belonging to the same liquid cluster with the considered pore A, the pore A will be invaded (the meniscus at the throat corresponding to the chosen $r_{c,e}$ is a moving meniscus). Otherwise, pore A will stay saturated. Then this rule is applied similarly to throat 3 of pore A. In case the 4th throat of pore A is reached by the gas phase (i.e. pore A remains saturated despite of three of its throats having been reached by the gas phase), pore A becomes an isolated liquid cluster (a liquid cluster that consists just of one single pore).

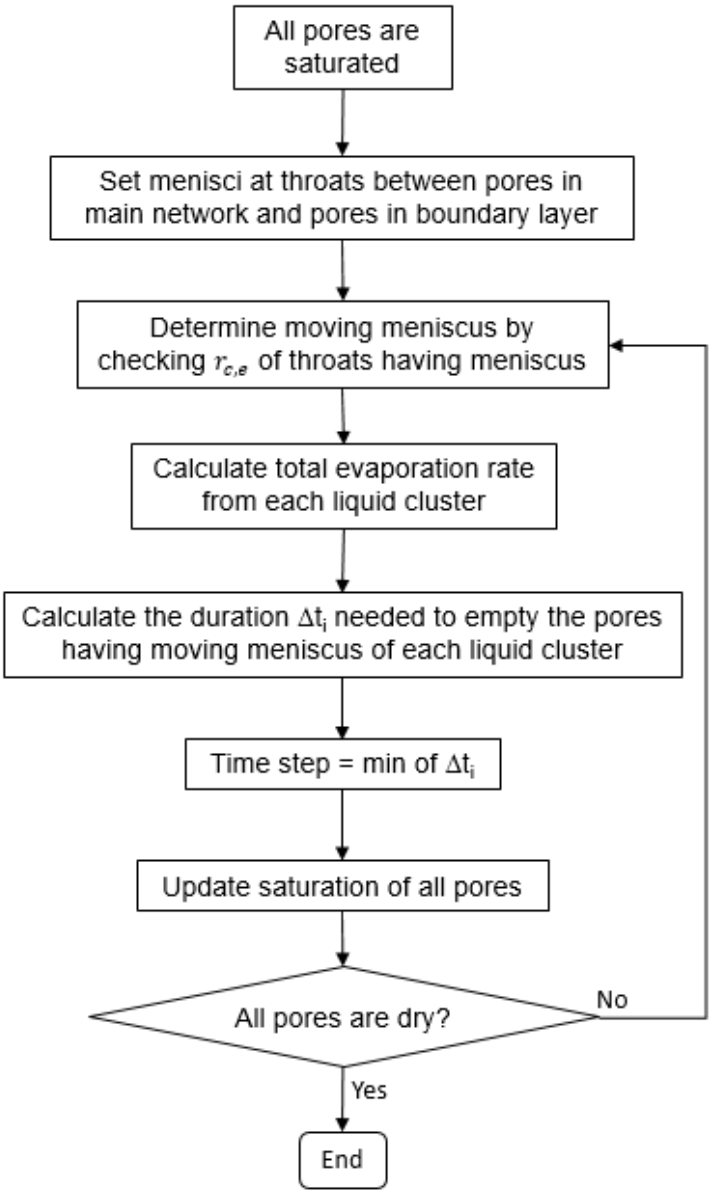

Figure 3.7: The drying algorithm used in TPNM.

During each simulation time step, it is assumed that there is no local accumulation of vapor in the gas phase (total gas pressure remains constant at ambient value). The vapor diffusion in gas-filled pores, driven by differences in the partial pressure of water vapor, is described by Stefan's law. Additionally, in the gas-filled region of partially saturated pores, it is assumed that the gas is saturated with vapor (local equilibrium), hence neglecting any vapor diffusion resistance therein. The exact calculation of the mass transfer between two adjacent irregularly shaped pores i and j (see Fig. 3.1b) through an irregularly shaped throat is computationally demanding. Thus, this mass transfer, in this study, is approximated by the mass transfer inside a cylindrical tube having a cross-sectional area A_{ij} equal to the area of the throat between these two adjacent pores. The length of this tube is set equal to the distance L_{ij} between the centers of two adjacent pores i and j, measured as distance between the respective Voronoi vertices. The following mass balances are applied for all gas-filled pores i with unknown vapor pressure $p_{v,i}$:

$$\sum_{j=1}^{k} \dot{M}_{v,ij} = \sum_{j=1}^{k} A_{ij} \frac{\delta}{L_{ij}} \frac{p\tilde{M}_v}{\tilde{R}T} ln\left(\frac{p-p_{v,i}}{p-p_{v,j}}\right) = 0, \tag{3.2}$$

where $\dot{M}_{v,ij}$ is the vapor mass flow rate; A_{ij} mass exchange area between pore i and its neighboring pore j; δ binary diffusion coefficient between vapor and air; L_{ij} distance between the centers (Voronoi vertices) of two adjacent tetrahedral cells i and j; $\tilde{M}_v$ molar vapor mass; $\tilde{R}$ universal gas constant; T absolute temperature; p total pressure of the gas phase (set equal to the total pressure of ambient air, p_g); $p_{v,i}$ and $p_{v,j}$ partial water vapor pressure of pores i and j. Closure conditions applied are the equilibrium vapor pressure p_v^* at liquid-gas interfaces (menisci, obtained at the moderate and spatially uniform temperature assumed for slow drying) and the partial pressure of vapor in the ambient gas $p_{v,\infty}$ at the top of the gas-side boundary layer (depending on ambient air humidity). The index k is the number of neighboring pores j of pore i (coordination number of pore i). The value of k is by definition of the triangulation four for every pore located inside the body. It is noticed that the boundaries (sides, top, bottom) of the body are represented by fictitious spheres having infinite radius and surface which is tangential to the particles located at the boundaries. Therefore, the value of k is formally also four in the main parts of the boundaries of the body. An exception are corner pores in contact with two boundaries (in 2D) or three boundaries

(in 3D). For a cubical simulation domain, the number of these exceptional pores is eight and the coordination number of each of them is three (further details in Appendix A2).

3.4 Model assessment

Simulation results obtained from our pore network model, called triangulation pore network model (TPNM), are compared with experimental results reported in [178]. The solid aggregate used in the experiment was an aggregate of glass beads. The glass beads were carefully selected one by one for the purpose of high sphericity and uniform size. The glass beads had according to the manufacturer a nominal diameter of 0.8 mm. These glass beads were stored in a cylindrical container having an inner diameter of 8 mm and a height of 10 mm. The container was filled with beads up to a height of approximately 6.5 mm, which results in an empty space of around 3.5 mm in height above the sample top surface. The evaporated water could only elude from the aggregate through the top surface of the sample. There was an air flow channel, closed from all sides but with an opening right above the top of the container. The air flowing inside this channel was controlled to maintain a temperature of 26 °C and velocity of 1 m/s. Due to the mentioned opening, some forced convection is expected to occur in the empty top space of the drying sample container. Consequently, conditions of diffusion in stagnant gas are expected to prevail for less than the previously stated 3.5 mm of empty space height. The glass bead aggregate was initially saturated with distilled water. The particle centroid coordinates and respective radii have been obtained using X-ray microtomographic technique. The solid phase in the TPNM simulation (the main aggregate) is defined based on the post-processed X-ray data for these solid particles, as shown in Fig. 3.8. The particle size distribution obtained by means of the μ-CT is also plotted in Fig. 3.8. It has an average diameter of 0.77 mm (somewhat smaller than the nominal diameter of the glass beads) and a standard deviation of 0.04 mm, meaning that the distribution is narrow but not exactly monodisperse.

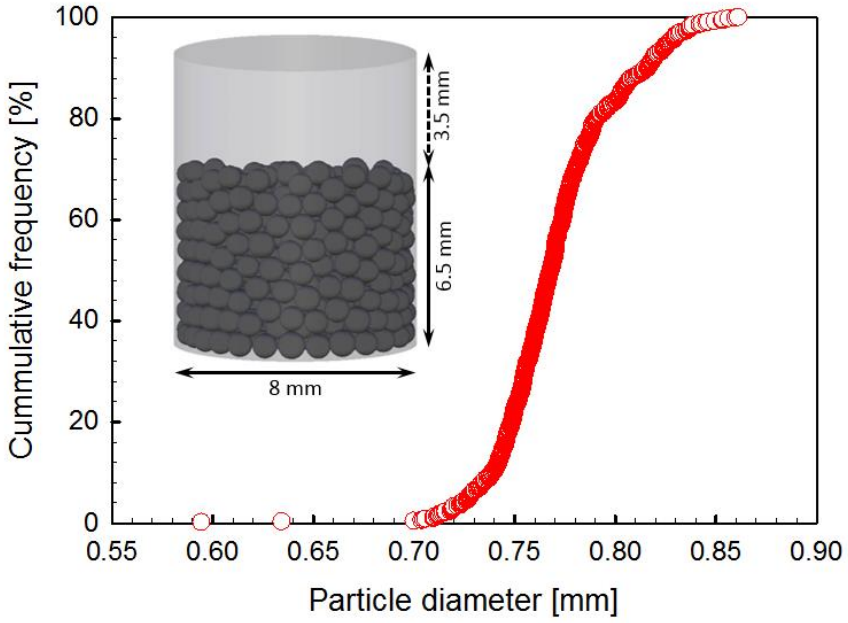

Figure 3.8. Particle size distribution obtained from the post-processed X-ray data of the glass bead aggregate used in the experiment. The inset visualizes the container and the glass beads based on the μ-CT data.

The simulation results obtained from the TPNM will be compared to the experimental results as well as to predictions obtained from a classical pore network model (CPNM) and the ring pore network model (RPNM) reported in [178]. The throat length value used as constant spacing in the regular grids of both CPNM and RPNM is 0.406 mm. The determination of the throat length in [178] is also based on Voronoi tessellation on processed μ-CT data, but without preceding Delaunay triangulation. There is an equivalent property in TPNM to the throat length in CPNM and RPNM, namely the distance between the Voronoi vertices of adjacent pairs of pores, denoted by L_{ij}. The size distribution of L_{ij} in the TPNM is shown in Fig. 3.9, and the mean value of L_{ij} in this plot is 0.388 mm. The reason for the difference between this value and the previously mentioned average throat length of 0.406 mm is that the throat length had been determined in [178] after the elimination of throats having L_{ij} lower than a threshold value, whereas all values of L_{ij} are kept in the present TPNM. The previously applied method of pore elimination has been presented in [26]. The reason for this elimination has been the relatively large overlap at the junctions of neighboring cylindrical throats. This is not the case in the present TPNM. Moreover, it is also noticed that the most frequent coordination number (number of neighboring pores to

which a certain pore is connected) before and after the throat elimination in [26] was four, which is equal to the coordination number of pores in the TPNM for an unconfined assembly of particles. However, and in full contrast to the uniform throat length in CPNM and RPNM, the throat length distribution of the TPNM is, according to Fig. 3.9, very broad. It starts with very short distances between neighboring Voronoi vertices of less than 0.1 mm. As already discussed in the context of Fig. 3.3, such short distances cannot exist in a regular packing of 0.8 mm spheres, but they are possible in random particle aggregates.

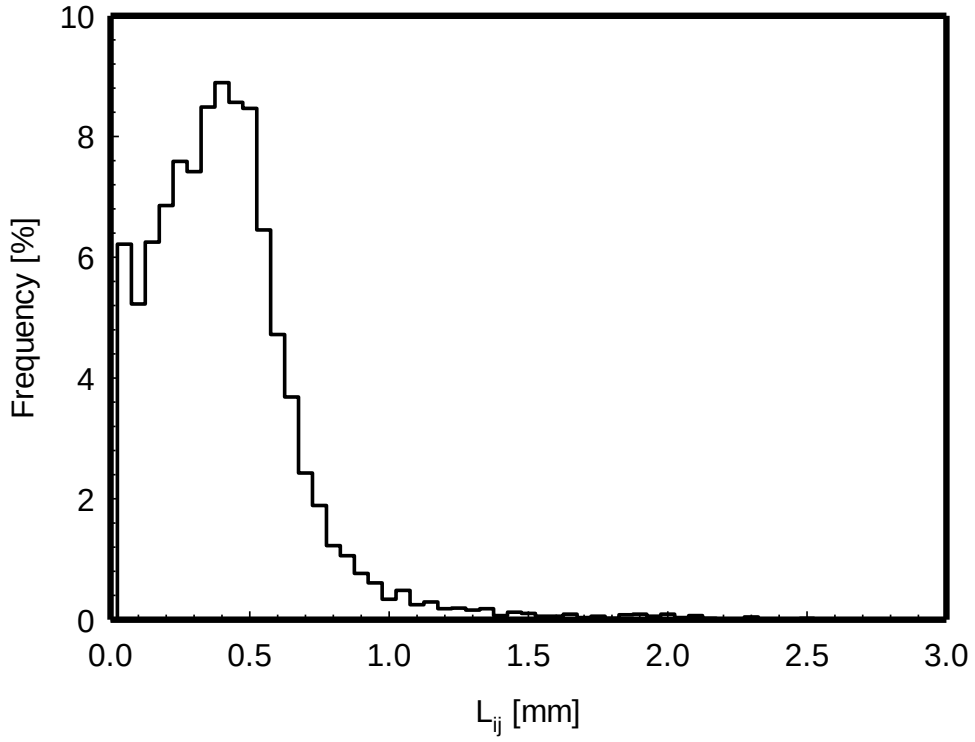

Figure 3.9. The size distribution of the distance between the Voronoi vertices of pairs of adjacent pores L_{ij}, determined by Yade for use in the TPNM from X-ray μ-CT data of the aggregate investigated experimentally in [178].

The total surface area to the ambient (counting both the solid phase and the voids) used in CPNM and RPNM [178] is approximated by the cross-sectional area of the circular cylindrical container having an inner diameter of 8 mm, which is 50.3 mm^2. Based on the throat length of 0.406 mm mentioned above and this surface area, and assuming a square cross-sectional plane of equal area, the number of throats in each lateral direction in CPNM and RPNM is calculated to 17.5. Rounding up and down, 18

and 17 throats in a rectangular but not exactly square cross section are obtained. The number of the throats along the vertical axis is calculated based on the aggregate height of 6.5 mm, as reported in [178], to nearly exactly 16. This results in a cuboid regular lattice of $18 \times 17 \times 16$ (width, depth, height) throats ($19 \times 18 \times 17$ pores (nodes)) that has been used in CPNM and RPNM.

The determination of the aggregate height used in TPNM is based on the post-processed data of X-ray images of the aggregate used in the experiment [178]. To this purpose, each particle radius is first added to the vertical coordinate of the respective particle position. These values are collected to make a list named “Top”. Then, each particle radius is subtracted from the vertical coordinate of the respective particle position. These values are collected in a “Bottom” list. The difference between the maximum value of the “Top” list and the minimum value of the “Bottom” list is the aggregate height, obtained at 6.4 mm. The outer diameter of the aggregate in TPNM is set as the inner diameter of the container reported in [178], namely 8 mm. The total solid volume results from the summation of the volumes of all solid particles (the radii of these particles are given by the post-processed data from X-ray imaging). The volume of a cylinder with height of 6.4 mm and diameter of 8 mm is taken as total volume. This way, the porosity of the aggregate is evaluated at 0.46.

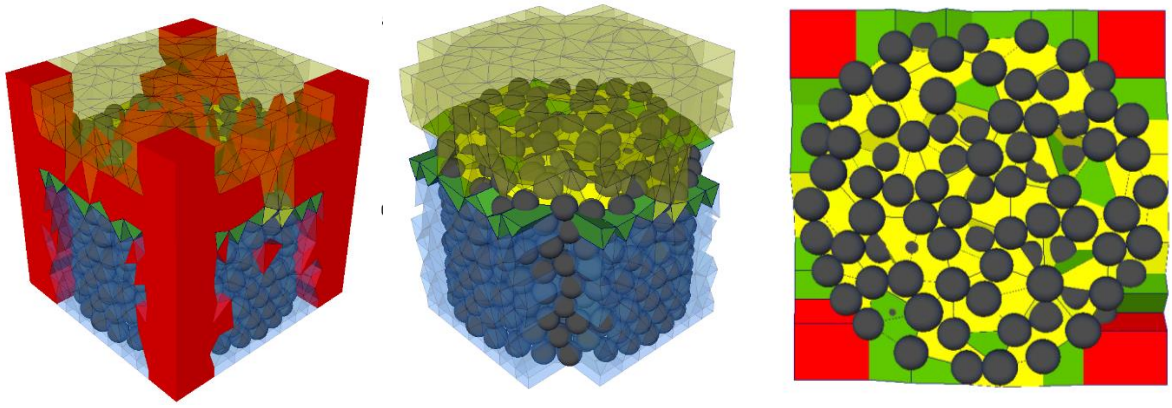

Figure 3.10. Illustration of the expanded and then partially shrunk aggregate used in the TPNM. The high porosity cells are shown in red. The cells which are located at the top surface but have lost their direct connection to the boundary layer due to the cell elimination process are shown in green, while top surface cells which still have direct connection to the boundary layer are shown in yellow.

The aggregate used in the experiment had a circular cylindrical shape. However, due to current restrictions of the triangulation process programmed in the open-source software Yade-DEM [179], the tessellation can only be implemented with flat boundary walls. Thus, a cuboid box is used as a boundary for the cylindrical aggregate. The aggregate (including the gas boundary layer above it) is inscribed in this cuboid box. The pore network in the TPNM is subdivided into the main network that corresponds to the particle aggregate and an adjoining network that represents the gas boundary layer. They are both defined by applying the void space discretization (Delaunay-Voronoi tessellation) on the particle packing that builds the main aggregate and on an artificial particle packing on top of it. The creation of this boundary layer particle packing will be presented later. Consequently, there are 4242 cells in the main network and 1332 cells in the boundary layer network. However, this configuration (a cylindrical aggregate inscribed in a cuboid box) results in that there are cells having high porosity (ratio of void volume over total volume of the tetrahedral cell) located mostly in the regions at the four vertical channels along the four corners of the cuboid box. 228 high porosity cells (having cell porosity larger than 80%), i.e. 4.10% of all cells, occupy 36.9% of the void volume of the whole medium. Most of these high porosity cells are in the region along the four corners of the cubic boundary box, which is unwanted because this region is not present in the experiment (in the experiment, a cylindrical aggregate is contained in a cylindrical container). It is therefore necessary to eliminate the high porosity cells located in the unwanted region, particularly in the four corners of the cubic box. A threshold cell porosity of 80% is chosen for the elimination of high porosity cells in unwanted regions. After this cell elimination process, 58 high porosity cells (1.1% of all cells) occupy 8.9% of the total void volume. These high porosity cells mostly belong to the regions near the boundary walls of the container. Due to this pore elimination, the surface area in the TPNM is 43.1 mm^2 (Fig. 3.10), smaller than the approximated values used in RPNM and CPNM.

The initial volume of liquid water in the experiment is reported in [178]. This value has been determined by processing of X-ray imaging data. Details on the respective image processing steps can be found in [26]. The initial liquid volume in CPNM is the total volume of all generated throats. The initial liquid volume in RPNM is the one of CPNM added by the volume of all rings in RPNM. The initial liquid volume in TPNM is the total volume of all pores in the main network (after cell elimination). The network porosity

in TPNM is calculated from the total volume of all tetrahedral cells and the initial liquid volume. All mentioned characteristics of the experimental aggregate and of the three PNM that have been used for simulations are tabulated in Tab. 3.1.

Table 3.1: Comparison on the characteristics of the aggregates used in the experiment (μ-CT) and in the three corresponding pore network simulations.

Parameter	μ-CT	CPNM	RPNM	TPNM
Surface area (mm^2)	50.3	50.4	50.4	43.1
Aggregate height (mm)	6.5	6.5	6.5	6.4
Initial volume of liquid water (mm^3)	132	148	160	144
Network porosity	0.46	0.45	0.49	0.45

In the experiment, the empty space above the top surface of the sample serves as a diffusive boundary layer (BL). In the TPNM simulations, a diffusive boundary layer is also built on top of the main aggregate. The pore network representing this boundary layer in TPNM is defined by applying Delaunay triangulation on a fictitious particle aggregate (BL aggregate) on top of the main aggregate. These fictitious particles are created by shifting vertically the particles of the main aggregate in the direction from bottom to top by a distance equal to the aggregate height in the experiment, namely 6.5 mm. The center coordinates of particles in the BL aggregate are, therefore, the center coordinates of particles in the main aggregate adjusted by a distance equal to the height of the main aggregate. The radii of particles in the BL aggregate are the same as the radii of corresponding particles in the main aggregate used for this duplication. However, not all particles in the boundary layer aggregate, after having been shifted from the main aggregate, are used for the next step. In fact, only particles having after the shift a vertical center coordinate smaller than the sum of the height of the main aggregate and the boundary layer thickness are kept for the next step, which is void space discretization (yellow particles in Fig. 3.11). All other fictitious particles which do not satisfy this condition are removed. The boundary layer thickness used in TPNM is 2 mm, equal to the value used in the simulations with the CPNM and the RPNM that have been reported in [178]. The void space discretization is then implemented to both the original and the BL aggregate. This ensures the connection

between the pores located at the top surface of the sample (main network) and the pores located at the bottom of the boundary layer network. The pore network representing the boundary layer provides the flow path for the vapor diffusion, both in the vertical direction toward the outer ambient and in the lateral direction within the boundary layer, as recommended in [21].

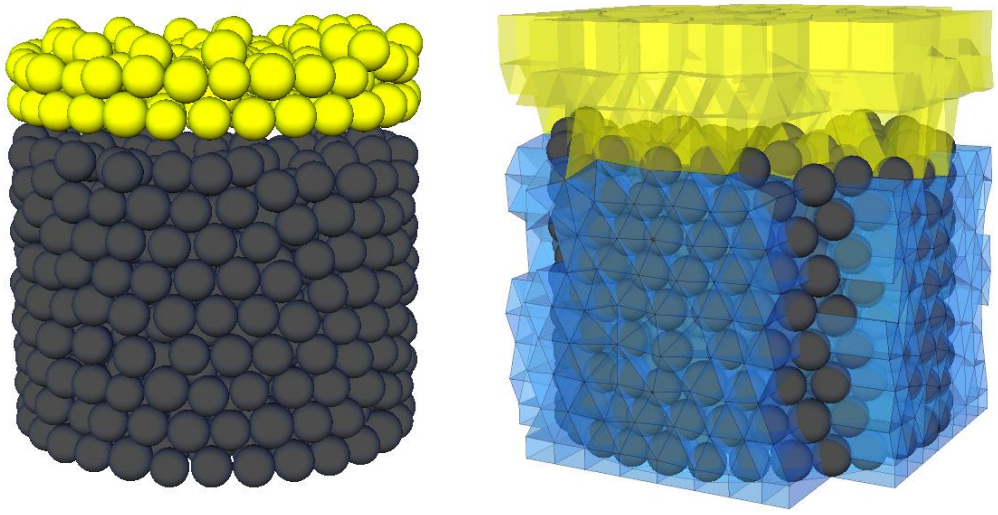

(a) (b)

Figure 3.11. (a) Illustration of the aggregate used in the TPNM. Particles in the main aggregate are represented by black spheres while particles used to define the diffusive boundary layer are represented by yellow spheres. (b) The pore network associated to the solid phase. Pores in the main network are shown in blue while pores in the boundary layer are shown in yellow. Solid phase is represented by black spheres. Particles in the BL aggregate are removed after the pores in the boundary layer have been defined.

As suggested in [188], for the case of a random packing of beads with relatively uniform size (diameter of the beads is at around 0.8 mm) drying isothermally at room temperature of 26°C in a cylindrical container with inner diameter of 8 mm with a velocity of the external air flow above the sample surface of 1 m/s, the distance over which viscous pressure differences become comparable to interfacial pressure differences (the so-called viscous length) is 146 m. This viscous length is much larger than the size of the sample investigated in the experiment that has been reported in [178], with a height of about 6.5 mm for the experimental aggregate. Thus, it is

reasonable to neglect the effect of liquid viscosity in this experiment. Also, as recommended by [188], the gravity length (the distance over which pressure differences due to gravity become comparable to interfacial pressure differences) of the considered experiment is 9.27 mm, which is larger than the height of the aggregate (6.4 mm from the μ-CT). This means that it is also acceptable to neglect the effect of gravity in this case.

The water vapor in the experiment can only elude from the aggregate through the top surface of the sample. Thus, the water vapor can only escape through the boundary layer located at the top surface of the sample, while a non-permeable to fluid boundary condition is applied to all other external surfaces in the simulation. It is also assumed that the bulk air is totally dry, i.e. vapor pressure in the ambient is equal to zero, $p_{v,\infty} = 0$. The temperature of the entire network is assumed to be uniform at 26°C, corresponding to an equilibrium vapor pressure of $p_v^* = 3365$ Pa.

To plot the saturation profile simulated by the TPNM, one must define slices of pores in the TPNM simulation. The position of a pore in the TPNM is represented by the Voronoi vertex associated with the Delaunay cell corresponding to this pore. The glass beads used in the experiment from [178] had a mean diameter of approximately 0.8 mm with a bed height of about 6.4 mm (from the μ-CT). Thus, the aggregate height in the TPNM has been divided into 8 segments. To start with, all pores having the vertical coordinate of their positions (Voronoi vertex) smaller than 0.8 mm are assigned to the bottom slice (first slice). The height of this bottom slice is represented by the average of the vertical coordinates of the position of the pores that belong to it. Saturation of the first slice will be assigned to this height value when plotting the saturation profile. The slice right above the bottom slice is defined by the collection of all additional pores having the vertical coordinate of their positions smaller than 1.6 mm (i.e., 2×0.8 mm). The average of the vertical coordinates of the position of these pores indicates the height of this slice. This bottom-up manner is applied similarly to the remaining pores to define the remaining slices, which finally results in a total of 8 slices of pores in the TPNM simulation (Fig. 3.12). The height of the slices presented in the saturation profile (Fig. 3.13) is normalized by the aggregate height of 6.4 mm.

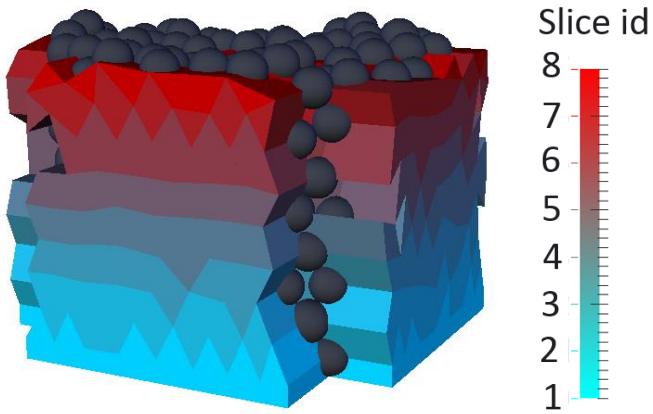

Figure 3.12. Slices of pores used for the calculation of saturation profiles obtained from TPNM. Pores belonging to the same slice are shown in same color.

The experimental saturation profiles reported in [178] are re-processed to become better comparable to the saturation profiles obtained from the TPNM simulations. There were 400 projections collected in each X-ray scan. Each projection is a nearly two-dimensional horizontal cross-section image of the sample, while a slice of pores in the pore network simulation is a much thicker three-dimensional volume. Thus, a series of adjacent μ-CT projections should be combined, so that one series of projections becomes approximately equivalent to one slice of pores in the pore network simulations. Since the mean diameter of the glass beads used in the experiment is ca. 0.8 mm, the projections are combined such that one series of projections has a distance between the top and the bottom projection equal to the approximate diameter of one glass bead. Consequently, the saturation profile data of the aggregate with a height of 6.4 mm according to the μ-CT is approximately equivalent to eight slices of pores in the TPNM simulation (Fig. 3.6). However, and contrary to the TPNM, those slices are defined in an equidistant way, and the mid-points of the slices, to which average saturation values are assigned, are also placed equidistantly. The combination of slices helps to reduce the short-range fluctuation in saturation profiles due to the sensitivity of the saturation value to the fraction of solid and void area ratio in each two-dimensional tomogram. This can be seen by comparing the plots of the same saturation profile data but being represented by 400 slices in the experimental profile of [178], by 16 slices obtained from the CPNM and the RPNM [178], and by 8 slices obtained from the TPNM in this study.

The experimental saturation profiles are compared to simulated results obtained from the TPNM, as well as to the predictions of the classical pore network model (CPNM) and the ring pore network model (RPNM). Latter have been taken as reported in [178] (see Fig. 3.13). The experimental profiles (Fig. 3.13a) and the profiles simulated by means of the TPNM (Fig. 3.13b) have been evaluated based on the division of the network height into 8 slices, while the profiles associated to the CPNM and the RPNM (Fig. 3.13c, d) have been evaluated based on the division of network height into 16 slices. However, the bottom-up definition of slices in the TPNM decreases the vertical position of the eighth (highest) slice compared to equidistant slice definition for the experimental data. This is observed as a wider empty region near to zero normalized height (top) in Fig. 3.13b (cf. top pore layer in Fig. 3.12). Top slice saturation is assigned to normalized height of zero, and bottom slice saturation to normalized height of one in CPNM and RPNM, reproducing the original plots of these results in [178].

It is noticed that the solid structure of the experiment and of the TPNM are identical, while the networks used in CPNM and RPNM simulations are only indirectly connected to the real placement of particles. Thus, the profiles obtained from the TPNM can be expected to quantitatively be comparable in terms of spatial distribution to the experimental findings, while profiles from CPNM and RPNM simulations may not even result in qualitative agreement with the experiment regarding the evolution of the remaining liquid volume in the network over time. This is the reason why the network surface and all layers higher than a normalized height of about 0.4 are supposed to be totally dry at a network saturation of 0.37 according to the CPNM (Fig. 3.13c), while this is not the case in the experimental profiles. Similarly, there is no place in the network having saturation higher than 0.4 at network saturation of 0.37 according to the RPNM simulation, and there is no liquid remaining in the region higher than a relative network height of 0.4 at the network saturation of 0.10. These results are evidently not matched with the experimental profiles. In contrast, the profiles predicted by means of the TPNM do not have these mismatches.

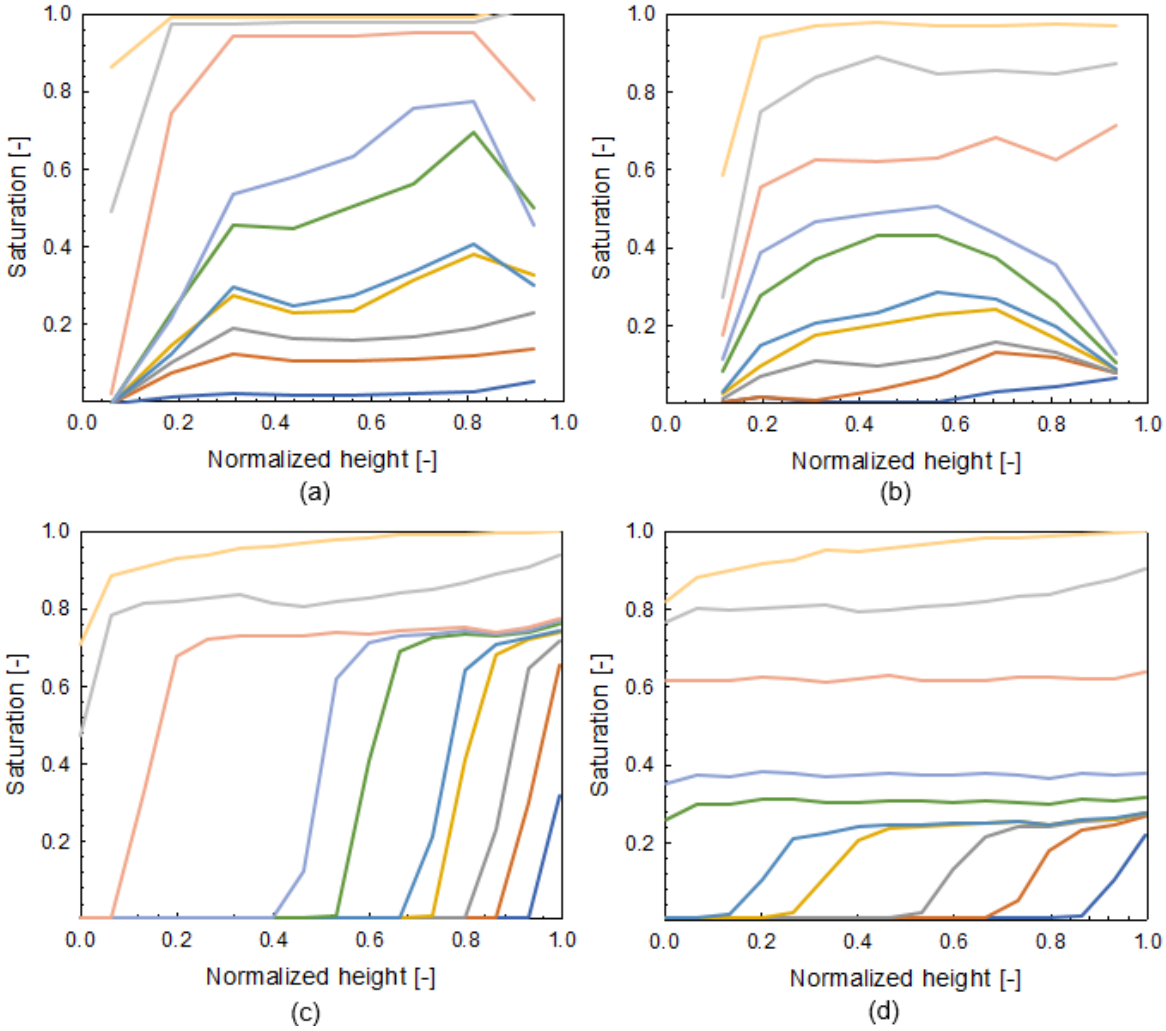

Figure 3.13. Saturation profiles obtained from X-ray images (a), TPNM (b), CPNM [178] (c) and RPNM [178] (d) simulations. From top the profiles belong to network saturations of 0.95, 0.82, 0.62, 0.37, 0.30, 0.19, 0.16, 0.10, 0.06 and 0.02, respectively.

Besides, saturation profiles can provide information on the liquid connectivity of the pore network. The saturation of the bottom layer in CPNM profiles almost does not decrease from a network saturation of 0.62 to a network saturation of 0.19. This can be interpreted as an interruption of liquid connectivity over the network height, which results in the liquid at the bottom not being pumped to supply the evaporation at the network surface. Consequently, there is a receding drying front that moves to the interior region of the aggregate at a network saturation of 0.37. Liquid connectivity to the aggregate surface is maintained better in RPNM and TPNM simulations. The

saturation of the bottom layer stops decreasing at a network saturation of 0.19 both in RPNM and TPNM.

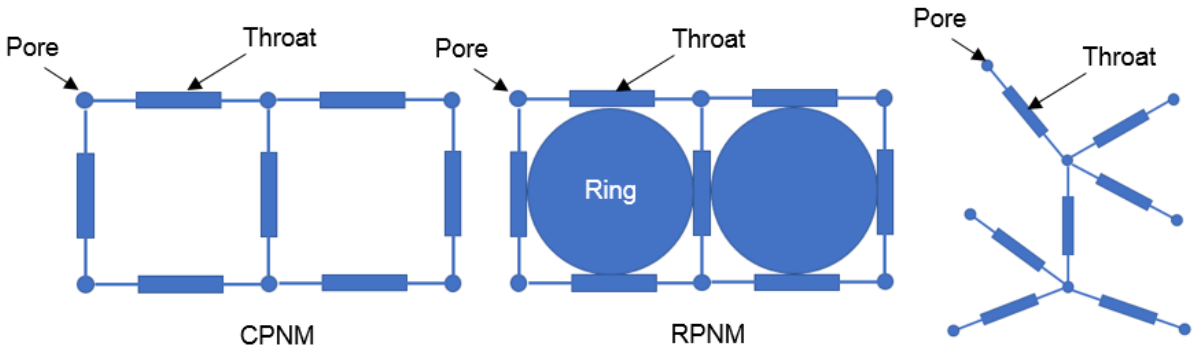

	CPNM		RPNM		TPNM	
	Volume	Capilarity	Volume	Capilarity	Volume	Capilarity
Pore	No	No	No	No	Yes	No
Throat	Yes	Yes	Yes	Yes	No	Yes
Ring	N/A	N/A	Yes	Yes	N/A	N/A

Figure 3.14. Comparison on the characteristics of pores and throats used in CPNM, RPNM and TPNM.

In RPNM and CPNM [178], the throats have volume and capillarity while the pores have no volume. Since the throats of these two PNMs have constant cross-sectional shape and uniform length, the volume and the capillarity are represented by one value only, the radius of the circular cylindrical throat (the throat length is the same for all throats). This is not the case in TPNM. The pores have volume but no capillarity while the throats have no volume but capillarity. The comparison on the characteristics of pores and throats among the three pore network models is shown in Fig. 3.14. The volume of pores and the capillary threshold value of throats in TPNM have their own size distributions (Fig. 3.15). A large pore volume can have a small throat entry capillary radius. In any case, the same large, local reservoir of liquid (a pore) is connected with several capillary elements that do not have any volume at all. The combination of the size distributions of the pores and throats in the pore invasion criteria of the TPNM (defined in the drying algorithm section) can, thus, increase the probability of a pore located at/near the top surface staying saturated longer. This is not possible to be simulated with the CPNM, having volume and capillarity represented by only one value. The ring (secondary capillary structure) in RPNM can help keeping

a throat saturated longer, due to the rule that a ring will only start being dried out once all of its neighboring throats have been occupied totally by gas phase. The introduction of the rings can, thus, be interpreted as presence of a secondary set of throats having capillarity size much smaller than the primary capillary structure. They can enhance the pumping of liquid to the evaporative surface, but not so strongly as the multiply connected reservoirs of the TPNM can do.

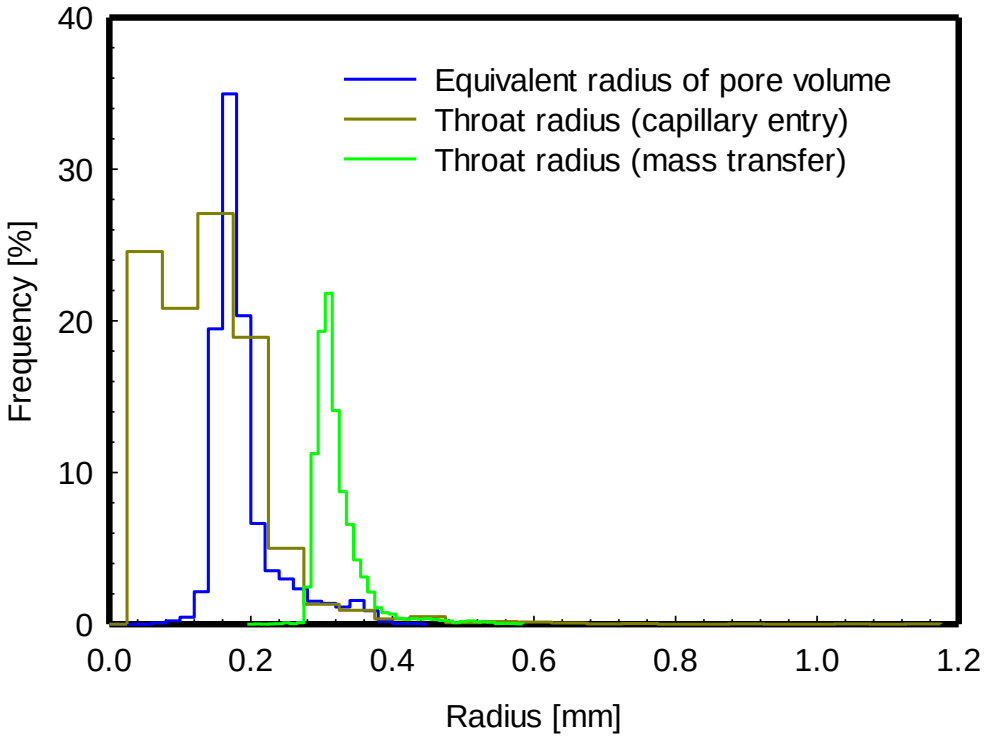

Figure 3.15. The size distribution of pore volume (equivalently converted to the radius of a sphere having same volume), the throat entry capillary threshold radius, and the mass exchange throat radius (equivalently converted from the area A_{ij} to the radius of a circle having same area) in TPNM.

Apart from the size distribution of pore volume and throat entry capillary radius, the distribution of throat radii that have been used for mass transfer (vapor diffusion in the already empty parts of the drying material) is also depicted in Fig. 3.15. As already mentioned, those have been obtained from the void area of the irregularly shaped throat A_{ij}, specifically as the equivalent radius of the circle having same area. Mass transfer throat radii are larger than the other radii used in the model, and play also a role in the evaporation rate calculation. Thus, besides the size distribution of pore

volume (how much liquid to be evaporated) and throat entry capillary radius (when the liquid will be evaporated), the size distribution of mass transfer equivalent radius from A_{ij} influences the emptying of pores in the TPNM and increases by its distributed nature the randomness of this process.

However, since the side boundary of TPNM is not exactly the same as the experimental one, there are still slight differences between the saturation profiles obtained by TPNM compared to the experimental profiles. Nevertheless, the general trends are captured quite well by the TPNM (compared Fig. 3.13b with Fig. 3.13a). Firstly, the layer at the top surface of the network dries faster than other layers located deeper inside the network due to the preferential pore invasion and evaporation at the top surface. Secondly, after the top layer has reached a saturation of nearly zero, the bottom layer dries faster than the layers located above it. This is not captured either by CPNM or by RPNM. The reason for this unexpected behavior is preferential channeling due to the wall effect [189, 190] at the lateral sides as well as at the bottom surface of the sample. Wall effect means that pores located near the wall have larger size. Once the invasion front has reached such pores, they will be preferentially invaded before other pores which are located in the interior of the sample. This wall effect is not (explicitly or implicitly) modelled in CPNM and RPNM, but it is naturally represented in TPNM by using more realistic and directly mapped morphology data of the porous medium. The wall effect will be less pronounced if the ratio of the dimension of the container and the particle size is large enough. For example, the wall effect was smaller in [112] (Fig. 9 therein) for glass beads with a diameter of 300 ± 50 μm mixed with pastes (particles in the order of 1 μm) packed in a cylindrical vessel with diameter of 34 mm and height of 17 mm. Otherwise it may also be suppressed, as it has been done in [191] by applying a cylindrical mask having a diameter of 18 mm on a Perspex column with inner diameter of 21.6 mm and a total length of 200 mm, which was filled with water-wet glass beads that had diameters of 0.5, 1.0 and 2.0 mm.

The global drying kinetics obtained from TPNM is compared in Fig. 3.16 to drying curves obtained from CPNM and RPNM as well as to the experimental result reported in [178]. The network on which the TPNM is based has the same boundary layer thickness but smaller surface area compared to the ones behind the CPNM and the RPNM. It should, though, be noticed that the pore structures used in the CPNM

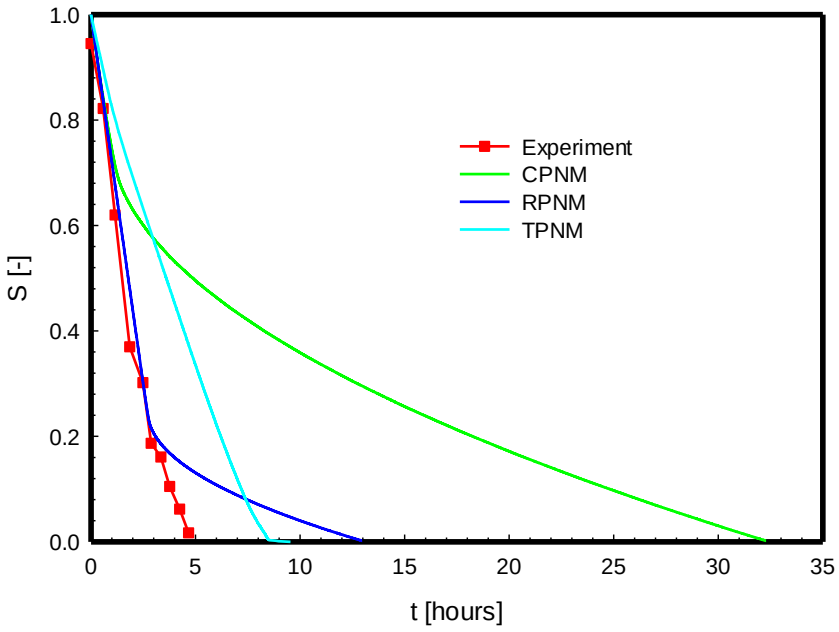

Figure 3.16. Evolution of network saturation S over time t. Results obtained from the TPNM of this study are compared with measurements by means of X-ray images, CPNM simulations and RPNM simulations reported in [178].

simulation and in the RPNM simulation are regular, while the one used in the TPNM simulation is irregular. Consequently, the effective thickness of the boundary layer in the TPNM simulation is larger than the one in the CPNM and the RPNM simulations. With simple cubical grid, BL throats create straight paths of diffusion through the boundary layer in CPNM and RPNM, the length of which is equal to BL thickness (2 mm). The irregular grid of the TPNM gives, in contrast, rise to tortuous diffusion paths, which are in total longer than the nominal thickness of the boundary layer (again 2 mm). These two factors (smaller surface area and tortuosity of boundary layer diffusion paths) result in smaller than measured first period drying rate (initial slope of the drying time curve, Fig. 3.16) for the TPNM. However, the first drying period (the drying period characterized by a relatively high and constant drying rate [18, 19]) is extended by the enhanced liquid connectivity throughout the aggregate. The liquid phase stays close to the top surface until very low network saturation of around 0.1 (Fig. 3.17). This results in the prediction of drying time by means of the TPNM being closer to the

experiment than the drying times predicted by the RPNM or the CPNM. Adaption of BL thickness would have even resulted in a nearly perfect match.

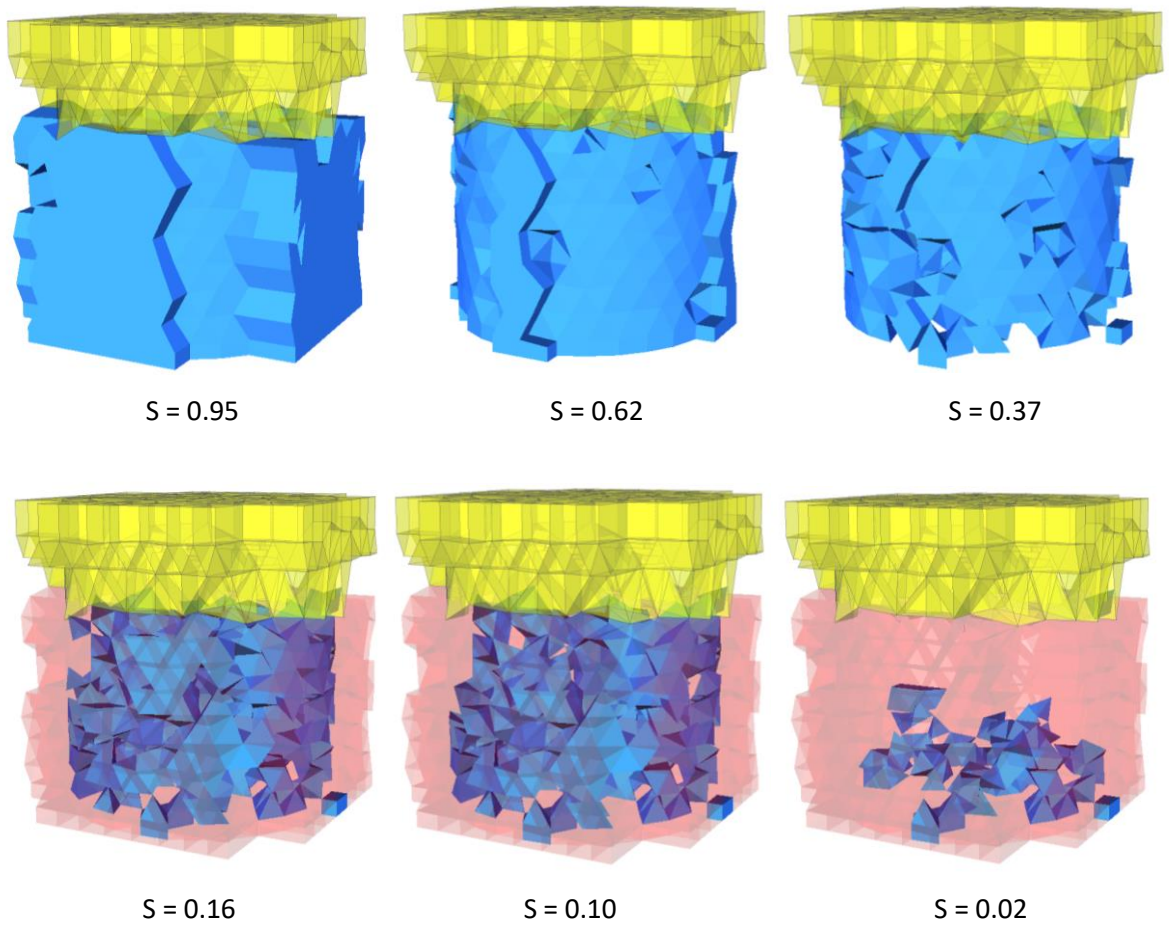

Figure 3.17. Illustration of the liquid phase distribution at different network saturations S simulated by the TPNM. The pores in the boundary layer are shown in yellow, the saturated (both partially and fully) pores are shown in blue. The dry pores are shown in red and are made transparent.

Influence of the pore size distribution on drying kinetics has been investigated for the case of a bundle of capillaries in [17]. It was found that the standard deviation of the capillary size distribution strongly affects the drying behavior, whereas the mean of the capillary size has negligible influence. At three different mean radii of the capillary tubes, 0.1 μm, 1 μm and 10 μm, there is almost no difference in terms of the duration of the constant rate period (CRP) when the standard deviation is the same. Whereas the duration of the CRP is significantly extended when standard deviation of the capillary tube radius increases from 1 nm to 50 nm. Throat entry capillary radii used in TPNM for this investigation have a mean value of 0.11 mm, standard deviation of 0.07

mm and coefficient of variation (COV) of 67.1%. The corresponding values of throat radii used in CPNM [178] are 0.084 mm, 0.001 mm and 1.2%. The finding in [17] suggests, consequently, another important reason for the favorable drying kinetics predicted by the TPNM compared to kinetics from the CPNM. The ring and throat configuration in the RPNM makes the size distribution in the RPNM being like a bimodal size distribution, which is not really comparable to the monomodal size distributions in TPNM and CPNM.

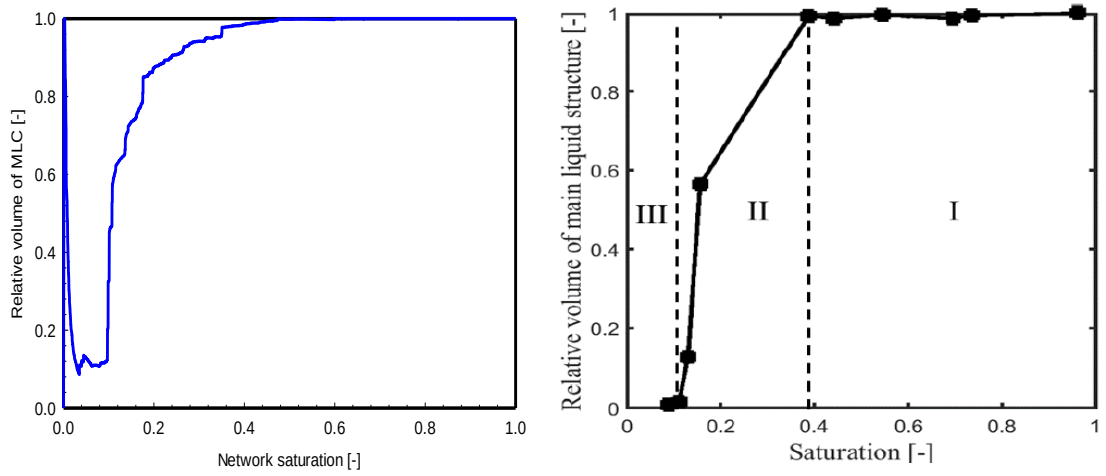

(a) (b)

Figure 3.18. Evolution of the volume ratio of main liquid cluster to the total volume of the remaining liquid over time: (a) Simulated data from TPNM; (b) Experimental result using a 73 wt% aqueous solution of potassium iodide as the liquid phase [178].

Most of the liquid that remains in the network of the TPNM during the drying process belongs to one big liquid cluster (termed main liquid cluster, MLC), which has also been experimentally observed in [139]. This spatial continuity and connectivity of the liquid phase ensures that liquid is transported to the surface, which sustains the evaporative demand there (i.e., evaporation is supplied mainly by liquid flow through the MLC). Liquid connectivity keeps the drying rate high and almost constant. As network saturation decreases to values lower than 0.4 (Fig. 3.18a), the volume ratio of MLC to the total remaining liquid starts being reduced slowly at first and significantly faster later on. Then, liquid connectivity throughout the aggregate is not maintained as it had been before – there is a disintegration of the liquid into different liquid clusters. This leads to a strong reduction in drying rate, and the amount of liquid that is located at the bottom of the network also stops decreasing (as shown in the saturation profile,

Fig. 3.13b). Experimental results used for comparison with predictions of the TPNM until now originated from measurement with pure water. However, the contrast in the X-ray images of this experiment was not sufficient for an accurate evaluation of liquid connectivity. Therefore, another experiment was also conducted in [178] by addition of contrast agent (73 wt% potassium iodide) to the water. Aggregate height was somewhat larger in this experiment (8 mm vs. 6.5 mm in the pure water experiment), but particulate material and other conditions were essentially the same. So experimental data from Fig. 3.18b can be compared to TPNM predictions (Fig. 3.18a), and the latter are found to quite well match the measured evolution of the main liquid cluster.

Chapter 4

Influence of particle aggregate structure on liquid phase distribution and drying kinetics

The triangulation pore network model (TPNM) introduced in Chapter 3 is utilized in this chapter to simulate the drying process of aggregates having different arrangement of the solid phase (particles) in space. Different arrangements of particles are not easy to produce and investigate experimentally, therefore synthetic aggregates are used. Such aggregates are generated numerically by the software Yade-DEM [179]. This means that the same software that has been used in Chapter 3 in order to derive from a known spatial configuration of particles the pore network model, is here used in dual purpose: To, first, generate the configuration of particles, and then transcribe the generated aggregates to TPNMs on which the course of the drying process can be simulated. Aggregates having different solid structure are firstly represented by different monodisperse assemblies of particles. Those have same aggregate dimensions (width × depth × height) but different number of particles, consequently also different particle radius. Secondly, with still the same external dimensions, bidisperse aggregates are generated by varying the size ratio between coarse and fine particles (d_c/d_f) as well as the volume fraction of the fine particles Q_f. Lastly, the aggregate dimensions are increased, and three aggregates are generated at this bigger aggregate size: One monodisperse as a reference, and two polydisperse aggregates with different spreads in particle size. In the following, the aggregate generation algorithm is presented first. Then, simulation setups are described in some

more detail. Simulation results are presented for each of the denoted cases (monodisperse, bidisperse, polydisperse) and discussed in terms of the evolution of liquid phase distribution and drying kinetics, in connection with the various evaluated structural and morphological characteristics of the investigated types of particle aggregates. Overviewing remarks will, finally, close the chapter.

4.1 Solid phase representation as an aggregate: Dynamic techniques

Porous materials are represented in the present work by aggregates of spherical particles. Such aggregates are prepared in this chapter synthetically by using the open-source software Yade-DEM [179]. The sample preparation procedure and its implementation will be explained in the following.

The algorithm used to generate a monodisperse aggregate consists of the following steps:

1. Set the values of input parameters. These parameters are number of particles, initial size (dimension) of the domain, confining pressure, initial aggregate porosity, and enlargement factor; moreover, parameters related to the DEM steps of aggregate generation.

2. Calculate the initial size of particles based on the prescribed number of particles (N_p), initial size of the domain and the initial aggregate porosity. The aggregates generated in this chapter have a cuboidal shape. Consequently, the domain in which aggregate generation will take place is bounded by six planes (Fig. 4.1) and set by definition of three dimensions, namely width × depth × height (W × D × H). The final aggregate will be inscribed in the domain confined by these planes. The initial aggregate porosity ($\varepsilon_{initial}$) is set to 0.7. This large value of porosity ensures that all generated particles can be placed in the prescribed domain.

The solid volume can be calculated as:

$$V_{solid} = V_{container} - V_{void} = W\ D\ H\ (1 - \varepsilon_{initial}). \quad (4.1)$$

The initial particle size can thus be calculated as:

$$r_{initial} = \sqrt[3]{\frac{V_{solid}/N_p}{\frac{4}{3}\pi}} \,. \tag{4.2}$$

The radius of these initial particles is not the final radius of particles in the aggregate. The radius of initial particles will be increased in Step 4 of the algorithm.

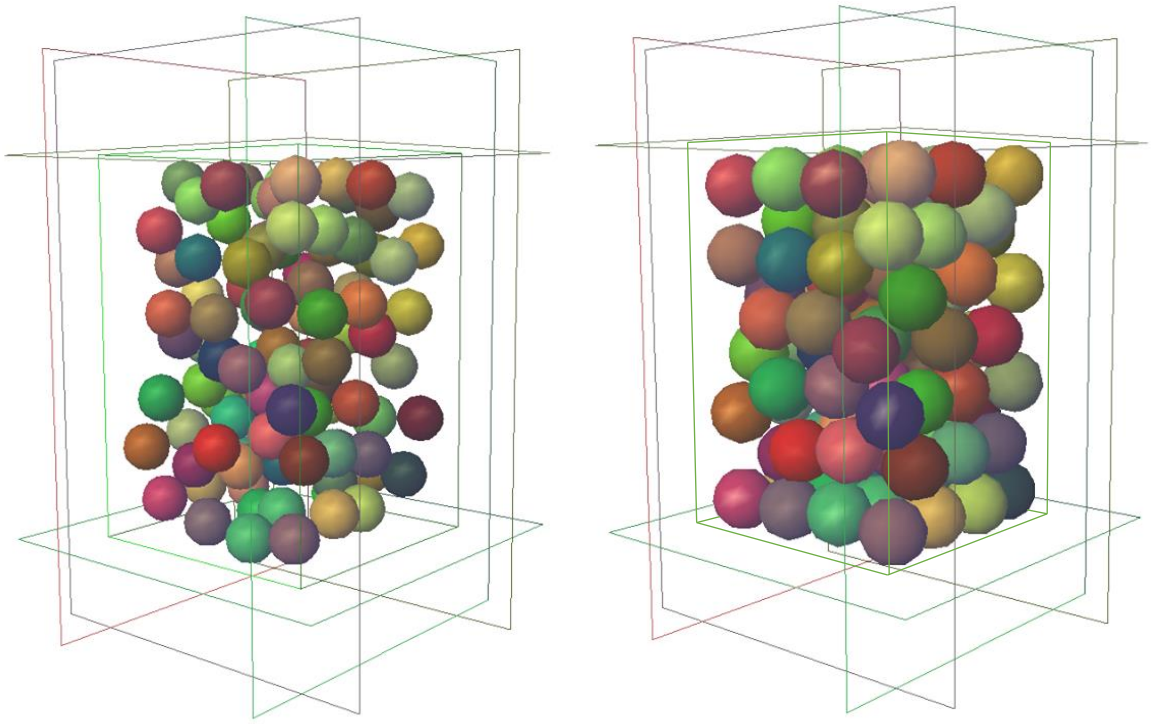

(a) (b)

Figure 4.1. Illustration of the generation of an aggregate with 100 spherical particles (Mono 100, cf. Section 4.2): (a) Initial loosely packed aggregate, no contact between particles (b) Final closely packed aggregate, after particle enlargement under isotropic compaction.

3. Place randomly the particles with sizes calculated in Step 2 into the domain, one by one and without overlap with each other. This step is completed as soon as the given number of particles has been placed. As indicated, a loosely packed (high porosity of 0.7) aggregate consisting of the initial spherical particles in a gas-like state with no interparticle contacts is the result (Fig. 4.1a).

4. Increase the particle sizes (diameter) while keeping the domain boundary planes (six planes) fixed. The increase in particle size takes place in steps, by multiplication

of the previous particle size with the given value of the enlargement factor (a value of 1.001 is used in this study). In this way of size-proportional growth, the particles are homogeneously enlarged and gradually come in contact with each other. Contacts are considered by DEM simulation with, in this stage, interparticle friction angle assigned at 9° (the smaller this value is, the denser the resulting packing is [33]). Domain walls are considered to be frictionless. The growing process continues until the preset value of the confining pressure is reached.

5. Check whether the equilibrium between the internal stress, which results from the interaction between the particles and the container walls, and the external confining pressure (external load) has been reached. The internal stress is zero in the early stage of the particle growth process, because there is yet no interaction between particles or between particles and walls, but it increases gradually with increasing number and extent of contacts until the equilibrium is reached.

6. If the condition in Step 5 is satisfied (internal stress has reached the preset value of the confining pressure), then go to Step 7. If the condition in Step 5 is not satisfied, then the particles will displace (DEM iteration) until the equilibrium is reached.

7. Implement isotropic compaction under modified conditions (increased interparticle contact angle and slightly moving walls) to confer a solid-like nature to the aggregate. In this stage, the interparticle friction angle is changed from, previously, 9° to 30°. Both those values are conventionally used in DEM simulations [33]. It should be noted that if the friction angle was set to 30° in Step 4, then this step would last for much longer time or even the equilibrium that is required in Step 5 would not be reached at all. So slippery particles are taken first in order to accelerate the process of structure formation, and rough particles are taken in the end for the final adjustment and finish of the evolving structure. Meanwhile, the container walls are moved very slowly. This movement supports the final organization of the particles to a fixed aggregate, but it does not change the size of the computational domain conceivably, i.e. it is negligible in this sense. Consequently, the prescribed aggregate size is preserved with high accuracy, and the respective volume can be used for, e.g., evaluation of porosity. The size of particles is final and fixed throughout Step 7. The described dynamic process ends when all particles reach their stable positions with zero velocity as the result of energy dissipation events.

8. Check whether the equilibrium condition between the internal stress and the external confining pressure is fulfilled. Renewed and repeated checking is required, because changes in Step 7 (larger friction angle, small displacement of the walls) disturb the previously attained equilibrium and result in particle movement that will continue until the equilibrium has been reached again.

9. If the condition in Step 8 is satisfied, then the generation process is considered to be finished and the final particle aggregate (Fig. 4.1b) is stored for further use (morphological evaluation and generation of TPNM for simulation of drying).

The steps to generate a bidisperse particle aggregate are identical to those followed to generate a monodisperse particle aggregate except the first step. In this case, the input parameters are diameter ratio of coarse to fine particles (d_c/d_f), volume fraction of fine particles (Q_f), initial size (dimension) of the domain, confining pressure, initial aggregate porosity, and enlargement factor. This means that the number of particles is not prescribed.

The steps to generate a polydisperse particle aggregate are again identical to those followed in the generation of monodisperse particle aggregates, except of the first step. In this case, an input parameter is (apart from domain size, confining pressure, initial aggregate porosity, and enlargement factor) the initial size distribution of particles. The volume distribution (Q_3) of the particles follows a uniform distribution function, i.e., all generated values have equal probability to be observed. This uniform distribution function is described by mean radius (r_{mean}) and deviation ($\pm\Phi$)). The radius of each initial particle is randomly generated according to the initial particle size distribution. Similar as for bidisperse aggregates, the number of particles is not preset.

Particle size is a result of the previous algorithm, not an input. Desired values of final particle size can be approximated iteratively, but they can never be met exactly, especially not after one-pass application of the algorithm. This is not a disadvantage in the present study, the target of which is to create solid structures, not to investigate a specific material. Some of the used values of algorithm parameters have already been mentioned. Remaining parameters, especially DEM input parameters, have been taken from previous applications of Yade-DEM for the generation of particle assemblies in literature [192] and are summarized in Tab. 4.1.

Table 4.1: Input DEM parameters of aggregate generation using Yade.

Parameter	Value
Confining pressure	275000 Pa
Elastic modulus	$30 \cdot 10^9$ Pa
Stiffness ratio	0.2
Tensile strength	$40 \cdot 10^5$ Pa
Cohesion	$40 \cdot 10^6$ Pa

4.2 Simulation setup and investigated aggregates

In order to investigate the impact of aggregate solid structure on the drying kinetics, different aggregates having different particle size and particle size distribution have been generated. Firstly, five monodisperse aggregates are generated (as indicated in Tab. 4.2) and are compared to each other. Then, the investigation is extended to aggregates made of bidisperse particles. Many such aggregates have been generated with different values of the diameter ratio of coarse to fine particles (d_c/d_f) and different volume fractions of the fine particles (Q_f), as summarized in Tab. 4.3, but only two of them have been selected for TPNM derivation and for investigation of their drying behavior. Monodisperse and bidisperse aggregates are of same size. The shape of the aggregates is chosen as a cuboid here in this chapter to avoid the cell elimination process encountered in Chapter 3 with cylindrical aggregates that corresponded to the experimentally investigated assembly of particles. The cuboid dimensions (width (W) × depth (D) × height (H)) are set at a relatively small size of 3 mm × 3 mm × 4.5 mm for monodisperse and bidisperse aggregates. Polydisperse aggregates are, though, larger in size with dimensions of 8 mm × 8 mm × 12 mm (Tab. 4.4). With same aggregate size, one more monodisperse aggregate is created and investigated as well. On one hand, this can be seen as a polydisperse aggregate with very small spread of particle size that complements a series with increasing values of this parameter (Tab. 4.4). On the other hand, it may be compared to smaller monodisperse aggregates from Tab. 4.2. As mentioned in Section 4.1, the number of particles in not prescribed in the case of generating bidisperse or polydisperse aggregates.

Table 4.2: Summary of input parameters specifying the solid phase for the generation of monodisperse aggregates of small size.

Aggregate	**Aggregate size** W × D × H (mm³)	**Number of particles**
Mono 37	3 × 3 × 4.5	37
Mono 100	3 × 3 × 4.5	100
Mono 200	3 × 3 × 4.5	200
Mono 500	3 × 3 × 4.5	500
Mono 1000	3 × 3 × 4.5	1000

Table 4.3: Summary of input parameters specifying the solid phase for the generation of bidisperse aggregates, two of which have been investigated in more detail.

Aggregate size W × D × H (mm³)	d_c/d_f (-)	Q_f (%)
3 × 3 × 4.5	1.43	50
3 × 3 × 4.5	2	30, 40, 50, 60
3 × 3 × 4.5	3.33	30, 40, 50, 60, 70
3 × 3 × 4.5	5	20, 30, 40, 50, 60
3 × 3 × 4.5	6.67	30, 40, 50, 60

Table 4.4: Summary of input parameters specifying the solid phase for the generation of polydisperse aggregates of large size, including a monodisperse reference aggregate; Half of the width of the initial particle size distribution (PSD) is given as % of the mean value of initial particle size.

Aggregate	**Aggregate size** W × D × H (mm³)	**Width of initial PSD** (%)
Mono 1600	8 × 8 × 12	0
Poly 1449	8 × 8 × 12	30
Poly 1164	8 × 8 × 12	50

An overview of all aggregates that have been investigated in detail is given in Tab. 4.5. As already mentioned, the first considered aggregate size is with 3 × 3 × 4.5 mm³ smaller than the aggregate size investigated in Chapter 3 (a cylinder having a diameter of 8 mm and a height of 6.5 mm), while the second aggregate size (8 × 8 × 12 mm³) is larger, especially in respect to the height. The purpose of these two aggregate sizes is to investigate the influence that this parameter might have on drying kinetics. The number of particles varied from 37 to 1600, with up to nearly 9000 pores and up to nearly 18000 throats. Aggregate height is evaluated by the method based on the

"Bottom" list and the "Top" list, as described in Section 3.4, and further used to, among others, obtain aggregate volume and, then, aggregate porosity. The particle radii of all investigated aggregates from Tab. 4.5 (as already stressed, a result of the aggregate generation algorithm, not an input) are in the same order of magnitude with the mean particle radius of the aggregate investigated in Chapter 3, which has approximately been equal to 0.4 mm. The particle mean radius in Tab. 4.5 is the arithmetic mean (average value) of all particles in each aggregate. Further going evaluation and discussion of aggregate morphology will be presented in the following Sections 4.3 to 4.5.

Table 4.5: Aggregates investigated in this chapter and their main features.

Case	Aggregate size (mm^3)	Number of particles	Number of pores (main network)	Number of throats (main network)	Porosity (-)	Particle mean radius (mm)
Mono 37	3 × 3 × 4.5	37	164	312	0.445	0.501
Mono 100	3 × 3 × 4.5	100	498	971	0.437	0.364
Mono 200	3 × 3 × 4.5	200	1016	2001	0.411	0.298
Mono 500	3 × 3 × 4.5	500	2719	5387	0.403	0.222
Mono 1000	3 × 3 × 4.5	1000	5539	11001	0.391	0.178
Bi 860	3 × 3 × 4.5	860	4328	8627	0.408	0.123
Bi 1047	3 × 3 × 4.5	1047	5640	11193	0.389	0.166
Mono 1600	8 × 8 × 12	1600	8938	17771	0.381	0.409
Poly 1449	8 × 8 × 12	1449	8007	15919	0.379	0.409
Poly 1164	8 × 8 × 12	1164	6234	12402	0.365	0.415

Regarding the drying simulation, the diffusive boundary layer on top of each of the investigated aggregates is developed on the basis of an additional, fictitious aggregate that expands the initial one (similarly to what has been done in Chapter 3). Here, the boundary layer aggregate for the case of the smaller aggregate size (3 mm × 3 mm × 4.5 mm) is based on the aggregate Mono 100. These fictitious particles are created by shifting vertically the particles of Mono 100 aggregate in the direction from bottom to top by a distance equal to the aggregate height, namely 4.5 mm. The center coordinates of particles in the boundary layer aggregate are, therefore, the center coordinates of particles in the Mono 100 aggregate adjusted by a distance of 4.5 mm. The radii of particles in the boundary layer aggregate are the same as the radii of

corresponding particles in the Mono 100 aggregate used for this duplication. However, not all particles in the boundary layer aggregate, after having been shifted from the Mono 100 aggregate, are used for the void space discretization. In fact, only particles having after the shift a vertical center coordinate smaller than the sum of the height of the main aggregate and the boundary layer thickness are kept for the next step. The thickness of the boundary layer has been selected to be 2.4 mm for all considered small aggregates. The ratio of boundary layer thickness of 2.4 mm to the aggregate height of 4.5 mm is, with a value of 0.533, approximately equal to the ratio of the empty space having a height of 3.5 mm in the specimen vial to the aggregate height of 6.5 mm used in the experiment [178]. It should though be noted that the so-called first period drying rate is controlled by the absolute value of boundary layer thickness, not by its relation to the height of the porous material. Moreover, a boundary layer thickness of, nominally, only 2 mm (not 2.4 mm) has been used in the simulations of Chapter 3, which might be seen as factually expanded by the tortuosity of gas-side diffusion paths that have been derived from a fictitious aggregate placed on top of the real one.

Table 4.6: Process conditions and material properties used in the drying simulations (same as Chapter 3).

Parameter	Value
Temperature, T (°C)	26
Total pressure of ambient air, p (bar)	1.0
Equilibrium vapor pressure, p_v* (Pa)	3365
Vapor pressure in the ambient, $p_{v,\infty}$ (Pa)	0.0
Molar mass of vapor, $\widetilde{M}_v$ (kg/kmol)	18.02
Diffusion coefficient (vapor in air), δ (m^2/s)	$2.5685 \cdot 10^{-5}$
Universal gas constant, $\tilde{R}$ (J/kmolK)	8314.5

The fictitious boundary layer aggregate for the bigger aggregate size (8 mm × 8 mm × 12 mm) is created similarly to what has been done for the smaller aggregate size. The aggregate used for the particle duplication is, in this case, the Mono 1600 aggregate. The boundary layer thickness is set as 6.5 mm, i.e. the ratio of this boundary layer thickness to the aggregate height of 12 mm is with a value of 0.542 approximately

equal to the corresponding ratio used for the aggregate size 3 mm × 3 mm × 4.5 mm. All other input parameters (process conditions and material properties) of the drying simulations are shown in Tab. 4.6. They are the same as in Chapter 3.

4.3 Influence of particle size on drying kinetics and liquid phase distribution of monodisperse aggregates

In order to investigate the impact of particle size on the drying kinetics, different monodisperse aggregates have been generated. Five different monodisperse particle aggregates are considered. These aggregates are prescribed to have different number of particles, which leads to being different in the particle radius. These aggregates are labelled “Mono X”, where X is the number of particles of the aggregate. Illustrations of these aggregates in 3D are shown in Fig. 4.2.

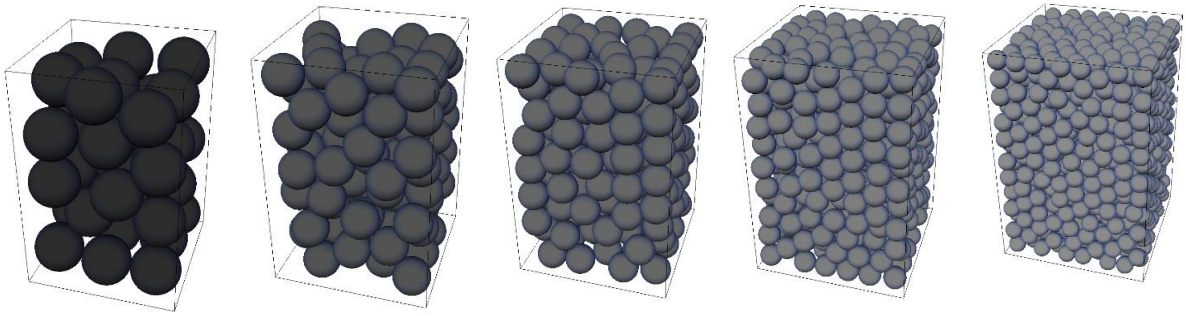

R = 0.50 mm, 37 particles | R = 0.36 mm, 100 particles | R = 0.30 mm, 200 particles | R = 0.22 mm, 500 particles | R = 0.18 mm, 1000 particles

Figure 4.2. Illustration of the solid phase of aggregates comprised of monodisperse primary particles.

The influence of the spatial distribution of solid particles on the size distributions of pores and throats has been investigated by analyzing different realizations of Mono 100 and Mono 500 aggregates. Each aggregate has been generated with the same parameters of the aggregate generation algorithm five different times for this analysis. The obtained five realizations of the Mono 100 aggregate and five realizations of the Mono 500 aggregate are depicted in Fig. 4.3 and Fig. 4.4, respectively.

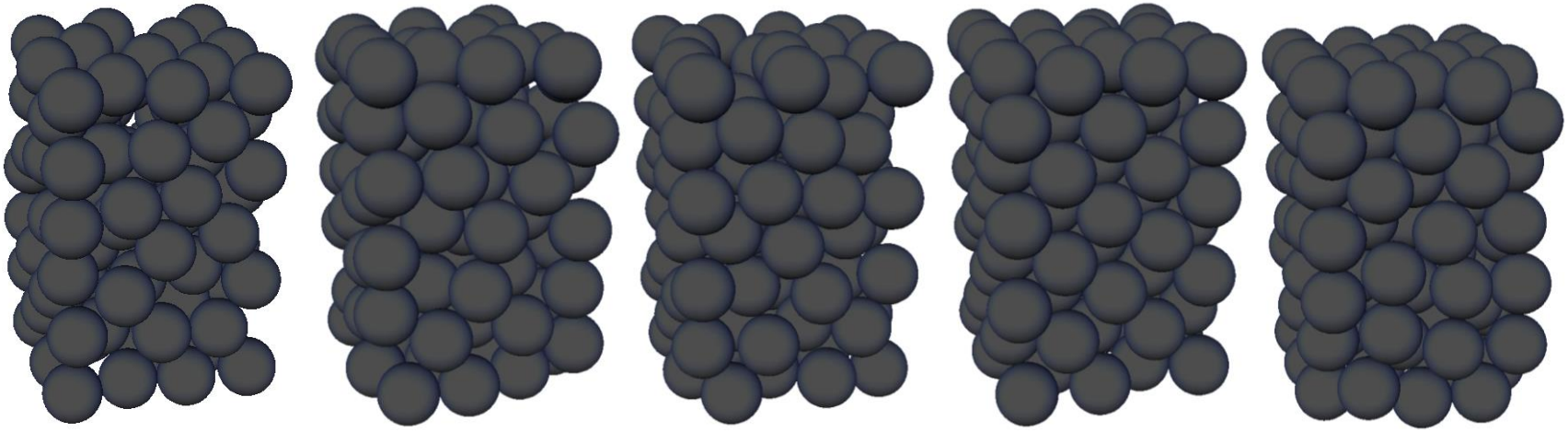

Figure 4.3. Illustration of the solid phase for five realizations of the Mono 100 aggregate.

Table 4.7: Statistical properties of the size distributions of pore volume (equivalently converted to the radius of a sphere having same volume), throat entry capillary threshold radius, and mass transfer throat radius (equivalently converted from the area A_{ij} to the radius of a circle having same area) for the five realizations of the Mono 100 aggregate.

Aggregate	Pore volume (equivalent radius)			Throat entry capillary radius			Throat mass transfer (equivalent radius)		
	Mean, mm	SD, mm	COV, %	Mean, mm	SD, mm	COV, %	Mean, mm	SD, mm	COV, %
Mono 100, R#1	0.1950	0.0417	21.40	0.1205	0.0633	52.51	0.3047	0.0306	10.03
Mono 100, R#2	0.1943	0.0403	20.74	0.1213	0.0604	49.81	0.3037	0.0285	9.40
Mono 100, R#3	0.1933	0.0415	21.45	0.1192	0.0591	49.59	0.3038	0.0284	9.36
Mono 100, R#4	0.1923	0.0416	21.64	0.1123	0.0630	56.08	0.3042	0.0287	9.42
Mono 100, R#5	0.1929	0.0406	21.07	0.1155	0.0582	50.34	0.3041	0.0267	8.77

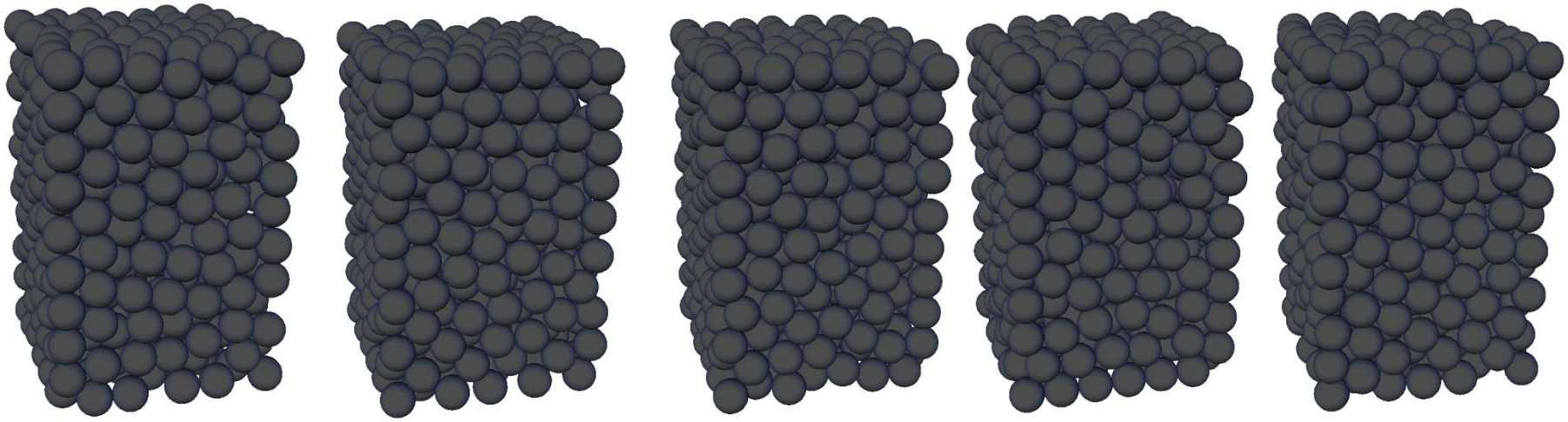

Figure 4.4. Illustration of the solid phase for five realizations of the Mono 500 aggregate.

Table 4.8: Statistical properties of the size distributions of pore volume (equivalently converted to the radius of a sphere having same volume), throat entry capillary threshold radius, and mass transfer throat radius (equivalently converted from the area A_{ij} to the radius of a circle having same area) for the five realizations of the Mono 500 aggregate.

Aggregate	Pore volume (equivalent radius)			Throat entry capillary radius			Throat mass transfer (equivalent radius)		
	Mean, mm	SD, mm	COV, %	Mean, mm	SD, mm	COV, %	Mean, mm	SD, mm	COV, %
Mono 500, R#1	0.1087	0.0203	18.65	0.0628	0.0333	52.98	0.1807	0.0139	7.68
Mono 500, R#2	0.1096	0.0199	18.16	0.0631	0.0325	51.48	0.1808	0.0139	7.68
Mono 500, R#3	0.1092	0.0201	18.44	0.0643	0.0329	51.23	0.1806	0.0141	7.79
Mono 500, R#4	0.1091	0.0201	18.44	0.0637	0.0335	52.68	0.1807	0.0141	7.79
Mono 500, R#5	0.1092	0.0204	18.64	0.0647	0.0339	52.38	0.1806	0.0142	7.87

Table 4.9: Statistical properties of the size distributions of pore volume (equivalently converted to the radius of a sphere having same volume), throat entry capillary threshold radius, and mass transfer throat radius (equivalently converted from the area A_{ij} to the radius of a circle having same area) for the five investigated monodisperse aggregates with size of 3 mm × 3 mm × 4.5 mm.

Aggregate	Pore volume (equivalent radius)			Throat entry capillary radius			Throat mass transfer (equivalent radius)		
	Mean, mm	SD, mm	COV, %	Mean, mm	SD, mm	COV, %	Mean, mm	SD, mm	COV, %
Mono 37	0.2805	0.0585	20.85	0.1756	0.0775	44.15	0.4183	0.0430	10.28
Mono 100	0.1944	0.0403	20.75	0.1278	0.0623	48.76	0.3037	0.0291	9.58
Mono 200	0.1512	0.0301	19.91	0.0865	0.0454	52.43	0.2430	0.0203	8.36
Mono 500	0.1089	0.0204	18.77	0.0651	0.0344	52.85	0.1807	0.0145	8.00
Mono 1000	0.0856	0.0147	17.17	0.0493	0.0263	53.24	0.1372	0.0049	3.54

Statistical properties (mean, standard deviation and coefficient of variation, COV) of the distributions of pore radius, throat entry capillary threshold radius, and throat mass transfer radius for the five realizations of the Mono 100 and the Mono 500 aggregates are shown in Tab. 4.7 and Tab. 4.8, respectively. Comparing between these two tables, it can be seen that the higher the number of particles is, the smaller the variations in the values of the considered statistical properties become. All three statistical properties of all three pore-throat size distributions are mostly varied within a range of 1%, and there is hardly any property having a variation larger than 5%. This means that a good repeatability of the generation process can be ascertained for both investigated aggregates (Mono 100 and Mono 500), so that the influence of the specific spatial distribution of particles can be considered as being negligible.

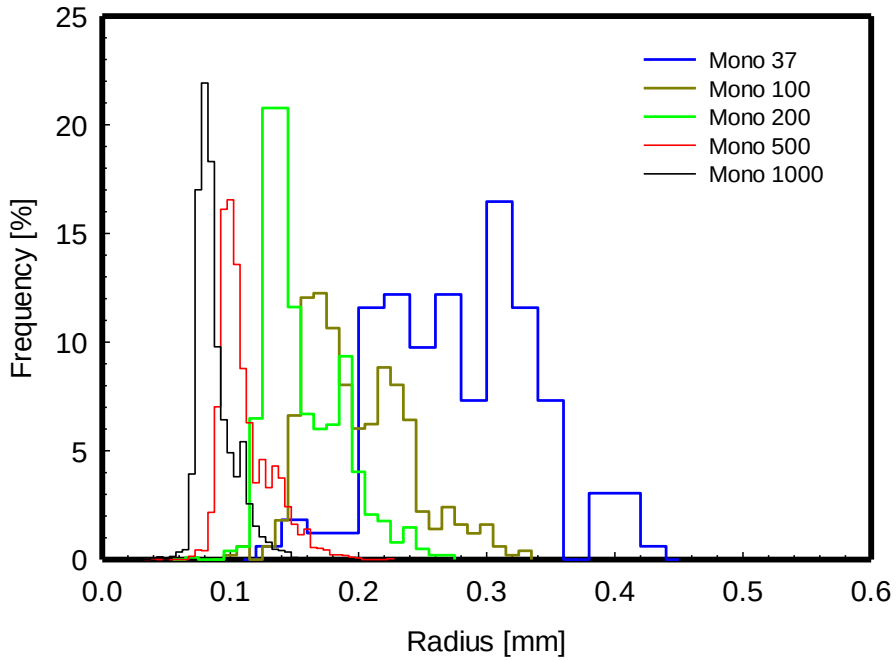

Figure 4.5. Distributions of pore radius (volume equivalent) for the five investigated small monodisperse aggregates.

Generalizing these findings to all other aggregates investigated in this study (listed in Tab. 4.5), it is reasonable to assume that the investigation may be conducted on the basis of just one aggregate each time, i.e., without multiple realizations. Respective results in terms of the statistical properties of the distributions of the size of the radii of

pores and throats (entry capillary and mass transfer) for each of the five investigated monodisperse aggregates are shown in Tab. 4.9 and graphically depicted in Figs. 4.5-4.7. It should be noted that values for the aggregates Mono 100 and Mono 500 do not correspond to one of the realizations from Tables 4.7 and 4.8, and are also not average values from these tables, but they have been obtained from one additional realization each time. The smaller the number of particles in the aggregate, the bigger the particle radius is, which also means bigger pores and bigger throats. This reflects the well-known fact that size metrics for voids scale with the particle size in porous media which resemble the packing of spheres. Pores (volume equivalent radius) are bigger than the capillary entry radii of throats. Clearly biggest are the mass transfer (vapor diffusion) radii of throats. Correspondingly, distributions are almost completely pulled apart in Fig. 4.7, whereas strongly overlapping in Figs. 4.6 and 4.7. Variability (COV) is smallest in pore radius and biggest in mass transfer throat radius.

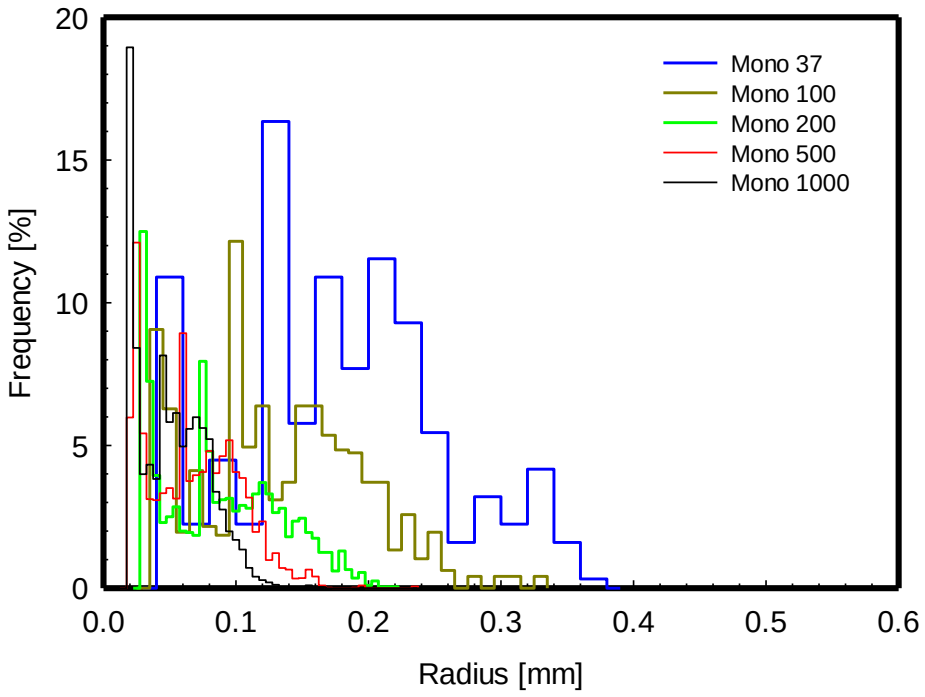

Figure 4.6. Distributions of throat entry capillary threshold radius for the five investigated small monodisperse aggregates.

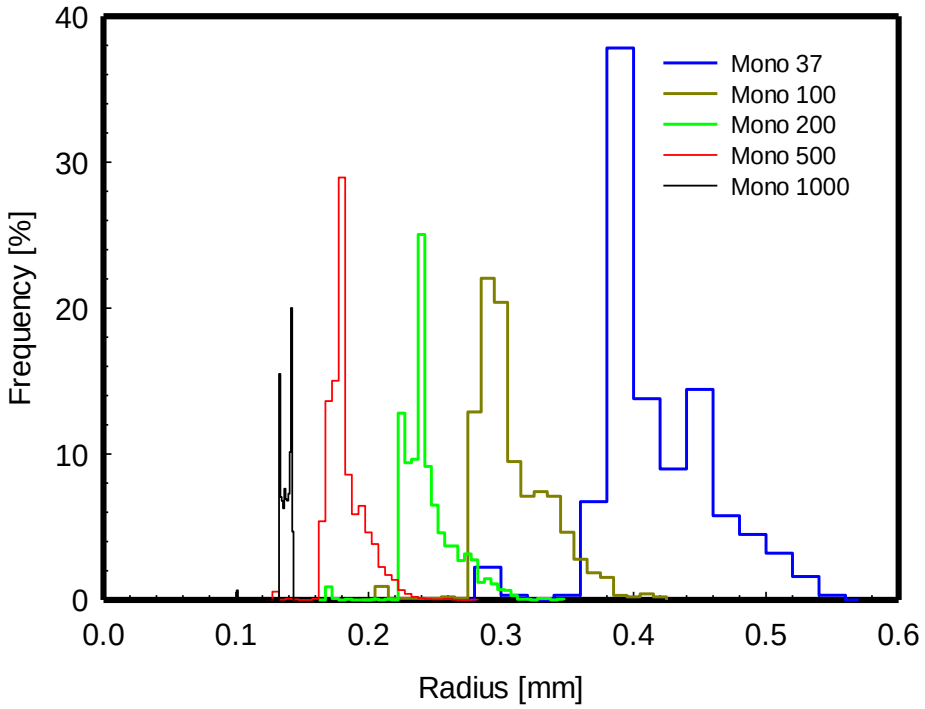

Figure 4.7. Distributions of mass transfer throat radius (area equivalent) for the five investigated small monodisperse aggregates.

In the preparation for the saturation profile plots, slices of pores of the monodisperse aggregates investigated in this chapter are defined similarly to what has been presented in Chapter 3. All aggregates are divided into the same number of slices to be comparable in terms of saturation profiles. The bigger the particle radius is, the smaller the possible number of slices can be. Thus, taking Mono 100 as reference, the particle radius of 0.36 mm (i.e., diameter of 0.72 mm) and an aggregate height of 4.5 mm result in a number of six slices. This is chosen to be the number of slices for all investigated aggregates in this chapter (monodisperse, bidisperse, polydisperse, both investigated aggregate sizes). Illustrations of the slices of pores of all monodisperse aggregates investigated in this chapter are shown in Fig. 4.8.

The saturation profiles showing the evolution of liquid phase distributions of all investigated monodisperse aggregates are shown in Fig. 4.9. When the particle size becomes smaller (i.e., higher number of particles), the influence of the wall on the saturation profile (local gradients in the saturation profiles) becomes weaker. This is shown by comparing the saturation profiles of Mono 37, Mono 100 and Mono 200

aggregates to the ones of Mono 500 and Mono 1000 aggregates. This is in accordance to what has been mentioned in Chapter 3, namely that the wall effect becomes weaker when the ratio of the particle size to the container size becomes smaller, i.e. the number of particles becomes higher. Besides, the difference in the saturation profiles between Mono 500 and Mono 1000 is much smaller compared to the differences between the profiles of Mono 37, Mono 100 and Mono 200 aggregates. This means that the influence of particle size on the saturation profiles for the same aggregate size become less pronounced once the number of particles is high enough, i.e., the size ratio of container dimension to the particle diameter is high enough.

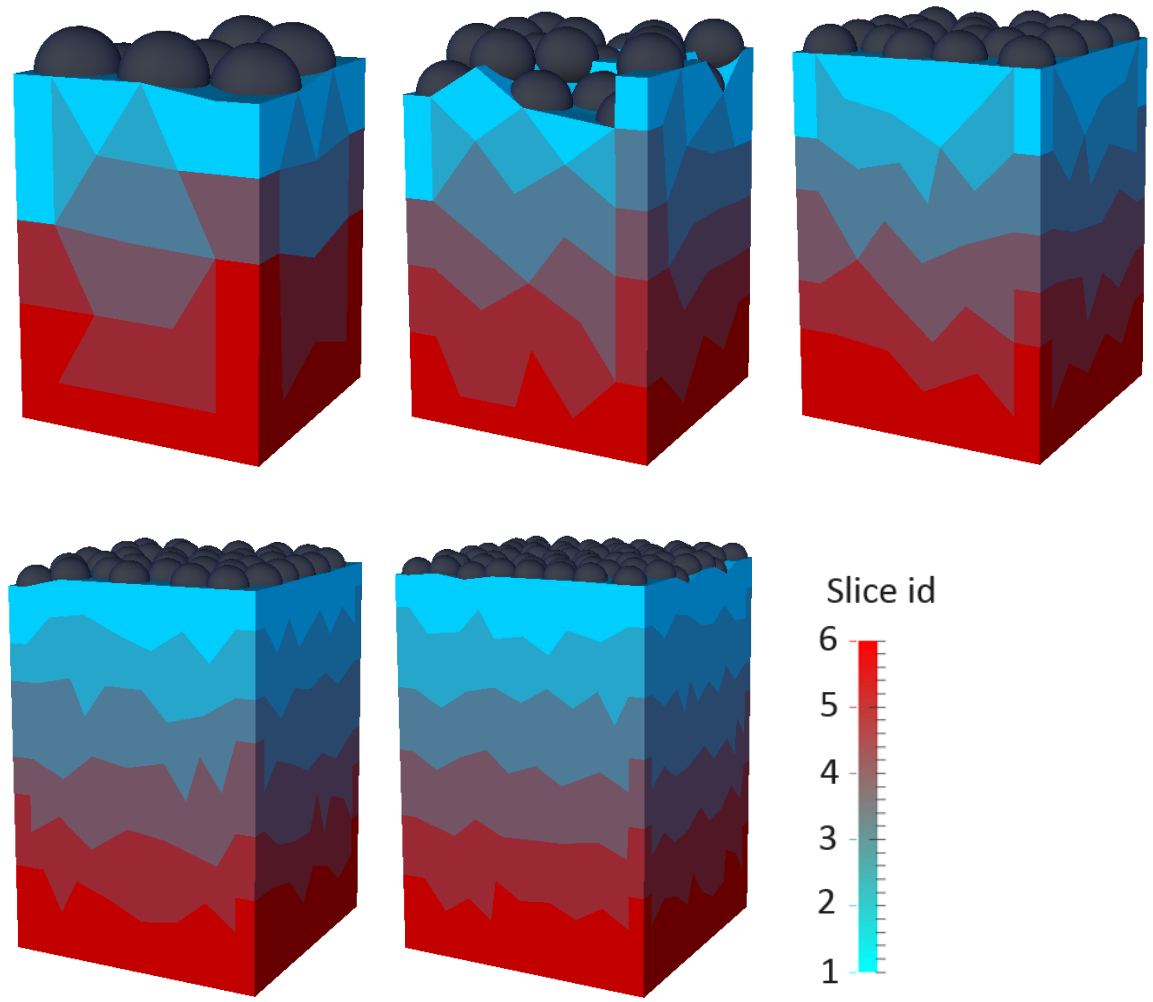

Figure 4.8. Slices of pores used for the calculation of saturation profiles obtained from TPNM for the cases of monodisperse aggregates having aggregate size as 3 mm × 3 mm × 4.5 mm. Pores belonging to the same slice are shown in same color.

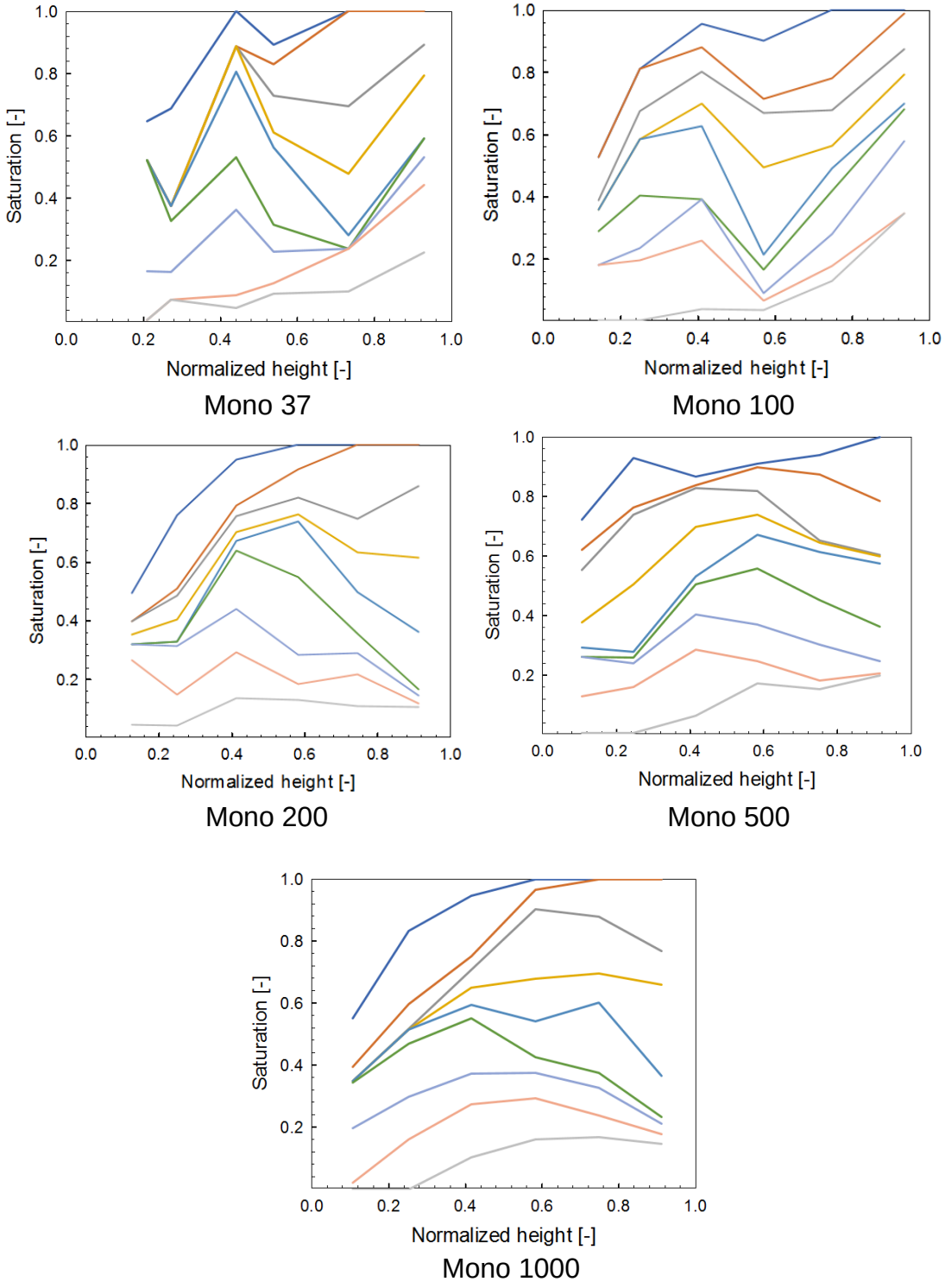

Figure 4.9. Saturation profile of monodisperse aggregates at different network saturations: from 0.9 to 0.1 with interval as 0.1.

The ratios between aggregate width or depth and particle diameter, as well as between aggregate height and particle diameter are shown in Tab. 4.10 for the investigated

monodisperse aggregates. It is known from packed tubes (e.g., packed bed reactors) that average porosity increases with decreasing tube-to-particle diameter ratio [193-195] and the same can be observed for the present data (Tab. 4.5). A respective plot is shown in Fig. 4.10. There, porosity of the monodisperse aggregates is also compared with the empirical equation of Sonntag [196]:

$$\varepsilon = \varepsilon_\infty + (1 - \varepsilon_\infty) \times \frac{0.526}{D_t/_d}\,, \tag{4.3}$$

where ε is the aggregate porosity, ε_∞ is the porosity of the unconfined (infinitely extended) aggregate, $D_t/_d$ is tube-to-particle diameter ratio (for particles packed in a cylindrical tube). Proper agreement is obtained when a porosity of 0.354 is used for the unconfined (infinitely extended) particle aggregate. It should be noted that D_t for the aggregates investigated in this chapter is approximated by the diameter of a circle with area equal to the cross-sectional area of the cuboid (W×D).

Table 4.10: Size ratios between the aggregate dimensions and particle diameter (horizontal: W/d = D/d, vertical: H/d) for the investigated monodisperse aggregates.

Aggregate	W/d	H/d
Mono 37	3.99	4.49
Mono 100	4.12	6.18
Mono 200	5.03	7.55
Mono 500	6.76	10.1
Mono 1000	8.43	12.6

The drying rate and drying time curves of the investigated monodisperse aggregates obtained by means of TPNM are shown in Fig. 4.11. Although all aggregates have the same boundary layer aggregate, the initial drying rates of these aggregates are not exactly the same. The reason is that the surface area of these aggregates is not identical (see the pores at the top of the aggregate in Fig. 4.8), which results from the void space discretization at the contact between the top surface of the main aggregate and the bottom part of the boundary layer aggregate. The top surface of Mono 100 is significantly rougher as the ones of other investigated monodisperse aggregates,

which leads to higher initial surface area. Consequently, the initial drying rate of Mono 100 is the highest rate among all investigated aggregates. However, the non-flat top surface also results in larger volume of big pores at the top of the Mono 100 aggregate compared to the other monodisperse aggregates. These large pores are more preferentially invaded during the drying process, which leads to a large dry region near the top surface of the aggregate. This is the reason why the drying rate of the Mono 100 aggregate drops remarkably right from the beginning. Regarding the initial drying rate of the Mono 37 aggregate, since the particle radius of this aggregate is significantly larger than the other investigated monodisperse aggregates (see Tab. 4.5), the area fraction of the solid phase is slightly higher, which leads to smaller void area. Consequently, the initial drying rate of the Mono 37 aggregate is slightly smaller than the ones of other monodisperse aggregates. The influence of differences in the initial drying rate of the investigated monodisperse aggregates can be eliminated by dividing running drying rates with the corresponding initial drying rate of each aggregate. This results in normalized drying rate curves, as shown in Fig. 4.12.

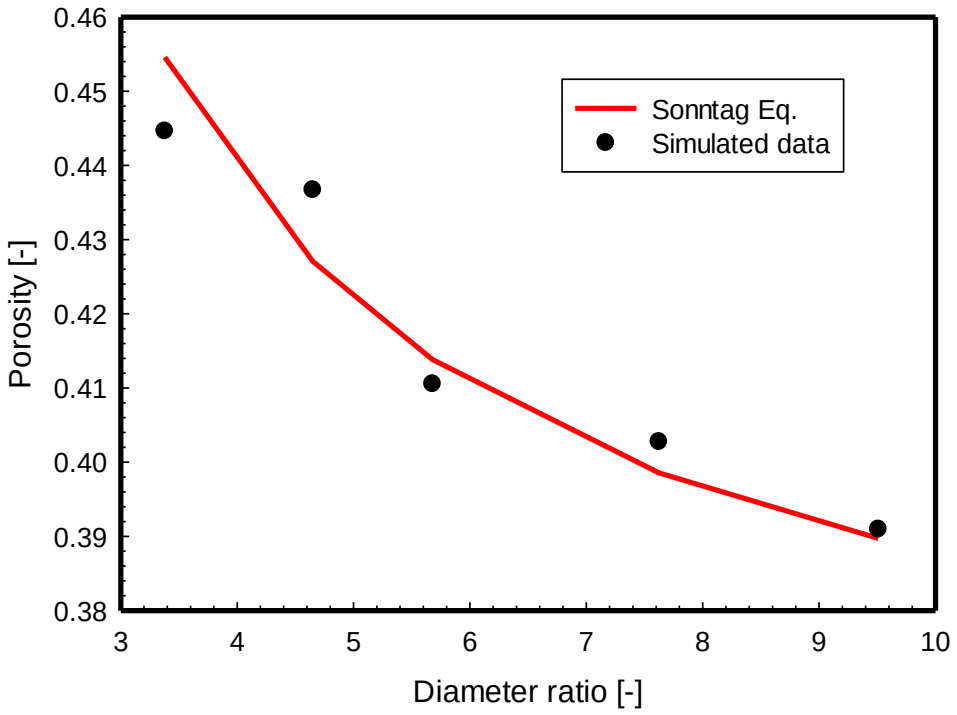

Figure 4.10. The dependence of aggregate porosity on the tube-to-particle diameter ratio for the case of monodisperse aggregates listed in Tab. 4.10.

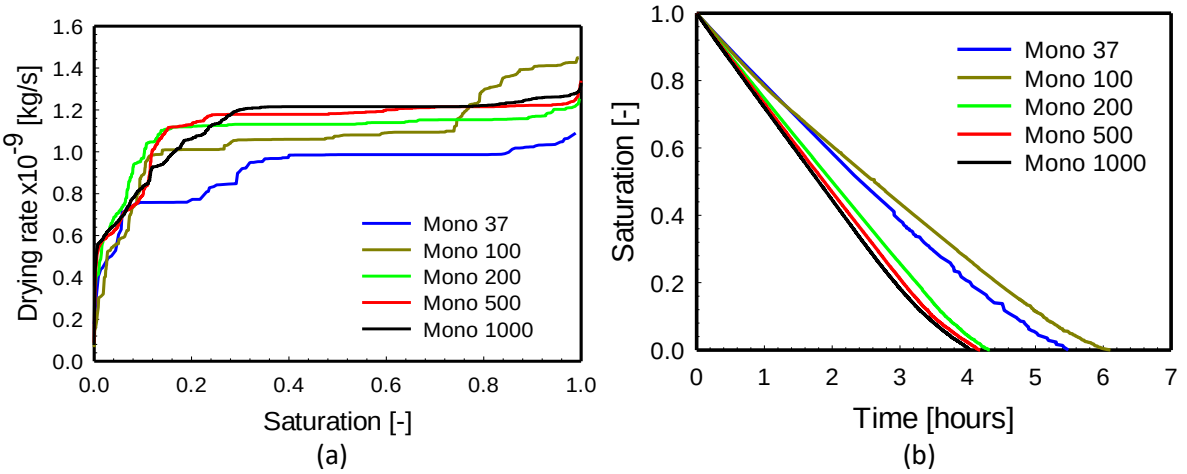

Figure 4.11. Drying kinetics of the investigated monodisperse aggregates: (a) Drying rate (b) Drying time.

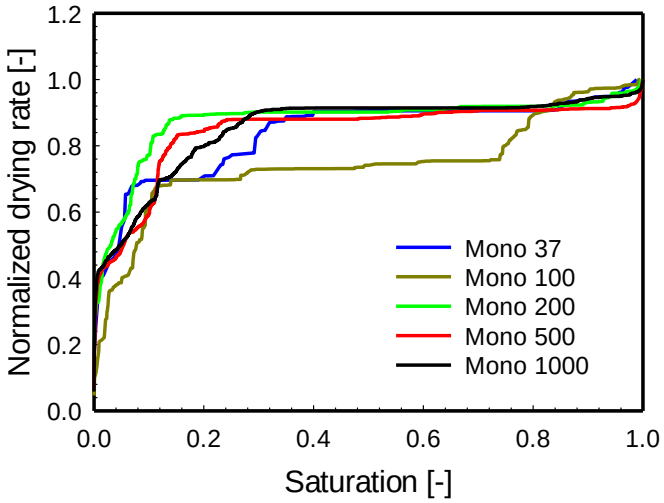

Figure 4.12. The drying rate of the investigated monodisperse aggregates (normalized by the corresponding initial drying rate of each aggregate).

One observation regarding drying kinetics is the long first drying period (the drying period characterized by a relatively high drying rate [18, 19]). The first drying period is extended because the liquid connectivity throughout the aggregate is maintained until low network saturation, expressed in Fig. 4.13 by the fact that all the liquid belongs to one and the same main liquid cluster (MLC). The long-lasting liquid connectivity of the synthetic monodisperse aggregates investigated in this chapter is similar to what has been obtained for the real aggregate investigated in Chapter 3, as the comparison between Fig. 4.13a and Fig. 4.13b shows. In both cases the spread in the distribution

of entry capillary radius of the throats, which is known to be an indicator for the duration of the first drying period (see discussion in Chapter 3) is very large: The respective coefficient of variation (COV) ranges from 44.2% to 53.2% for the synthetic aggregates (Tab. 4.9), whereas it has been with 67.1% even higher for the real aggregate, which at this level does not play a role.

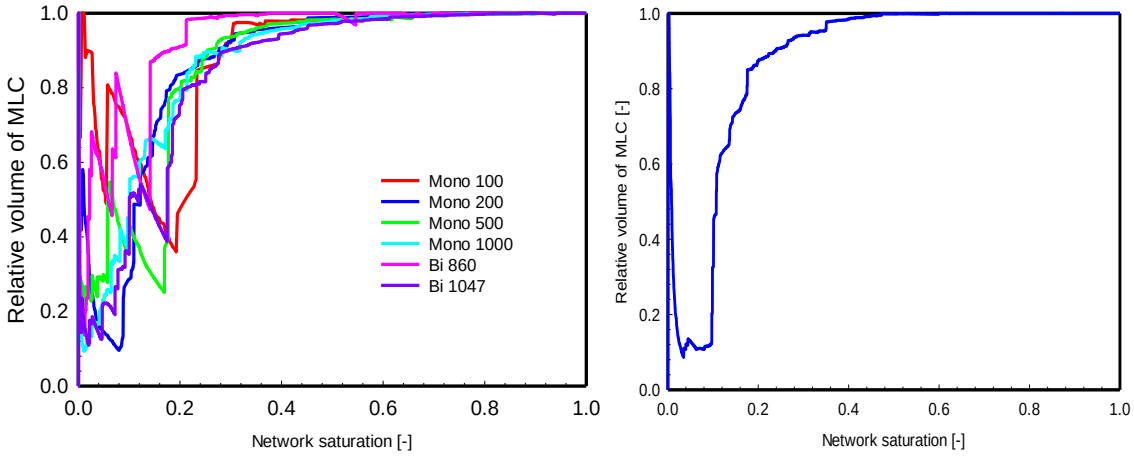

Figure 4.13. Evolution of the volume ratio of main liquid cluster to the total volume of the remaining liquid over time: (a) Simulated data from TPNM for the case of monodisperse and bidisperse aggregates investigated in this chapter and (b) for the aggregate investigated in Chapter 3.

A second observation are the small differences in the drying rate of investigated monodisperse aggregates in the second drying period. There is an opposing trend of COV of entry throat radius increasing with increasing number of particles in the aggregate (from Mono 37 to Mono 1000), but decreasing COV of the mass transfer throat radius and of pore radius in Tab. 4.9. At the same time, it can be observed in Fig. 4.12 that in the first stage of the second drying period the drying rate increases from Mono 37 to Mono 200, to then decrease again for Mono 500 and Mono 1000. However, it is difficult to say whether those two effects correlate with each other, or whether the small differences among the drying curves of monodispersed aggregates are, at all, significant.

4.4 Influence of particle size distribution on drying kinetics and liquid phase distribution of bidisperse aggregates

A large body of reported literature considered the solid phase as a monodisperse system. However, most of particle aggregates involved in industrial and natural processes are composed of particles with a broad range of particle sizes. Binary mixtures consisting of coarse particles (e.g., rock, gravel, and sand) and fine particles (e.g., sand, clay and silt) represent the simplest case of non-uniformly sized particulate systems. Thus, the influence of particle size on drying kinetics is further investigated by the comparison between monodisperse aggregates and bidisperse aggregates (mixtures of fine and coarse particles).

The bidisperse aggregates are generated by varying the volume fraction of fine particles Q_f as well as the size ratio between coarse and fine particles d_c/d_f. As pointed out in Sections 4.1 and 4.2, particle sizes cannot be met exactly by the used aggregate generation method, but aggregate Mono 37 served as a reference for the size of the coarse particles, whereas the size of fine particles was oriented upon the Mono 500 and the Mono 1000 aggregates. Fig. 4.14 and Tab. 4.11 present all generated bidisperse aggregates. It has been drawn with two limiting curves for very large d_c/d_f ratio according to [197], as also presented in [198]:

$$\varepsilon = \left(1 - \frac{1-\varepsilon_{mono}}{\varepsilon_{mono}} \frac{Q_f}{1-Q_f}\right) \varepsilon_{mono} \,, \tag{4.4}$$

$$\varepsilon = \frac{Q_f}{1-\varepsilon_{mono}+\varepsilon_{mono}Q_f} \varepsilon_{mono} \,. \tag{4.5}$$

The porosity ε_{mono} of the monodisperse packing, which constitutes the upper bound of the region of bidisperse aggregates in the plot but is also necessary for the calculation of the lower limit curves, was set to 0.4. With this choice, not all points that characterize bidisperse aggregates are located in the theoretically expected region of the plot. It should, however, be noted that this contemplation is not exact, because there is a strong wall effect in the present data, whereas the limiting curves for d_c/d_f going to infinity have been derived for the theoretical case of unconfined particle assemblies. This is also the reason for monodisperse aggregate porosity in Fig. 4.14 being larger than the porosity ε_∞ of the unconfined monodisperse packing in Fig. 4.10, but obviously still not large enough.

Table 4.11: Summary of final values of parameters defining the solid phase of generated bidisperse aggregates.

Aggregate	d_c (mm)	d_f (mm)	d_c/d_f (-)	Q_f Set value (%)	Q_f Final value (%)	Porosity (-)	Mean radius (mm)	Tube-to-particle diameter ratio (-)
Bi 180	0.383	0.268	1.43	50.0	50.0	0.465	0.298	5.7
Bi 250	0.410	0.205	2.00	30.0	30.7	0.433	0.250	6.8
Bi 285	0.418	0.209	2.00	40.0	38.2	0.414	0.244	6.9
Bi 316	0.422	0.211	2.00	50.0	44.9	0.409	0.239	7.1
Bi 341	0.442	0.221	2.00	60.0	61.2	0.426	0.237	7.1
Bi 679	0.472	0.142	3.33	30.0	29.1	0.356	0.162	10.4
Bi 684	0.546	0.164	3.33	40.0	47.3	0.362	0.175	9.7
Bi 807	0.555	0.167	3.33	50.0	60.5	0.373	0.173	9.8
Bi 903	0.550	0.165	3.33	60.0	66.7	0.381	0.170	10.0
Bi 1047	0.542	0.163	3.33	70.0	75.7	0.389	0.166	10.2
Bi 860	0.539	0.108	5.00	20.0	18.1	0.408	0.123	13.8
Bi 1052	0.576	0.115	5.00	30.0	25.5	0.364	0.126	13.5
Bi 1434	0.612	0.122	5.00	40.0	38.6	0.306	0.119	14.3
Bi 1381	0.636	0.127	5.00	50.0	42.1	0.309	0.133	12.7
Bi 1760	0.685	0.137	5.00	60.0	73.7	0.366	0.139	12.2
Bi 1222	0.752	0.113	6.67	30.0	29.0	0.381	0.118	14.3
Bi 1506	0.768	0.115	6.67	40.0	38.7	0.389	0.250	6.8
Bi 2959	0.729	0.109	6.67	50.0	58.7	0.321	0.111	15.3
Bi 3026	0.792	0.119	6.67	60.0	83.6	0.373	0.119	14.2

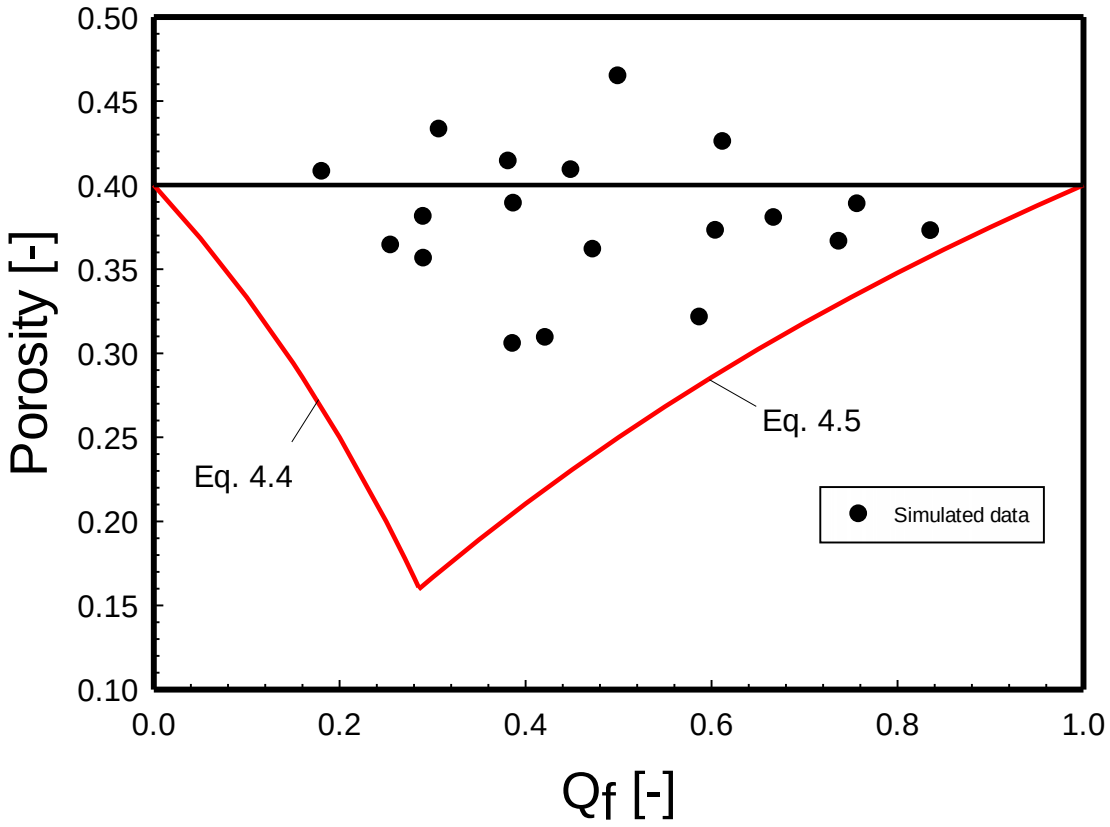

Figure 4.14. The dependence of bidisperse aggregate porosity ε on the size ratio (d_c/d_f) and the volume fraction of the fine particles Q_f. Limiting curves for $d_c/d_f \rightarrow \infty$ according to [197], ε_{mono} = 0.4.

Figure 4.14 shows that the porosity of bidisperse aggregates is, expectedly, mostly smaller than monodisperse aggregate porosity. The tube-to-particle diameter ratios of the aggregates having porosity higher than 0.4 are significantly smaller than the aggregates having porosity smaller than 0.4 (5.7 to 7.1 compared to 9.7 to 15.3, respectively). The only two exceptions are Bi 860 and Bi 1506 aggregates, but these two aggregates are not densely packed as the other generated bidisperse aggregates are.

The compaction effect of particle size dispersity is easy to compute analytically for d_c/d_f going to infinity, but analytical solutions don't exist otherwise. Therefore, an empirical correlation has been proposed by Tsotsas [199], see also [200, 201], which enables to obtain bed porosity from an expression for the spread of the particle size distribution:

$$\varepsilon = (-0.112\,\zeta^3 + 0.017\,\zeta^2 - 0.259\,\zeta + 1)\varepsilon_{mono}\,, \tag{4.6}$$

where ζ reflects the impact of particle size dispersity and can be calculated for the case of bidisperse aggregate as:

$$\zeta = \sqrt{\frac{\frac{Q_f}{{d_f}^2}+\frac{Q_c}{{d_c}^2}}{\left(\frac{Q_f}{d_f}+\frac{Q_c}{d_c}\right)^2} - 1}\,, \tag{4.7}$$

where Q_c is volume fraction of coarse particles, $Q_c = 1 - Q_f$. Multiplying both numerator and denominator of Eq. 4.7 by ${d_f}^2$ gives:

$$\zeta = \sqrt{\frac{Q_f+\frac{1-Q_f}{\left(d_c/d_f\right)^2}}{\left(Q_f+\frac{1-Q_f}{d_c/d_f}\right)^2} - 1}\quad. \tag{4.8}$$

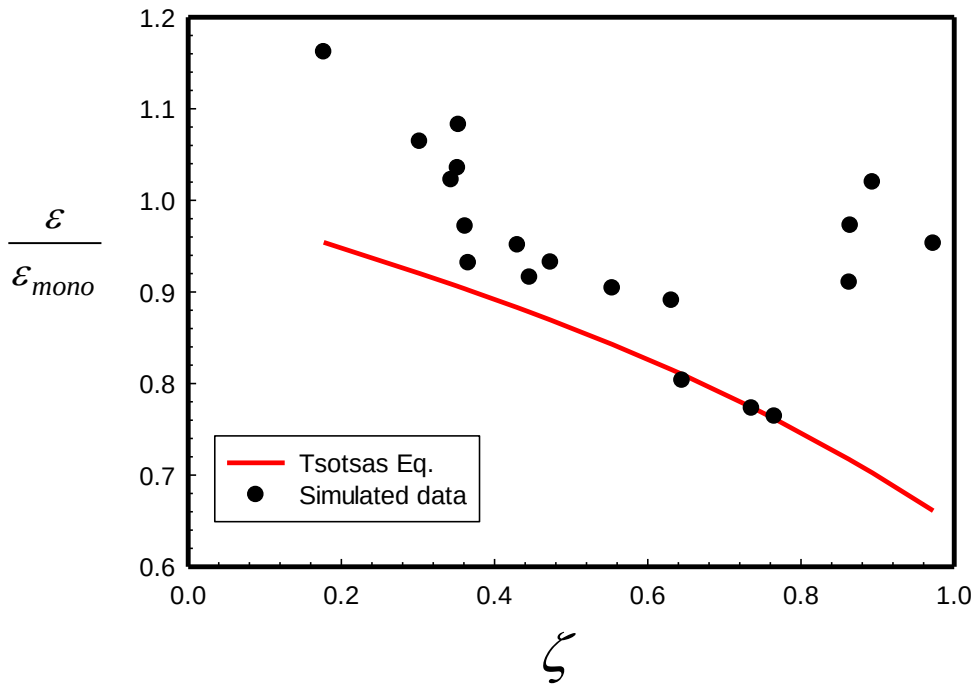

Figure 4.15. The dependence of porosity ratio between bidisperse aggregate ε and monodisperse aggregate ε_{mono} on the particle size dispersity ζ. The red line is calculated according to empirical correlation proposed by Tsotsas [199], ε_{mono} = 0.400 for monodisperse aggregate.

In general, ζ is identical to the coefficient of variation (COV) (i.e., the relative standard deviation: standard deviation by mean value) of particle diameter. The correlation according to Eqs. 4.6 and 4.8 is compared with the present data for bidisperse aggregates in Fig. 4.15 by using the same monodisperse aggregate porosity as in Fig. 4.14. Again, the comparison is not ideal because of the simultaneous existence of wall effect and particle size dispersity effect on aggregate porosity. However, the qualitative trend of porosity decreased with increasing ζ is obtained.

From the various generated aggregates, two bidisperse aggregates having the most significant differences in terms of the solid structure have been chosen for further investigation. The two further investigated aggregates are illustrated in Fig. 4.16 while the illustration of other generated bidisperse aggregates is presented in Appendix A3. The first bidisperse aggregate with (Q_f = 18.1% (final value), d_c/d_f = 5.0) has 860 particles (hereafter termed Bi 860) and the second bidisperse aggregate with (Q_f, d_c/d_f) as (75.7%, 3.33) has 1047 particles (termed Bi 1047). The radii of the fine and coarse particles of Bi 860 are 0.108 mm and 0.539 mm, respectively, while the corresponding values of the Bi 1047 aggregate are 0.163 mm and 0.542 mm, respectively.

Statistical properties (mean, standard deviation and coefficient of variation, COV) of the size distributions of pore volume, throat entry capillary threshold radius, and throat mass exchange radius for the two investigated bidisperse aggregates are shown in Tab. 4.12. The Bi 1047 aggregate has its pore and throat size distributions not so much different in comparison to the monodisperse aggregates investigated in Section 4.3, especially the ones of the Mono 1000 aggregate. Whereas the Bi 860 aggregate has a significant difference in all considered statistical properties of the pore and throat size distributions. The obvious reason for this is that Bi 860 has a totally different solid structure compared to other investigated aggregates. While Bi 1047 has fine particles dominant and being almost uniformly distributed in the void space between coarse particles, Bi 860 has coarse particles dominant (80% in solid volume) and the fine particles in Bi 860 are not equally distributed in the void space between coarse particles. The fine particles in the upper part of the Bi 860 aggregate do not fill all the void space between coarse particles so densely as in the lower part of this aggregate (Fig. 4.16a). This solid skeleton of Bi 860 is, thus, atypical and similar to a layered

Table 4.12: Statistical properties of the distributions of pore radius (from volume equivalent sphere), throat entry capillary threshold radius, and mass exchange throat radius (from surface equivalent circle) for the two further investigated bidisperse aggregates.

Aggregate	Pore volume (equivalent radius)			Throat entry capillary radius			Throat mass transfer (equivalent radius)		
	Mean, mm	SD, mm	COV, %	Mean, mm	SD, mm	COV, %	Mean, mm	SD, mm	COV, %
Bi 860	0.0743	0.0330	44.37	0.0591	0.0740	125.09	0.0981	0.0204	20.75
Bi 1047	0.0823	0.0163	19.83	0.0478	0.0269	56.29	0.1262	0.0046	3.62

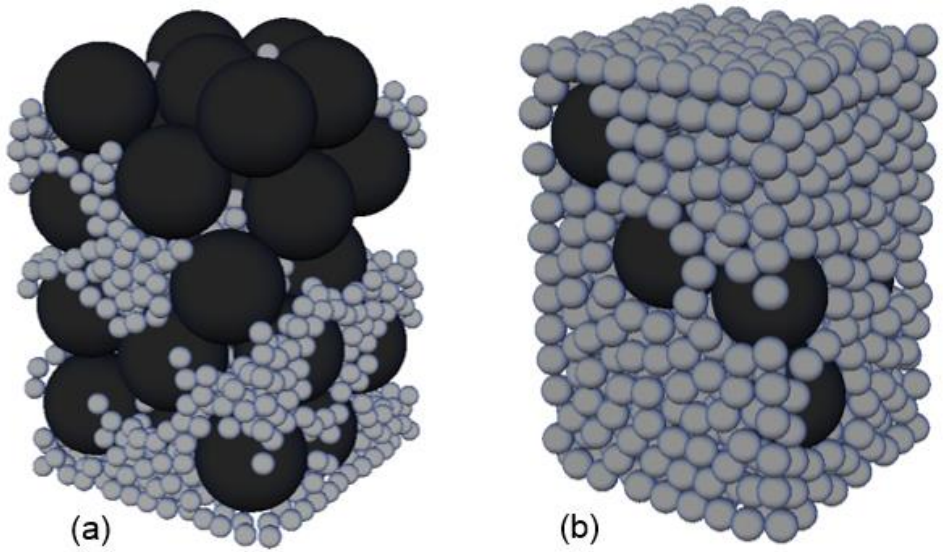

Figure 4.16. Illustration of the solid phase of (a) aggregate Bi 860 with 20% (solid volume) fine particles, and (b) aggregate Bi 1047 with 70% fine particles (Bi 1047).

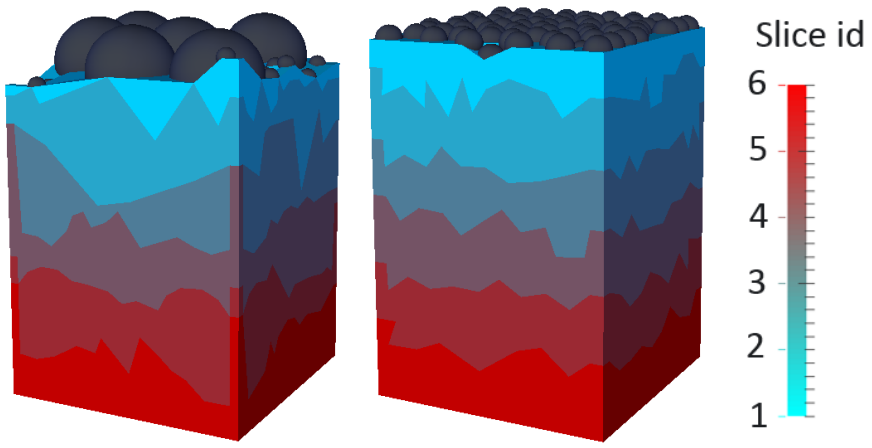

Figure 4.17. Slices of pores used for the calculation of saturation profiles obtained from TPNM for bidisperse aggregates of size 3 mm × 3 mm × 4.5 mm. Pores belonging to the same slice are shown in same color.

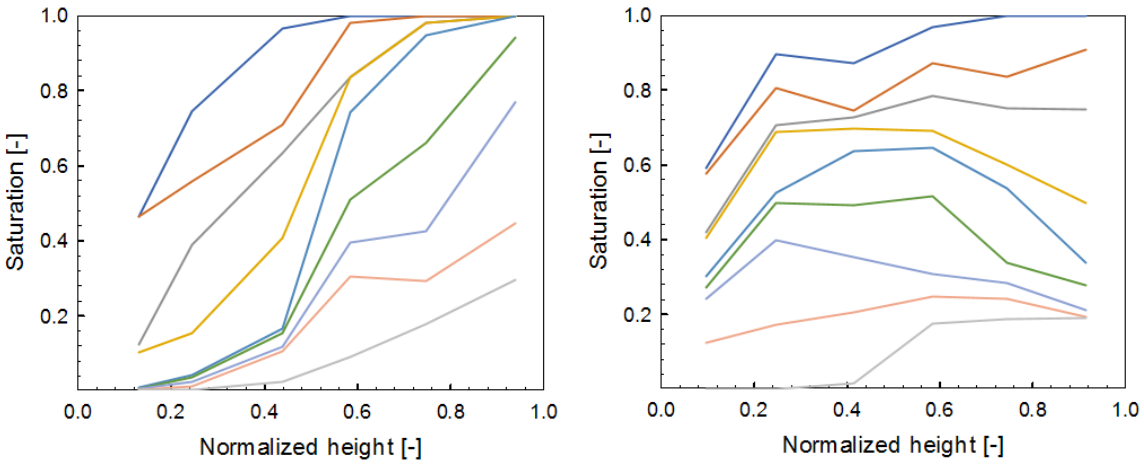

Figure 4.18. Saturation profile of (a) Bi 860 and (b) Bi 1047 aggregates at different network saturations: from 0.9 to 0.1 with interval as 0.1.

porous medium. The influence of this on saturation profile and drying kinetics will be discussed later on.

In the preparation for the saturation profile plots, slices of pores of the bidisperse aggregates are defined similarly to what has been presented in Chapter 3. And, as it has been discussed in Section 4.3, all aggregates investigated in this chapter are divided into the same number of slices (six) to be comparable in terms of saturation

profiles. Illustrations of the slices of pores of the bidisperse aggregates investigated in this chapter are shown in Fig. 4.17.

The Bi 1047 aggregate consists of coarse particles having radius (0.536 mm) almost equal to the radius of the Mono 37 aggregate (0.501 mm) and fine particles having radius (0.163 mm) almost equal to the radius of particles in the Mono 1000 aggregate (0.178 mm). The saturation profile of the Bi 1047 aggregate is, therefore, similar to the one of the Mono 1000 aggregate. This can be seen by comparing Fig. 4.18b with the last plot of Fig. 4.9. Moreover, the dependence of the relative volume of the main liquid cluster on global saturation is very similar for aggregate Bi 1047 and aggregate Mono 1000, as Fig. 4.13a shows. It may be concluded that the solid volume dominating fine particles do not only control the pore and throat size distributions but also control the liquid phase distribution in the drying Bi 1047 aggregate.

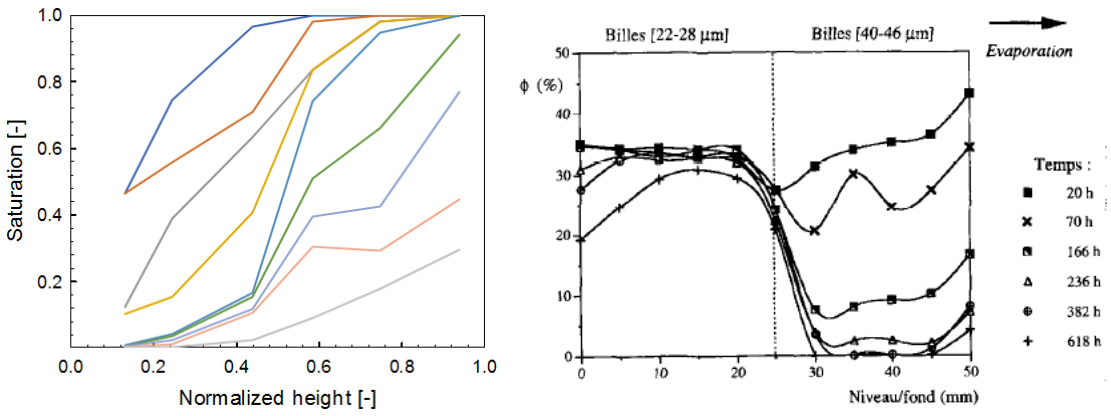

(a) (b)

Figure 4.19. Saturation profiles at different times during the drying of: (a) Bi 860 aggregate, profiles corresponding to network saturation decreasing in steps of 0.1 from 0.9 to 0.1 (evaporation to the left, in opposite direction as in the second plot); (b) Layered composite reported in [134], with coarse particles (40-46 µm) on top of fine particles (22-28 µm).

In contrast to Bi 1047, the solid volume of aggregate Bi 860 is dominated by coarse particles. Moreover, the minority fine particles are not evenly distributed in the void space between coarse particles. Specifically, there are regions in the upper part of the Bi 860 aggregate that have almost no fine particles between the coarse particles. Consequently, the upper part rapidly dries while the lower part remains close to

saturation until network saturation of 0.5, the moment when the liquid saturation in locations of the upper part has become smaller than 0.2. Similar patterns of moisture distribution as in the Bi 860 aggregate (Fig. 4.19a, evaporation through coarse layer to the left) were observed in an experiment reported in [134], see Fig. 4.19b (evaporation through coarse layer to the right). This experiment had a similar drying setup as the one used in this chapter. The experimental aggregate consisted of two layers. Each layer was a nearly monodisperse particle packing. The packing having larger particle size (40-46 µm) was placed on top of the packing having smaller particle size (22-28 µm). As in our case, evaporation could only occur at the top of the aggregate. However, the drying time of this experiment is not in the same order of magnitude as the one of Bi 860 aggregate. Possible reasons are different drying conditions (temperature, air velocity, etc.) and, especially, different aggregate dimension (apparently larger in [134], but not reported there).

The drying rate and drying time curves of the investigated bidisperse aggregates obtained by means of TPNM are shown in Fig. 4.20. The two different drying stages of the Bi 860 aggregate can be seen clearly from these kinetic curves. In fact, there are two quasi-constant drying rate periods in case of the Bi 860 aggregate, corresponding to different levels of drying rate in Fig. 4.20a and different slopes of global saturation decrease in Fig. 4.20b. The drying time of aggregate Bi 1047 is with around 4.5 h in Fig. 4.20b somewhat larger than the drying time of the similarly behaving Mono 1000 aggregate of ca. 4 h in Fig. 4.11b.

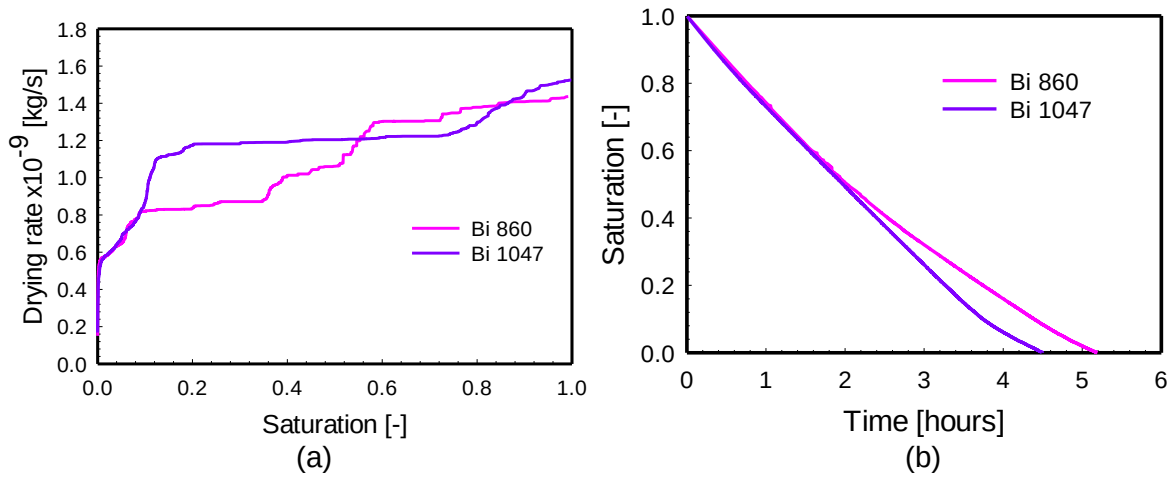

Figure 4.20. Drying kinetics of bidisperse aggregates: (a) Drying rate (b) Drying time.

4.5 Influence of particle size distribution on drying kinetics and liquid phase distribution of polydisperse aggregates

The influence of particle size heterogeneity (or polydispersity) on drying kinetics is further investigated by the comparison between monodisperse aggregates and

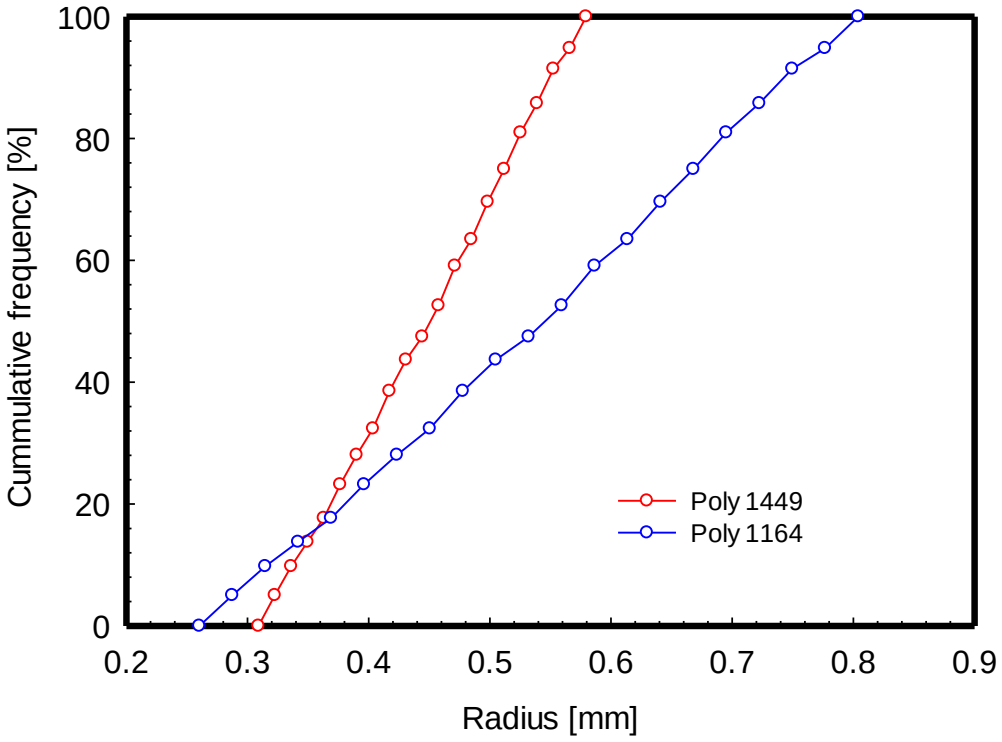

Figure 4.21. Final particle volume distributions of Poly 1449 and Poly 1164 aggregates.

polydisperse aggregates. These aggregates have the same cuboid envelope shape but larger dimensions: 8 mm × 8 mm × 12 mm compared to 3 mm × 3 mm × 4.5 mm of the aggregates investigated in previous sections. The reference aggregate consists of 1600 particles with a uniform radius of 0.409 mm, hereafter termed Mono 1600. The polydisperse aggregates are generated such that their mean particle radius is relatively close to the particle radius of Mono 1600. The first polydisperse aggregate has been generated from an initial distribution with a width of 30% of the initial mean value on each side of it. Aggregate generation resulted in this case in 1449 particles with final particle radii in the range from 0.31 to 0.58 mm. This aggregate is termed Poly 1449. Starting with an initial width of 50%, the final range of particle radii of the second polydisperse aggregate is from 0.27 to 0.82 mm. There are 1164 particles in this second polydisperse aggregate that is termed Poly 1164. Final particle volume

Table 4.13: Statistical properties of the distributions of pore radius (volume equivalent), throat entry capillary threshold radius, and mass transfer throat radius (surface equivalent) for the case of one monodisperse (reference) and two polydisperse aggregates having large aggregate size of 8 mm × 8 mm × 12 mm.

Aggregate	Pore volume (equivalent radius)			Throat entry capillary radius			Throat mass transfer (equivalent radius)		
	Mean, mm	SD, mm	COV, %	Mean, mm	SD, mm	COV, %	Mean, mm	SD, mm	COV, %
Mono 1600	0.1947	0.0334	17.17	0.1085	0.0588	54.19	0.3293	0.0228	6.93
Poly 1449	0.1990	0.0367	18.43	0.1158	0.0627	54.12	0.3400	0.0413	12.13
Poly 1164	0.2113	0.0455	21.52	0.1261	0.0715	56.69	0.3645	0.0677	18.58

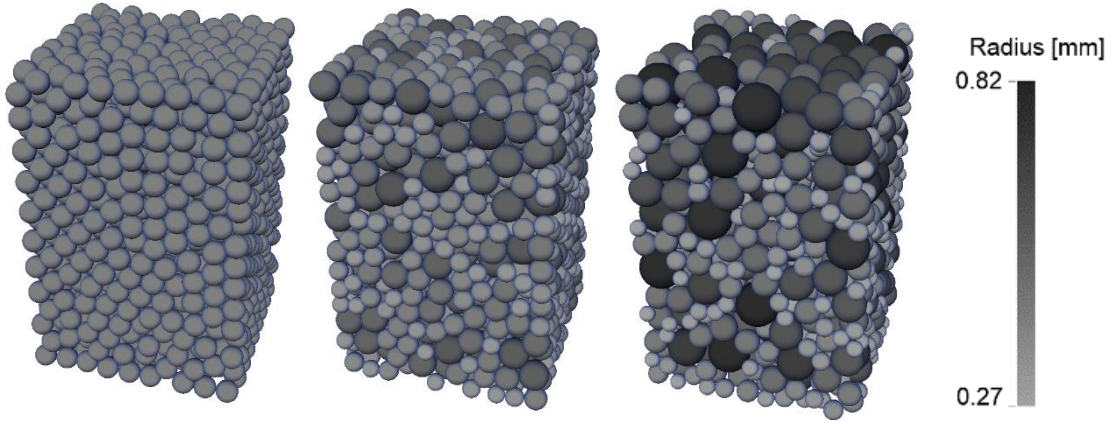

Figure 4.22. Illustration of the solid phase of large aggregates comprised of (a) monodisperse primary particles (Mono 1600), (b) polydisperse primary particles with narrow particle radius distribution (width of initial distribution at 2x30% of the mean), (Poly 1449), and (c) polydisperse primary particles with broader particle radius distribution (width of initially 2x50% of the mean), (Poly 1164).

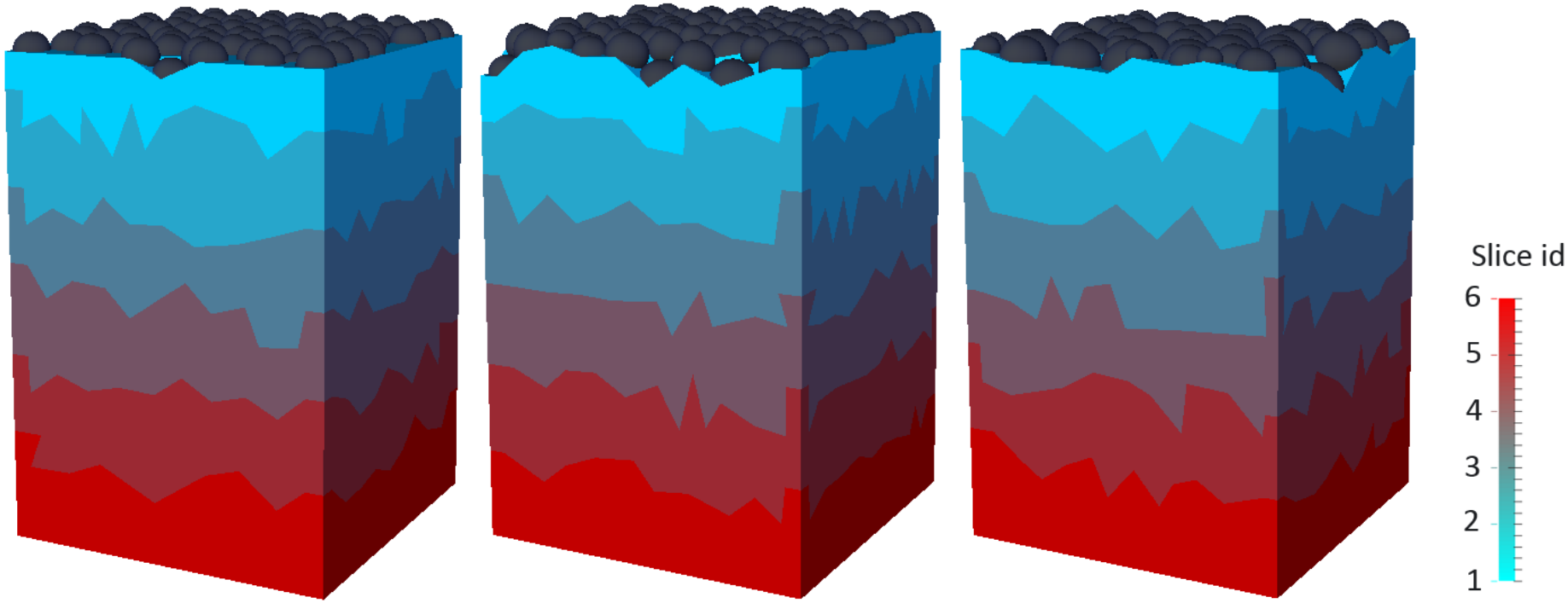

Figure 4.23. Slices of pores used for the calculation of saturation profiles obtained from TPNM for the cases of one monodisperse and two polydisperse aggregates of large size (8 mm × 8 mm × 12 mm). Pores belonging to the same slice are shown in same color.

distributions of these two polydisperse aggregates are shown in Fig. 4.21. As expected, they are nearly straight lines. Half (50%) of the particle volume of the aggregate comes from particles having radius smaller than 0.442 mm for Poly 1449 and 0.540 mmm for Poly 1164. Arithmetic means of particle radii (which have been given in Tab. 4.5) are 0.409 mm for Poly 1449 and 0.415 mm for Poly 1164. The solid phase of each of the three synthetic aggregates of this series is illustrated in Fig. 4.22.

Statistical properties (mean, standard deviation and coefficient of variation, COV) of the distributions of the radii of pores, throats (entry capillary threshold), and throats (mass transfer) for the three investigated large aggregates of size 8 mm × 8 mm × 12 mm are shown in Tab. 4.13. The broader the particle size distribution is, the broader become also the size distributions of pores and throats, but this effect is pronounced only in respect to the coefficient of variance of mass transfer radius, which is not important for drying kinetics. Contrary, the COV values of quantities that can seriously influence liquid transport (primarily the capillary entry threshold of throat radius, secondarily the volume equivalent radius of pores) do not change significantly from Mono 1600 to Poly 1449 and then to Poly 1164.

In the preparation for the saturation profile plots, slices of pores of the aggregates investigated in this section are defined similarly to the previous sections. It remains that all aggregates investigated in this chapter have been divided into the same number of six slices, to promote the comparability of saturation profiles. Illustrations of the slices of pores of the aggregates investigated in this section are shown in Fig. 4.23.

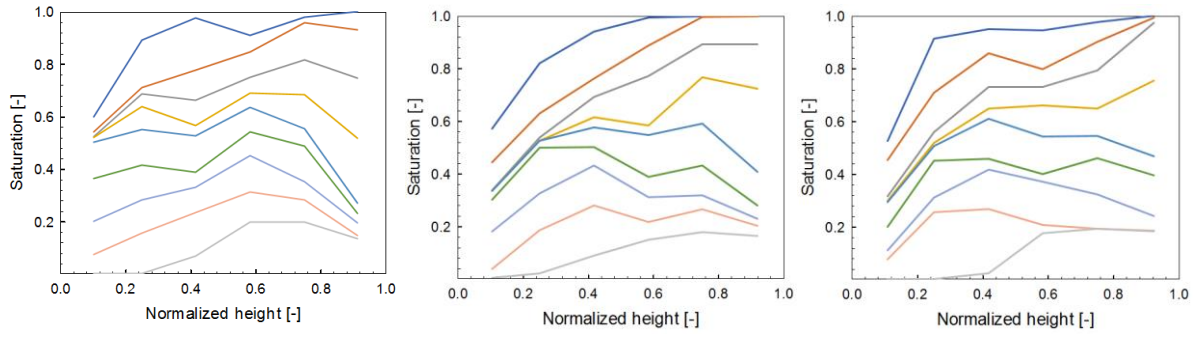

Figure 4.24. Saturation profiles of (a) Mono 1600, (b) Poly 1449 and (c) Poly 1164 aggregates at different network saturations: from 0.9 to 0.1 in steps of 0.1.

Table 4.14: Size ratios of aggregate dimensions to particle diameter (horizontal: W/d, vertical: H/d) for the investigated large aggregates (one monodisperse and two polydisperse).

Aggregate	W/d	H/d
Mono 1600	9.78	14.7
Poly 1449	9.78	14.7
Poly 1164	9.64	14.5

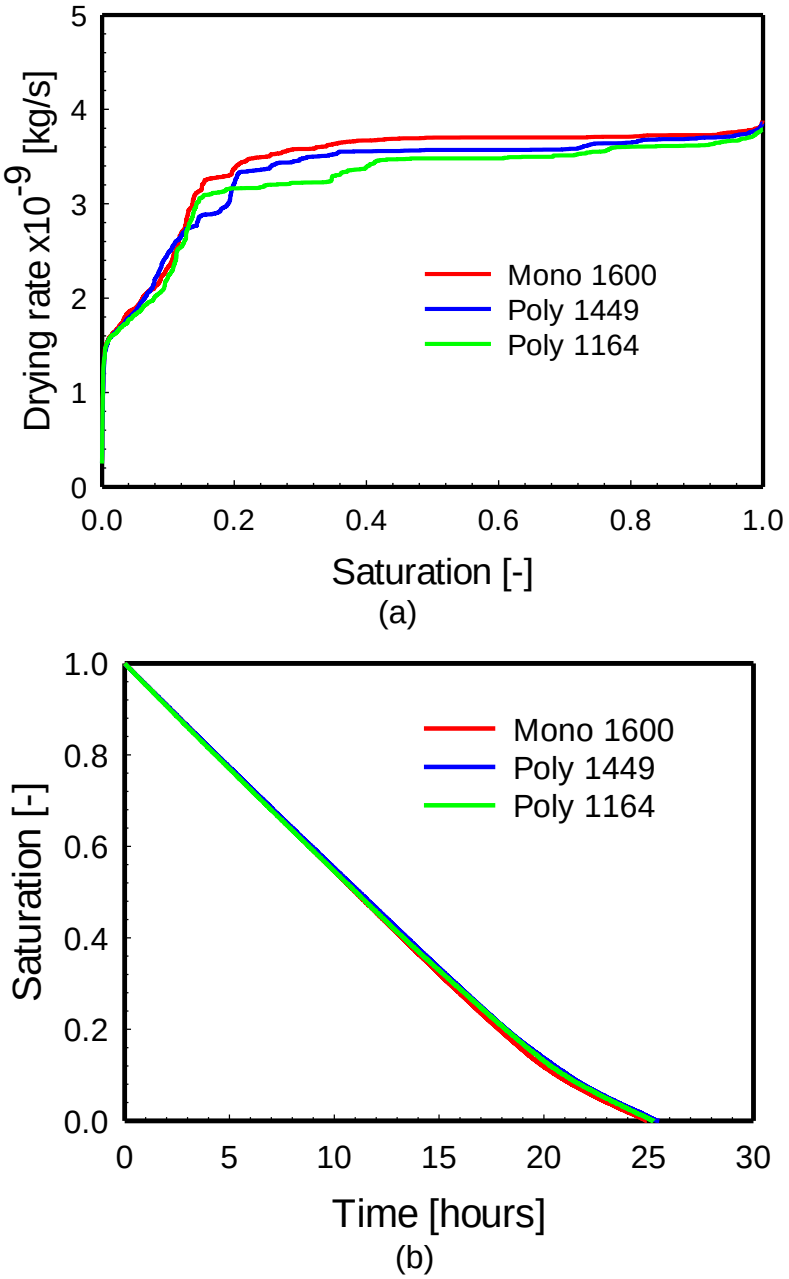

Figure 4.25. Drying kinetics comparison between Monodisperse and Polydisperse aggregates having dimensions of 8 mm × 8 mm × 12 mm: (a) Drying rate (b) Drying time.

It is noticed that the size ratios of container dimension to the mean particle diameter of the three aggregates investigated in this section are almost the same (Tab. 4.14) and somewhat larger than the largest respective values (for Mono 1000) in Tab. 4.10. In combination with almost the same size distribution of throat entry capillary radius (coefficients of variation between 54.2% and 56.7%, Tab. 4.13), these two factors can be the reason why the saturation profiles of these three aggregates are almost the same (Fig. 4.24a). Besides, small wall effect and constantly large variance of capillary radius can also explain why there is almost no significant difference in the drying kinetics (Fig. 4.25). This means that the influence of particle size distribution on liquid distribution as well as on drying kinetics is negligibly small for the aggregates considered in this section.

Long first drying periods with nearly constant drying rate (Fig. 4.25a) continue to belong to the observable drying characteristics. To this respect the behavior of aggregate Mono 1600 is similar to the behavior of aggregate Mono 37 that has similar particle size. Much lower COV of the capillary entry pressure in Mono 37 (20.85%, see Tab. 4.9) indicates that even that level of capillary variability has been high enough for preserving the connectivity of the liquid phase. Consequently, drying characteristics discussed in Section 4.3 do not seem to be due to thinness of the porous medium in terms of the H/d metric. Drying time is around 26 hours for Mono 1600 (Fig. 4.25b), compared to around 5.5 hours for Mono 37 (Fig. 4.11b). Two parameters certainly contribute to the increase in drying time when going from Mono 37 to Mono 1600. First, more water to be evaporated per unit surface area, which can coarsely be approximated by the ratio of the respective aggregate height equal to 12/4.5 = 2.67. Second, less evaporative flux by thicker boundary layer, with an impact factor of 6.5/2.4 = 2.71. Since the two effects are synergetic, they combine to a factor of 7.23, which would yield from 5.5 hours of drying time for Mono 37, 39.7 hours of drying time for Mono 1600. Latter are not extraordinarily different from the simulated ca. 26 hours. Same assessment that would start from around 4.2 hours of drying time for the majority of small monodisperse aggregates (Fig. 4.11b) results in 30 hours for Mono 1600 – still closer to the simulated 26 hours. It should be noted that the rate of diffusion controlled moisture removal (with constant diffusion coefficient) would approximately scale with the square of aggregate heights, namely $(12/4.5)^2 = 7.11$, which together with the increased ratio of water to be removed (factor 2.67, again) would result to a

conjugate effect by factor 19.0, meaning something like 80 to 104 h for the large aggregate. This is much larger than simulated results, underlying once more the importance of liquid transport for porous media like the ones that have here been investigated.

In general, the drying behavior seems to be dominated by the fundamental nature of the porous medium, namely solid skeleton made of spherical particles and the complementary, foam-like void phase. Details and variations that take place within this frame seem to be of secondary importance for moisture distribution during the drying process and global drying rate. As expected, global porosity and the mean size of void space features do not seem to be overly significant, whereas the variance of pore space metrics appears to be securely in a range of values which are large enough as to provide sufficient liquid transport. These conclusions can though not be generalized to other classes of materials with other ranges of pore and throat sizes. Conditions of high resistance to liquid transport by viscosity would create a fundamentally different setting, and the same is true for conditions of high, size-dependent transport resistances in the gas phase, for example by Knudsen diffusion in very small pores. Moreover, high drying rates and/or steep temperature gradients may play an important role.

Chapter 5

Capillary forces in the drying particle aggregates of different structure

In Chapter 3 a novel three-dimensional triangulation pore network model (TPNM) has been introduced, which was used in Chapter 4 to simulate the drying process of several different particle aggregates. In such simulations liquid phase distributions are computed. The key idea is now to use the computed liquid phase distributions as inputs for the calculation of respective capillary forces. In this way we can build an explicit link between the liquid phase distribution and the capillary forces that act on primary particles in a drying aggregate.

This chapter is organized as follows: First, computation of capillary forces is presented. Then, evolution of capillary forces together with liquid phase distributions are exemplarily visualized and discussed for one monodisperse aggregate (Mono 100) and two bidisperse aggregates (Bi 860 and Bi 1047). Subsequently, distributions of local capillary forces are presented for all ten aggregates that have already been analyzed in terms of structural properties and drying behavior in Chapter 4. These are five monodisperse and two bidisperse aggregates with dimensions of 3 mm × 3 mm × 4.5 mm as well as one monodisperse and two polydisperse aggregates with dimensions of 8 mm × 8 mm × 12 mm. The results of which are then compared and assessed in regard of the influence of the solid skeleton on the capillary forces.

Finally, the discussion is focused on the maximal capillary force, i.e., on the maximum of all local capillary forces at a certain global saturation as well as on the distribution of such maxima over the whole range of network saturations from unity to zero.

5.1 Capillary force computation

At equilibrium liquid distribution the total capillary force acting on the k[th] primary particle, $\vec{F}_{cap,k}$, consists of two contributions:

$$\vec{F}_{cap,k} = \vec{F}_{sl,k} + \vec{F}_{slg,k}. \tag{5.1}$$

In Eq. 5.1 the first contribution $\vec{F}_{sl,k}$ is induced by the liquid pressure, while the second contribution $\vec{F}_{slg,k}$ is the result of the surface tension of the liquid, σ, acting on the three-phase contact line. Following the method proposed for single-phase flow in [77] and its extension to problems of two-phase flow in granular porous media [197], $\vec{F}_{sl,k}$ is calculated as:

$$\vec{F}_{sl,k} = \sum_{i,j} A_{k,ij}(p_i - p_j)\,\vec{n}_{ij}, \tag{5.2}$$

where p_i, p_j are the liquid or gas pressure in adjacent pores i and j, and $\vec{n}_{ij}$ is the unit normal vector pointing from the Voronoi center of pore i to the Voronoi center of pore j. Denoted by $A_{k,ij}$ is the area calculated from the intersection of the spherical particle k with the common triangle between pores i and j, on which the throat which connects those two pores is also located (Fig. 5.1). Summing up of the force contributions of pairs of pores attached to particle k results in the total capillary force induced by the liquid pressure.

With the assumption that the force resulting from the surface tension is in balance with the pressure force at the three-phase contact line (not to be confused with pressure force exerted on wetted area), the second force contribution $\vec{F}_{slg}$ is estimated as:

$$\vec{F}_{slg} = A_{f,ij}(p_i - p_j)\vec{n}_{ij}, \tag{5.3}$$

where $A_{f,ij}$ is the cross-sectional area of the fluid flow pathway within the common triangular facet between pore i and pore j as depicted in Fig. 5.1. It should be noted that $A_{f,ij}$ is equal to the mass transfer area of the respective throat, which has been

introduced and denoted by A_{ij} in Chapter 3. In Chapter 4, this area was used to derive throat mass transfer radii. Since $A_{f,ij}$ is contributed from three particles with their centroids as the vertices of the common triangular facet of the two adjacent tetrahedral cells corresponding to pore i and pore j, $\vec{F}_{slg}$ is distributed to the associated particle k by:

$$\vec{F}_{slg,k} = \vec{F}_{slg}\left(\frac{\ell_{k,ij}}{\sum_{k=1}^{3}\ell_{k,ij}}\right), \tag{5.4}$$

where $\ell_{k,ij}$ is the approximate length of the three-phase contact line attached to particle k within the domain confined by the void space of pores i and j. Note that in addition to liquid-filled pores, the pores which are partially filled with liquid also contribute to capillary forces, but in a simplistic way. That is, as long as liquid exists in a pore (i.e., saturation is larger than zero) its capillary force contribution is approximated to be the same as the force contribution of that pore when it is saturated with liquid.

When referring to the capillary force in the following, the total capillary force will always be meant. Splitting to the liquid pressure and surface tension contributions is not foreseen in the Yade-DEM software that has been used in this work, so that the relative magnitude of these contributions cannot be reliably analyzed. In coarse consideration, the void space between particles is smaller than the solid volume for the case of closely packed aggregates (porosity in the range of 0.30 to 0.45 considered in this study). Consequently, throat area $A_{f,ij}$ will typically be smaller than the sum of involved particle phase areas, in some cases even smaller than the individual particle phase area $A_{k,ij}$, see Figs. 5.1b and 5.1c). On the other hand, triangulation may also result in throat triangles with large distances between the centers of the involved particles in comparison to their size, with throat area larger than the related particle areas. The frequency with which this kind of geometrical relationship appears is expected to increase in loosely packed aggregates with high porosity and large distances between particles in throat triangle planes (Fig. 5.1d). Particle aggregates as such, however, are out of the scope of this thesis.

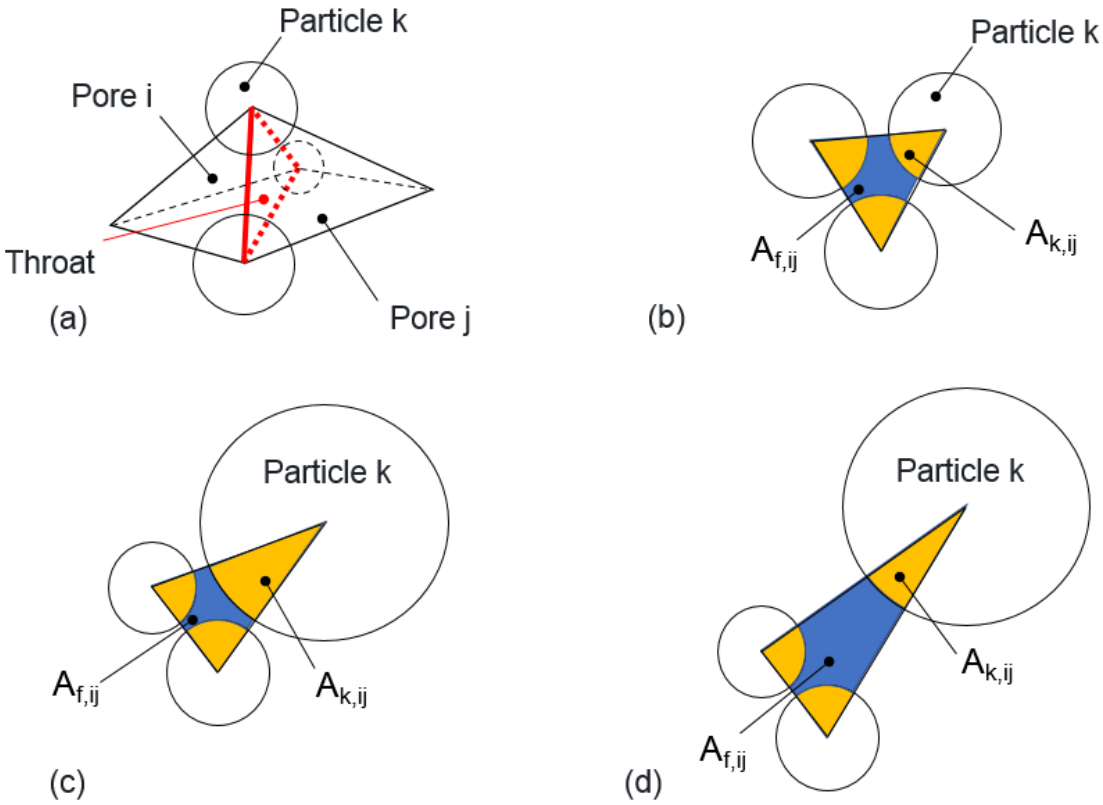

Figure 5.1. Schematic of the areas used in the capillary force calculation. (a) The common triangular facet (red triangle) associated with the throat between two adjacent pores i and j. Particle k has its centroid at the vertex of this triangle. The common triangular facet for (b) the case of monodisperse particles densely packed (low porosity, e.g., 0.4), (c) for the case of polydisperse particles densely packed, and (d) for the case of polydisperse particles loosely packed (high porosity, e.g., 0.7).

5.2 Evolution of capillary forces and liquid phase distribution during drying

The variation over time of the capillary force acting on a particle in Mono 100 aggregate, together with the evolution of liquid phase distribution around the considered particle during drying are visualized in Fig. 5.2. Initially, the pores surrounding the particle are filled with liquid and the capillary force exerted on the particle is zero. This is typical for situations in which all pores attached to the considered solid particle are fully occupied by liquid phase (i.e., there is no meniscus at any throat between pores attached to this solid particle). As, however, one of these pores empties, the capillary force appears. While additional surrounding pores are gradually depleted of liquid during the drying process, the direction and magnitude of

the capillary force keep changing. Eventually, all pores are drained by the gas phase and their saturations become zero; thus, the capillary force vanishes.

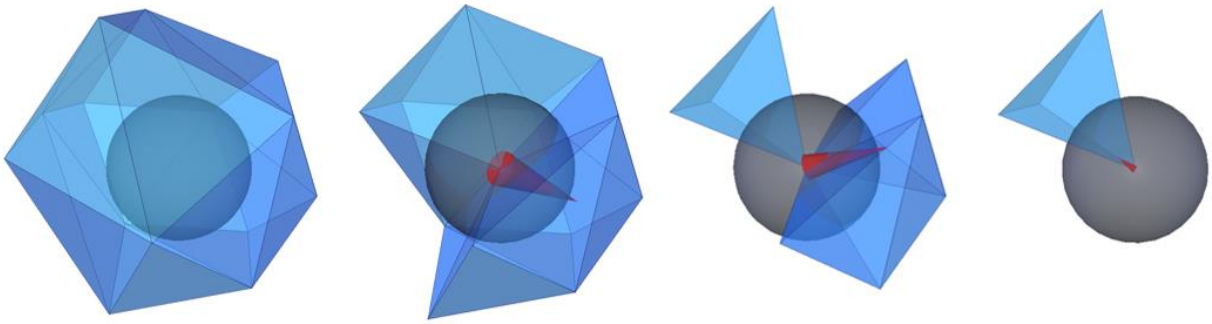

Figure 5.2. Evolution of net capillary force (red cone) and liquid saturation (blue tetrahedral cells) during drying. Cells that have been drained by the gas phase are not shown anymore.

The evolution of the capillary forces during drying of three different aggregates (Mono 100, Bi 860 and Bi 1047) is illustrated in Fig. 5.3. The capillary force associated to each particle is represented by a red cone with size being proportional to the force magnitude. Initially, capillary forces appear mostly at the top surface of the aggregates. This corresponds to the position of pores with menisci which are directly exposed to the gas-side diffusive boundary layer. Once the drying front has propagated deeper into the aggregates, new capillary forces appear at locations in the interior of the aggregates. Capillary forces eventually vanish at the bottom of the aggregates by the end of the drying process.

Similar observation has been reported for the case of three-dimensional aggregates packed regularly with monodisperse particles [71]. Each particle therein is in contact with six neighboring particles and surrounded by 12 pores. However, the pore space surrounding particles in the aggregates considered here is discretized finer, which leads to more contributions and components in the total capillary force that is exerted on each solid particle. Specifically, particles in aggregate Mono 100 are surrounded by 18.0 ± 5.6 pores each, while this value increases to 18.8 ± 15.1 and 20.6 ± 8.7 for aggregates Bi 860 and Bi 1047, respectively. This may infer that the direction of

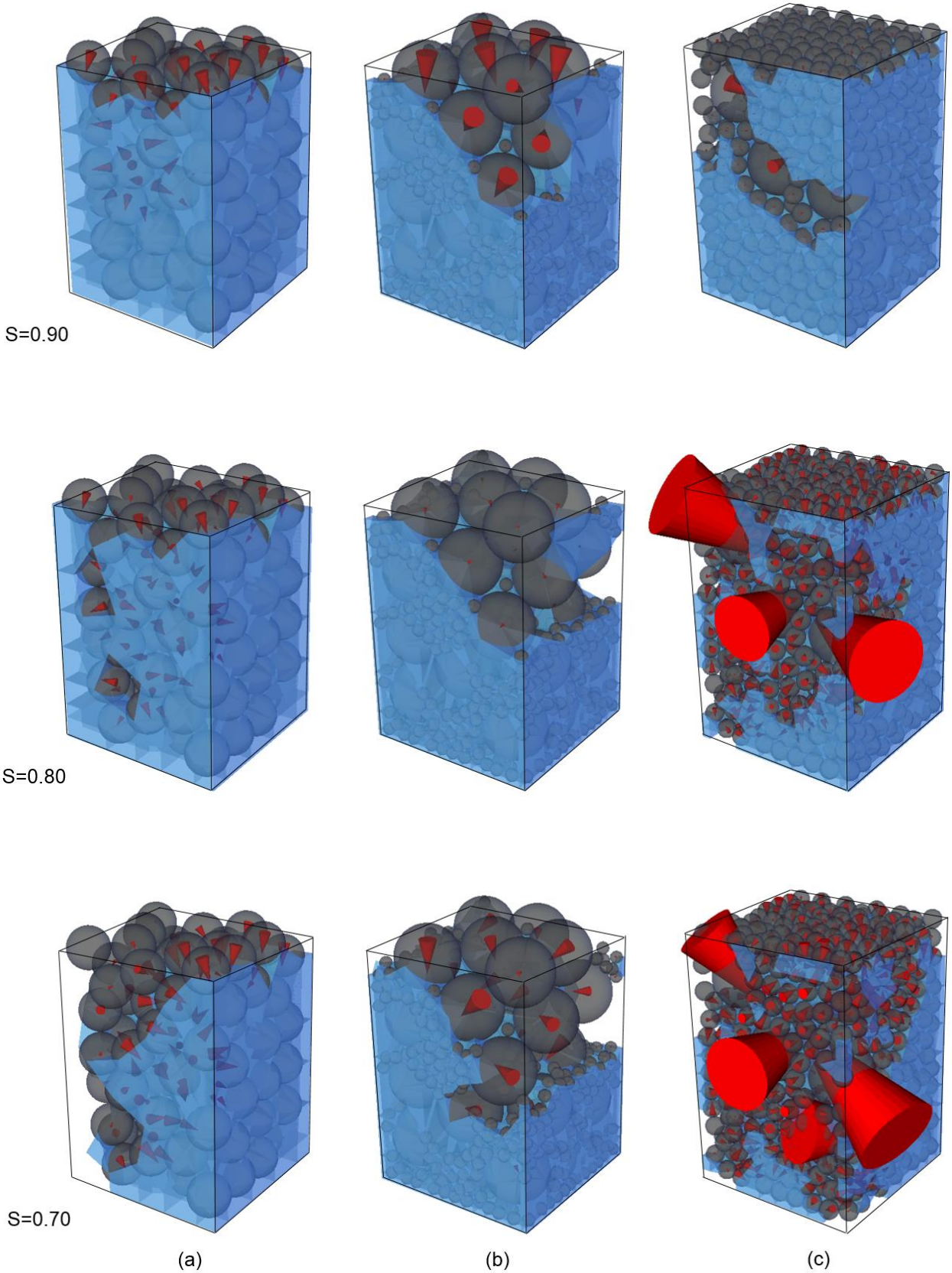

Figure 5.3, continued.

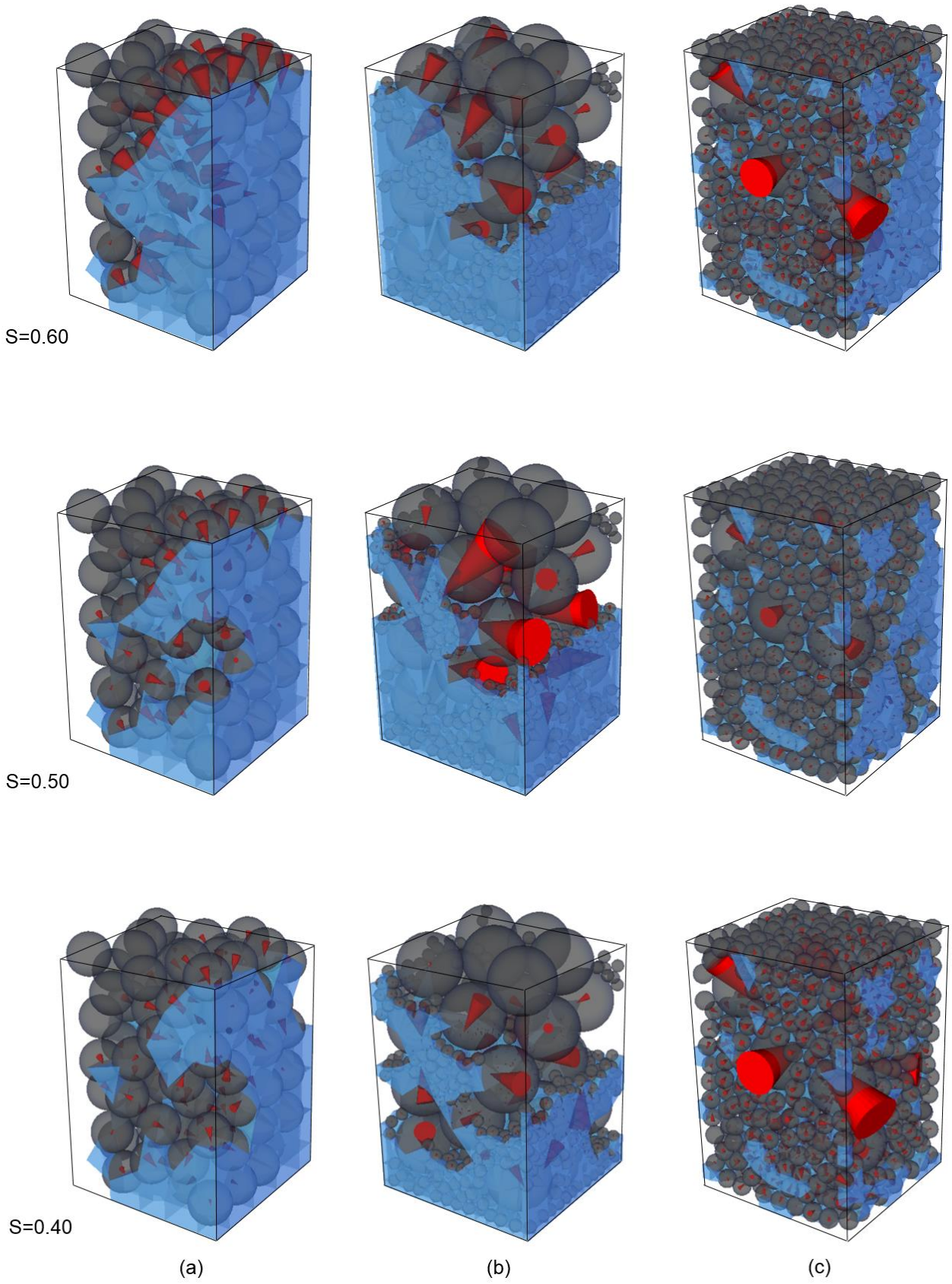

Figure 5.3, continued.

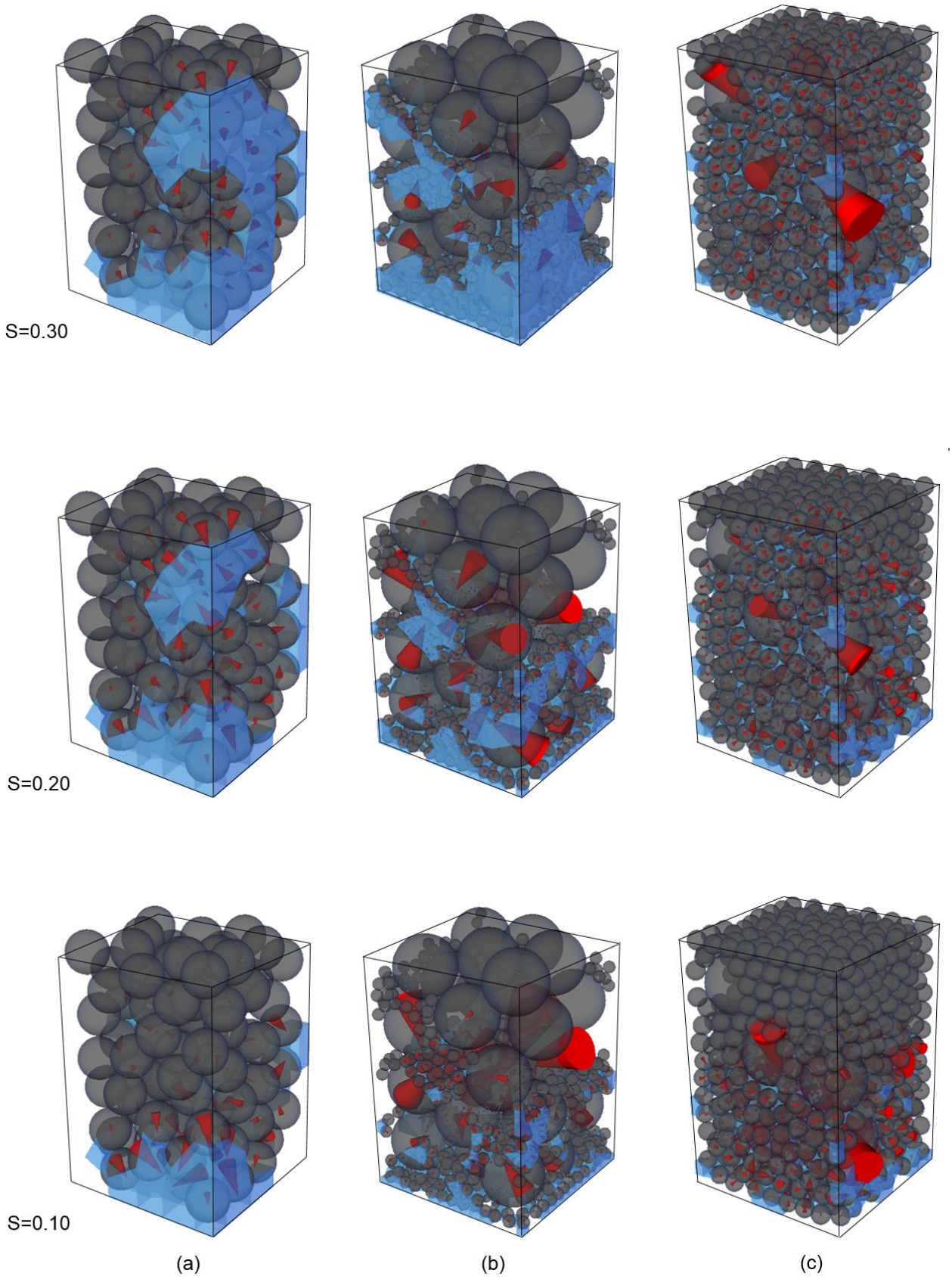

Figure 5.3, continued.

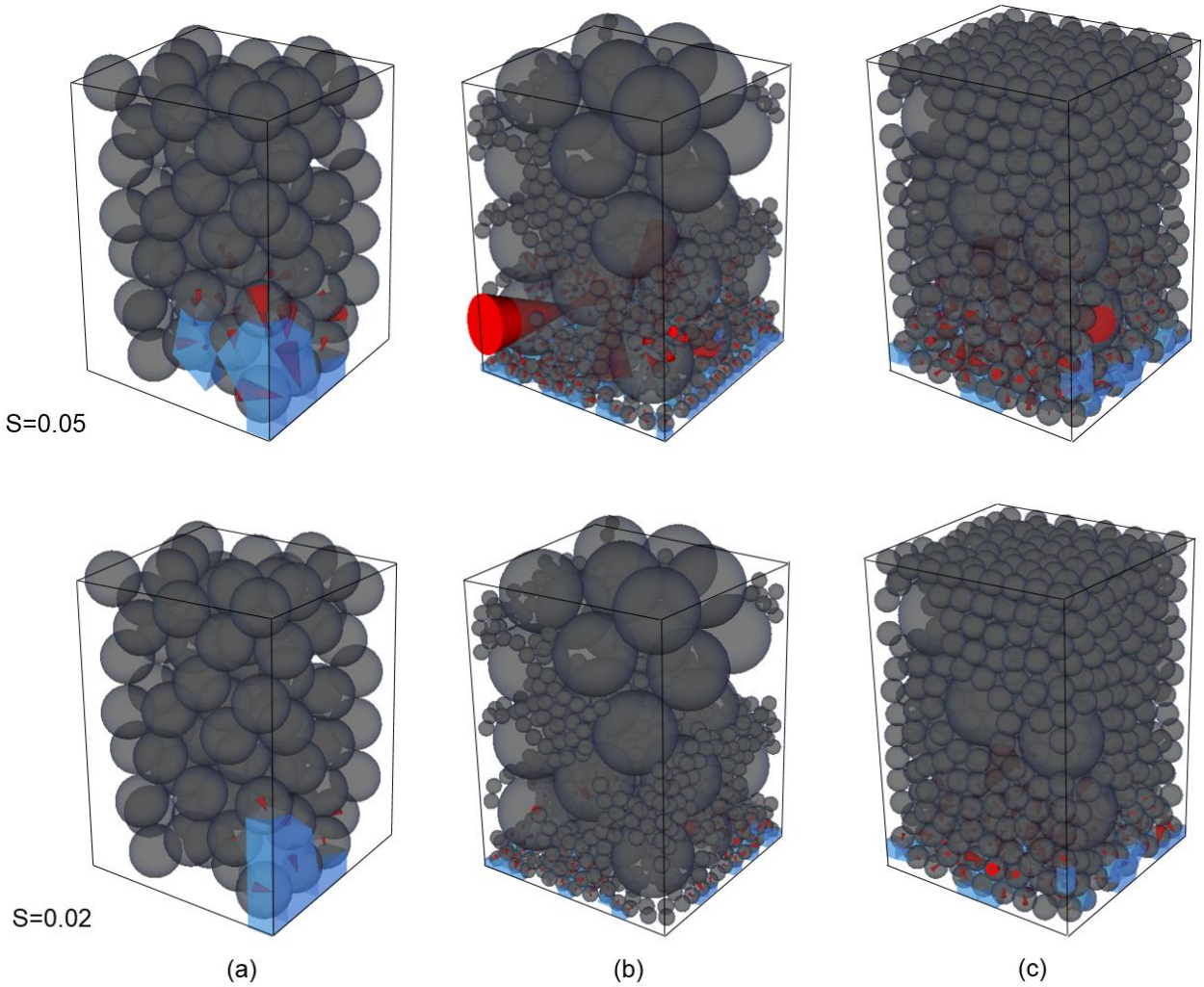

Figure 5.3. Evolution of capillary forces during drying of three different aggregates at different network saturations S: Column (a) Mono 100, column (b) Bi 860 and column (c) Bi 1047. Capillary forces are represented by red cones where the cone size scales with the force magnitude. Cells filled with liquid are shown in blue and are hidden after having been occupied by gas. Transparent grey spheres represent the solid phase of the respective aggregates.

capillary force in irregular monodisperse aggregates, as those considered in this study, varies more than that in regular aggregates made of monodisperse particles.

The simulation results show that capillary forces acting on the primary particles of bidisperse aggregates are larger than those acting on the primary particles of monodisperse aggregates during almost the entire drying process. This can be seen pictorially in Fig. 5.3, where bigger cones correspond to larger forces. To quantify this observation, the magnitudes of capillary forces of all primary particles having non-zero

capillary force (i.e., associated pores which are not all fully saturated or all totally dry) in the three here considered aggregates are presented in Fig. 5.4. It can be seen that the range in which the magnitude of the capillary force varies is generally smaller for the monodisperse particle aggregate compared to those of both bidisperse aggregates. This behavior starts when the aggregates contain a large amount of liquid and continues nearly consistently until the end of the drying process. Similar observations can be made for the case of the large Mono 1600 aggregate and the two respectively large polydisperse aggregates (Poly 1449 and Poly 1164). However, the difference in the force magnitude between Mono 1600 and those polydisperse aggregates are smaller compared to the corresponding differences between Mono 100 and the two mentioned bidisperse aggregates. Similar visualizations as the one in Fig. 5.3 for the case of Mono 1600 and the two polydisperse aggregates are presented in Appendix A4.

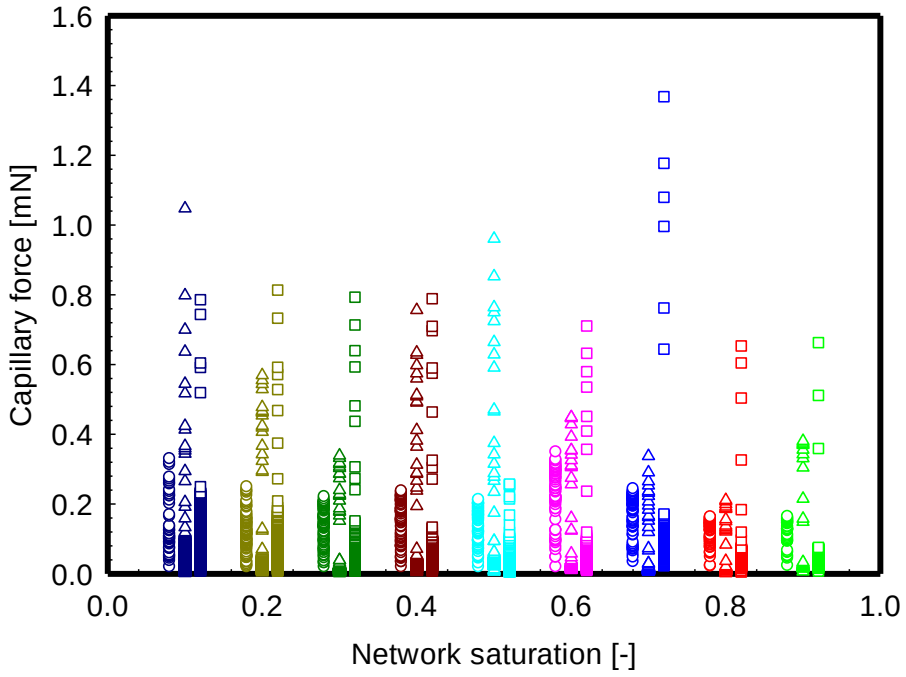

Figure 5.4. The magnitudes of net capillary forces as a function of network saturation obtained from drying simulations of three different particle aggregates: Mono 100 (○), Bi 860 (△) and Bi 1047 (□). Same colors of the markers indicate same network saturation values.

Besides, the force exerted on smaller particles has generally smaller magnitude than the one on larger particles (Fig. 5.5). This is expected, since a bigger particle leads to

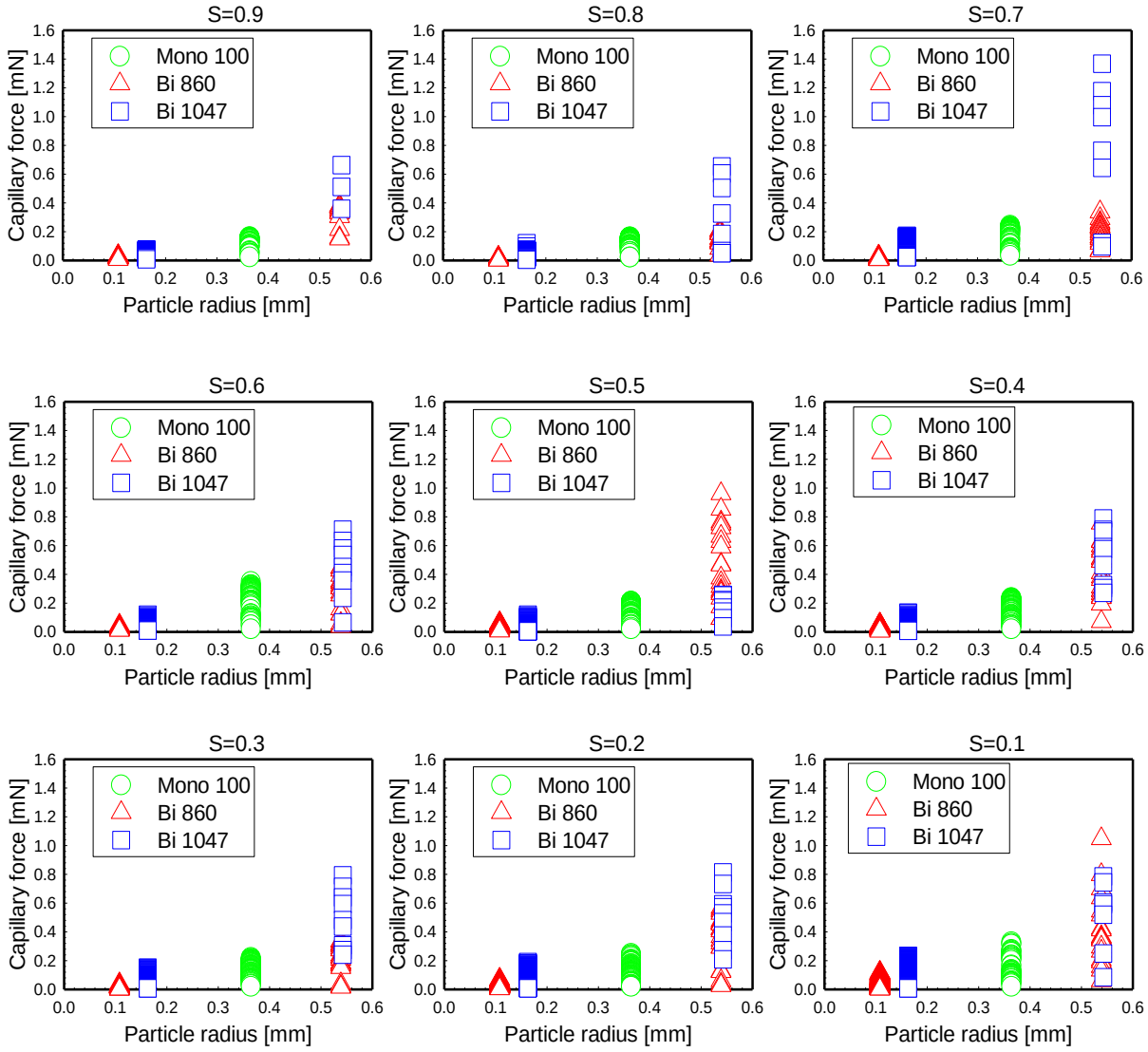

Figure 5.5. The magnitudes of the net capillary forces of primary particles with respect to their radii at different network saturations S during drying of three different aggregates: Mono 100 (○), Bi 860 (△) and Bi 1047 (□).

larger $A_{k,ij}$ (see Eq. 5.2), and also to larger throat area $A_{f,ij}$, thus increasing the magnitude of the capillary force. However, big particles can also experience a small capillary force. The reason for this is in the distribution of liquid surrounding the particle, which can be unfavorable for the development of a high compound capillary force. For example, the liquid may be located at two opposite sides of the particle, so that the capillary force contributions from liquid-filled pores cancel out each other. There are similar observations in a numerical study on single-phase flow in samples

with linearly graded and bimodal pore structures [202] as well as in an analytical study on two-phase flow of aggregates made of colloidal particles [203].

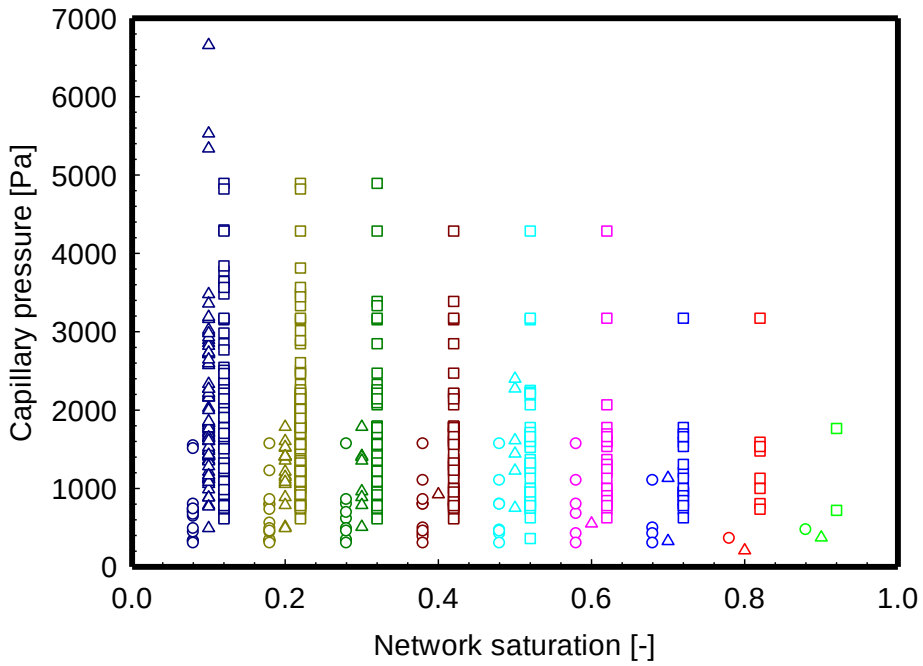

Figure 5.6. The capillary pressure as a function of network saturation obtained from drying simulations of three different particle aggregates: Mono 100 (○), Bi 860 (△) and Bi 1047 (□). Same colors of the markers indicate same network saturation values.

Another factor that impacts the magnitude of the capillary force is the capillary pressure. The variation of capillary pressure over time for the Mono 100, Bi 860 and Bi 1047 aggregates is shown in Fig. 5.6. At first, there is only one value of capillary pressure for the whole aggregate Mono 100 as well as for the whole aggregate Bi 860 at network saturations of 0.9 and 0.8. The reason for this is that all pores containing liquid belong to the same liquid cluster. Thus, the capillary pressure has no influence on the capillary force of the Mono 100 and Bi 860 aggregates. Whereas there are more than two values of capillary pressure for the case of Bi 1047 aggregate at network saturation of 0.9 and 0.8. However, as shown in Fig. 5.4, the variation of capillary forces for the case of the Bi 1047 aggregate at network saturation of 0.9 and 0.8 is almost the same. Thus, the impact of the capillary pressure on the force magnitude of the Bi 1047 aggregate is negligible at these two network saturations. One possible reason for this is that most of the liquid-filled pores in the Bi 1047 aggregate belong to the same liquid cluster. As it has been pointed out in Chapter 4, the evolution of the

main liquid cluster volume in an aggregate shows that most of the liquid stays in the main liquid cluster from the beginning of the drying process until network saturation reaches 0.3 (see Fig. 4.13). Since the effects which can be caused by the liquid viscosity are neglected in the TPNM, the capillary pressure remains nearly uniform throughout the entire particle aggregates. This implies that the impact of the capillary pressure on the force magnitude is negligible at network saturations larger than 0.3.

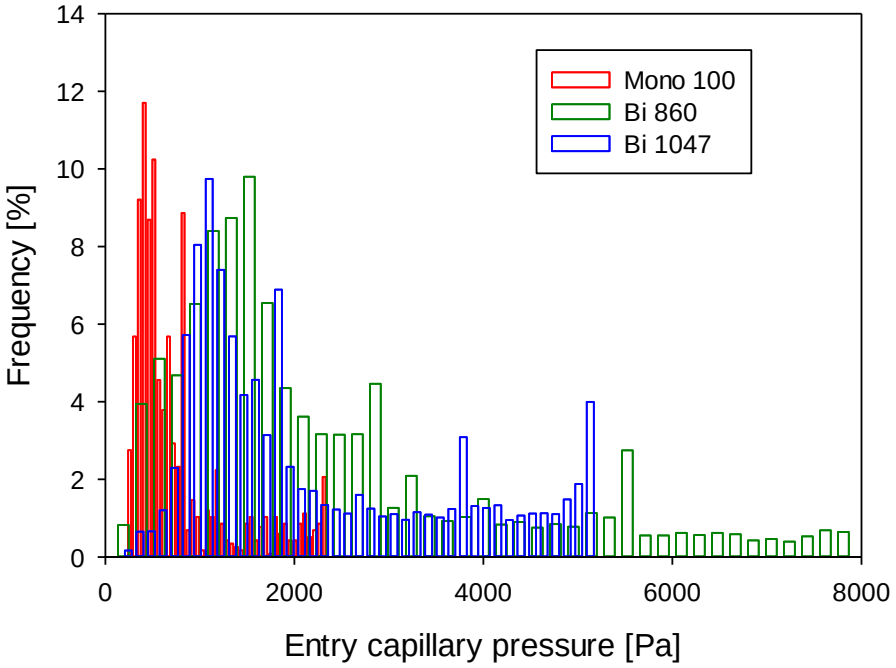

Figure 5.7. The distributions of throat entry capillary pressure of three different aggregates: Mono 100, Bi 860 and Bi 1047.

Significantly higher capillary forces for the case of bidisperse aggregates are attributed to the presence of coarse particles to which menisci with high capillary pressures are attached. It is trivial that the void space between coarse particles is larger than that between fine particles. Capillary pressure is inversely proportional to the void space size, which is expressed in this work by means of the throat radius. In fact, capillary pressure is determined based on the entry capillary pressure $p_{c,e}$ of moving meniscus throats, see Eq. 3.1. Seen very coarsely, throat diameter is proportional to particle size, so that capillary pressure is inversely proportional to particle size. To obtain, however, the force exerted on particles, pressure must be multiplied by the cross-

sectional area, which is proportional to the square of particle diameter. Consequently, capillary force is expected to be directly proportional to particle size. Reality is certainly more complicated in monodisperse assemblies of particles, and still much more in bidisperse aggregates. The pore space in a bidisperse aggregate made of coarse and fine particles consists of: (i) the pore space between fine particles only, (ii) the pore space between coarse particles only and (iii) the pore space between both fine and coarse particles. This results in a broader range of variation in the size of throats that interconnect pore spaces and, thus, in the capillary pressure for the case of bidisperse aggregates (see Fig. 5.7). Higher capillary pressure (because of meniscus pinned at throats having small entry radius, which are associated with small particles) coping with larger particles (when all pores belong to the same liquid cluster having same capillary pressure) results in a significantly larger capillary force in bidisperse aggregates compared to monodisperse aggregate.

5.3 Influence of solid aggregate structure on the distribution of capillary force

In a particle aggregate the imbalance of the capillary forces acting on primary particles creates stress in the solid phase. Such stress can be catastrophic for the integrity of the aggregate and is, thus, usually undesirable in the context of the drying of porous materials. In this section, a systematic study is conducted that brings some insights into the role and significance of capillary forces in aggregates having different solid structure. In order to investigate the impact of aggregate structure on the capillary force, aggregates generated in Chapter 4 are utilized in this chapter. Firstly, distributions of capillary force at three network saturation values of five small monodisperse aggregates with dimensions of 3 mm × 3 mm × 4.5 mm are compared to each other. Then, the influence of the coexistence of fine and coarse particles on capillary force is investigated by comparing the distribution of capillary force in the two bidisperse aggregates of same aggregate dimension, namely Bi 860 and Bi 1047. Finally, the influence of particle size distribution on capillary force is analyzed by comparing the capillary force distribution of the three large aggregates with dimensions of 8 mm × 8 mm × 12 mm, Mono 1600, Poly 1449 and Poly 1164.

The comparison of the distribution of capillary forces for the five monodisperse aggregates is shown in two ways. First, capillary forces for the different aggregates

are compared at same network saturation in Tab. 5.1. Second comparison takes place for each of the aggregates at different values of global saturation, as graphically shown

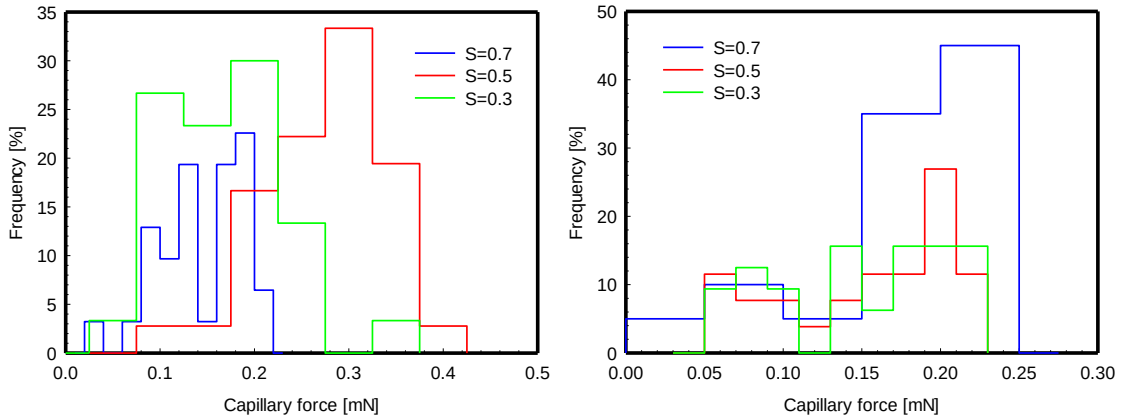

(a)

(b)

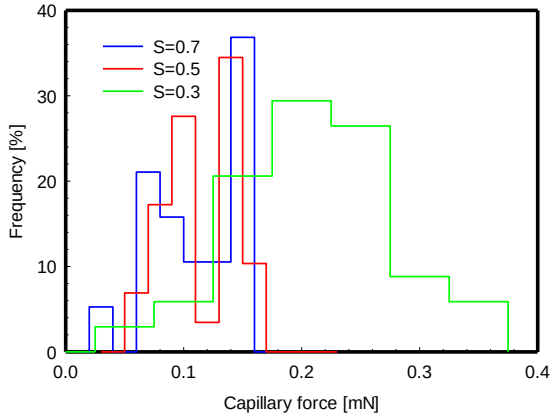

(c)

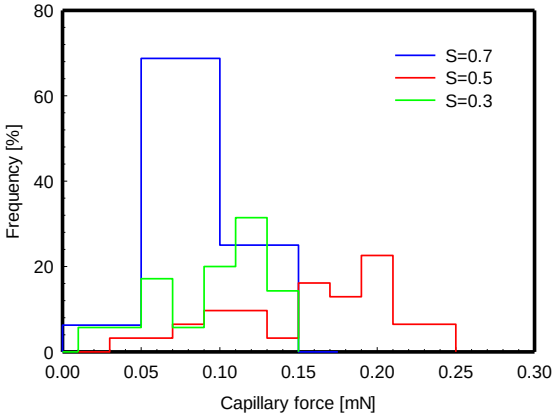

(d)

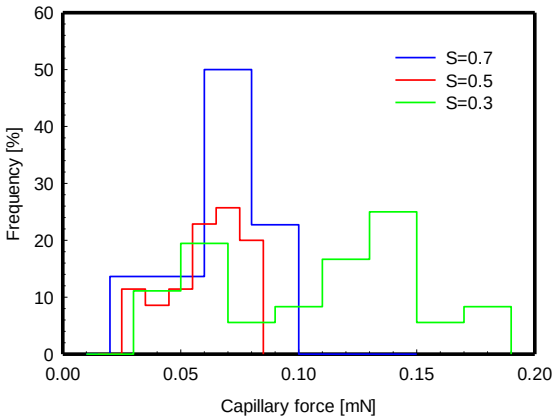

(e)

Figure 5.8. The distributions of capillary force at three different network saturations during the drying of five monodisperse aggregates: (a) Mono 37, (b) Mono 100, (c) Mono 200, (d) Mono 500 and (e) Mono 1000.

Table 5.1: Stochastic characteristics of the distributions of capillary force for the case of five monodisperse aggregates having dimensions of 3 mm × 3 mm × 4.5 mm.

Aggregate	Network saturation	Mean, mN		SD, mN	COV, %	Particle radius, mm
Mono 37		0.145	(2.20)	0.043	29.7	0.501 (2.81)
Mono 100		0.175	(4.34)	0.055	31.6	0.364 (2.04)
Mono 200	0.7	0.112	(1.70)	0.037	33.0	0.298 (1.67)
Mono 500		0.088	(1.33)	0.018	21.0	0.222 (1.25)
Mono 1000		0.066	(1)	0.017	25.9	0.178 (1)
Mono 37		0.246	(4.47)	0.066	27.0	0.501
Mono 100		0.145	(2.63)	0.055	37.6	0.364
Mono 200	0.5	0.105	(1.91)	0.029	27.7	0.298
Mono 500		0.150	(2.72)	0.050	33.4	0.222
Mono 1000		0.055	(1)	0.015	27.8	0.178
Mono 37		0.148	(1.53)	0.061	41.2	0.501
Mono 100		0.141	(1.45)	0.054	38.1	0.364
Mono 200	0.3	0.187	(1.93)	0.063	33.9	0.298
Mono 500		0.088	(0.91)	0.035	39.9	0.222
Mono 1000		0.097	(1)	0.042	43.6	0.178

in Fig. 5.8. The mean value of the capillary force generally increases when the particle radius increases. This is expected, having been explained in the previous section. In fact, the coarse expectation of the capillary force being directly proportional to the particle size is often fulfilled with astonishing accuracy when the mean value of capillary force is considered. To work out this aspect, scaling factors of particle radius and of mean capillary force have been added to Tab. 5.1, taking the aggregate with the smallest particles (Mono 1000) as a reference. Same scaling factor of mean capillary force and particle radius means exactly direct proportionality. However, clear exceptions to this pattern can also be observed. For example, mean capillary force appears to be too high for Mono 37 at network saturation S = 0.5, for Mono 100 at S = 0.7 and for Mono 500 at S = 0.5, being too small (with a scaling factor of even less than unity) for Mono 500 at S = 0.3. These exceptions can be due to the influence of capillary pressure (Fig. 5.9) as well as to the influence of the non-uniform distribution

of liquid around the solid particles (as illustrated for Mono 100 in Fig. 5.2 and Fig. 5.3). When the network saturation decreases, the coefficient of variation (COV) of capillary force increases, which can clearly be seen for S = 0.3 in Tab. 5.1. The increment in the variation of capillary pressure (both in number of values as well as in the range of the values, see Fig. 5.9) may contribute to this effect. Regarding the mean capillary force, its dependence on particle radius is clearly below direct proportionality at S = 0.3 (particle radius scales up by a factor of 2.81 from Mono 1000 to Mono 37, but mean capillary force scales up by only 1.53, see Tab. 5.1).

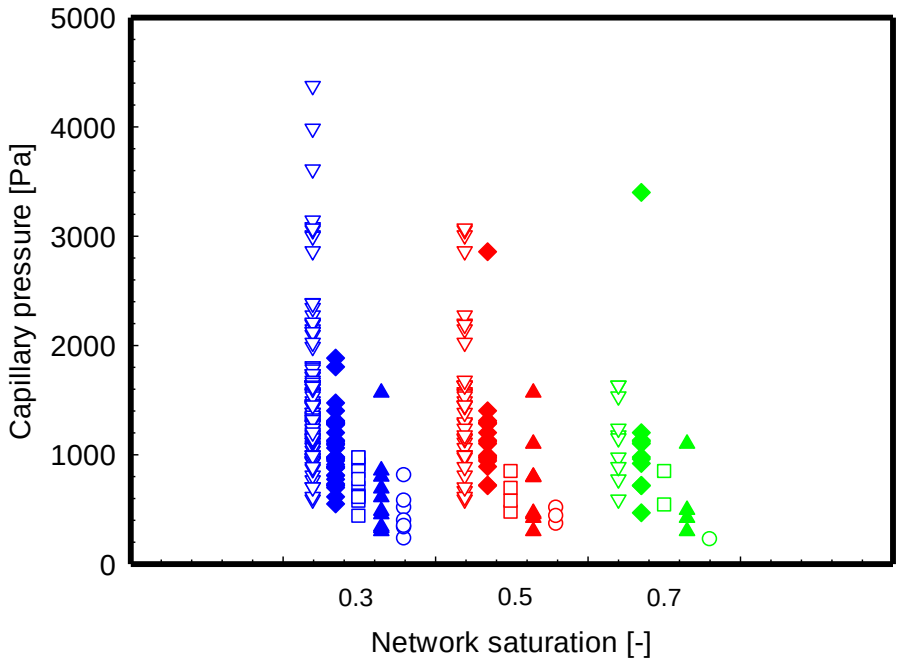

Figure 5.9. The capillary pressure as a function of network saturation obtained from drying simulations of five different monodisperse aggregates: Mono 37 (○), Mono 100 (▲), Mono 200 (□), Mono 500 (◆) and Mono 1000 (▽). Same colors of the markers indicate same network saturation values.

The influence of particle size on the capillary force is further investigated by means of results for the bidisperse aggregates: The Bi 860 aggregate in Tab. 5.2 and Fig. 5.10, and the Bi 1047 aggregate in Tab. 5.3 and Fig. 5.11. Such results can be compared with the statistical features of the distributions of capillary force at the three used values of network saturation for the five monodisperse aggregates, Tab. 5.1. The range of the mean value of capillary force for the five monodisperse aggregates is

from 0.055 mN (Mono 1000, S = 0.5) to 0.246 mN (Mono 37, S = 0.5). The particle radius of the five monodisperse aggregates varies between 0.178 mm (Mono 1000) and 0.501 mm (Mono 37). The two bidisperse aggregates, Bi 860 and Bi 1047, have

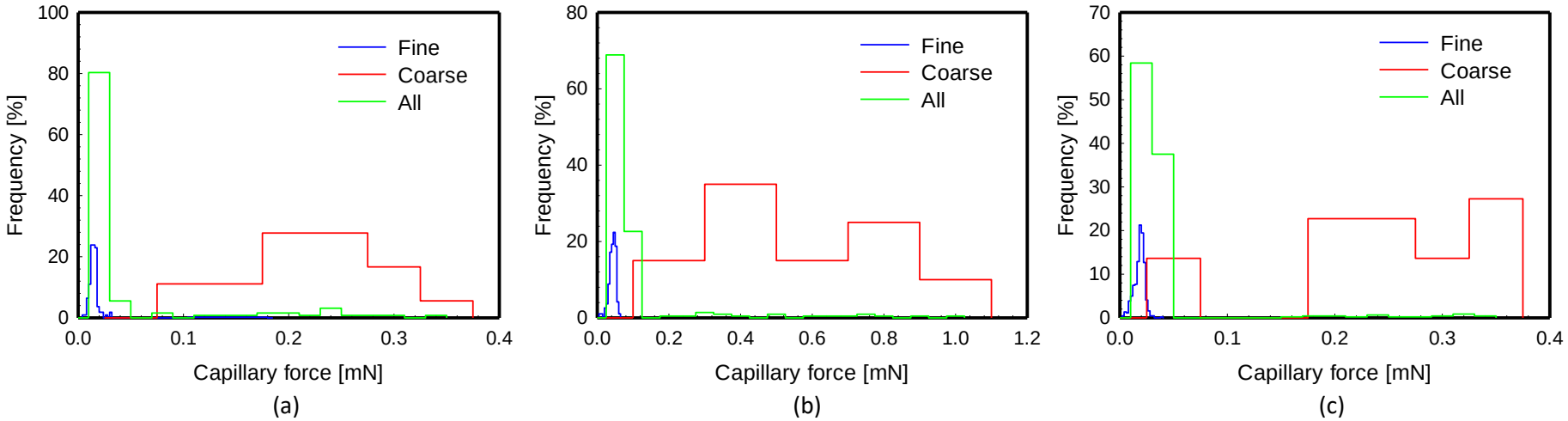

Figure 5.10. The distributions of capillary force during drying of bidisperse aggregate Bi 860 at three different network saturations: (a) 0.7; (b) 0.5 and (c) 0.3. Three separate plots correspond to the distributions of capillary forces acting on fine only, on coarse only and on all particles of the aggregate, respectively.

Table 5.2: Stochastic characteristics of the distributions of capillary force for the case of bidisperse aggregate Bi 860.

Network saturation		Mean, mN	SD, mN	COV, %	Particle radius, mm
S= 0.7	All	0.040	0.069	170.3	0.123 (mean value)
S= 0.5		0.083	0.147	176.9	
S= 0.3		0.028	0.048	171.9	
S= 0.7	Coarse	0.197	0.070	35.6	0.539
S= 0.5		0.467	0.253	54.2	
S= 0.3		0.220	0.095	43.2	
S= 0.7	Fine	0.015	0.004	26.9	0.108
S= 0.5		0.043	0.010	22.3	
S= 0.3		0.018	0.005	26.6	

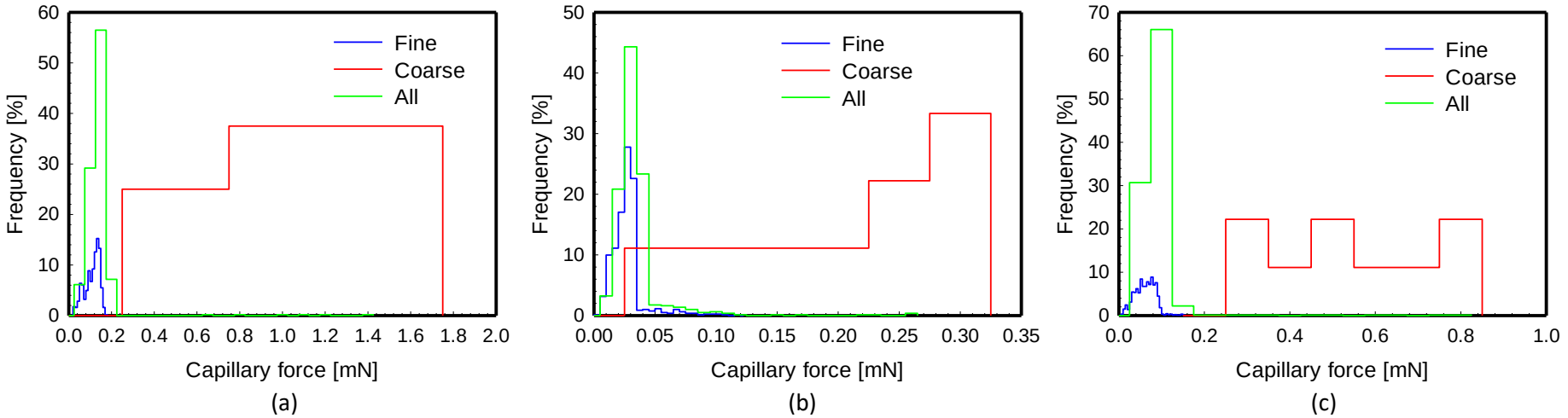

Figure 5.11. The distributions of capillary force during drying of bidisperse aggregate Bi 1047 at three different network saturations: (a) 0.7; (b) 0.5 and (c) 0.3. Separately plotted are the distributions of capillary forces on fine only, coarse only, and all particles of the aggregate.

Table 5.3: Stochastic characteristics of the distributions of capillary force for the case of bidisperse aggregate Bi 1047.

Network saturation		Mean, mN	SD, mN	COV, %	Particle radius, mm
S= 0.7	All	0.119	0.101	84.6	0.166 (mean value)
S= 0.5		0.029	0.023	78.0	
S= 0.3		0.066	0.052	78.2	
S= 0.7	Coarse	0.781	0.441	56.5	0.542
S= 0.5		0.183	0.074	40.3	
S= 0.3		0.498	0.188	37.9	
S= 0.7	Fine	0.109	0.034	31.5	0.163
S= 0.5		0.027	0.014	50.3	
S= 0.3		0.062	0.023	37.6	

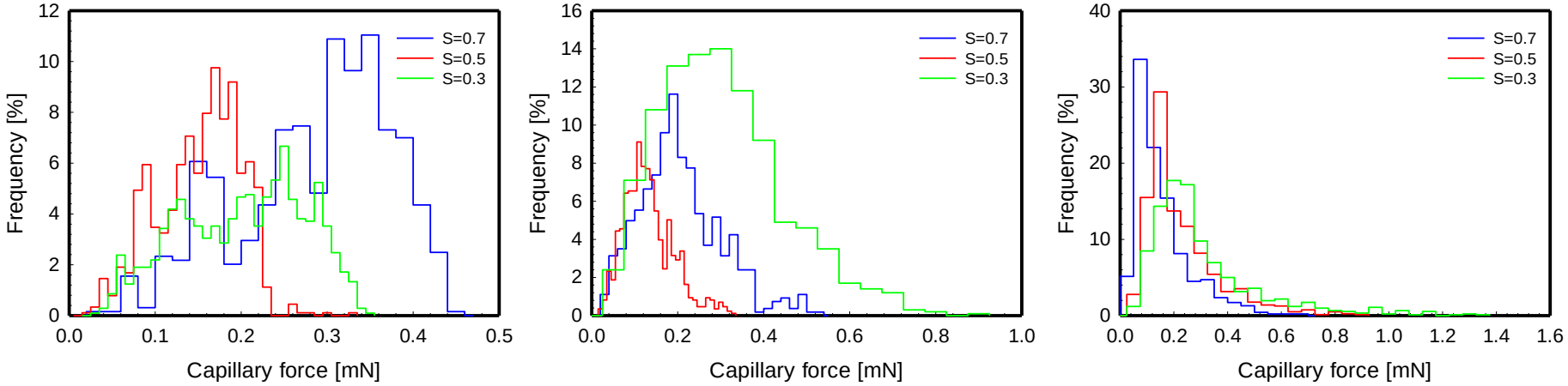

Figure 5.12. The distributions of capillary force at three different network saturations during the drying of large aggregates with dimension of 8 × 8 × 12 mm^3: (a) Mono 1600; (b) Poly 1449 and (c) Poly 1164 aggregate.

Table 5.4: Stochastic characteristics of the distributions of capillary force for the three large aggregates with dimension of 8 × 8 × 12 mm^3.

Aggregate	Network saturation	Mean, mN	SD, mN	COV, %	Particle radius, mm		
					Mean, mm	Max, mm	Min, mm
Mono 1600	0.7	0.286	0.089	31.1	0.409	0.409	0.409
Poly 1449		0.206	0.096	46.4	0.409	0.586	0.316
Poly 1164		0.156	0.105	67.3	0.415	0.818	0.274
Mono 1600	0.5	0.146	0.048	32.96	0.409	0.409	0.409
Poly 1449		0.127	0.057	45.09	0.409	0.586	0.316
Poly 1164		0.205	0.140	68.67	0.415	0.818	0.274
Mono 1600	0.3	0.196	0.073	37.13	0.409	0.409	0.409
Poly 1449		0.277	0.145	52.42	0.409	0.586	0.316
Poly 1164		0.286	0.210	73.51	0.415	0.818	0.274

coarse particle radii of 0.539 mm and 0.542 mm, respectively, and fine particle radii of 0.108 mm and 0.163 mm, respectively. That means, the coarse particles of bidisperse aggregates are somewhat larger than in the monodisperse aggregate with the largest particles, but not very much larger. Similarly, fine particles in the bidisperse aggregates are smaller than in the monodisperse aggregate with smallest particles, but not very much smaller.

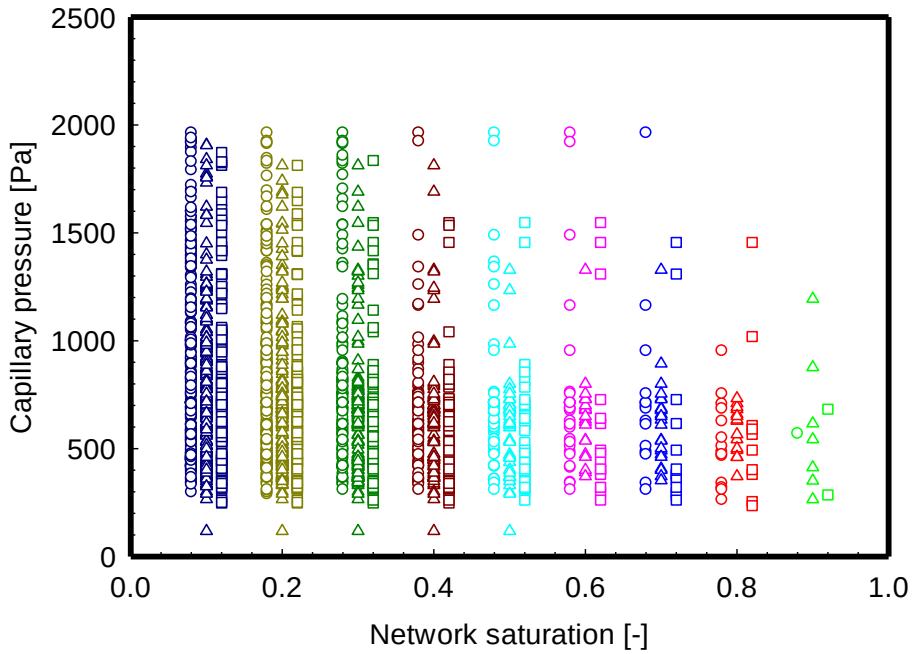

Figure 5.13. The capillary pressure as a function of network saturation obtained from drying simulations of three different particle aggregates: Mono 1600 (○), Poly 1449 (△) and Poly 1164 (□). Same colors of the markers indicate same network saturation values.

However, the mean value of capillary force of the two bidisperse aggregates varies much stronger, namely from 0.015 mN (fine, Bi 860 at S = 0.7) to 0.781 mN (coarse, Bi 1047 at S = 0.7). Consequently, it is much more than the particle size out of the range when compared to the capillary force of the five monodisperse aggregates. As mentioned in the previous section, the mixture of fine and coarse particles in bidisperse aggregates Bi 860 and Bi 1047 results in an amplification of high capillary forces (coarse particle coping with high capillary pressure at meniscus pinned in throat associated with fine particles) as well as a deterioration of low capillary forces (fine

particle coping with low capillary pressure at meniscus pinned in throat associated with coarse particles). Similarly, capillary force COV is much bigger than in monodisperse aggregates or among only the fine or only the coarse particles of the bidisperse aggregates.

Distributions of capillary force for the case of the three aggregates (Mono 1600, Poly 1449 and Poly 1164) that have bigger dimensions ($8 \times 8 \times 12$ mm^3) are shown in Tab. 5.4 and Fig. 5.12. The mean particle radii of these three aggregates are almost the same, i.e., 0.409 mm, 0.409 mm and 0.415 mm for Mono 1600, Poly 1449 and Poly 1164 aggregates, respectively. The differences in the variation of capillary pressure at different network saturations of these three aggregates (Fig. 5.13) are smaller compared to the differences for the five monodisperse aggregates (Fig. 5.9) as well as the two bidisperse aggregates (Fig. 5.9). The range of the capillary pressure values for the case of Mono 1600 and the two polydisperse aggregates is from about 100 to 2000 Pa, while the range for the case of the five monodisperse aggregates is 200 to 4400 Pa, and for the two bidisperse aggregates it is from 200 to 6600 Pa. These can be the reasons for the smaller variation in terms of mean capillary force at three different network saturations among Mono 1600 and the two polydisperse aggregates, compared to the cases of the five monodisperse aggregates as well as the two bidisperse aggregates.

On the one hand, the polydisperse aggregates, Poly 1449 and Poly 1164, have similar mean particle size and, thus, similar mean capillary force as the monodisperse aggregate Mono 1600. On the other hand, however, particle radius is spread around the mean in the two polydisperse aggregates. This seems to be the reason for higher COV of capillary force at all three network saturation values for the two polydisperse aggregates compared to the Mono 1600 aggregate. Comparing the two polydisperse aggregates with each other, Poly 1164 is the one with significantly broader range of particle radii. Consequently, the Poly 1164 aggregate has a higher COV in terms of capillary force compared to Poly 1449.

5.4 Influence of solid aggregate structure on maximal capillary force

Previous sections investigated the influence of the solid skeleton on the capillary force by analyzing the distribution of capillary force of the ten considered aggregates at specific network saturation values (0.9 down to 0.1 with an interval of 0.1 in Fig. 5.3 of Section 5.2, or 0.7 down to 0.3 with an interval of 0.2 in Section 5.3). In this section, the distribution of capillary force is further investigated for the whole drying process, i.e. at all network saturation values of the drying simulation. This is done by considering the variations in the minimum, the maximum as well as the mean value of capillary forces experienced by solid particles in each drying simulation step. Figure 5.14 shows these three variations for the aggregates Mono 200, Mono 1000, Bi 860, Bi 1047, Mono 1600, Poly 1449 and Poly 1164. The four former aggregates are of smaller dimensions (3 mm × 3 mm × 4.5 mm) while the latter three aggregates are bigger (8 mm × 8 mm × 12 mm). The variation in the minimum and the mean values of the capillary forces seems to be small compared to the variation in the maximum capillary

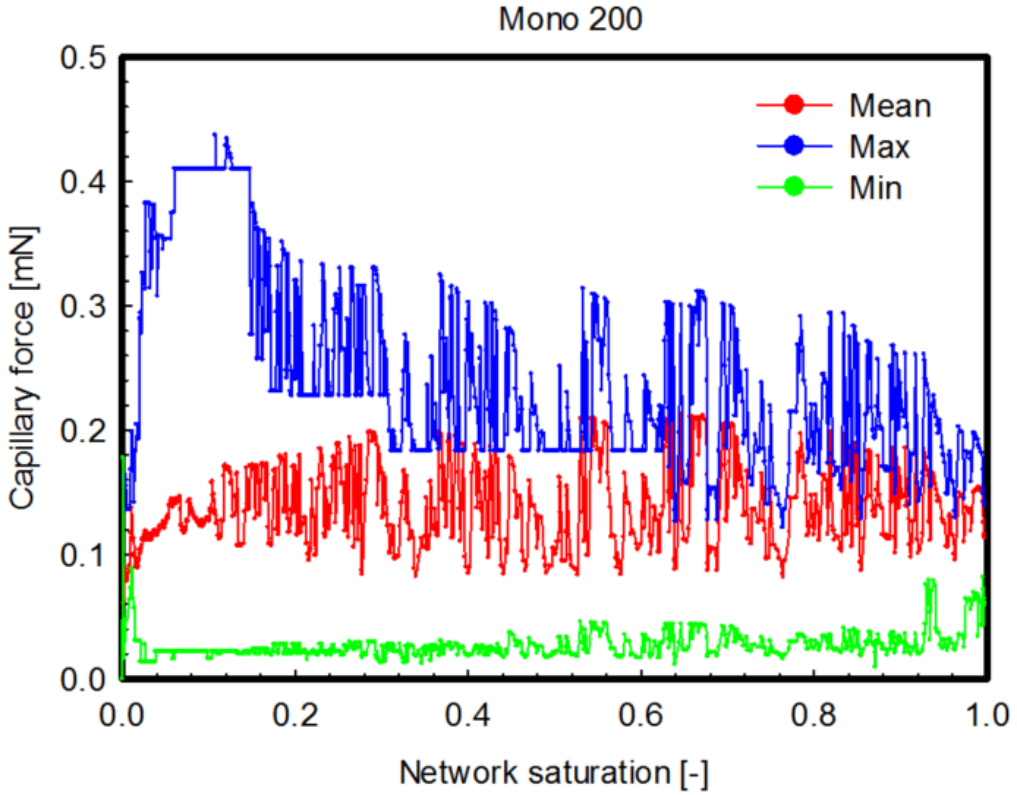

Figure 5.14, continued.

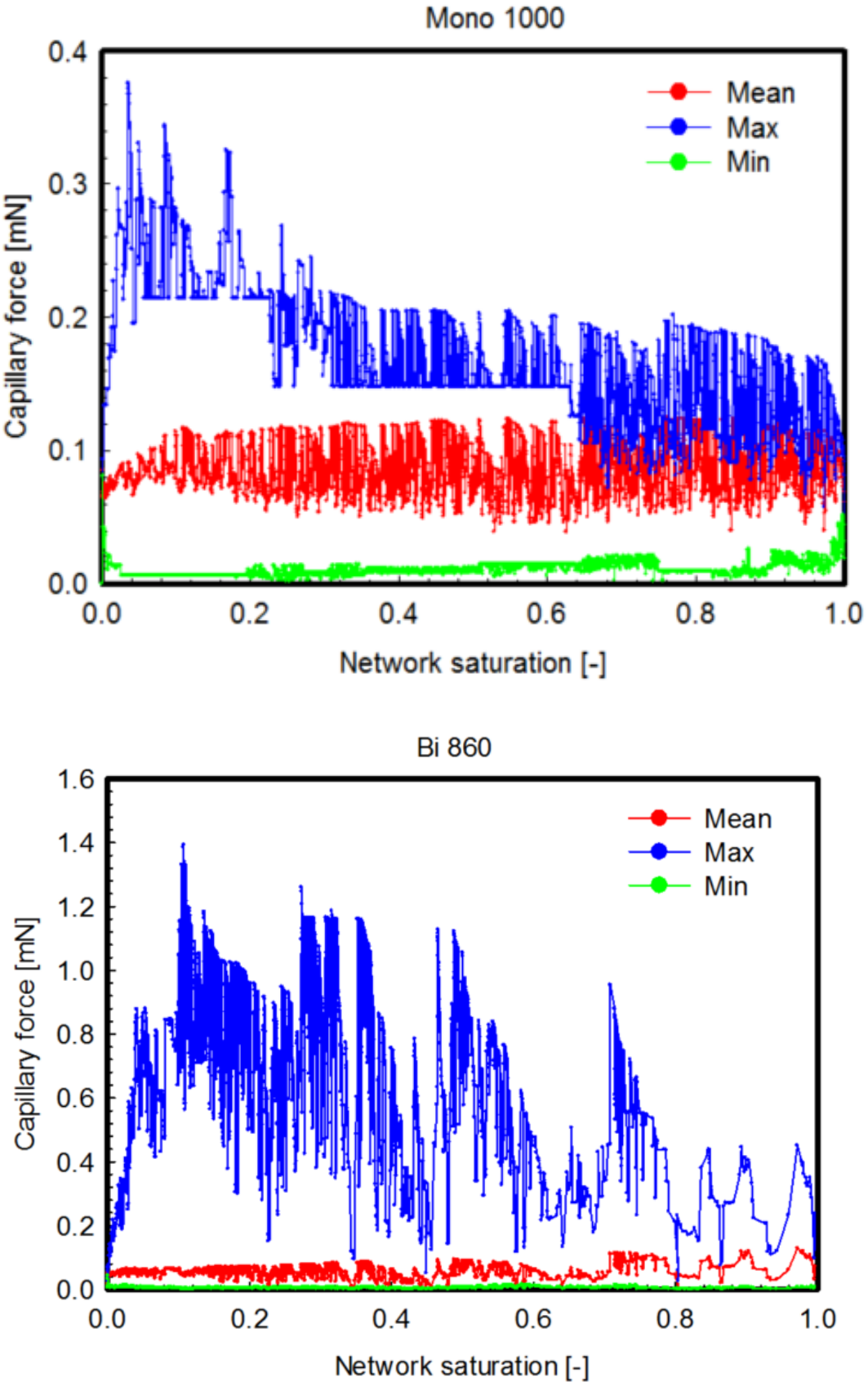

Figure 5.14, continued.

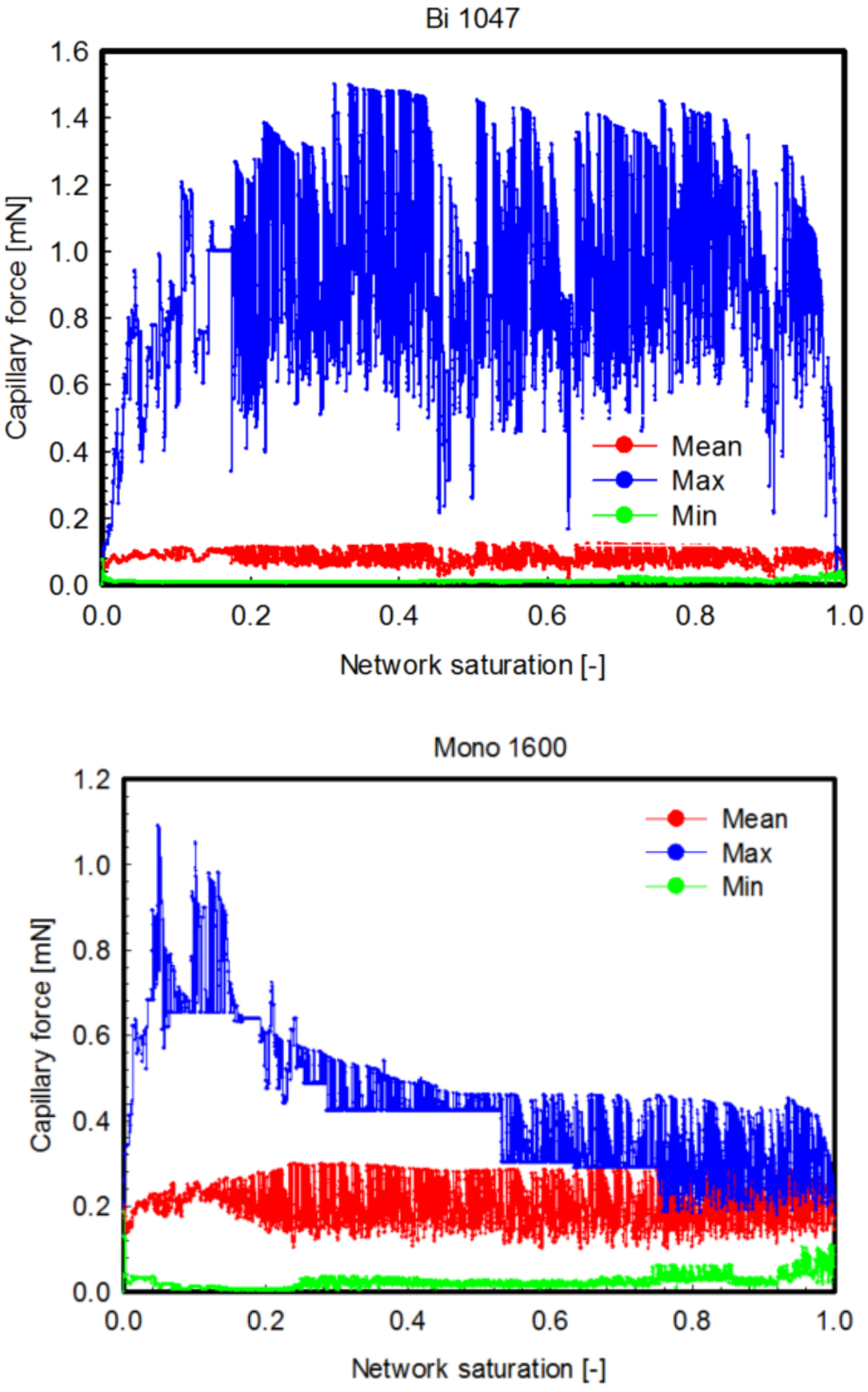

Figure 5.14, continued.

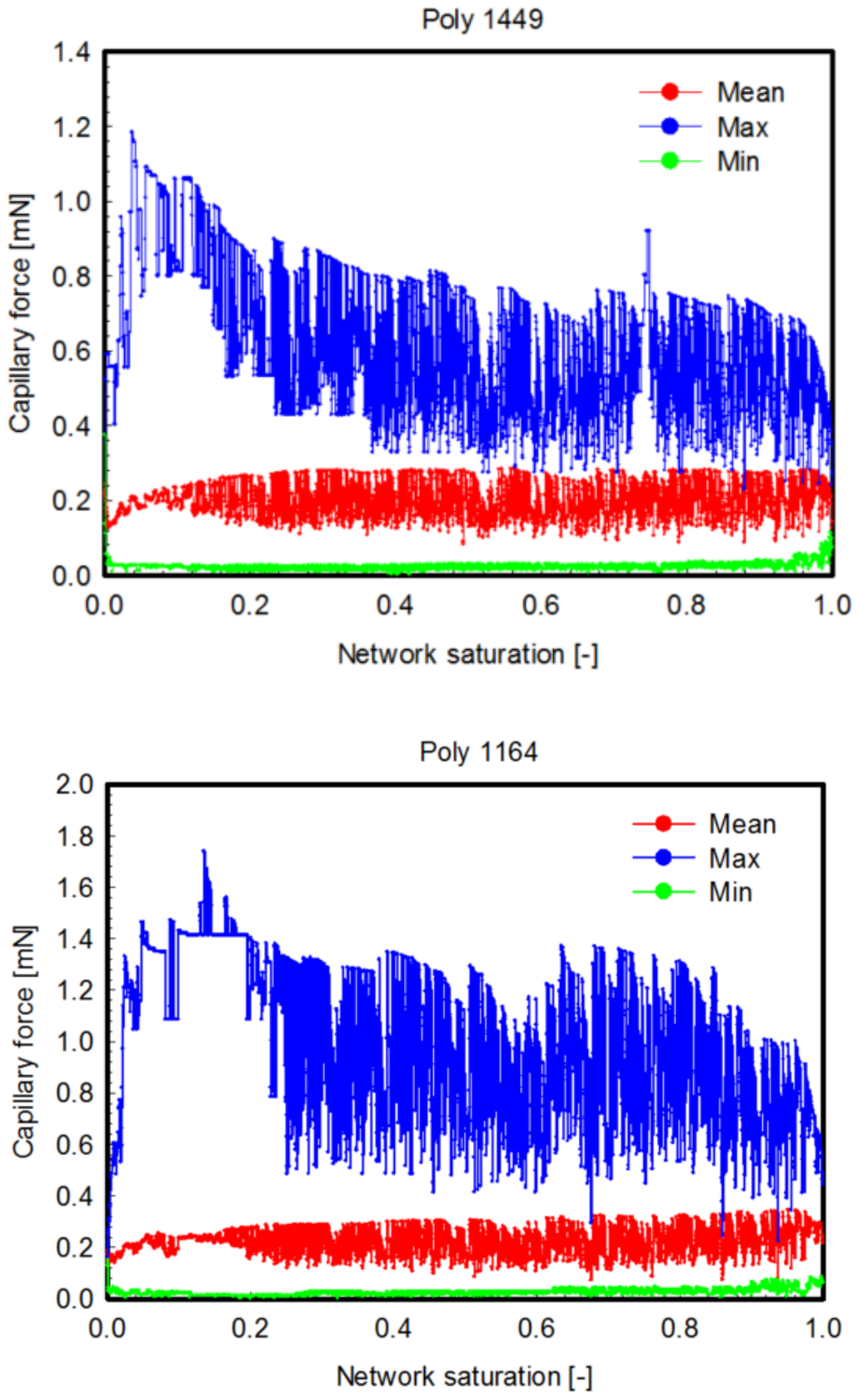

Figure 5.14. Evolution of capillary forces (mean, maximum and minimum value in each drying step) with respect to network saturation during drying of different aggregates.

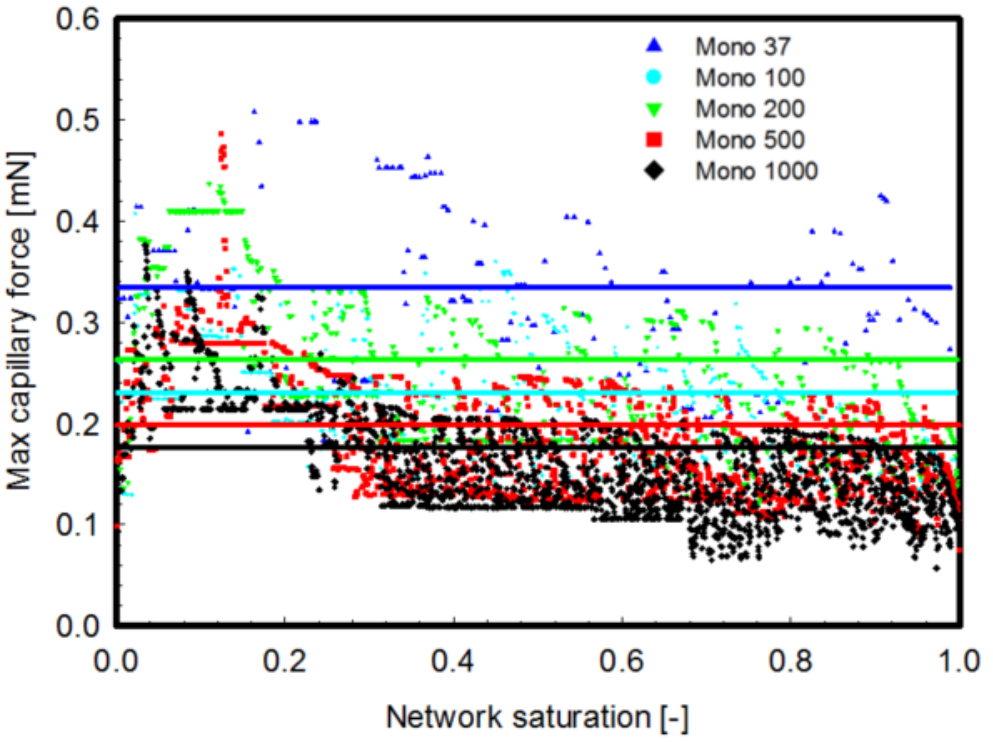

(a)

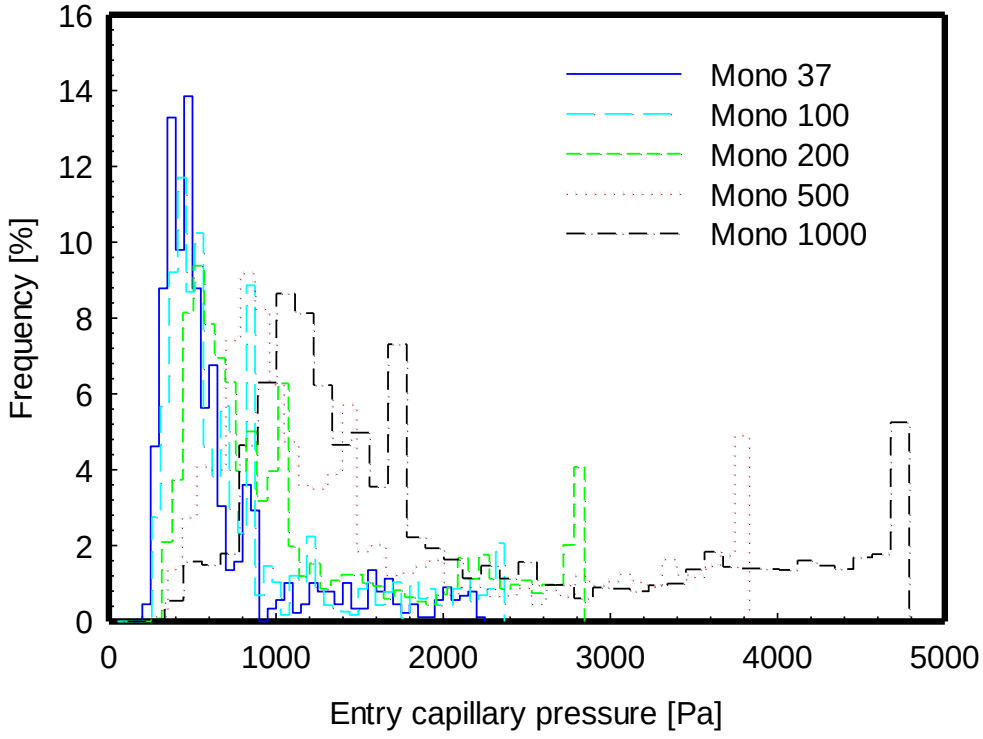

(b)

Figure 5.15. (a) Maximum capillary force in each drying simulation step as a function of network saturation and (b) the distributions of entry capillary pressure for the five different monodisperse particle aggregates. The solid lines in (a) indicate the arithmetic means of the maximum capillary force magnitudes associated to the aggregates.

force during the course of the drying process. However, the mean value of the maximum capillary force is also much larger, so that this observation may be deceiving in relative terms (i.e., when the coefficient of variation is considered). Anyway, since the maximum capillary force is the one that is expected to potentially damage the drying aggregate, investigation on the distribution of capillary forces during the whole drying process of each aggregate is hereafter based only on the maximum value of the capillary force magnitudes.

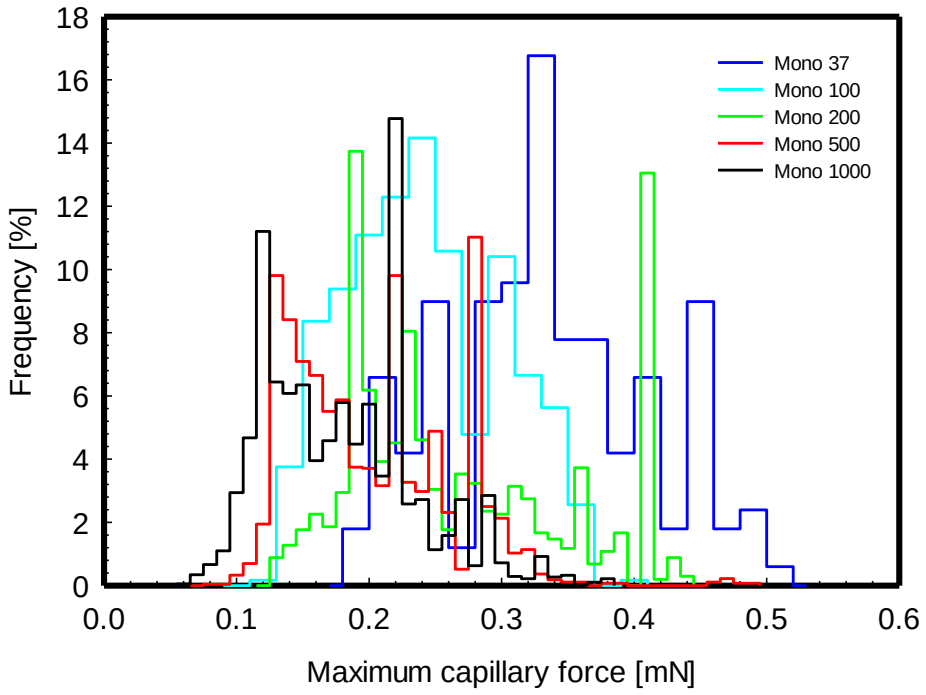

Figure 5.16. The distributions of the maximum capillary force in each drying simulation step during the whole drying process for the case of the five monodisperse aggregates.

Table 5.5: Stochastic characteristics of the distributions of the maximum capillary force in each drying simulation step during the whole drying process for the case of five monodisperse aggregates.

Aggregate	Mean, mN		SD, mN	COV, %	Particle radius, mm
Mono 37	0.334	(1.90)	0.077	23.1	0.501 (2.81)
Mono 100	0.230	(1.31)	0.058	25.3	0.364 (2.04)
Mono 200	0.263	(1.49)	0.084	32.1	0.298 (1.67)
Mono 500	0.198	(1.13)	0.061	30.7	0.222 (1.25)
Mono 1000	0.176	(1)	0.057	32.5	0.178 (1)

The influence of particle size on the maximal value of the capillary force is investigated by comparing the results obtained from the five different monodisperse particle aggregates. The evolution of the maximum capillary force magnitude in each simulation step of those five monodisperse aggregates during the course of the drying process is illustrated in Fig. 5.15a. The corresponding distributions of entry capillary pressure of these five monodisperse aggregates are shown in Fig. 5.15b. The distributions of the maximum capillary force during the whole drying process of the five monodisperse aggregates are graphically depicted in Fig. 5.16, whereas the main features of these distributions are tabulated in Tab. 5.5.

The mean value of the maximum capillary force increases when the particle size increases in Tab. 5.5, i.e. when for same total volume the number of particles decreases. Respective scaling factors are somewhat smaller than the scaling factors for the mean capillary force at S = 0.7 and S = 0.5 in Tab. 5.1, but comparable to the scaling factors found for the mean capillary force at S = 0.3. Coefficients of variation (COV) don't differ very much between maximum capillary force and mean capillary force, as comparison between Tab. 5.5 and Tab. 5.1 shows. In general, the change in maximal capillary force caused by changing particle size in monodisperse aggregates is similar to the change in mean capillary force. In case of maximal capillary force, the aggregate Mono 100 seems to be an exception from the general pattern. Particles in the Mono 100 aggregate are larger than particles in the Mono 200 aggregate, but the average value of the maximum capillary force of the Mono 100 aggregate is somewhat smaller than the one of the Mono 200 aggregate according to Tab. 5.5 and Fig. 5.15a. As already mentioned, the interplay between capillary pressure being inversely proportional to particle size and cross-sectional area on which this pressure applies being proportional to the square of particle size is much more complex in real or synthetic particle aggregates than this simple consideration implies. This may result in the exceptional behavior of the Mono 100 aggregate, for which the capillary pressure decrement (Fig. 5.8b) seems to dominate the decrease in particle size.

It should be noted that the overlaying pattern of capillary force increasing with particle size is in agreement with numerical results reported in [204]. It is also worth mentioning that experimentally determined capillary forces ranged from 0.1 to 0.7 mN in [38]. That study investigated two spherical glass beads with a diameter of 8 mm under constant

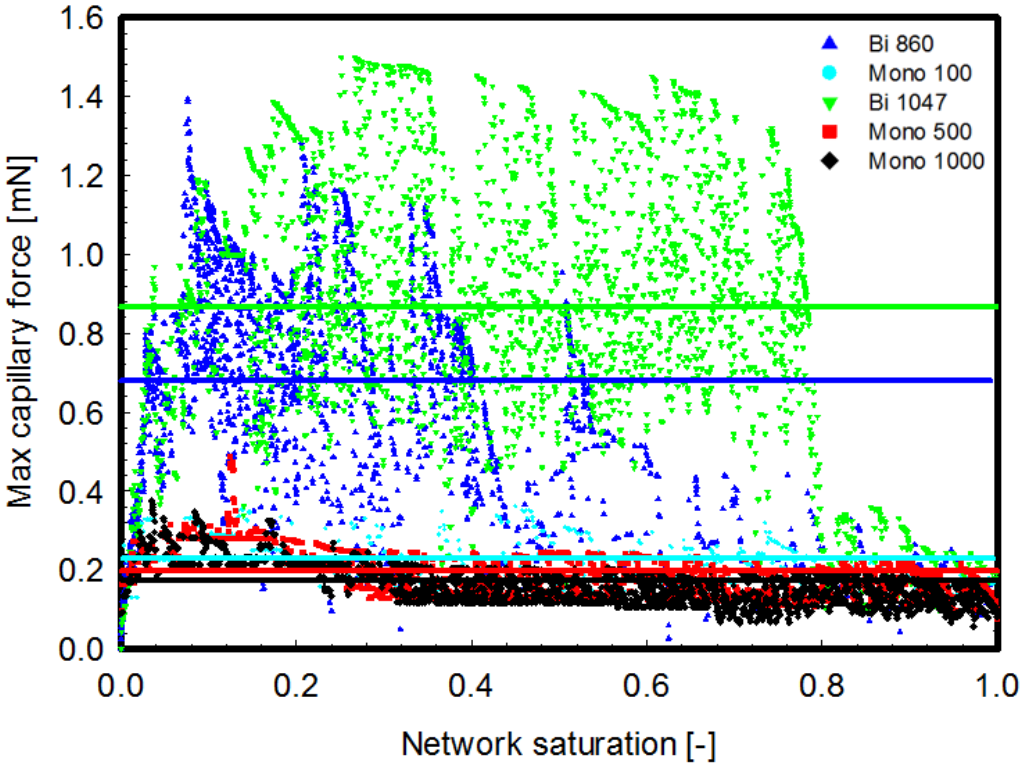

(a)

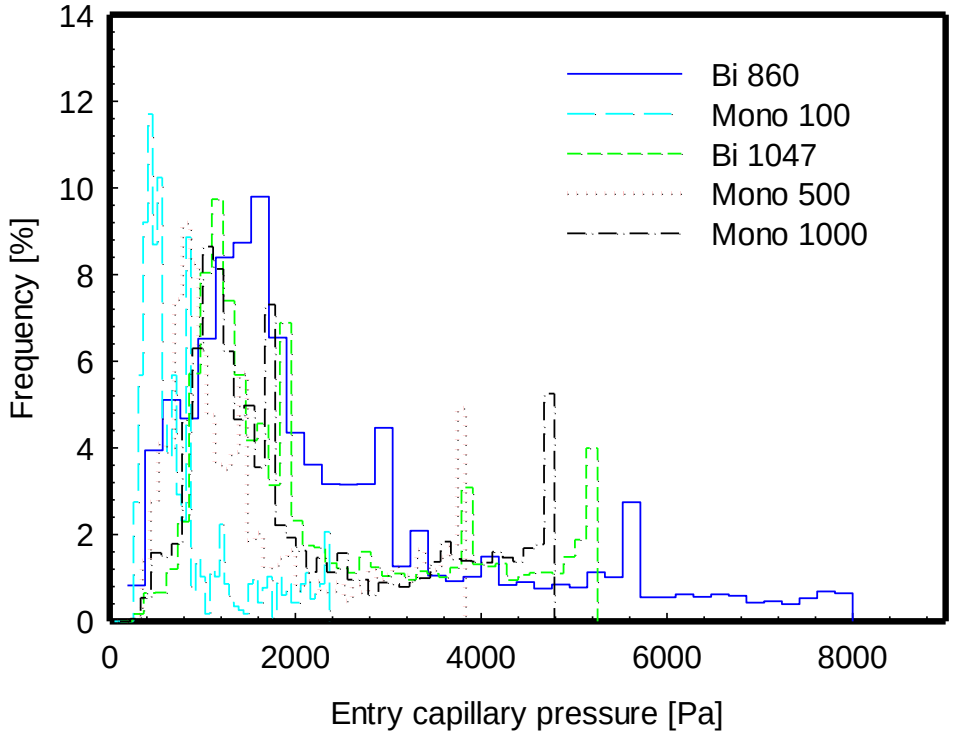

(b)

Figure 5.17. (a) Evolution of maximum capillary force during drying and (b) distributions of entry capillary pressure for three monodisperse and two bidisperse aggregates. The solid lines in (a) indicate the arithmetic means of maximum capillary force in the aggregates.

relative humidity of 25% and constant air temperature of 21 °C. Although the particles therein were significantly larger than the particles investigated in the present work (with radii of 0.1 to 0.5 mm), capillary forces appear to be of similar magnitude. The reason is that the capillary force reported in [38] had been calculated for only one liquid bridge between two particles. In this work, however, the capillary forces are calculated for aggregates made of many particles among which multiple liquid bridges may develop and coexist. Therefore, the capillary forces resulting from different liquid bridges can amplify or cancel out each other.

The influence of the particle size on capillary forces is further investigated by the comparison between the monodisperse and bidisperse aggregates. As shown in Fig. 5.17, Fig. 5.18 and Tab. 5.6, the mean values of the maximum capillary forces in each drying step for the bidisperse aggregates are significantly higher than those for the comparable monodisperse aggregates. There are two reasons for this discrepancy: (i) The coarse particles in bidisperse aggregates lead to higher capillary forces, and (ii) the fine particles of the bidisperse aggregates result in higher capillary pressure when the meniscus is pinned in the void space between these fine particles. Figure 5.17b illustrates that bidisperse aggregates have significantly broader capillary pressure ranges. Besides, the evolution of maximum capillary force magnitudes in Fig. 5.17a is of interest. At the beginning (network saturation higher than 0.8), the menisci are pinned at throats between coarse particles, because these throats are bigger (lower capillary pressure, higher liquid pressure) and are preferentially invaded first. The capillary forces of the bidisperse and the comparable monodisperse aggregates are of similar magnitude during this period. At network saturations lower than 0.8, the gas phase invades deeply into the aggregate, so that aggregate heterogeneity becomes significant in terms of throats, in which the menisci are pinned, and particles, on which the capillary forces are exerted. This results in significantly higher maximal capillary forces in bidisperse aggregates.

Besides, the void space between coarse particles in the upper part of the Bi 860 aggregate is not filled with fine particles as densely as it is in the Bi 1047 aggregate. Consequently, the maximum capillary force of the Bi 860 aggregate is lower than that of the Bi 1047 aggregate at network saturations higher than 0.4. At network saturations lower than 0.4, the gas phase invades the lower part of the Bi 860 aggregate (Fig.

5.3). The void space between coarse particles located in the lower part of the Bi 860 aggregate is, though, filled by fine particles in the same way as the void space of the Bi 1047 aggregate (cf. Fig. 4.16). Moreover, the size of fine particles of Bi 860 (0.11 mm) and Bi 1047 (0.16 mm) are not so much different. Thus, the difference in maximal capillary force of these two aggregates becomes smaller at network saturations lower than 0.4.

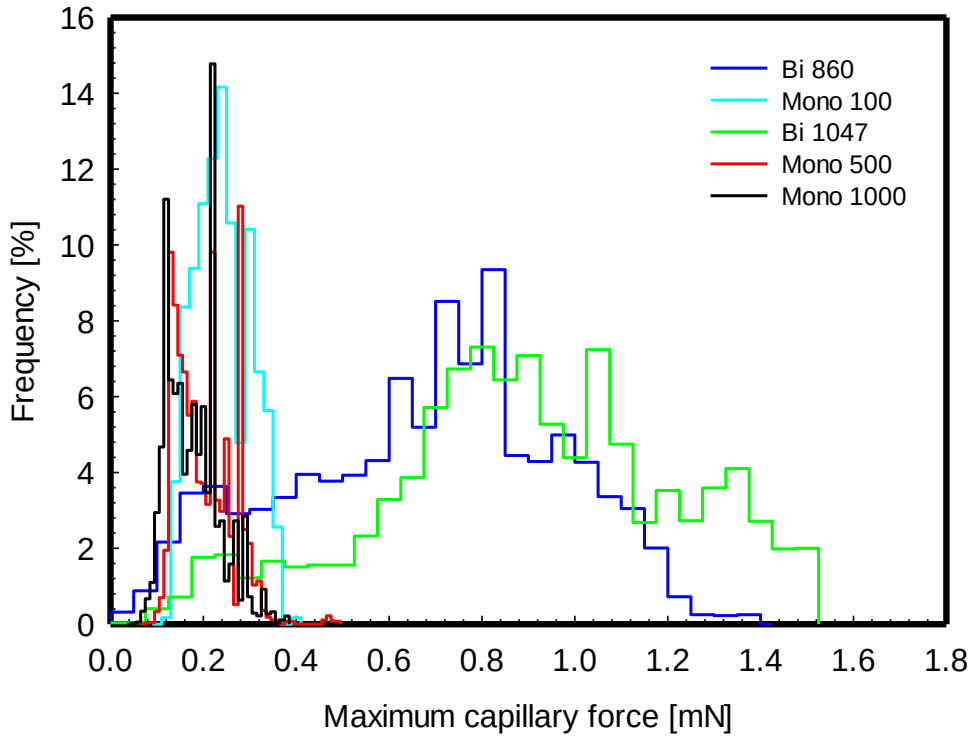

Figure 5.18. Distributions of maximum capillary force in each drying simulation step during the whole drying process for the case of three monodisperse and two bidisperse aggregates.

Table 5.6: Stochastic characteristics of the distributions of the maximum capillary force in each drying simulation step during the whole drying process for three monodisperse and two bidisperse aggregates of dimension 3 mm × 3 mm × 4.5 mm.

Aggregate	Mean, mN	SD, mN	COV, %	Particle radius, mm
Mono 100	0.230	0.058	25.3	0.364
Bi 860	0.680	0.289	42.4	0.108 (fine) - 0.539 (coarse)
Bi 1047	0.867	0.318	36.7	0.163 (fine) - 0.542 (coarse)
Mono 500	0.198	0.061	30.7	0.222
Mono 1000	0.176	0.057	32.5	0.178

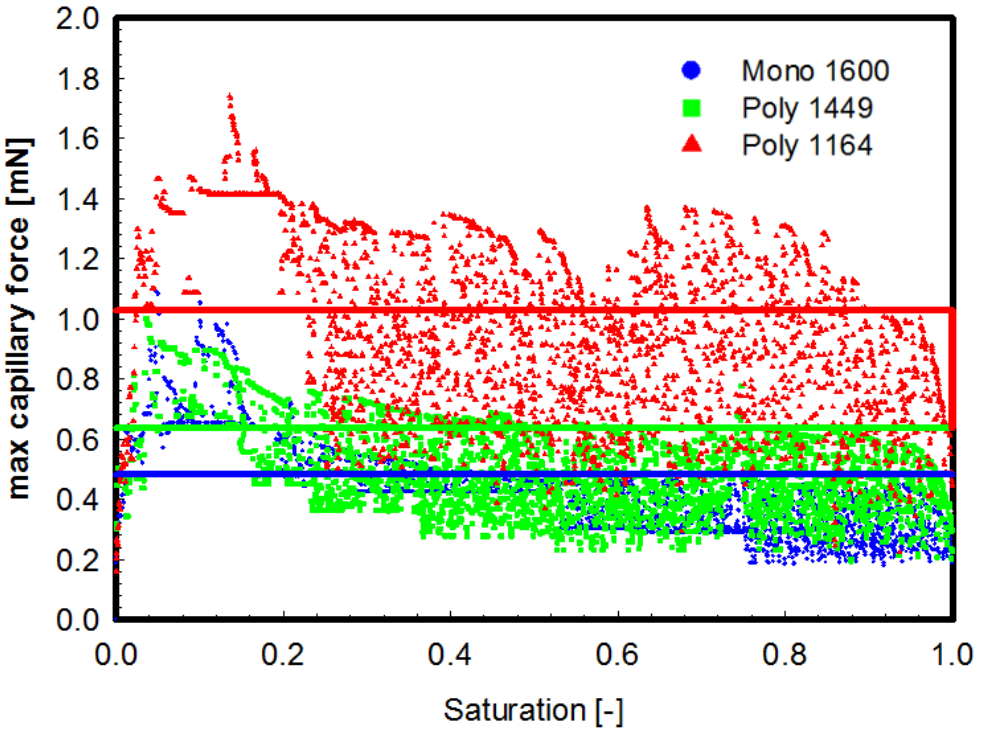

(a)

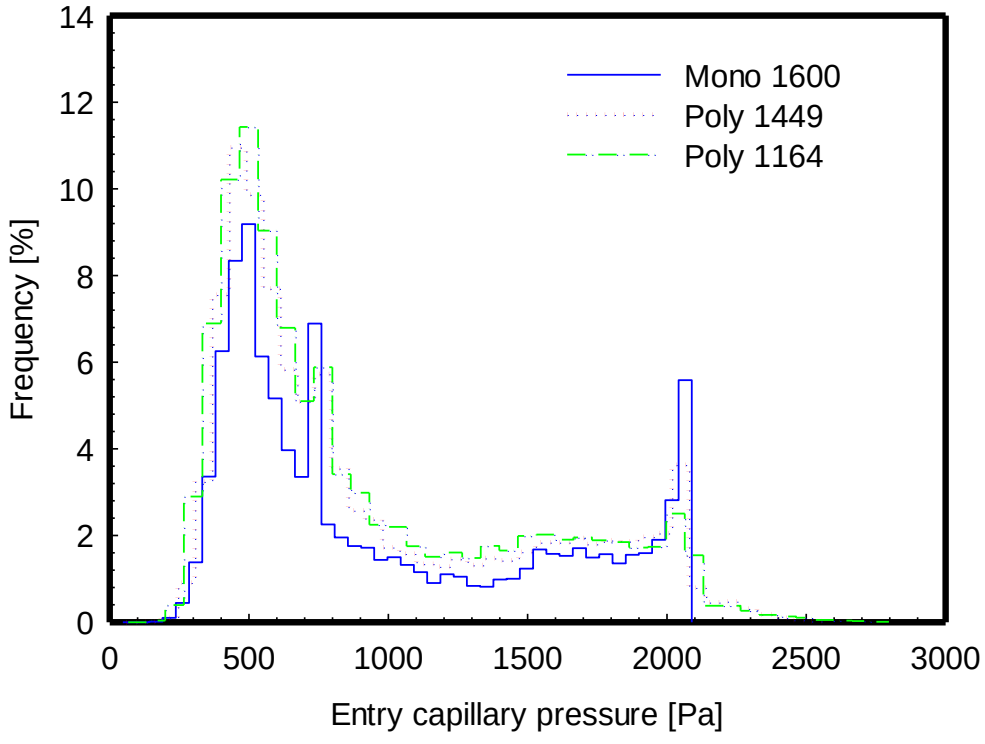

(b)

Figure 5.19. (a) Evolution of maximal capillary forces during drying and (b) distributions of entry capillary pressure for one monodisperse and two polydisperse aggregates. Solid lines in (a) indicate the arithmetic means of maximum capillary force in the aggregates.

Table 5.7: Stochastic characteristics of the distributions of maximum capillary force during the whole drying process for comparable monodisperse and polydisperse aggregates of large size (8 × 8 × 12 mm³).

Aggregate	Mean, mN	SD, mN	COV, %	Particle radius, mm		
				Mean, mm	Max, mm	Min, mm
Mono 1600	0.482	0.176	36.5	0.409	0.409	0.409
Poly 1449	0.539	0.171	31.8	0.409	0.586	0.316
Poly 1164	1.027	0.308	30.0	0.415	0.818	0.274

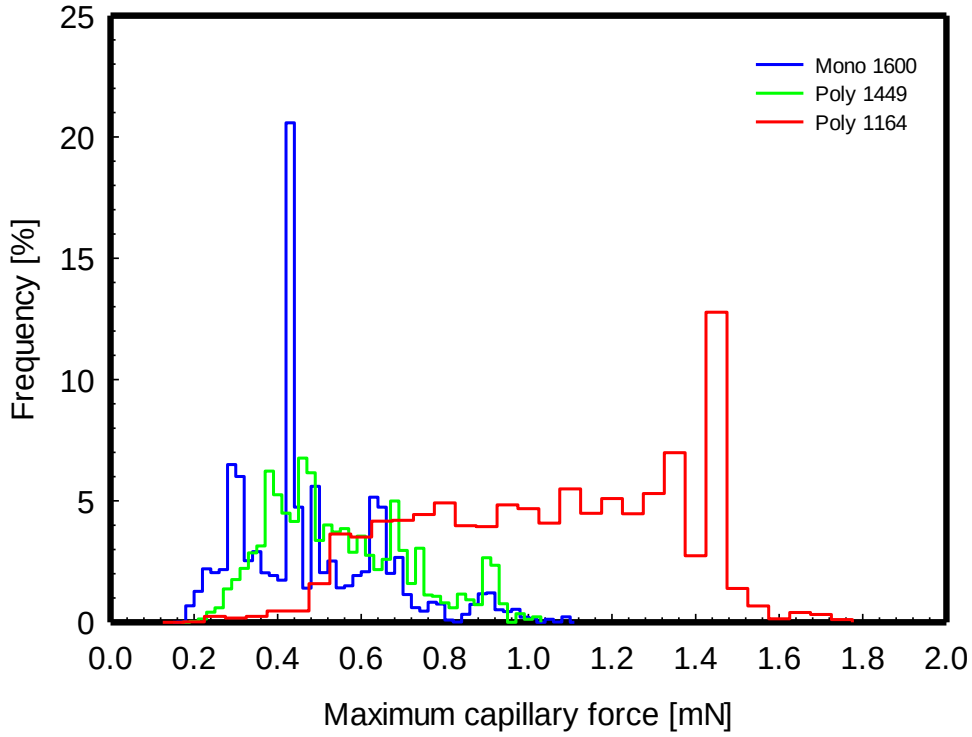

Figure 5.20. The distributions of maximum capillary force during the whole drying process for comparable monodisperse and polydisperse aggregates of large size (8 × 8 × 12 mm³).

The influence of particle size heterogeneity on the maximum capillary force is further investigated for the three aggregates with larger dimensions (8 mm × 8 mm × 12 mm): The monodisperse aggregate Mono 1600, and the polydisperse aggregates Poly 1449 and Poly 1164. Results are presented in Fig. 5.19, Fig. 5.20 and Tab. 5.7. Since the distributions of throat entry radius of these aggregates are almost the same (Tab. 4.12), the distributions of entry capillary pressure of these aggregates are also almost

the same (Fig. 5.19b and Fig. 5.13). Despite of such coincidence, maximal capillary force is not the same for those three aggregates. Much more equal is the mean capillary force in Tab. 5.4, but large differences in maximal capillary force are a striking result of our analysis. In fact, maximal capillary force in Tab. 5.7 behaves much more similarly to the COV of capillary force from Tab. 5.4 than to the mean value of capillary force from the same table. In other words, maximal capillary force distinctly depends on the spread of particle size distribution in the aggregate. The broader particle size distribution results in bigger coarse particles (higher particle radius) as well as smaller fine particles (higher capillary pressure). This is the reason why the maximum capillary force of the Poly 1164 aggregate with the highest spread of particle size is larger than the maximum capillary force of Poly 1449 with smaller spread of particle size, which in turn is higher than the maximum capillary force in the Mono 1600 aggregate with particles of equal size (Fig. 5.20 and Tab. 5.7). Correspondingly, the COV of the capillary force at specific network saturation (Section 5.3) for the case of polydisperse aggregates is significantly higher than the one of Mono 1600 aggregate (Tab. 5.4). Whereas, and in contrast, the COV of the maximum capillary force over the whole drying process of the polydisperse aggregates is smaller than the one of the Mono 1600 aggregate (Tab. 5.7).

5.5 Concluding remarks

Investigations on synthetic aggregates presented in Chapter 4 have shown that the solid skeleton of such aggregates has not significant influence on the drying kinetics, either in terms of liquid phase distribution (saturation profile) or in terms of drying time and drying rate. Morphology characteristics (represented by size distributions of pores and throats) of the void volume of the porous media (represented by the investigated aggregates) have been shown to be remarkably different in Chapter 4, but decisive morphological descriptors, such as the spread of throat size, are at a level in which variations are of low interest for drying kinetics.

However, this is not the case for the capillary force analysis in Chapter 5. Same differences in morphology that don’t change the drying kinetics significantly, have large influence on capillary forces. Which also means that capillary forces can be different at same drying kinetics, contrary to what one might expect by intuition. Following intuition and highly simplified analytical considerations, mean capillary force scales up

in nearly direct proportionality to particle size in monodisperse aggregates, and the same holds also for the maximum capillary forces. However, there are numerous and strong outliers from this general pattern, indicating that the morphology of particle aggregates is much more complex than simple considerations can reflect. Mean capillary force is not very strongly influenced by particle size dispersity in bidisperse and polydisperse aggregates, but maximal capillary force is. Indeed, we have found the maximal capillary force to increase significantly with increasing spread of particle size in such cases.

Chapter 6

Microcracks in the drying particle aggregates of different structure

The evolution of liquid distribution over the course of drying obtained by triangulation pore network model (TPNM) (introduced in Chapter 3) for the case of synthetic aggregates (introduced in Chapter 4) results in the distribution of capillary force exerting on primary particles of these aggregates (analyzed in Chapter 5). The difference in solid skeleton represented by different aggregates results in no remarkable difference in drying kinetics as being shown in Chapter 4. However, investigations in Chapter 5 have shown that the heterogeneity of sizes of particles comprising the aggregates has significant influence on the capillary force experienced by particles. The purpose of Chapter 6 is to use a one-way coupling approach to study the mechanical response of these aggregates upon local capillary forces during drying. The discrete element method (DEM) is employed to calculate the net capillary force on each particle from pore saturation obtained from TPNM simulations. Using DEM, the capillary force on each particle is added to the respective contact force. The resulting total force is then used in the Newton's second law to calculate new position of each particle. A bonded particle model is utilized to simulate microcracks induced by interparticle bond breakages. Microcracks are recorded during drying to obtain spatial and temporal information on damage.

6.1 Coupling method

To simulate microcracks in the drying particle aggregates, the TPNM and DEM are coupled via capillary forces. On this basis, the total force $\vec{F}_{tot,i}$ acting on particle i having N_c neighboring particles j is calculated as:

$$\vec{F}_{tot,i} = -\sum_{j=1}^{N_c} \vec{F}_{ij} + \vec{F}_{cap,i}, \tag{6.1}$$

where $\vec{F}_{cap,i}$ is the total capillary force acting on particle i (see Chapter 5 for the formulation and computation of capillary forces). The position of particle i is given by the position of its center of mass, $\vec{x}_i$. The relation between the particle acceleration $\ddot{\vec{x}}_i$ induced by $\vec{F}_{tot,i}$ and the particle mass is given by Newton's second law:

$$\vec{F}_{tot,i} = m\ddot{\vec{x}}_i. \tag{6.2}$$

The contact force $\vec{F}_{ij}$ acting on a bond between two neighboring particles i and j can be resolved into normal and shear components with respect to the contact plane. The normal contact force $\vec{F}_{ij}^n$ is calculated directly from the normal displacement U_{ij}^n (the overlap between particles i and j):

$$\vec{F}_{ij}^n = K_{ij}^n U_{ij}^n \vec{n}_{ij}, \tag{6.3}$$

where K_{ij}^n is the normal contact stiffness and $\vec{n}_{ij}$ is the normal vector pointing from the center of particle i to the center of particle j. In this study, K_{ij}^n is defined in relation to the bulk elastic modulus denoted by E [216, 205, 206] (see Tab. 4.1 for numerical value of E) as:

$$K_{ij}^n = 2E\frac{R_1 R_2}{R_1 + R_2}, \tag{6.4}$$

where R_1, R_2 denote the radii of two adjacent particles in contact. These particles stay in contact until the bond breaks.

The shear contact force $\vec{F}_{ij}^s$ is set zero when the contact is initially formed. After that, the shear contact is computed from the relative incremental tangential displacement as:

$$\vec{F}_{ij}^s = \vec{F}_{ij}^{s,old} + K_{ij}^s \vec{U}_{ij}^s, \tag{6.5}$$

where $\vec{U}_{ij}^{s}$ is the relative incremental shear displacement and is perpendicular to $\vec{n}_{ij}$, $\vec{F}_{ij}^{s,old}$ is the shear contact force of previous time step, K_{ij}^{s} is the shear contact stiffness defined as:

$$K_{ij}^{s} = \psi K_{ij}^{n}, \tag{6.6}$$

where ψ is a dimensionless parameter relating to the Poisson's ratio of the material. The numerical values of stiffness ratio used for simulations presented in this chapter can be found in Tab. 4.1.

In bonding model used here, there are two criteria for a bond breakage [192]. The first criterion is for the case of tension. A maximum normal force is defined based on the interparticle tensile strength φ:

$$F_{max,ij}^{n} = \pi R_{min}^{2} \varphi, \tag{6.7}$$

where R_{min} is the smaller radius between particles i and j. If $\vec{F}_{ij}^{n}$ reaches or exceeds the maximum normal force (bond strength), the bond breaks. This situation is referred to as mode 1.

The maximum shear force is the second mode for the bond failure, which is defined according to Mohr-Coulomb failure criterion:

$$F_{max,ij}^{s} = \tau\pi R_{min}^{2} + R_{min} tan\phi, \tag{6.8}$$

where τ is the interparticle shear strength (called cohesion in Tab. 4.1) and ϕ is the interparticle friction angle. Once $\vec{F}_{ij}^{s}$ reaches or exceeds maximum shear force, the bond rupture occurs (mode 2).

The breakage of bonds which occurs either in the first mode or in the second mode is interpreted as microcracks in the simulations presented in this chapter. Note that if two particles collide when their interparticle bond has broken, the interaction forces are computed again but the cohesive force components, i.e., interparticle tensile strength φ and interparticle shear strength τ, are set to zero.

Mechanical equilibrium state of an aggregate composed of N_p particles is reached if:

$$\sum_{i=1}^{N_p} \vec{F}_{tot,i} = 0. \tag{6.9}$$

However, the absolute zero value of this condition is not practical in numerical simulations due to the finite precision calculated using the computer. Thus, a numerical equilibrium is determined based on the unbalanced force ratio ξ defined as the ratio of the mean total force acting on particles to the mean contact force acting at the bonds between particles:

$$\xi = \frac{\frac{1}{N_p}\sum_{i=1}^{N_p}|F_{tot,i}|}{\frac{1}{N_c}\sum_{j=1}^{N_c}|F_{ij}|}, \tag{6.10}$$

The numerical mechanical equilibrium is reached once ξ approaches a sufficiently small value (e.g., 0.01 or 0.001).

The values of the DEM micromechanical parameters for all aggregates investigated in this chapter are identical to those listed in Tab. 4.1, except the value of interparticle friction angle. An interparticle friction angle of 9° is used in Chapter 4, whereas a much large value of the friction angle, i.e. 30°, is used for the coupled DEM-TPNM simulations. The purpose for using a smaller friction angle was to reduce the computation time required to generate the particle aggregates.

The algorithm for the coupling of TPNM and DEM is illustrated in Fig. 6.1. For the aggregates considered in this study (dense packing, porosity of about 0.4), the particle displacements are assumed to be very small compared to the size of the particles as well as the pores and throats. Thus, it is reasonable to neglect the influence of the solid phase (particle displacement) on the fluid phase (pore and throat sizes). This means the TPNM and DEM simulations are carried out in the frame of a one-way coupling scheme. However, the scheme implemented in this study can technically be expanded to two-way coupling since both the TPNM and DEM codes are implemented using Python programming language which is executed in the same computation platform. By contrast, the fluid-solid coupling simulations in [71,72] were carried out essentially in two separated passes. In the first pass the distributions of liquid saturation and capillary force over time in a regular pore network are computed using a code implemented in MATLAB. In the second pass, the capillary forces are recalled and consecutively applied as external loads to primary particles using Particle Flow Code (PFC). This coupling procedure has been implemented in two-dimensional [72] and three-dimensional space [71], but only for the case of monodisperse aggregates.

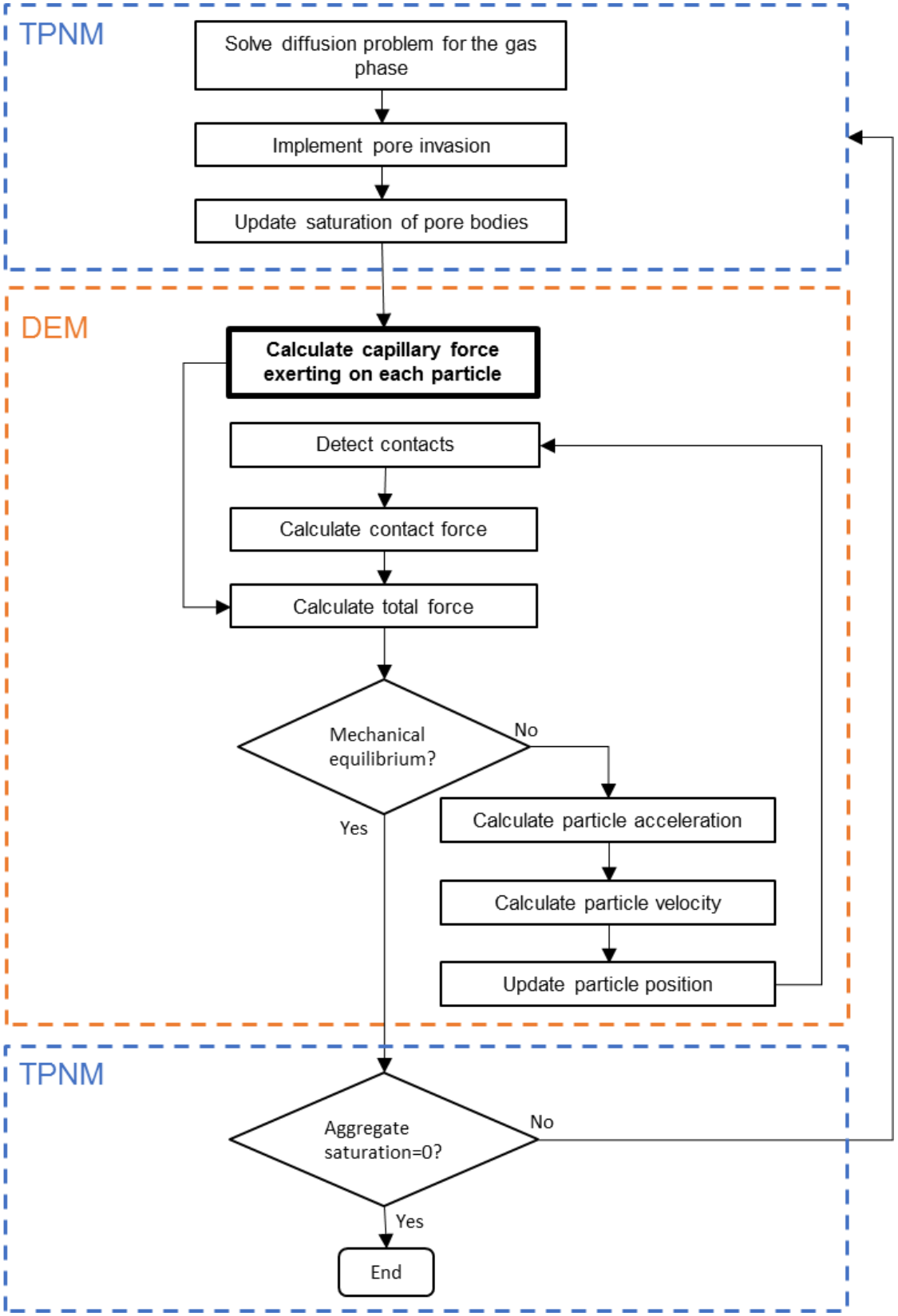

Figure 6.1: The flow chart for the coupling of triangulation pore network model (TPNM) and discrete element method (DEM).

6.2 Influence of particle size on bond breakage

In this section, the influence of primary particle radius on bond breakage is explored by performing simulations on the five monodisperse aggregates with the same dimension (3 mm × 3 mm × 4.5 mm) but different particle radius (Fig. 6.2). The results obtained from these simulations are compared against each other.

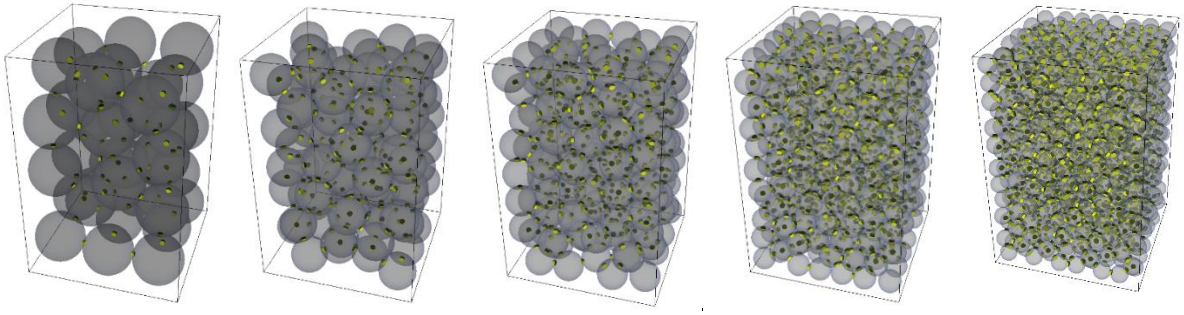

R = 0.50 mm, 37 particles | R = 0.36 mm, 100 particles | R = 0.30 mm, 200 particles | R = 0.22 mm, 500 particles | R = 0.18 mm, 1000 particles

Figure 6.2: Illustration of bonds formed between particles in five different monodisperse aggregates. The particles are shown as transparent gray spheres. Bonds are visualized by cylinders shown in yellow. The black frame is the domain of the container.

The evolution of broken bonds recorded during the drying of Mono 500 and Mono 1000 aggregate is illustrated in Fig. 6.3 and 6.4, respectively. Microcracks formed during drying of these two aggregates tend to follow a similar pattern. The microcracks (visualized by purple cylinders in Figs. 6.3, 6.4) generally appear in the vicinity of the drying front, i.e. the interface between the wet and dry regions. This could be attributed to gradient in capillary force which is caused by difference in pore saturation. At the very early stage of drying, the front is near the surface of the aggregates (Fig. 6.3a, 6.4a) where the gas phase starts invading the liquid phase and penetrates the aggregate. As drying front retreats into the aggregates, the number of broken bonds increases progressively (Fig. 6.3b, 6.4b). By the end of drying, the broken bonds spread nearly the entire aggregate (Fig. 6.3c, 6.4c).

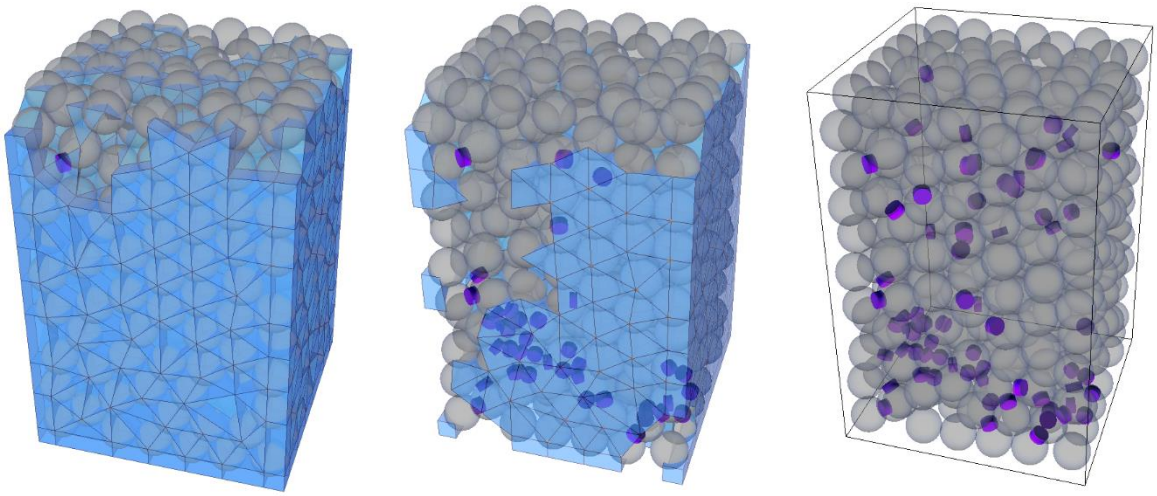

(a) (b) (c)

Figure 6.3: Illustration of broken bonds (purple cylinders) during the drying of Mono 500 aggregate (primary particles are shown as transparent gray spheres, the liquid phase is shown in blue): (a) Bonds ruptured at the very beginning of drying appear near the top surface; (b) Bonds broken in the middle of the drying process; (c) All broken bonds at the end of the drying process. The aggregate is subjected to drying at the top.

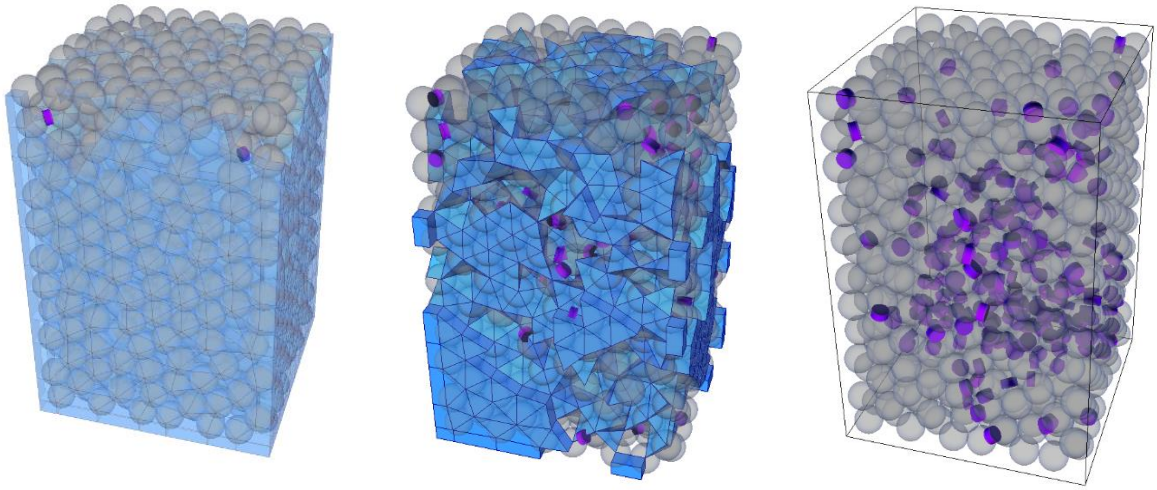

(a) (b) (c)

Figure 6.4: Illustration of broken bonds (purple cylinders) during the drying of Mono 1000 aggregate (primary particles are shown as transparent gray spheres, the liquid phase is shown in blue): (a) Bonds ruptured at the very beginning of drying appear near the top surface; (b) Bonds broken in the middle of the drying process; (c) All broken bonds at the end of the drying process. The aggregate is subjected to drying at the top.

It is important to note that throughout this thesis damage is represented by microcracks which are resulted from gradient in local capillary forces. Two main

reasons could be conjectured for the absence of catastrophic macroscopic cracks during the drying of these aggregates. The first reason is related to drying conditions. In this study we assume that the drying process takes place under isothermal slow conditions. Under these conditions, the gas phase percolates essentially throughout the aggregates, resulting in capillary forces that span the entire aggregates. Therefore, macroscopic gradient in capillary forces is less likely to be established, especially during the first drying period. The fact that the aggregates are relatively small could also attribute to maintaining the mechanical integrity of the aggregate during drying.

On one hand, the monodisperse aggregate comprised of bigger particles (except the Mono 100 aggregate) leads to higher capillary force as shown in Chapter 5. On the other hand, the bigger particles are bonded to each other more firmly than small particles. The reason is that maximum normal and shear forces (for bond failure criteria) are proportional to the particle radius (Eqs. 6.7 and 6.8)

Table 6.1: Comparison on the bond breakage induced by drying for the case of five monodisperse aggregates.

	Number of initiated bonds	Number of broken bonds	Damage percentage	Particle radius, mm
Mono 37	65	0	0.0%	0.501
Mono 100	208	0	0.0%	0.364
Mono 200	446	0	0.0%	0.298
Mono 500	1209	70	5.8%	0.222
Mono 1000	2537	238	9.4%	0.178

For the situation (Tab. 6.1) where the DEM parameter values are set equal to the ones in Tab. 4.1 there is less damage when the particle size increases (number of particles decreases). This appears to be qualitatively in accordance with the experimental study on the drying of a colloidal drop consisting of silica nanoparticles on a floating membrane [70]. Drying stress of pure suspension of coarse particles is smaller than pure suspension of fine particles. Another investigation on colloidal suspension using confocal microscopy also shows that there are many cracks for the sample made of

particles with 0.22 μm diameter but no crack for the sample made of 2 μm diameter [132].

Table 6.2: Comparison on the bond breakage induced by drying for the case of five monodisperse aggregates when the bond strength is reduced by half.

	Number of initiated bonds	Number of broken bonds	Damage percentage	Particle radius, mm
Mono 37	64	3	4.7%	0.501
Mono 100	208	48	23.1%	0.364
Mono 200	443	53	12.0%	0.298
Mono 500	1208	409	33.9%	0.222
Mono 1000	2534	1183	46.7%	0.178

In order to evaluate the influence of the mechanical properties on the drying-induced cracks of the considered aggregates without targeting any specific material, the bond strength (tensile strength and cohesion in Tab. 4.1) is reduced by half. Simulations conducted with this new set of parameters show less damage when the particle size increases, except for the case of Mono 100 aggregate (Tab. 6.2). As shown in Chapter 5, Mono 100 aggregate has higher capillary force than Mono 200 aggregate. The above exception means that the impact of bond strength becomes less dominant compared to the one of capillary force for the case of Mono 100 aggregate.

6.3 Influence of particle size distribution on bond breakage

Most of the aggregates encountered in many natural or technical porous systems are composed of a broad range of particle sizes. The influence of particle size distribution on bond breakage is investigated by considering the two limiting cases: The Bi 860 and Bi 1047 aggregates, the mixture of fine and coarse particles (introduced in Chapter 4). The initiated bonds of these two bidisperse aggregates are illustrated in Fig. 6.5. As explained in previous chapter, the combination of small void between fine particles and bigger radius of coarse particles results in significantly higher capillary forces (both in the mean of capillary force in each network saturation as well as the

maximal capillary force over the whole drying simulation) for the case of bidisperse aggregates. Regarding the bond failure criteria, the bond strength for the case of unequal size particles depends on the smaller particle radius between the two particles in contact (Eqs. 6.7 and 6.8). Thus, there are many weaker bonds for the case of bidisperse aggregate compared to the equivalent monodisperse aggregate. These two factors lead to a greater number of broken bonds in the bidisperse aggregate than the monodisperse aggregates (see Tab. 6.3).

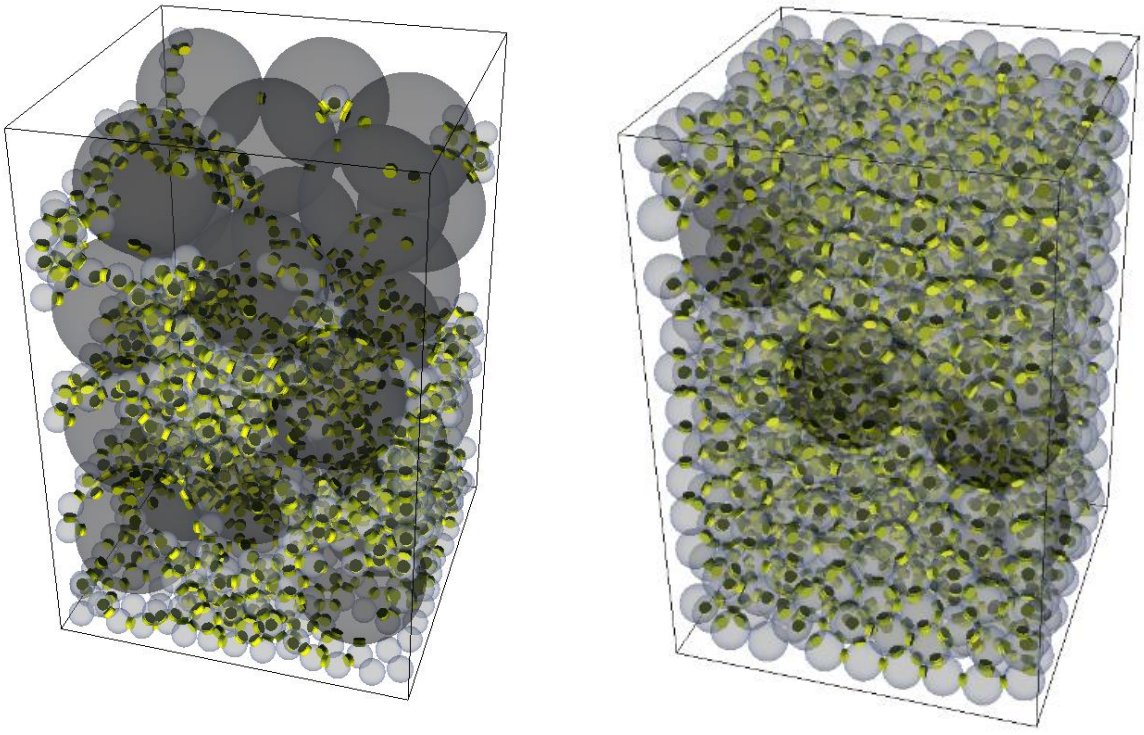

(a) (b)

Figure 6.5: Illustration of initiated bonds (yellow cylinders) of two bidisperse aggregates: (a) Bi 860; (b) Bi 1047. Solid phase is represented by transparent spheres. Color of the spheres indicates the particle size. The black frame is the domain of the container.

With the same DEM parameter values as the case shown in Tab. 6.1, all bonds in the Bi 860 aggregate are broken while the extent of damage in the monodisperse aggregates are less than 10% (Tab. 6.3). Beside particle size, another factor contributes to this significant bond failure. The Bi 860 aggregate is loosely packed. Thus, there is more space for particle movement compared to other denser-packed

aggregates. This could result in more broken bonds for the case of Bi 860. This is not the case for the closely-packed Bi 1047 aggregate. The space for the movement of particles is limited, leading to less number of broken bonds for the case of Bi 1047 compared to the Bi 860 aggregate. Additionally, the particles in Mono 37 have radius 0.50 mm which is almost equal to the radius of coarse particles (0.54 mm) in the Bi 860 aggregate. There is no broken bond for the case of Mono 37 aggregate, but all bonds in the Bi 860 aggregate are broken. This may mean that the addition of fine particles leads to the breakage of all bonds of the aggregate, despite the fact that the bonds between coarse particles are strong. The reason is the amplification in capillary force resulted from the combination of high capillary pressure (induced by the meniscus pinned at the void space between fine particles) and the large particle size, as explained in Chapter 5.

Table 6.3: Comparison on the bond breakage between the monodisperse and bidisperse aggregates. For bidisperse aggregates, f is fine and c is coarse.

	Mono 37	Mono 1000	Bi 860	Bi 1047
Number of initiated bonds	65	2537	1576	2628
Number of broken bonds	0	238	1576	370
Damage percentage	0.0%	9.4%	100%	14.08%
Particle radius, mm	0.501	0.178	0.108 (f)	0.163 (f)
			0.539 (c)	0.542 (c)

Table 6.4: Damage comparison between monodisperse and bidisperse aggregates when the bond strength is reduced by half. For bidisperse aggregates, f is fine and c is coarse.

	Mono 37	Mono 1000	Bi 860	Bi 1047
Number of initiated bonds	64	2534	1576	2625
Number of broken bonds	6	1183	1576	2625
Damage percentage	4.7%	46.7%	100%	100%
Particle radius, mm	0.501	0.178	0.108 (f)	0.163 (f)
			0.539 (c)	0.542 (c)

The particle radius of Mono 1000 aggregate (0.18 mm) is almost equal to the radius of fine particles of Bi 1047 (0.16 mm). When the bond strength is reduced by half (Tab. 6.4) the degree of damage in the Mono 1000 aggregate is 46.7% while all bonds in the Bi 1047 aggregates are broken. This means that the addition of coarse particles leads to a greater number of microcracks. The possible reason could be that the influence of coarse particle size on stronger bond strength becomes weaker compared to the higher capillary force resulted from higher capillary pressure (induced by fine particles) and bigger particle size.

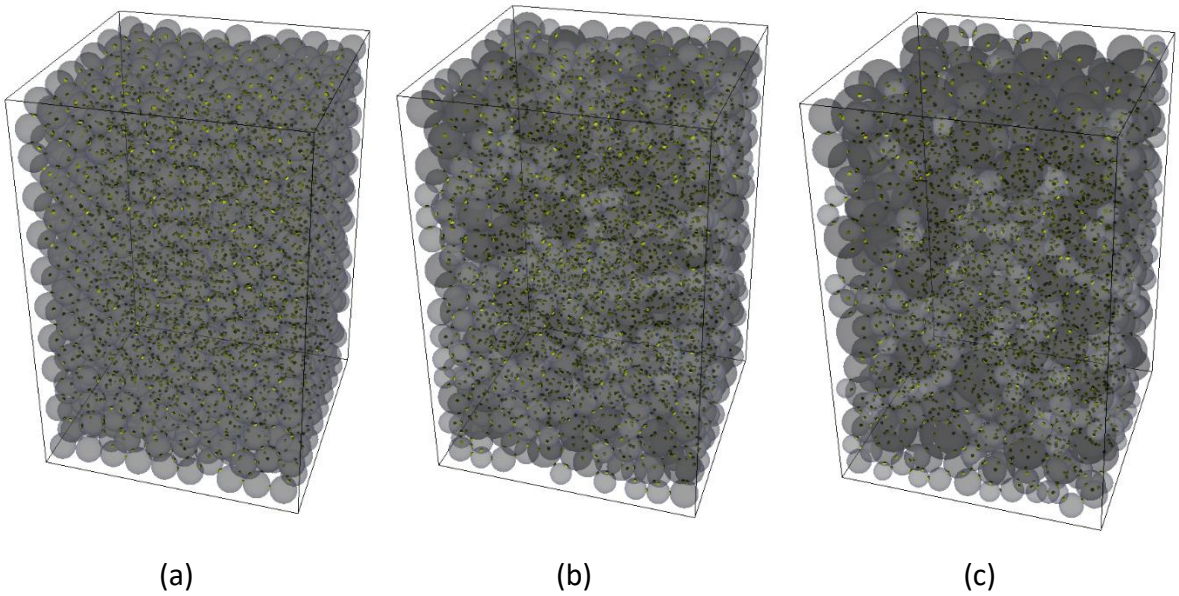

Figure 6.6: Illustration of initiated bonds of (a) Mono 1600, (b) Poly 1449 and (c) Poly 1164 aggregates. Bonds: yellow cylinders; particles: transparent grey spheres; container: the black box.

Table 6.5: Damage comparison between monodisperse and polydisperse aggregates.

	Mono 1600	Polydisperse 1449	Polydisperse 1164
Number of initiated bonds	3364	3641	2700
Number of broken bonds	265	760	1001
Damage percentage	7.9%	20.9%	37.1%
Mean particle radius, mm	0.409	0.409	0.415
Max particle radius, mm	0.409	0.586	0.818
Min particle radius, mm	0.409	0.316	0.274

Bidisperse aggregate represents a special case of polydisperse aggregate. The influence of particle size polydispersity on the bond breakage is further investigated by the comparison between the monodisperse aggregate (Mono 1600) and polydisperse aggregates (Poly 1449, Poly 1164) (introduced in Chapter 4). The initiated bonds of these three aggregates are illustrated in Fig. 6.6. With the same DEM parameter values as the cases shown in Tabs. 6.1 and 6.3, the data on broken bonds for the case of Mono 1600, Poly 1449 and Poly 1164 aggregates is shown in Tab. 6.5. Mono 1000 and Mono 1600 aggregates have damaged to an extent of 9.4% and 7.9%, respectively. The fact that these values are similar may suggest that the extent of damage in the monodisperse aggregates is independent of the particle size and of the aggregate dimension; however, this needs to be confirmed with representative simulations in future.

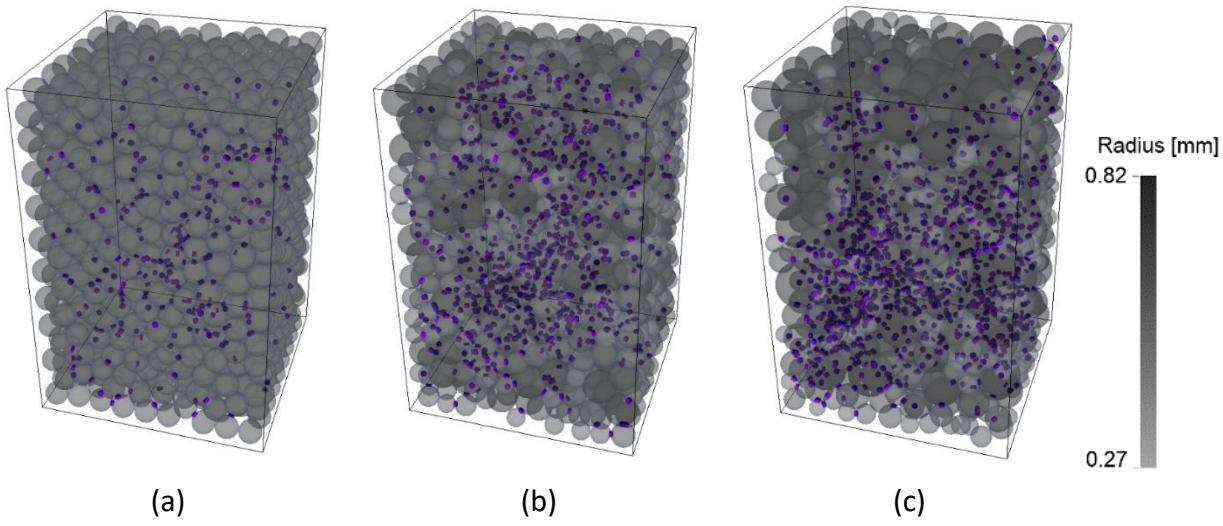

Figure 6.7: Illustration of broken bonds (purple cylinders) at the end of the drying of Mono 1600 (a), Poly 1449 (b) and Poly 1164 (c) aggregates. Solid phase is represented by transparent spheres. Color of the spheres indicates the particle size. The black frame is the domain of the container. The aggregate is subjected to drying at the top.

Regarding the influence of non-equal sized particle aggregates on the extent of damage, similar to the comparison made between monodisperse and bidisperse aggregates (Tab. 6.3), the particle size polydispersity increases the bond damage significantly (Tab. 6.5). The higher the particle size polydispersity, the larger the extent of bond breakage (20.9% and 37.1%, Tab. 6.5). Poly 1449 has the deviation in initial

particle size distribution of 30% while this value of Poly 1164 aggregate is 50%. This results in a broader range in the final particle size distribution, i.e. bigger maximal particle radius and smaller minimal particle radius. Similar to what has been explained for the case of bidisperse aggregate, the combination of larger coarse particles and smaller fine particle results in higher capillary force (exerted on coarse particles) and weaker bond strength (the bond between fine particles and their neighboring particles). All broken bonds recorded during the drying of Mono 1600, Poly 1449 and Poly 1164 aggregates are illustrated in Fig. 6.7.

Summing up, simulations presented in this chapter serve as first step towards the coupling of the fluid phase and solid phase in drying aggregates made of spherical particles of unequal sizes. The results presented here cannot be generalized because of several reasons: Physical effects such the liquid viscous effect are extremely important when simulation of realistic drying conditions is aimed. This effect was completely neglected in the drying algorithm presented here. Another major issue is the system size which was limited to aggregates with relatively small dimensions. Moreover, a macroscopic liquid pressure gradient that can lead to solid tension build-up and thus macroscopic cracks was neglected. Therefore, the results presented here could only be generalized if simulations with aggregates of larger dimensions were performed in the presence of those effects.

Chapter 7

Conclusions and future research work

7.1 Conclusions

A novel three-dimensional triangulation pore network model (TPNM) has been developed that can simulate the drying behavior of capillary porous aggregates made of spherical primary particles with different size distributions. Given the centroid coordinates and radii of primary particles, an irregular network of pores and throats is generated using the regular Delaunay triangulation and its dual Voronoi tessellation. Since drying occurs in the limiting condition of capillary-dominated regime (negligible liquid viscosity), liquid water evaporateds from all the menisci in a liquid cluster but only the meniscus in the pore with the largest entry capillary radius retreats. In the wake of evaporation, vapor molecules are generated. The standard mass balance equations are employed to compute the quasi-static molecular diffusion of vapor. The liquid phase distribution during drying is represented by the saturation profile calculated from the evolution of the saturation of pores. Evaluation of drying kinetics is based on the evolution of drying time and drying rate with respect to network saturation.

The reliability of developed TPNM is assessed by comparing the predictions of liquid phase distribution and drying kinetics obtained from the TPNM to corresponding experimental results reported in [178]. Besides, these predictions are also compared to the ones obtained from classical pore network model (CPNM) and ring pore network

model (RPNM) simulations reported in [178]. The liquid phase distribution predicted by the TPNM is in much better agreement with experimental results than those obtained from the other two pore network models, CPNM and RPNM. The main reason for this is the difference in the morphological characteristics of the pore network representing the void space of the porous medium. The pore network in TPNM has broad distributions of pore volume, throat entry capillary radius (which defines capillarity), as well as throat length and area (used for mass transfer calculation). Whereas cylindrical throats in CPNM and RPNM have uniform throat length and only narrowly distributed cross-sectional area. The capillary effect in CPNM and RPNM can only be applied by varying the size distribution of the throat radius. This results in a limited ability of representing the geometrical as well as physical characteristics of porous structures in reality. Moreover, the solid skeletons in TPNM simulation (obtained by X-ray tomography images) and in the experiment are the same, while the ones used in CPNM and RPNM simulations are only based on approximate considerations. This shows the advantage of the irregular arrangement of capillary elements in TPNM compared to the regular arrangement used in CPNM and RPNM. Higher diversity in terms of size distribution as well as irregular arrangement of capillary elements are the reasons why the liquid connectivity simulated by TPNM is close to the one experimentally observed in the literature.

However, at the current state of model development, the triangulation process can only be implemented with flat boundary walls. Since the shape of the experimental aggregate in [178] was that of a circular cylinder, a pore elimination is required. This results in a smaller surface area in TPNM compared to the ones used in CPNM and TPNM. Besides, given the same nominal boundary layer thickness, the irregular arrangement of pores in the boundary layer of the TPNM (leading to tortuous diffusion path) unintentionally increases the effective thickness of the boundary layer compared to the ones used in CPNM and RPNM. These two factors result in a smaller value of drying rate in the first period for the TPNM. However, the enhanced liquid connectivity in TPNM keeps liquid staying close to the top surface until very low network saturation of about 0.1. Thus, the total drying time predicted by TPNM is still much closer to the experimental value than those obtained from the CPNM and the RPNM.

To further utilize the versatility of TPNM, the influence of particle size distribution on the liquid phase distribution and drying kinetics is investigated in Chapter 4. Three sets of aggregates have been numerically generated using discrete element method (DEM) approach. The shape of the aggregate is cuboid to avoid pore elimination encountered in Chapter 3. The influence of particle size is first implemented by generating five monodisperse aggregates having the same aggregate dimensions (width × depth × height = 3 × 3 × 4.5 mm³) but different number of particles (consequently, different particle radius). Influence of spatial distribution of particles is negligible in the statistical comparison of pore size distribution for the case of five realizations of Mono 100 and Mono 500 aggregates. The second set of aggregates has the same aggregate dimension, but these aggregates are bidisperse to investigate the effect of particle size distribution. Taking the monodisperse aggregates as reference, the solid volume fraction of fine particles Q_f as well as the diameter ratio of coarse to fine particles d_c/d_f have been varied to generate 19 different bidisperse aggregates. The two bidisperse aggregates having smallest and highest set value of Q_f, namely Bi 860 and Bi 1047, respectively, have been chosen for further investigations. The porosity of the numerically generated aggregates is in qualitative agreement with empirical correlations reported in literature, for the case of monodisperse as well as bidisperse aggregates. The third set of investigated aggregates consisted of three aggregates: one monodisperse as reference and two polydisperse aggregates to investigate the impact of particle polydispersity. The third aggregate set had same aggregate shape but bigger aggregate dimensions, 8 × 8 × 12 mm³.

For the case of the five monodisperse aggregates, the influence of the boundary walls on liquid phase distribution decreases with increasing number of particles, i.e. increment of the aggregate-to-particle size ratio. Regarding the drying kinetics, extended first period is observed for all five investigated monodisperse aggregates, similar to what has been obtained from the TPNM simulation in Chapter 3. This is interpreted by an enhanced aggregate-spanning liquid connectivity induced from a large spread in the distribution of throat entry capillary radius (represented by coefficient of variance (COV) ranging from 44.2% to 53.2%, comparable to 67.1% obtained in Chapter 3).

The pore and throat size distributions of the Bi 1047 aggregate are not so much different in comparison to those of the five monodisperse aggregates. Moreover, in Bi 1047 fine particles (particle radius almost equal to the one of Mono 1000 aggregate) are dominant (75.7% in volume). The porosities of these two aggregates are almost equal as well, 0.389 and 0.391, respectively. These factors can be the reason for the similarity in not only pore and throat size distribution but also in saturation profile between the Bi 1047 and Mono 1000 aggregates. In contrast, coarse particles are dominant in the Bi 860 aggregate, and the filling of fine particles in the void space between coarse particles is not spatially uniform, the void space in the lower part is filled up much more than the void space in the upper part. This results in a solid skeleton of the Bi 860 aggregate similar to a layered porous medium. Saturation profile of Bi 860 aggregate is indeed similar to an experimental profile obtained in literature for an aggregate having similar configuration of solid structure. There is no remarkable difference in terms of drying kinetics obtained for the investigated two bidisperse aggregates in comparison to the five monodisperse aggregates.

The two polydisperse configurations in the last investigated set of three aggregates have different spread of the particle size distribution. The COV of throat mass transfer size distribution increases with increasing standard deviation of the particle size distribution, while there is almost no difference in the COV of pore volume and throat capillary radius size distributions. Additionally, aggregate-to-particle size ratio of the three aggregates in this third set is higher than the respective values of previously investigated aggregates (at smaller aggregate dimension). Thus, it is concluded that the influence of particle size distribution on liquid distribution and drying kinetics is negligible, at least at this higher aggregate dimension.

Based on the pore scale saturation obtained from the triangulation pore network model (TPNM), capillary forces exerted on solid particles can be computed numerically for all investigated aggregates. In Chapter 5, the evolution of liquid distribution and the corresponding capillary forces of exemplary modisperse, bidisperse and polydisperse aggregates is first visualized in three-dimensions. For the case of Mono 100 and the two bidisperse aggregates, the capillary forces exerted on coarse particles of the bidisperse aggregates are larger than those acting on particles of the Mono 100 aggregate. This difference in force magnitude with respect to particle size becomes

weaker in the comparison between Mono 1600 and the two polydisperse aggregates. Three factors are found to have an influence on the capillary force acting on a primary particle: particle size, capillary pressure and liquid distribution around the considered particle.

Further statistical analyses of the distribution of capillary force at specific network saturation and of maximal capillary force over the whole drying simulation have shown that capillary force scales up almost direct proportionally to particle size in monodisperse aggregates. Besides, the influence of particle size dispersity (bidisperse and polydisperse aggregates) on the maximal capillary force over the whole drying course is stronger than the influence on the mean value of capillary force at specific network saturation.

Different solid structures do not result in remarkable difference in drying kinetics (Chapter 4) but they do give rise to significantly different capillary forces (Chapter 5). These capillary forces are then used as input for the PNM–DEM coupling simulation in Chapter 6, which relates the evolution of the fluid phase distribution (represented by the saturation of the pores) to the damage of the solid phase (represented by the breakage of the bonds between solid particles). For the case of monodisperse aggregates, simulation results show that bigger particles lead to less damage, as also observed in literature. The investigations on bidisperse and polydisperse aggregates show that higher heterogeneity in particle size leads to more drying-induced damage.

7.2 Future research work

Several assumptions which have been made in the development of our drying pore network model, i.e. TPNM, are not inherent to the modeling approach and can be relaxed by future model extensions. The TPNM can be extended by additional transport phenomena, namely viscous capillary flow and heat transfer. Incorporation of such physical effects is essentially important for the simulation of rapid drying of porous materials, of large-size porous materials, or of porous materials that contain small pores with a narrow size distribution. An advanced version of the coupled TPNM-DEM shall account for significant displacement of the solid particles during the drying process (two-way coupling), to address remarkable solid structure changes (e.g.

shrinkage, large-scale fracture). Another appealing research direction would be to extend the fluid-solid coupling approach presented herein to situations where the solid phase is represented by primary particles with non-spherical shapes.

Appendix

A1. Calculation of entry capillary radius

After the pore network has been defined by applying Delaunay triangulation on the particle aggregate, the entry capillary radius $r_{c,e}$ at each throat, in this study, is determined following the MS-P (Mayer and Stowe-Princen) method [181, 182]. This kind of calculation of the entry capillary pressure was previously applied to several similar problems [181, 183, 184, 77] and is implemented in Yade-DEM. Figure A1.1 illustrates the MS-P principle. It shows one corner of a throat that has been obtained by the triangulation (cf. Fig. A1.2), where a meniscus is located and defines the boundary between the liquid and the gas phase. Though this does not reflect the reality, menisci and interfaces are supposed to extend with infinite longitudinal curvature in the third dimension, like in case of prims with irregular cross section. Corresponding to drying (replacement of liquid as the wetting fluid by gas as the non-wetting fluid), the meniscus moves by an infinitesimal distance dx from Z_1Z_2 to $Z'_1Z'_2$ in Fig. A1.1. Quasi-equilibrium conditions are assumed during this movement, so that work rendered by the capillary pressure is set equal to the work provided by surface forces at the three binary interfaces which are involved in this problem:

$$p_c dV = \sigma_{lg} dS_{lg} + \sigma_{sg} dS_{sg} + \sigma_{sl} dS_{sl} \,. \tag{A1.1}$$

Here, p_c is capillary pressure across the meniscus; V, σ and S denote volume, surface tension and surface area, respectively. The subscripts l, g and s refer to liquid, gas and solid, respectively.

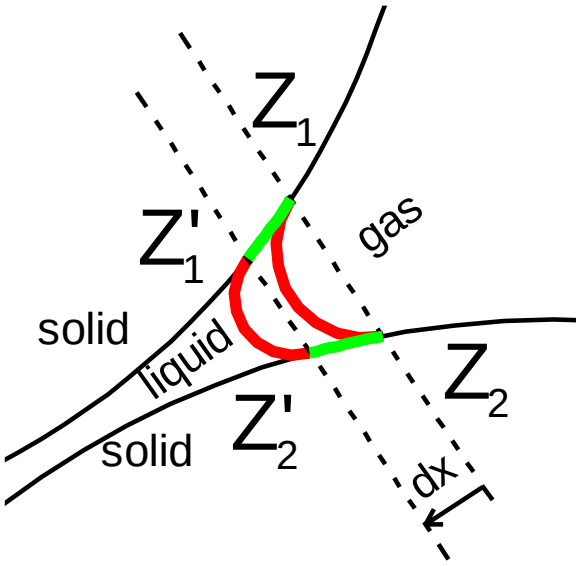

Figure A1.1. Illustration of the meniscus movement from Z_1Z_2 to $Z'_1Z'_2$. Z_i and Z'_i are on the three-phase contact line. The liquid-gas interface is shown in red. The trajectory of the three-phase contact points during this meniscus movement is shown in green.

With the previously mentioned considerations the incremental volume changes can approximately be expressed as

$$dV = A_g \, \mathrm{dx} \, , \tag{A1.2}$$

where A_g is the cross-sectional area of the gas phase in the throat.

The incremental surface area changes are given by:

$$dS_{lg} = L_{lg} \, \mathrm{dx} \, , \tag{A1.3}$$

$$dS_{sl} = L_{sl} \, \mathrm{dx} \, , \tag{A1.4}$$

$$dS_{sg} = L_{sg} \, \mathrm{dx} \, , \tag{A1.5}$$

where L is the perimeter of the interfacial cross-section at Z_1Z_2.

Since the changes in solid-liquid and solid-vapor surface area during this meniscus movement are equal but in opposite direction with respect to the three-phase contact line, this means that:

$$dS_{sg} = -\,dS_{sl}\ . \tag{A1.6}$$

Then, Eq. A1.1 can be rewritten as:

$$p_c A_g = \sigma_{lg} L_{lg} - \sigma_{sg} L_{sl} + \sigma_{sl} L_{sl}\ . \tag{A1.7}$$

Multiphase interfacial tensions are interrelated by Young's equation:

$$\sigma_{sg} - \sigma_{sl} = \sigma_{lg} cos\theta\ , \tag{A1.8}$$

where θ is the contact angle.

Substituting Eq. A1.8 into Eq. A1.7 gives:

$$p_c A_g = \sigma_{lg} L_{lg} + \sigma_{sg} L_{sg} - \sigma_{sl} L_{sg}\ ,$$

$$p_c A_g = \sigma_{lg} L_{lg} + L_{sg}\left(\sigma_{sg} - \sigma_{sl}\right),$$

$$p_c A_g = \sigma_{lg} L_{lg} + L_{sg}\,\sigma_{lg} cos\theta\ ,$$

$$p_c A_g = \sigma_{lg}\left(L_{lg} + L_{sg}\,cos\theta\ \right). \tag{A1.9}$$

The calculation of A_g, L_{lg} and L_{sg} is based on throat geometry, as shown in Fig. A1.2. Firstly, A_g can be obtained as following:

$$A_g = A_{\Delta ABC} - A_l - A_s\ , \tag{A1.10}$$

The area of triangle $A_{\Delta ABC}$ can be calculated as:

$$A_{\Delta ABC} = \frac{1}{2} bcsin\alpha\ . \tag{A1.11}$$

Applying law of cosines to triangle ABC gives:

$$a^2 = b^2 + c^2 - \frac{1}{2} bccos\alpha\ , \tag{A1.12}$$

$$b^2 = a^2 + c^2 - \frac{1}{2} accos\beta\ , \tag{A1.13}$$

$$c^2 = a^2 + b^2 - \frac{1}{2}abcos\gamma\ . \tag{A1.14}$$

The center coordinates of the particles are given, thus, A, B, C are known. From this, a = BC, b = AC, c = AB can be calculated. From Eqs. A1.12 to A1.14 the angles α, β, γ can be solved. Subsequently, the area of triangle ABC is calculated following Eq. A1.11.

With the interface at equilibrium, the positions of points O_1, O_2 and O_3 depend on the value of the capillary radius r_c. Applying what has been done with triangle ABC to triangles AO_3B, BO_1C and AO_2C, the area of these triangles and the angles φ_{ij} can be calculated.

In general, the area of a sector (central angles φ_{ij}, in radian) of a circle (radius R) is:

$$A_{\varphi_{ij}} = \pi R^2 \frac{\varphi_{ij}}{2\pi} = \frac{1}{2}\varphi_{ij}R^2. \tag{A1.15}$$

The total area of the liquid phase within the throat is calculated as:

$$\begin{aligned} A_l = &\left(A_{\Delta AO_3B} - \frac{1}{2}\varphi_{31}R_1^2 - \frac{1}{2}\varphi_{32}R_2^2 - \frac{1}{2}\varphi_{33}r_c^2\right) \\ &+ \left(A_{\Delta BO_1C} - \frac{1}{2}\varphi_{12}R_2^2 - \frac{1}{2}\varphi_{13}R_3^2 - \frac{1}{2}\varphi_{11}r_c^2\right) \\ &+ \left(A_{\Delta AO_2C} - \frac{1}{2}\varphi_{21}R_1^2 - \frac{1}{2}\varphi_{23}R_3^2 - \frac{1}{2}\varphi_{22}r_c^2\right)\ . \end{aligned} \tag{A1.16}$$

The total area of the solid phase in triangle ABC is:

$$A_s = \frac{1}{2}\alpha R_1^2 + \frac{1}{2}\beta R_2^2 + \frac{1}{2}\gamma R_3^2. \tag{A1.17}$$

From Eqs. A1.10, A1.11, A1.16 and A1.17, A_g as a function of r_c can be obtained.

The length of an arc (central angles φ_{ij}, in radian) of a circle (radius R) is:

$$L_{\varphi_{ij}} = 2\pi R\frac{\varphi_{ij}}{2\pi} = \varphi_{ij}R. \tag{A1.18}$$

The total length of the liquid-gas interface L_{lg} and the total length of the solid-gas interface L_{sg} can be calculated as:

$$L_{lg} = \varphi_{11} r_c + \varphi_{22} r_c + \varphi_{33} r_c, \tag{A1.19}$$

$$L_{sg} = (\alpha - \varphi_{21} - \varphi_{31}) R_1 + (\beta - \varphi_{32} - \varphi_{12}) R_2 + (\gamma - \varphi_{13} - \varphi_{23}) R_3. \tag{A1.20}$$

Substituting Eqs. A1.19 and A1.20 into Eq. A1.9, along with the previously mentioned expression for A_g and with the expression that connects capillary pressure p_c to the capillary radius r_c, a function with r_c as the only unknown is obtained. Equations are somewhat simplified by assuming perfect wetting condition (contact angle $\theta = 0$).

In this way, r_c is calculated based on the geometry of the throat, which is determined based on the spatial correlation as well as the sizes of the solid particles confining the associated pore. The upper bound of this r_c is the radius of the circle inscribed in the throat and the lower bound of r_c is half of the maximum distance between particles associated to the considered throat [77]. The entry capillary radius $r_{c,e}$ is chosen as the smallest r_c for which the force balance still holds, i.e., there is no meniscus having r_c smaller than $r_{c,e}$.

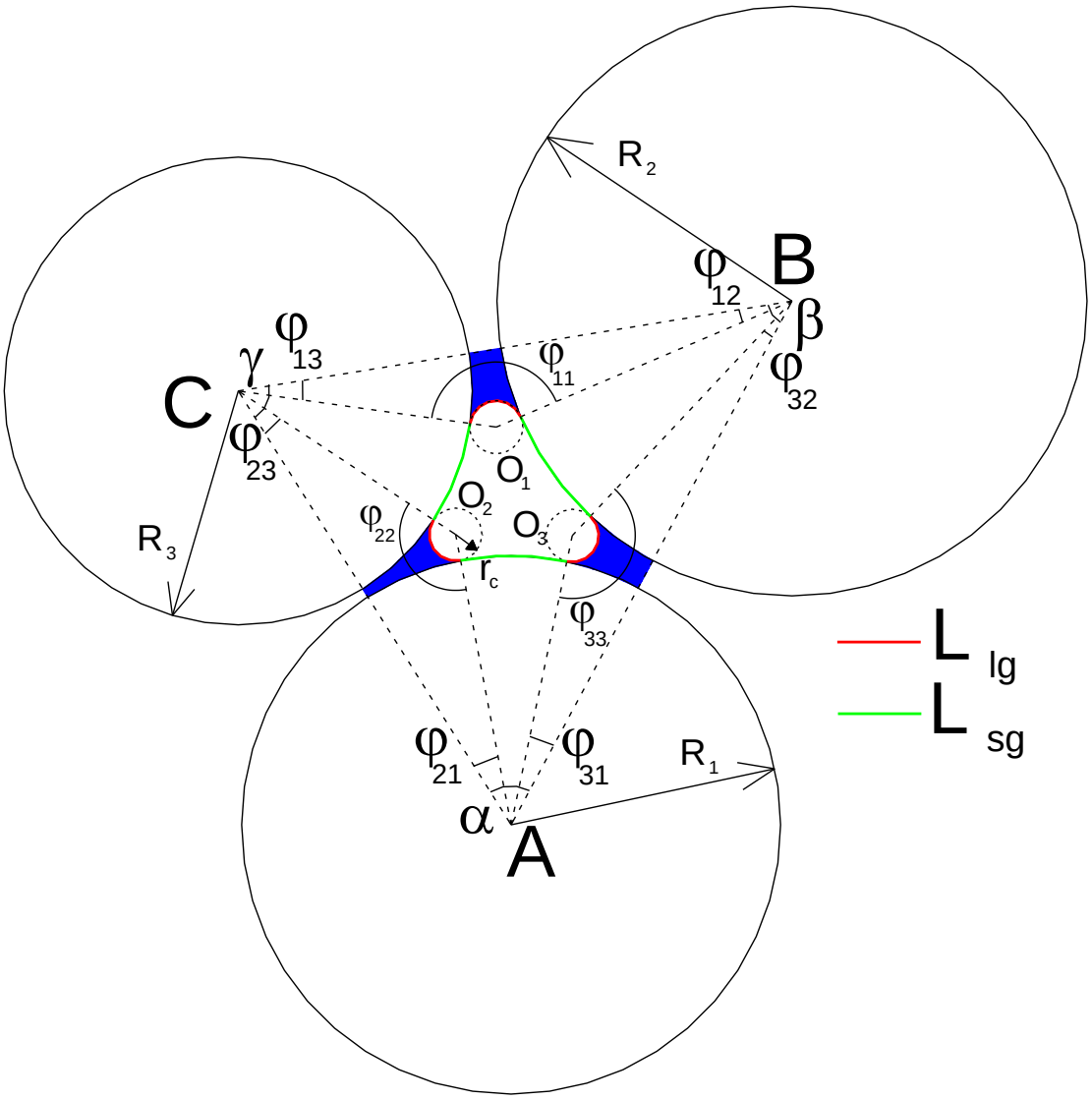

Figure A1.2. Illustration of the geometry of a partially wet throat defined by three particles having their centers at A, B and C.

A2. Boundary cells

The Delaunay triangulation groups the four nearest points in 3D or three nearest points in 2D to create a Delaunay cell. In the interior of the solid particle aggregate, these Delaunay cells have the shape of a triangle (in 2D) or a tetrahedron (in 3D). One Delaunay cell defines one pore, and each facet of the Delaunay cell defines a throat. A tetrahedron has four facets, which results in a coordination number of four for the pores located in the interior of the particle aggregate. In 2D domain, a triangular Delaunay cell has a coordination number of three.

The boundaries (top, bottom, sides) in the Delaunay triangulation used in this study are represented by fictitious spheres having infinite radius. Those are tangent to the particles located at the boundaries. The Delaunay edge is the line connecting two particle centers. Thus, the Delaunay edge of the cells located at the boundaries is the line connecting the center of the particle and its projection on the corresponding boundary. This transforms the shape of the Delaunay cells from triangular (in 2D) to quadrilateral (Fig. A2.1); or, from tetrahedral (in 3D) to a triangular cuboid (5 faces) or cuboid (6 faces) (Fig. A2.2). In 2D domain, the quadrilateral Delaunay cell has one more face compared to the triangular Delaunay cell located in the interior of the packing. Thus, if this quadrilateral Delaunay cell is bounded by one boundary, its coordination number is still three, equal to the triangular Delaunay cell in the interior. However, if the boundary cell is neighbor to two boundaries, its coordination number is only two, smaller than the coordination number of triangular Delaunay cells in the interior of the aggregate. This concept is applied similarly to the 3D domain.

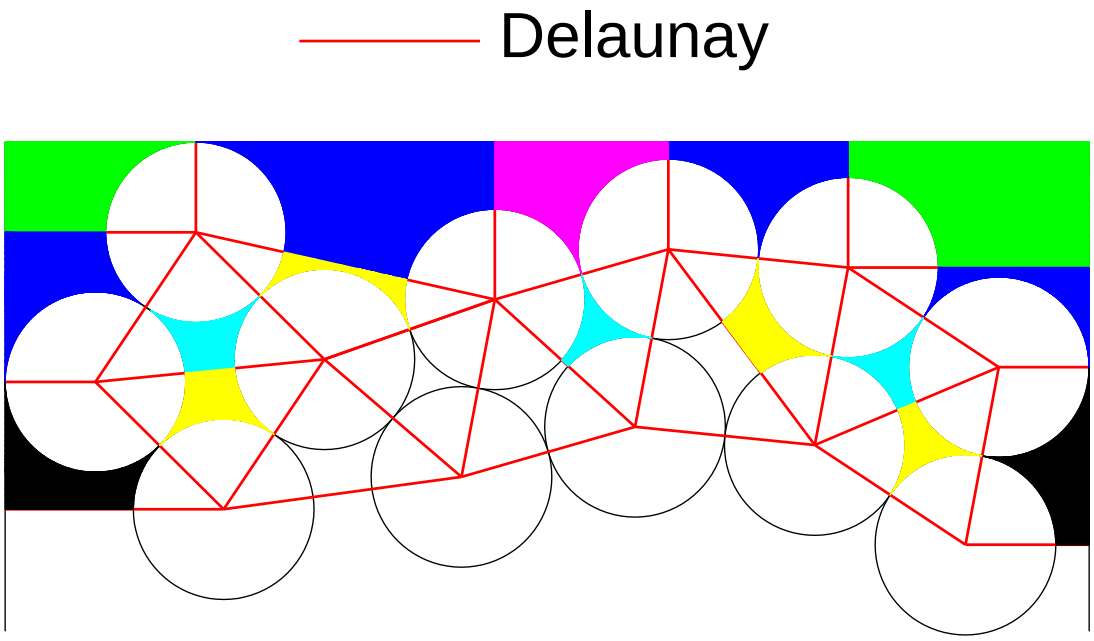

Figure A2.1. Illustration of the Delaunay cells at the boundary in a 2D domain. The boundary Delaunay cells bounded by one boundary have their void area shown in blue, black and pink while the ones bounded by two boundaries are in green. The triangular Delaunay cells adjacent to these boundary cells have their void areas shown in yellow and cyan.

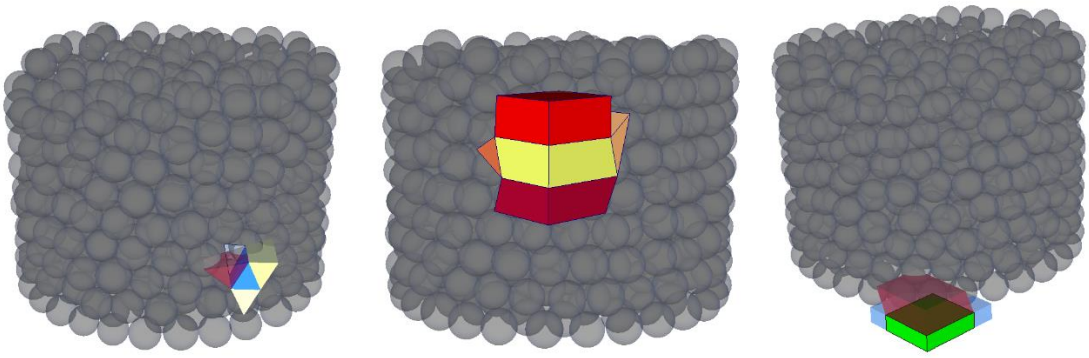

(a) (b) (c)

Figure A2.2. Illustration of the Delaunay cells at the boundary in a 3D domain: (a) Triangular cuboid (the one in blue, 5 faces), bounded by one boundary; (b) Cuboid (the one in yellow, 6 faces), bounded by two boundaries; (c) Cuboid (the one in green, 6 faces), bounded by three boundaries.

A3. Bidisperse aggregates

The solid phases of Bi 860 and Bi 1047 aggregates have been illustrated in Fig. 4.16, while the illustrations of all other generated bidisperse aggregates are presented in Fig. A3.1. The aggregates are labeled as Bi X, where X is the total number of particles in each bidisperse aggregate.

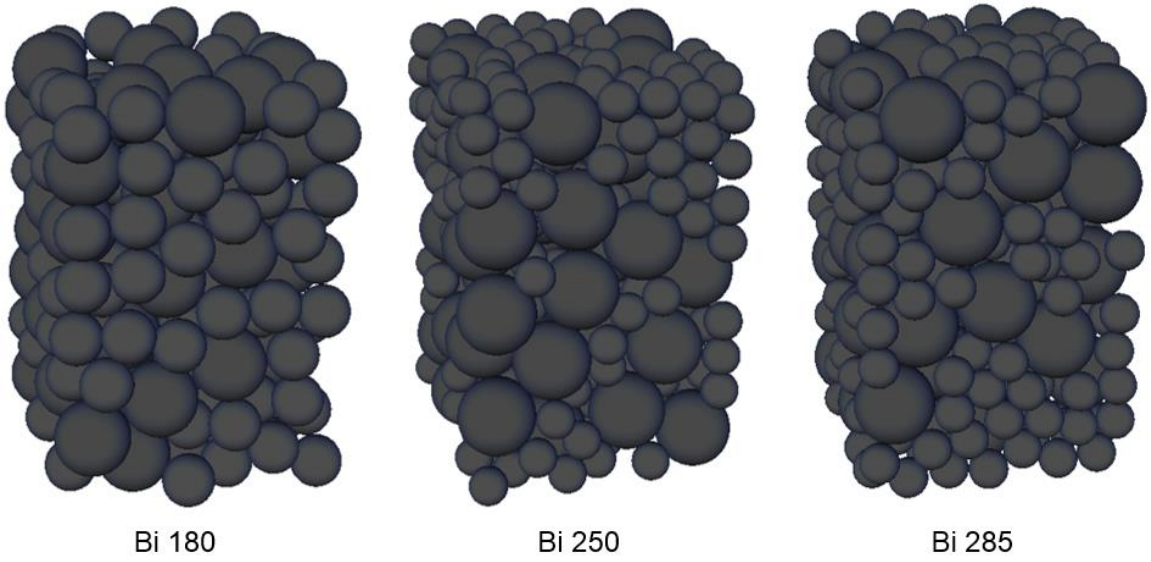

Figure A3.1, continued.

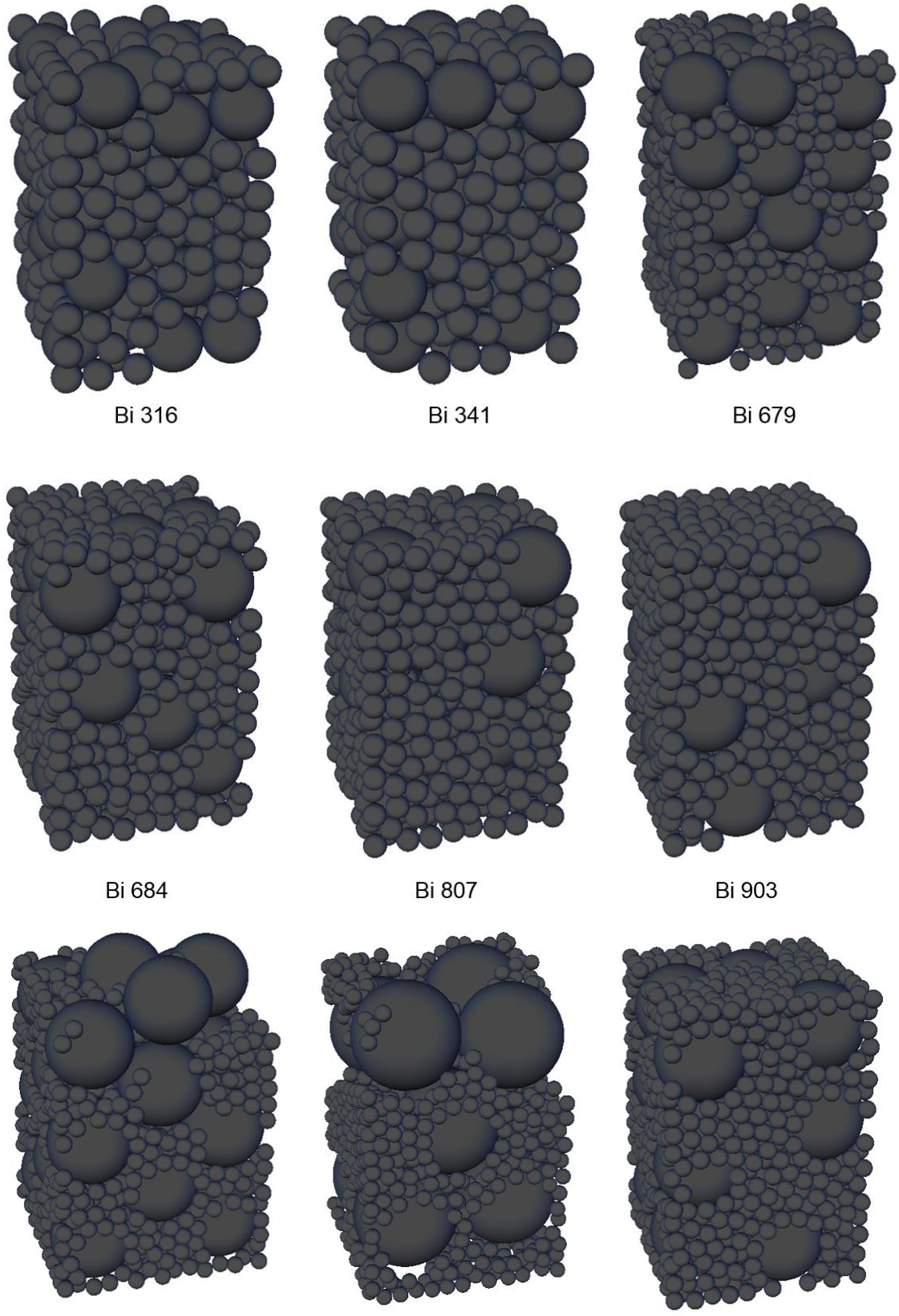

Figure A3.1, continued.

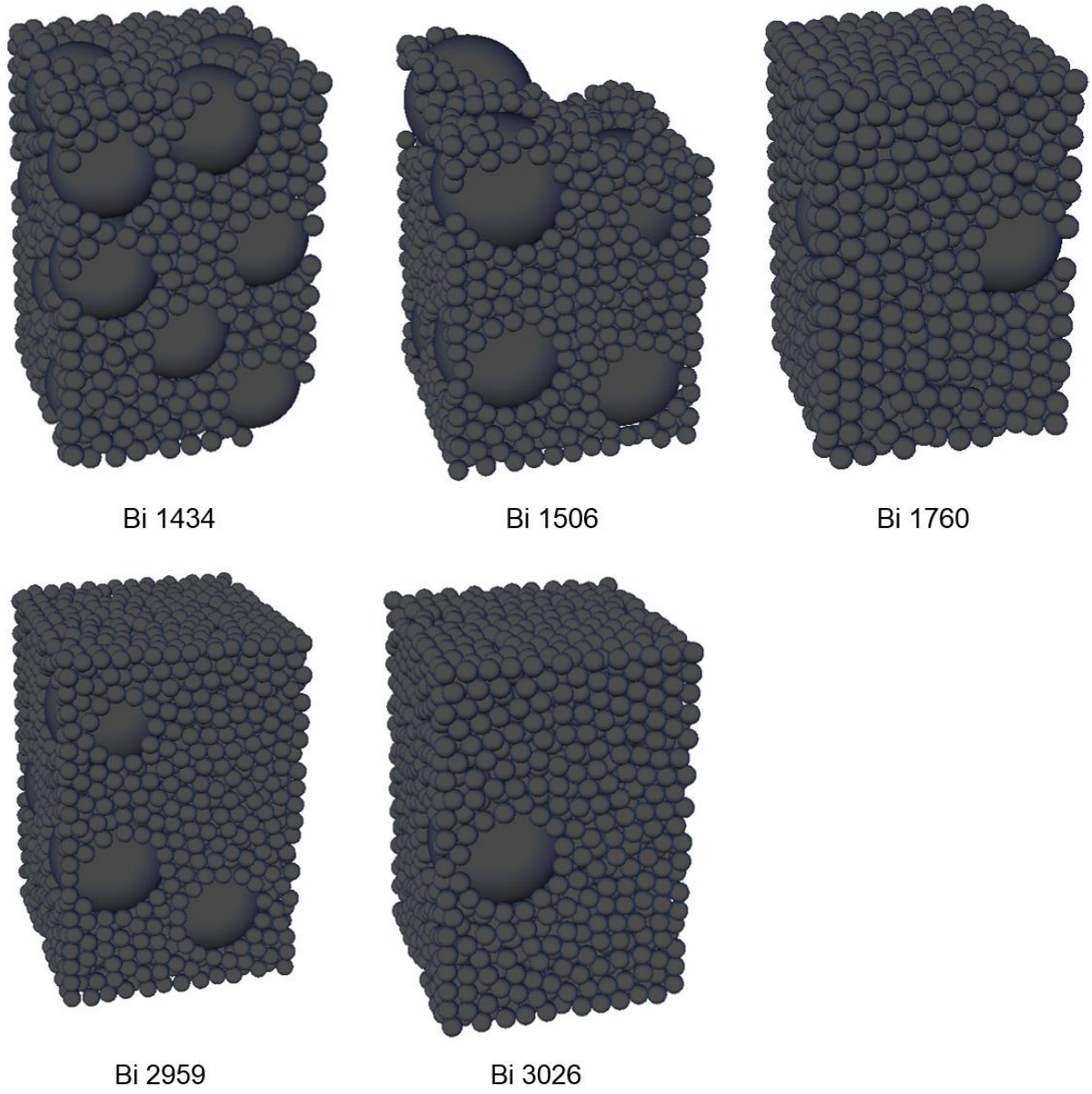

Figure A3.1. Illustration of the solid phase of bidisperse aggregates mentioned in chapter 4.

A4. Visualization of capillary force and liquid phase distribution

Referring to Chapter 5, this appendix illustrates the evolution of liquid phase distribution as well as the capillary forces been exerted on solid particles for the case of the aggregates Mono 1600, Poly 1449 and Poly 1164.

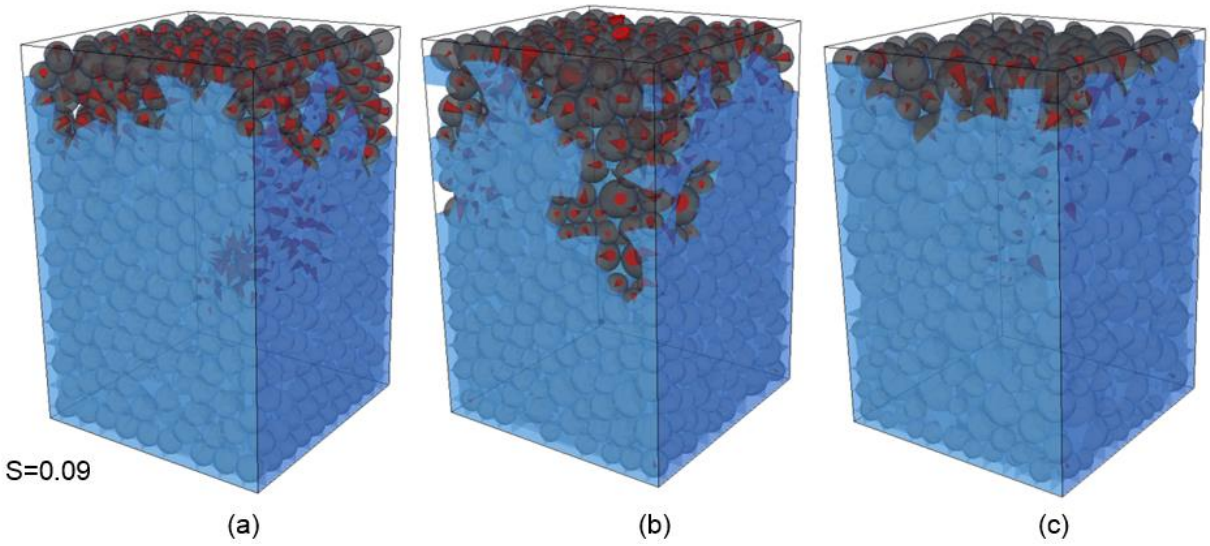

Figure A4.1, continued.

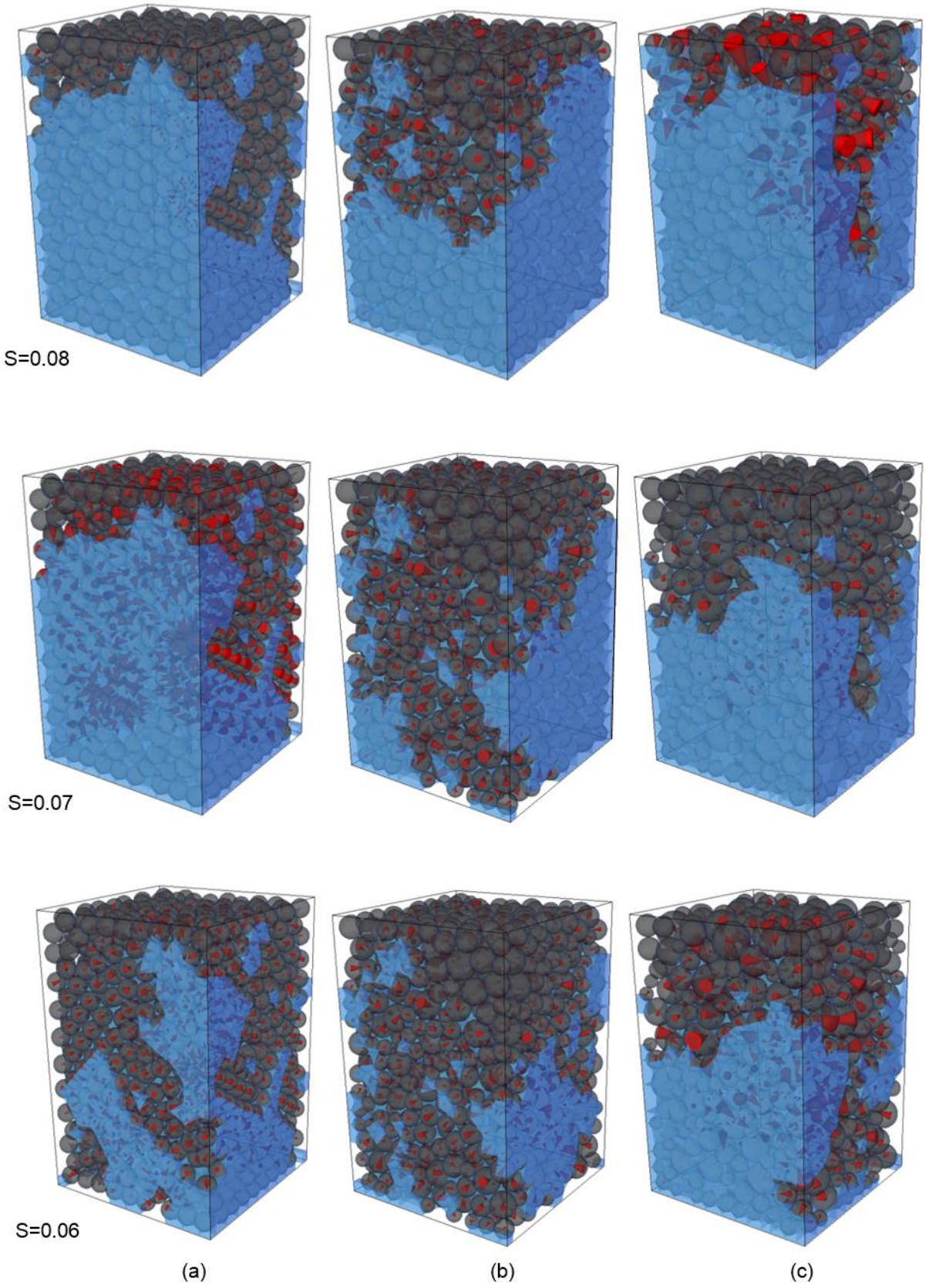

Figure A4.1, continued.

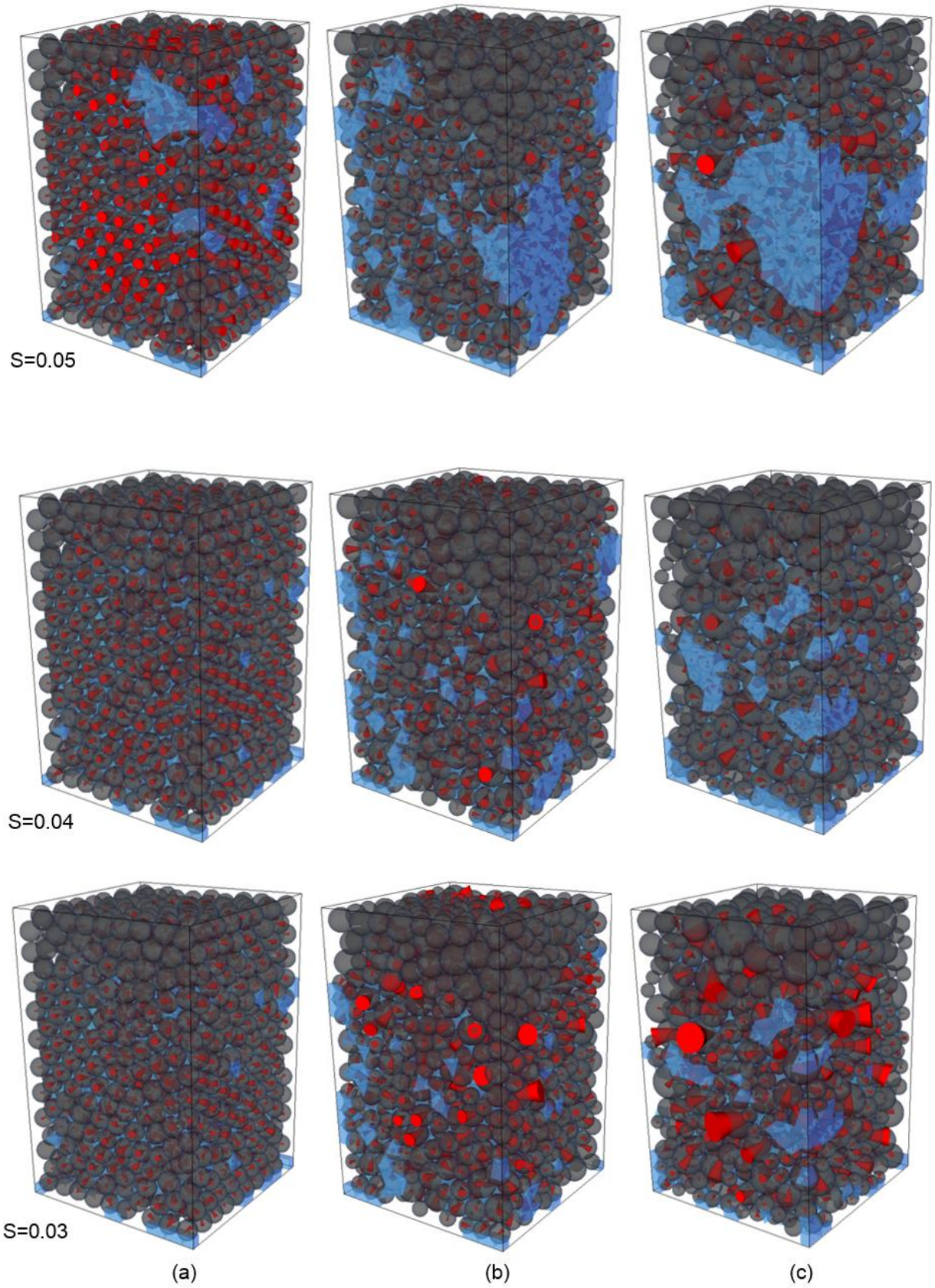

Figure A4.1, continued.

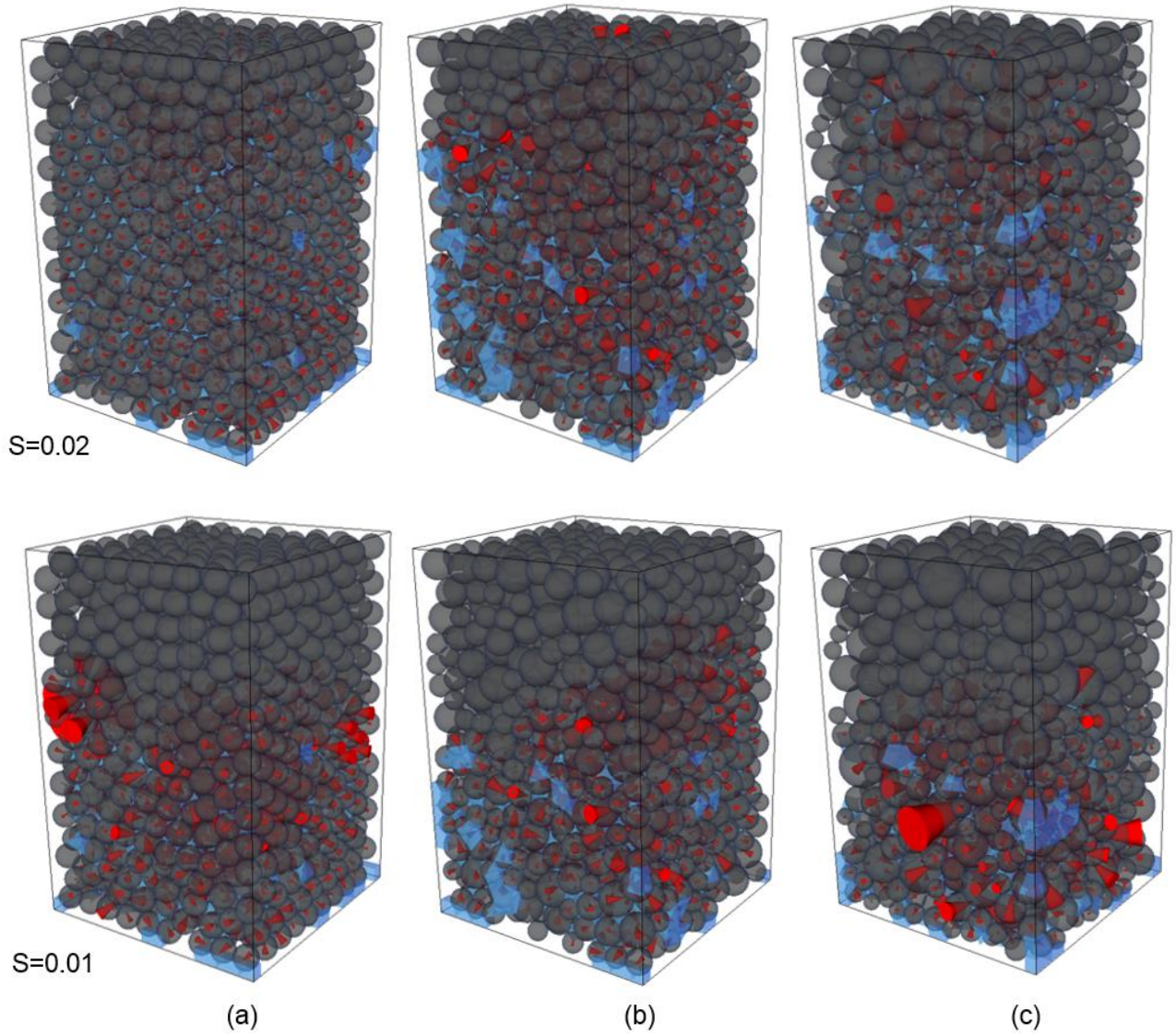

Figure A4.1. Evolution of capillary forces during drying of three different aggregates at different network saturations S: Column (a) Mono 1600, column (b) Poly 1449 and column (c) Poly 1164. Capillary forces are represented by red cones where the cone size scales with the force magnitude. Cells filled with liquid are shown in blue and are hidden after having been occupied by gas. Transparent grey spheres represent the solid phase of the respective aggregates.

Bibliography

1. Lekhal, A.; Glasser, B.J.; Khinast, J.G. Impact of drying on the catalyst profile in supported impregnation catalysts. Chemical Engineering Science 2001, 56(15), 4473–4487, DOI: 10.1016/S0009-2509(01)00120-8.
2. Liu, X.; Khinast, J.G.; Glasser, B.J. A parametric investigation of impregnation and drying of supported catalysts. Chemical Engineering Science 2008, 63(18), 4517–4530, DOI: 10.1016/j.ces.2008.06.013.
3. Börnhorst, M.; Walzel, P.; Rahimi, A.; Kharaghani, A.; Tsotsas, E.; Nestle, N.; Besser, A.; Kleine Jäger, F.; Metzger, T. Influence of pore structure and impregnation–drying conditions on the solid distribution in porous support materials. Drying Technology 2016, 34(16), 1964–1978, DOI: 10.1080/07373937.2016.1147048.
4. Guzlena, S.; Sakale, G.; Certoks, S.; Grase, L. Sand size particle amount influence on the full brick quality and technical properties. Construction and Building Materials 2019, 220, 102–109, DOI: 10.1016/j.conbuildmat.2019.05.170.
5. Duran, J.; Luding, S.; Clément, E.; Rajchenbach, J. Decompaction, fragmentation and self organization of granular materials. Journal of Molecular Liquids 1998, 76(3), 221–235, DOI: 10.1016/S0167-7322(98)80004-4.
6. Ceylan, K.; Kelbalıyev, G. Stochastical modeling of the granule size distribution in the agglomeration processes of powdered materials. Powder Technology 2001, 119(2-3), 173–180, DOI: 10.1016/S0032-5910(00)00415-0.
7. Wang, J.-P.; François, B.; Lambert, P. Equations for hydraulic conductivity estimation from particle size distribution: A dimensional analysis. Water Resources Research 2017, 53(9), 8127–8134, DOI: 10.1002/2017WR020888.
8. Wang, J.-P.; Hu, N.; François, B.; Lambert, P. Estimating water retention curves and strength properties of unsaturated sandy soils from basic soil gradation parameters. Water Resources Research 2017, 53(7), 6069–6088, DOI: 10.1002/2017WR020411.

9. Larrard, F. de; Sedran, T. Mixture-proportioning of high-performance concrete. Cement and Concrete Research 2002, 32(11), 1699–1704, DOI: 10.1016/S0008-8846(02)00861-X.
10. Assouline, S.; Rouault, Y. Modeling the relationships between particle and pore size distributions in multicomponent sphere packs: Application to the water retention curve. Colloids and Surfaces A: Physicochemical and Engineering Aspects 1997, 127(1-3), 201–210, DOI: 10.1016/S0927-7757(97)00144-1.
11. Luckham, P.F.; Ukeje, M.A. Effect of particle size distribution on the rheology of dispersed systems. Journal of Colloid and Interface Science 1999, 220(2), 347–356, DOI: 10.1006/jcis.1999.6515.
12. Semmler, M.; Rička, J.; Borkovec, M. Diffusional deposition of colloidal particles: Electrostatic interaction and size polydispersity effects. Colloids and Surfaces A: Physicochemical and Engineering Aspects 2000, 165(1-3), 79–93, DOI: 10.1016/S0927-7757(99)00438-0.
13. Leon, A. de; Pizio, O.; Sokołowski, S. Chemical potential of a hard sphere fluid adsorbed in model disordered polydisperse matrices. Journal of Colloid and Interface Science 2006, 298(1), 306–312, DOI: 10.1016/j.jcis.2005.11.056.
14. Xiong, Q.; Baychev, T.G.; Jivkov, A.P. Review of pore network modelling of porous media: Experimental characterisations, network constructions and applications to reactive transport. Journal of Contaminant Hydrology 2016, 192, 101–117, DOI: 10.1016/j.jconhyd.2016.07.002.
15. Blunt, M.J.; Bijeljic, B.; Dong, H.; Gharbi, O.; Iglauer, S.; Mostaghimi, P.; Paluszny, A.; Pentland, C. Pore-scale imaging and modelling. Advances in Water Resources 2013, 51, 197–216, DOI: 10.1016/j.advwatres.2012.03.003.
16. Blunt, M.J.; Jackson, M.D.; Piri, M.; Valvatne, P.H. Detailed physics, predictive capabilities and macroscopic consequences for pore-network models of multiphase flow. Advances in Water Resources 2002, 25(8-12), 1069–1089, DOI: 10.1016/S0309-1708(02)00049-0.
17. Metzger, T.; Tsotsas, E. Influence of pore size distribution on drying kinetics: A simple capillary model. Drying Technology 2005, 23(9-11), 1797–1809, DOI: 10.1080/07373930500209830.

18. Prat, M. Percolation model of drying under isothermal conditions in porous media. International Journal of Multiphase Flow 1993, 19(4), 691–704, DOI: 10.1016/0301-9322(93)90096-D.
19. Schlünder, E.-U. Drying of porous material during the constant and the falling rate period: A critical review of existing hypotheses. Drying Technology 2004, 22(6), 1517–1532, DOI: 10.1081/DRT-120038738.
20. Prat, M. Recent advances in pore-scale models for drying of porous media. Chemical Engineering Journal 2002, 86(1-2), 153–164, DOI: 10.1016/S1385-8947(01)00283-2.
21. Metzger, T.; Irawan, A.; Tsotsas, E. Influence of pore structure on drying kinetics: A pore network study. AIChE Journal 2007, 53(12), 3029–3041, DOI: 10.1002/aic.11307.
22. Borgman, O.; Fantinel, P.; Lühder, W.; Goehring, L.; Holtzman, R. Impact of spatially correlated pore-scale heterogeneity on drying porous media. Water Resources Research 2017, 53(7), 5645–5658, DOI: 10.1002/2016WR020260.
23. Chen, C.; Duru, P.; Joseph, P.; Geoffroy, S.; Prat, M. Control of evaporation by geometry in capillary structures: From confined pillar arrays in a gap radial gradient to phyllotaxy-inspired geometry. Scientific Reports 2017, 7(1), 15110, DOI: 10.1038/s41598-017-14529-z.
24. Yiotis, A.G.; Salin, D.; Tajer, E.S.; Yortsos, Y.C. Drying in porous media with gravity-stabilized fronts: Experimental results. Physical Review E, Statistical, Nonlinear, and Soft Matter Physics 2012, 86(2 Pt 2), 26310, DOI: 10.1103/PhysRevE.86.026310.
25. Shokri, N.; Or, D. What determines drying rates at the onset of diffusion controlled stage-2 evaporation from porous media? Water Resources Research 2011, 47(9), DOI: 10.1029/2010WR010284.
26. Wang, Y.; Kharaghani, A.; Metzger, T.; Tsotsas, E. Pore network drying model for particle aggregates: Assessment by X-ray microtomography. Drying Technology 2012, 30(15), 1800–1809, DOI: 10.1080/07373937.2012.713422.
27. Hamaker, H.C. The London-van der Waals attraction between spherical particles. Physica 1937, 4(10), 1058–1072, DOI: 10.1016/S0031-8914(37)80203-7.
28. Aranson, I.S.; Blair, D.; Kalatsky, V.A.; Crabtree, G.W.; Kwok, W.; Vinokur, V.M.; Welp, U. Electrostatically driven granular media: Phase transitions and coarsening.

Physical Review Letters 2000, 84(15), 3306–3309, DOI: 10.1103/PhysRevLett .84.3306.

29. Fisher, R.A. On the capillary forces in an ideal soil: Correction of formulae given by W. B. Haines. The Journal of Agricultural Science 1926, 16(3), 492–505, DOI: 10.1017/S0021859600007838.
30. Zhu, H.P.; Zhou, Z.Y.; Yang, R.Y.; Yu, A.B. Discrete particle simulation of particulate systems: Theoretical developments. Chemical Engineering Science 2007, 62(13), 3378–3396, DOI: 10.1016/j.ces.2006.12.089.
31. Soulié, F.; Cherblanc, F.; El Youssoufi, M.S.; Saix, C. Influence of liquid bridges on the mechanical behaviour of polydisperse granular materials. International Journal for Numerical and Analytical Methods in Geomechanics 2006, 30(3), 213–228, DOI: 10.1002/nag.476.
32. Richefeu, V.; El Youssoufi, M.S.; Azéma, E.; Radjaï, F. Force transmission in dry and wet granular media. Powder Technology 2009, 190(1-2), 258–263, DOI: 10.1016/j.powtec.2008.04.069.
33. Scholtès, L.; Chareyre, B.; Nicot, F.; Darve, F. Micromechanics of granular materials with capillary effects. International Journal of Engineering Science 2009, 47(11-12), 1460–1471, DOI: 10.1016/j.ijengsci.2009.10.003.
34. Delenne, J.-Y.; Richefeu, V.; Radjaï, F. Liquid clustering and capillary pressure in granular media. Journal of Fluid Mechanics 2015, 762, DOI: 10.1017/jfm.2014.676.
35. Pouragha, M.; Wan, R.; Duriez, J.; Sultan, N.H. Statistical analysis of stress transmission in wet granular materials. International Journal for Numerical and Analytical Methods in Geomechanics 2018, 42(16), 1935–1956, DOI: 10.1002/nag .2814.
36. Richefeu, V.; El Youssoufi, M.S.E.; Radjaï, F. Shear strength properties of wet granular materials. Physical Review E, 2006, 73(5 Pt 1), 51304, DOI: 10.1103/ PhysRevE.73.051304#.
37. Voivret, C.; Radjaï, F.; Delenne, J.-Y.; El Youssoufi, M.S. Multiscale force networks in highly polydisperse granular media. Physical Review Letters 2009, 102(17), 178001, DOI: 10.1103/PhysRevLett.102.178001.
38. Mielniczuk, B.; Hueckel, T.; Youssoufi, M.S.E. Evaporation-induced evolution of the capillary force between two grains. Granular Matter 2014, 16(5), 815–828, DOI: 10.1007/s10035-014-0512-6.

39. Mielniczuk, B.; Hueckel, T.; El Youssoufi, M.S. Laplace pressure evolution and four instabilities in evaporating two-grain liquid bridges. Powder Technology 2015, 283, 137–151, DOI: 10.1016/j.powtec.2015.05.024.
40. Gao, C. Theory of menisci and its applications. Applied Physics Letters 1997, 71(13), 1801–1803, DOI: 10.1063/1.119403.
41. Maeda, N.; Israelachvili, J.N.; Kohonen, M.M. Evaporation and instabilities of microscopic capillary bridges. Proceedings of the National Academy of Sciences 2003, 100(3), 803–808, DOI: 10.1073/pnas.0234283100.
42. Cutts, R.E.; Burns, S.E. Evolution of surface area-to-volume ratio for a water meniscus evaporating between contacting silica spheres. Journal of Colloid and Interface Science 2010, 343(1), 298–300, DOI: 10.1016/j.jcis.2009.11.011.
43. Zhou, Z.; Li, Q.; Zhao, X.S. Evolution of interparticle capillary forces during drying of colloidal crystals. Langmuir 2006, 22(8), 3692–3697, DOI: 10.1021/la052934c.
44. Dufresne, E.R.; Stark, D.J.; Greenblatt, N.A.; Cheng, J.X.; Hutchinson, J.W.; Mahadevan, L.; Weitz, D.A. Dynamics of fracture in drying suspensions. Langmuir 2006, 22(17), 7144–7147, DOI: 10.1021/la061251+.
45. Dufresne, E.R.; Corwin, E.I.; Greenblatt, N.A.; Ashmore, J.; Wang, D.Y.; Dinsmore, A.D.; Cheng, J.X.; Xie, X.S.; Hutchinson, J.W.; Weitz, D.A. Flow and fracture in drying nanoparticle suspensions. Physical Review Letters 2003, 91(22), 224501, DOI: 10.1103/PhysRevLett.91.224501.
46. Xu, Y.; German, G.K.; Mertz, A.F.; Dufresne, E.R. Imaging stress and strain in the fracture of drying colloidal films. Soft Matter 2013, 9(14), 3735, DOI: 10.1039/C3SM27912J.
47. Man, W.; Russel, W.B. Direct measurements of critical stresses and cracking in thin films of colloid dispersions. Physical Review Letters 2008, 100(19), 198302, DOI: 10.1103/PhysRevLett.100.198302.
48. Mathews, N.; Lam, Y.M.; Mhaisalkar, S.G.; Grimsdale, A.C. Printing materials for electronic devices. International Journal of Materials Research 2010, 101(2), 236–250, DOI: 10.3139/146.110260.
49. Juillerat, F.; Bowen, P.; Hofmann, H. Formation and drying of colloidal crystals using nanosized silica particles. Langmuir 2006, 22(5), 2249–2257, DOI: 10.1021/la052304a.

50. Park, J.-H.; Cho, J.-H.; Park, W.; Ryoo, D.; Yoon, S.-J.; Kim, J.H.; Jeong, Y.U.; Lee, S.-Y. Close-packed SiO2/poly(methyl methacrylate) binary nanoparticles-coated polyethylene separators for lithium-ion batteries. Journal of Power Sources 2010, 195(24), 8306–8310, DOI: 10.1016/j.jpowsour.2010.06.112.
51. Bardosova, M.; Dillon, F.C.; Pemble, M.E.; Povey, I.M.; Tredgold, R.H. Langmuir-Blodgett assembly of colloidal photonic crystals using silica particles prepared without the use of surfactant molecules. Journal of Colloid and Interface Science 2009, 333(2), 816–819, DOI: 10.1016/j.jcis.2009.02.006.
52. Prevo, B.G.; Hon, E.W.; Velev, O.D. Assembly and characterization of colloid-based antireflective coatings on multicrystalline silicon solar cells. Journal of Materials Chemistry 2007, 17(8), 791–799, DOI: 10.1039/B612734G.
53. Özgür, C.; Şan, O. Fabrication of superhydrophilic membrane filters using spherical glass particles obtained by ultrasonic spray pyrolysis. Ceramics International 2011, 37(3), 965–970, DOI: 10.1016/j.ceramint.2010.11.007.
54. Colina, H.; Acker, P. Drying cracks: Kinematics and scale laws. Materials and Structures 2000, 33(2), 101–107, DOI: 10.1007/BF02484164.
55. Chiu, R.C.; Cima, M.J. Drying of granular ceramic films, Part 2: Drying stress and saturation uniformity. Journal of the American Ceramic Society 1993, 76(11), 2769–2777, DOI: 10.1111/j.1151-2916.1993.tb04014.x.
56. Weinberger, R. Initiation and growth of cracks during desiccation of stratified muddy sediments. Journal of Structural Geology 1999, 21(4), 379–386, DOI: 10.1016/S0191-8141(99)00029-2.
57. Colina, H.; Roux, S. Experimental model of cracking induced by drying shrinkage. The European Physical Journal E 2000, 1(2), 189, DOI: 10.1007/s101890050021.
58. Nairn, J.A.; Sung-Ryong, K. A fracture mechanics analysis of multiple cracking in coatings. Engineering Fracture Mechanics 1992, 42(1), 195–208, DOI: 10.1016/0013-7944(92)90291-L.
59. Scherer, G.W. Theory of drying. Journal of the American Ceramic Society 1990, 73(1), 3–14, DOI: 10.1111/j.1151-2916.1990.tb05082.x.
60. Chiu, R.C.; Garino, T.J.; Cima, M.J. Drying of granular ceramic films, Part 1: Effect of processing variables on cracking behavior. Journal of the American Ceramic Society 1993, 76(9), 2257–2264, DOI: 10.1111/j.1151-2916.1993.tb07762.x.

61. Schneider, M.; Maurath, J.; Fischer, S.B.; Weiß, M.; Willenbacher, N.; Koos, E. Suppressing crack formation in particulate systems by utilizing capillary forces. ACS Applied Materials & Interfaces 2017, 9(12), 11095–11105, DOI: 10.1021/acsami.6b13624.
62. Koos, E.; Willenbacher, N. Capillary forces in suspension rheology. Science 2011, 331(6019), 897–900, DOI: 10.1126/science.1199243.
63. Koos, E. Capillary suspensions: Particle networks formed through the capillary force. Current Opinion in Colloid & Interface Science 2014, 19(6), 575–584, DOI: 10.1016/j.cocis.2014.10.004.
64. Hoffmann, S.; Koos, E.; Willenbacher, N. Using capillary bridges to tune stability and flow behavior of food suspensions. Food Hydrocolloids 2014, 40, 44–52, DOI: 10.1016/j.foodhyd.2014.01.027.
65. Wollgarten, S.; Yuce, C.; Koos, E.; Willenbacher, N. Tailoring flow behavior and texture of water based cocoa suspensions. Food Hydrocolloids 2015, 52, 167–174, DOI: 10.1016/j.foodhyd.2015.06.010.
66. Bitsch, B.; Dittmann, J.; Schmitt, M.; Scharfer, P.; Schabel, W.; Willenbacher, N. A novel slurry concept for the fabrication of lithium-ion battery electrodes with beneficial properties. Journal of Power Sources 2014, 265, 81–90, DOI: 10.1016/j.jpowsour.2014.04.115.
67. Schneider, M.; Koos, E.; Willenbacher, N. Highly conductive, printable pastes from capillary suspensions. Scientific Reports 2016, 6, 31367, DOI: 10.1038/srep31367.
68. Zhang, Y.; Allen, M.C.; Zhao, R.; Deheyn, D.D.; Behrens, S.H.; Meredith, J.C. Capillary foams: Stabilization and functionalization of porous liquids and solids. Langmuir 2015, 31(9), 2669–2676, DOI: 10.1021/la504784h.
69. Dittmann, J.; Koos, E.; Willenbacher, N. Ceramic capillary suspensions: Novel processing route for macroporous ceramic materials. Journal of the American Ceramic Society 2012, 96(2), 391-397, DOI: 10.1111/jace.12126.
70. Boulogne, F.; Kong, Y.L.; Nunes, J.K.; Stone, H.A. Effect of the polydispersity of a colloidal drop on drying induced stress as measured by the buckling of a floating sheet. Physical Review Letters 2016, 116(23), DOI: 10.1103/PhysRevLett.116 .238001.

71. Kharaghani, A.; Metzger, T.; Tsotsas, E. A proposal for discrete modeling of mechanical effects during drying, combining pore networks with DEM. AIChE Journal 2011, 57(4), 872–885, DOI: 10.1002/aic.12318.
72. Kharaghani, A.; Metzger, T.; Tsotsas, E. An irregular pore network model for convective drying and resulting damage of particle aggregates. Chemical Engineering Science 2012, 75, 267–278, DOI: 10.1016/j.ces.2012.03.038.
73. Voronoi, G. Nouvelles applications des paramètres continus à la théorie des formes quadratiques, Premier mémoire: Sur quelques propriétés des formes quadratiques positives parfaites. Journal für die reine und angewandte Mathematik (Crelles Journal) 1908, 1908(133), 97–102, DOI: 10.1515/crll.1908.133.97.
74. Edelsbrunner, H.; Shah, N.R. Incremental topological flipping works for regular triangulations. Algorithmica 1996, 15(3), 223–241, DOI: 10.1007/BF01975867.
75. Chareyre, B.; Cortis, A.; Catalano, E.; Barthélemy, E. Pore-scale modeling of viscous flow and induced forces in dense sphere packings. Transport in Porous Media 2012, 92(2), 473–493, DOI: 10.1007/s11242-011-9915-6.
76. Catalano, E.; Chareyre, B.; Barthélémy, E. Pore-scale modeling of fluid-particles interaction and emerging poromechanical effects. International Journal for Numerical and Analytical Methods in Geomechanics 2014, 38(1), 51–71, DOI: 10.1002/nag.2198.
77. Yuan, C.; Chareyre, B.; Darve, F. Pore-scale simulations of drainage in granular materials: Finite size effects and the representative elementary volume. Advances in Water Resources 2016, 95, 109–124, DOI: 10.1016/j.advwatres.2015.11.018.
78. Sweijen, T.; Chareyre, B.; Hassanizadeh, S.M.; Karadimitriou, N.K. Grain-scale modelling of swelling granular materials: Application to super absorbent polymers. Powder Technology 2017, 318, 411–422, DOI: 10.1016/j.powtec.2017.06.015.
79. Raoof, A.; Hassanizadeh, S.M. Upscaling transport of adsorbing solutes in porous media. Journal of Porous Media 2010, 13(5), 395–408, DOI: 10.1615/JPorMedia .v13.i5.10.
80. Fatt, I. The network model of porous media. Transactions of the AIME 1956, 207(01), 144–181, DOI: 10.2118/574-G.
81. Balhoff, M.T.; Wheeler, M.F. A predictive pore-scale model for non-Darcy flow in porous media. SPE Journal 2009, 14(04), 579–587, DOI: 10.2118/110838-PA.

82. Lopez, X.; Valvatne, P.H.; Blunt, M.J. Predictive network modeling of single-phase non-Newtonian flow in porous media. Journal of Colloid and Interface Science 2003, 264(1), 256–265, DOI: 10.1016/S0021-9797(03)00310-2.
83. Ryazanov, A.V.; van Dijke, M.I.J.; Sorbie, K.S. Two-phase pore-network modelling: Existence of oil layers during water invasion. Transport in Porous Media 2009, 80(1), 79–99, DOI: 10.1007/s11242-009-9345-x.
84. Yiotis, A.G.; Tsimpanogiannis, I.N.; Stubos, A.K.; Yortsos, Y.C. Pore-network study of the characteristic periods in the drying of porous materials. Journal of Colloid and Interface Science 2006, 297(2), 738–748, DOI: 10.1016/j.jcis.2005.11.043.
85. Slichter, C.S. Theoretical investigation of the motion of ground waters. U.S. Geological Survey, 19th Annual Report 2 1899, 295–384.
86. Graton, L.C.; Fraser, H.J. Systematic packing of spheres: With particular relation to porosity and permeability. The Journal of Geology 1935, 43(8, Part 1), 785–909, DOI: 10.1086/624386.
87. Hackett, F.E.; Strettan, J.S. The capillary pull of an ideal soil. The Journal of Agricultural Science 1928, 18(4), 671–681, DOI: 10.1017/S0021859600009242.
88. Haines, W.B. Studies in the physical properties of soil, Part 5: The hysteresis effect in capillary properties, and the modes of moisture distribution associated therewith. The Journal of Agricultural Science 1930, 20(1), 97–116, DOI: 10.1017/S002185960008864X.
89. Haines, W.B. Studies in the physical properties of soils, Part 2: A note on the cohesion developed by capillary forces in an ideal soil. The Journal of Agricultural Science 1925, 15(4), 529–535, DOI: 10.1017/S0021859600082460.
90. Haines, W.B. Studies in the physical properties of soils, Part 4: A further contribution to the theory of capillary phenomena in soil. The Journal of Agricultural Science 1927, 17(2), 264–290, DOI: 10.1017/S0021859600018499.
91. Smith, W.O. Capillary flow through an ideal uniform soil. Physics 1932, 3(3), 139–146, DOI: 10.1063/1.1745090.
92. Smith, W.O. The final distribution of retained liquid in an ideal uniform soil. Physics 1933, 4(12), 425–438, DOI: 10.1063/1.1745156.
93. Smith, W.O. Minimum capillary rise in an ideal uniform soil. Physics 1933, 4(5), 184–193, DOI: 10.1063/1.1745177.

94. Bernal, J.D.; Cherry, I.A.; Finney, J.L.; Knight, K.R. An optical machine for measuring sphere coordinates in random packings. Journal of Physics E: Scientific Instruments 1970, 3(5), 388–390, DOI: 10.1088/0022-3735/3/5/312
95. Finney, J.L. Random packings and the structure of simple liquids, Part 1: The geometry of random close packing. Proceedings of the Royal Society of London, A: Mathematical and Physical Sciences 1970, 319(1539), 479–493, DOI: 10.1098/rspa.1970.0189.
96. Mason, G. A model of the pore space in a random packing of equal spheres. Journal of Colloid and Interface Science 1971, 35(2), 279–287, DOI: 10.1016/0021-9797(71)90121-4.
97. Beard, D. C.; Weyl, P.K. Influence of texture on porosity and permeability of unconsolidated sand. AAPG Bulletin 1973, 57, DOI: 10.1306/819A4272-16C5-11D7-8645000102C1865D.
98. Bryant, S.L.; King, P.R.; Mellor, D.W. Network model evaluation of permeability and spatial correlation in a real random sphere packing. Transport in Porous Media 1993, 11(1), 53–70, DOI: 10.1007/BF00614635.
99. Bryant, S.L.; King, P.R.; Mellor, D.W. Quantification of spatial correlation in porous media and its effect on mercury porosimetry. Journal of Colloid and Interface Science 1996, 177(1), 88–100, DOI: 10.1006/jcis.1996.0009.
100. Bryant, S.L.; Mellor, D.W.; Cade, C.A. Physically representative network models of transport in porous media. AIChE Journal 1993, 39(3), 387–396, DOI: 10.1002/aic.690390303.
101. Mason, G.; Mellor, D.W. Simulation of drainage and imbibition in a random packing of equal spheres. Journal of Colloid and Interface Science 1995, 176(1), 214–225, DOI: 10.1006/jcis.1995.0024.
102. Bryant, S.; Johnson, A. Wetting phase connectivity and irreducible saturation in simple granular media. Journal of Colloid and Interface Science 2003, 263(2), 572–579, DOI: 10.1016/S0021-9797(03)00371-0.
103. Thompson, K.E.; Fogler, H.S. Modeling flow in disordered packed beds from pore-scale fluid mechanics. AIChE Journal 1997, 43(6), 1377–1389, DOI: 10.1002/aic.690430602.

104. Al-Raoush, R.; Thompson, K.; Willson, C.S. Comparison of network generation techniques for unconsolidated porous media. Soil Science Society of America Journal 2003, 67(6), 1687–1700, DOI: 10.2136/sssaj2003.1687.

105. Hilpert, M.; Glantz, R.; Miller, C.T. Calibration of a pore-network model by a pore-morphological analysis. Transport in Porous Media 2003, 51(3), 267–285, DOI: 10.1023/A:1022384431481.

106. Mellor, D.W. Random close packing (RCP) of equal spheres: Structure and implications for use as a model porous medium, PhD thesis The Open University 1989, DOI: 10.21954/ou.ro.0000dfc0.

107. Gladkikh, M.; Bryant, S. Prediction of imbibition in unconsolidated granular materials. Journal of Colloid and Interface Science 2005, 288(2), 526–539, DOI: 10.1016/j.jcis.2005.03.029.

108. Bryant, S.L.; Johnson, A.S. Theoretical evaluation of the interfacial area between two fluids in a model soil. In: Chemicals in the Environment; Lipnick, R.L., Mason, R.P., Phillips, M.L., Pittman, C.U., Eds.; American Chemical Society: Washington, DC, 2002; 26–41.

109. Bhattad, P.; Willson, C.S.; Thompson, K.E. Effect of network structure on characterization and flow modeling using X-ray micro-tomography images of granular and fibrous porous media. Transport in Porous Media 2011, 90(2), 363–391, DOI: 10.1007/s11242-011-9789-7.

110. Hall, C.; Hoff, W.D. Water Transport in Brick, Stone and Concrete; CRC Press, 2011.

111. Coussot, P. Scaling approach of the convective drying of a porous medium. The European Physical Journal B 2000, 15(3), 557–566, DOI: 10.1007/s100510051160.

112. Faure, P.; Coussot, P. Drying of a model soil. Physical Review E, Statistical, Nonlinear, and Soft Matter Physics 2010, 82(3), 36303, DOI: 10.1103/PhysRevE.82.036303.

113. Lehmann, P.; Assouline, S.; Or, D. Characteristic lengths affecting evaporative drying of porous media. Physical Review E, Statistical, Nonlinear, and Soft Matter Physics 2008, 77(5), 56309, DOI: 10.1103/PhysRevE.77.056309.

114. Or, D.; Lehmann, P.; Shahraeeni, E.; Shokri, N. Advances in soil evaporation physics: A review. Vadose Zone Journal 2013, 12(4), vzj2012.0163, DOI: 10.2136/vzj2012.0163.

115. Yiotis, A.G.; Stubos, A.K.; Boudouvis, A.G.; Tsimpanogiannis, I.N.; Yortsos, Y.C. Pore-network modeling of isothermal drying in porous media. Transport in Porous Media 2005, 58(1-2), 63–86, DOI: 10.1007/s11242-004-5470-8.

116. Shokri, N.; Lehmann, P.; Or, D. Characteristics of evaporation from partially wettable porous media. Water Resources Research 2009, 45(2), DOI: 10.1029/2008WR007185.

117. Belhamri, A. Characterization of the first falling rate period during drying of a porous material. Drying Technology 2003, 21(7), 1235–1252, DOI: 10.1081/DRT-120023178.

118. Cejas, C.M.; Castaing, J.-C.; Hough, L.; Frétigny, C.; Dreyfus, R. Experimental investigation of water distribution in a two-phase zone during gravity-dominated evaporation. Physical Review. E 2017, 96(6-1), 62908, DOI: 10.1103/PhysRevE.96.062908

119. Shahidzadeh-Bonn, N.; Azouni, A.; Coussot, P. Effect of wetting properties on the kinetics of drying of porous media. Journal of Physics: Condensed Matter 2007, 19(11), 112101, DOI: 10.1088/0953-8984/19/11/112101.

120. Kohout, M.; Grof, Z.; Stepánek, F. Pore-scale modelling and tomographic visualisation of drying in granular media. Journal of Colloid and Interface Science 2006, 299(1), 342–351, DOI: 10.1016/j.jcis.2006.01.074.

121. Shokri, N.; Lehmann, P.; Or, D. Liquid-phase continuity and solute concentration dynamics during evaporation from porous media: pore-scale processes near vaporization surface. Physical Review E 2010, 81(4 Pt 2), 46308, DOI: 10.1103/PhysRevE.81.046308.

122. Yang, F.; Griffa, M.; Bonnin, A.; Mokso, R.; Di Bella, C.; Münch, B.; Kaufmann, R.; Lura, P. Visualization of water drying in porous materials by X-ray phase contrast imaging. Journal of Microscopy 2015, 261(1), 88–104, DOI: 10.1111/jmi.12319.

123. Shokri, N.; Lehmann, P.; Vontobel, P.; Or, D. Drying front and water content dynamics during evaporation from sand delineated by neutron radiography. Water Resources Research 2008, 44(6), DOI: 10.1029/2007WR006385.

124. Prat, M. On the influence of pore shape, contact angle and film flows on drying of capillary porous media. International Journal of Heat and Mass Transfer 2007, 50(7-8), 1455–1468, DOI: 10.1016/j.ijheatmasstransfer.2006.09.001.

125. Dong, M.; Chatzis, I. The imbibition and flow of a wetting liquid along the corners of a square capillary tube. Journal of Colloid and Interface Science 1995, 172(2), 278–288, DOI: 10.1006/jcis.1995.1253.

126. Chauvet, F.; Duru, P.; Geoffroy, S.; Prat, M. Three periods of drying of a single square capillary tube. Physical Review Letters 2009, 103(12), 124502, DOI: 10.1103/PhysRevLett .103.124502.

127. Chauvet, F.; Cazin, S.; Duru, P.; Prat, M. Use of infrared thermography for the study of evaporation in a square capillary tube. International Journal of Heat and Mass Transfer 2010, 53(9-10), 1808–1818, DOI: 10.1016/j.ijheatmasstransfer. 2010.01.008.

128. Chen, C.; Joseph, P.; Geoffroy, S.; Prat, M.; Duru, P. Evaporation with the formation of chains of liquid bridges. Journal of Fluid Mechanics 2018, 837, 703–728, DOI: 10.1017/jfm.2017.827.

129. Herminghaus, S. Dynamics of wet granular matter. Advances in Physics 2005, 54(3), 221–261, DOI: 10.1080/00018730500167855.

130. Rieser, J.M.; Arratia, P.E.; Yodh, A.G.; Gollub, J.P.; Durian, D.J. Tunable capillary-induced attraction between vertical cylinders. Langmuir 2015, 31(8), 2421–2429, DOI: 10.1021/la5046139.

131. Cejas, C.M.; Hough, L.A.; Frétigny, C.; Dreyfus, R. Effect of geometry on the dewetting of granular chains by evaporation. Soft Matter 2018, 14(34), 6994–7002, DOI: 10.1039/C8SM01179F.

132. Xu, L.; Davies, S.; Schofield, A.B.; Weitz, D.A. Dynamics of drying in 3D porous media. Physical Review Letters 2008, 101(9), 94502, DOI: 10.1103/PhysRevLett. 101.094502.

133. Brocken, H.J.P.; Spiekman, M.E.; Pel, L.; Kopinga, K.; Larbi, J.A. Water extraction out of mortar during brick laying: A NMR study. Materials and Structures 1998, 31(1), 49–57, DOI: 10.1007/BF02486414.

134. Coussot, P.; Gauthier, C.; Nadji, D.; Borgotti, J.-C.; Vié, P.; Bertrand, F. Mouvements capillaires durant le séchage d'une pâte granulaire. Comptes Rendus

de l'Académie des Sciences, Series IIB: Mechanics-Physics-Astronomy 1999, 327(10), 1101–1106, DOI: 10.1016/S1287-4620(00)87024-6.

135. Ben Abdelouahab, N.; Gossard, A.; Rodts, S.; Coasne, B.; Coussot, P. Convective drying of a porous medium with a paste cover. The European Physical Journal E, Soft Matter 2019, 42(5), 66, DOI: 10.1140/epje/i2019-11829-4.

136. Pierrat, P.; Caram, H.S. Tensile strength of wet granula materials. Powder Technology 1997, 91(2), 83–93, DOI: 10.1016/S0032-5910(96)03179-8.

137. Rondeau, X.; Affolter, C.; Komunjer, L.; Clausse, D.; Guigon, P. Experimental determination of capillary forces by crushing strength measurements. Powder Technology 2003, 130(1-3), 124–131, DOI: 10.1016/S0032-5910(02)00255-3.

138. Chen, J.; Williams, K.; Chen, W.; Shen, J.; Ye, F. A review of moisture migration in bulk material. Particulate Science and Technology 2020, 38(2), 247–260, DOI: 10.1080/02726351.2018.1504152.

139. Scheel, M.; Seemann, R.; Brinkmann, M.; Di Michiel, M.; Sheppard, A.; Herminghaus, S. Liquid distribution and cohesion in wet granular assemblies beyond the capillary bridge regime. Journal of Physics: Condensed Matter 2008, 20(49), 494236, DOI: 10.1088/0953-8984/20/49/494236.

140. Mason, G.; Clark, W.C. Liquid bridges between spheres. Chemical Engineering Science 1965, 20(10), 859–866, DOI: 10.1016/0009-2509(65)80082-3.

141. Hotta, K.; Takeda, K.; Iinoya, K. The capillary binding force of a liquid bridge. Powder Technology 1974, 10(4-5), 231–242, DOI: 10.1016/0032-5910(74)85047-3.

142. Lian, G.; Thornton, C.; Adams, M.J. A Theoretical study of the liquid bridge forces between two rigid spherical bodies. Journal of Colloid and Interface Science 1993, 161(1), 138–147, DOI: 10.1006/jcis.1993.1452.

143. Willett, C.D.; Adams, M.J.; Johnson, S.A.; Seville, J.P.K. Capillary bridges between two spherical bodies. Langmuir 2000, 16(24), 9396–9405, DOI: 10.1021/la000657y.

144. Lambert, P.; Chau, A.; Delchambre, A.; Régnier, S. Comparison between two capillary forces models. Langmuir 2008, 24(7), 3157–3163, DOI: 10.1021/la7036444.

145. Rabinovich, Y.I.; Esayanur, M.S.; Moudgil, B.M. Capillary forces between two spheres with a fixed volume liquid bridge: Theory and experiment. Langmuir 2005, 21(24), 10992–10997, DOI: 10.1021/la0517639.

146. Harireche, O.; Faramarzi, A.; Alani, A.M. A toroidal approximation of capillary forces in polydisperse granular assemblies. Granular Matter 2013, 15(5), 573–581, DOI: 10.1007/s10035-013-0425-9.

147. Scholtès, L.; Hicher, P.-Y.; Nicot, F.; Chareyre, B.; Darve, F. On the capillary stress tensor in wet granular materials. International Journal for Numerical and Analytical Methods in Geomechanics 2009, 33(10), 1289–1313, DOI: 10.1002/ nag.767.

148. Gras, J.-P.; Delenne, J.-Y.; El Youssoufi, M.S. Study of capillary interaction between two grains: a new experimental device with suction control. Granular Matter 2013, 15(1), 49–56, DOI: 10.1007/s10035-012-0388-2.

149. Gillespie, T.; Settineri, W.J. The effect of capillary liquid on the force of adhesion between spherical solid particles. Journal of Colloid and Interface Science 1967, 24(2), 199–202, DOI: 10.1016/0021-9797(67)90220-2.

150. Orr, F.M.; Scriven, L.E.; Rivas, A.P. Pendular rings between solids: Meniscus properties and capillary force. Journal of Fluid Mechanics 1975, 67(4), 723–742, DOI: 10.1017/S0022112075000572.

151. Dörmann, M.; Schmid, H.-J. Simulation of capillary bridges between nanoscale particles. Langmuir 2014, 30(4), 1055–1062, DOI: 10.1021/la404409k.

152. Mikami, T.; Kamiya, H.; Horio, M. Numerical simulation of cohesive powder behavior in a fluidized bed. Chemical Engineering Science 1998, 53(10), 1927–1940, DOI: 10.1016/S0009-2509(97)00325-4.

153. Mehrotra, V.P.; Sastry, K.V.S. Pendular bond strength between unequal-sized spherical particles. Powder Technology 1980, 25(2), 203–214, DOI: 10.1016/0032-5910(80)87031-8.

154. Israelachvili, J.N. Intermolecular and Surface Forces, 2nd ed; Academic Press: London and San Diego, 1991.

155. McFarlane, J.S.; Tabor, D. Relation between friction and adhesion. Proceedings of the Royal Society of London, A: Mathematical and Physical Sciences 1950, 202(1069), 244–253, DOI: 10.1098/rspa.1950.0097.

156. Marmur, A. Tip-surface capillary interactions. Langmuir 1993, 9(7), 1922–1926, DOI: 10.1021/la00031a047.

157. Mani, R.; Kadau, D.; Or, D.; Herrmann, H.J. Fluid depletion in shear bands. Physical Review Letters 2012, 109(24), 248001, DOI: 10.1103/PhysRevLett.109. 248001.

158. Butt, H.-J.; Kappl, M. Normal capillary forces. Advances in Colloid and Interface Science 2009, 146(1-2), 48–60, DOI: 10.1016/j.cis.2008.10.002.

159. Scheel, M.; Seemann, R.; Brinkmann, M.; Di Michiel, M.; Sheppard, A.; Breidenbach, B.; Herminghaus, S. Morphological clues to wet granular pile stability. Nature Materials 2008, 7(3), 189–193, DOI: 10.1038/nmat2117.

160. Mitarai, N.; Nori, F. Wet granular materials. Advances in Physics 2006, 55(1-2), 1–45, DOI: 10.1080/00018730600626065.

161. Herminghaus, S. Wet Granular Matter; Volume 6 in: Series in Soft Condensed Matter. World Scientific, 2013.

162. Sun, X.; Sakai, M. A liquid bridge model for spherical particles applicable to asymmetric configurations. Chemical Engineering Science 2018, 182, 28–43, DOI: 10.1016/j.ces.2018.02.034.

163. Wang, J.-P.; Gallo, E.; François, B.; Gabrieli, F.; Lambert, P. Capillary force and rupture of funicular liquid bridges between three spherical bodies. Powder Technology 2017, 305, 89–98, DOI: 10.1016/j.powtec.2016.09.060.

164. Pitois, O.; Moucheront, P.; Chateau, X. Liquid bridge between two moving spheres: An experimental study of viscosity effects. Journal of Colloid and Interface Science 2000, 231(1), 26–31, DOI: 10.1006/jcis.2000.7096.

165. Johnson, K.L.; Kendall, K.; Roberts, A.D.; Tabor, D. Surface energy and the contact of elastic solids. Proceedings of the Royal Society of London, A: Mathematical and Physical Sciences 1971, 324(1558), 301–313, DOI: 10.1098/rspa.1971.0141.

166. Yang, F.; Prade, F.; Griffa, M.; Kaufmann, R.; Herzen, J.; Pfeiffer, F.; Lura, P. X-ray dark-field contrast imaging of water transport during hydration and drying of early-age cement-based materials. Materials Characterization 2018, 142, 560–576, DOI: 10.1016/j.matchar.2018.06.021.

167. Rajabipour, F.; Weiss, J.; Lura, P.; Pease, B.; Mazzotta, G. Influence of shrinkage-reducing admixtures on development of plastic shrinkage cracks. ACI Materials Journal 2007, 104(2), DOI: 10.14359/18582.

168. Jensen, O.M.; Lura, P. Techniques and materials for internal water curing of concrete. Materials and Structures 2006, 39(9), 817–825, DOI: 10.1617/s11527-006-9136-6.

169. Panda, D.; Supriya, B.; Kharaghani, A.; Tsotsas, E.; Surasani, V.K. Lattice Boltzmann simulations for micro-macro interactions during isothermal drying of bundle of capillaries. Chemical Engineering Science 2020, 220, 115634, DOI: 10.1016/j.ces.2020.115634.

170. Panda, D.; Bhaskaran, S.; Paliwal, S.; Kharaghani, A.; Tsotsas, E.; Surasani, V.K. Pore-scale physics of drying porous media revealed by Lattice Boltzmann simulations. Drying Technology 2020, 1–16, DOI: 10.1080/07373937.2020 .1850469.

171. Panda, D.; Paliwal, S.; Sourya, D.P.; Kharaghani, A.; Tsotsas, E.; Surasani, V.K. Influence of thermal gradients on the invasion patterns during drying of porous media: A lattice Boltzmann method. Physics of Fluids 2020, 32(12), 122116, DOI: 10.1063/5.0031349.

172. Jiang, Z.; Rieck, C.; Bück, A.; Tsotsas, E. Modeling of inter- and intra-particle coating uniformity in a Wurster fluidized bed by a coupled CFD-DEM-Monte Carlo approach. Chemical Engineering Science 2020, 211, 115289, DOI: 10.1016/j.ces.2019.115289.

173. Kharaghani, A.; Kirsch, C.; Metzger, T.; Tsotsas, E. Micro-scale fluid model for drying of highly porous particle aggregates. Computers & Chemical Engineering 2013, 52, 46–54, DOI: 10.1016/j.compchemeng.2012.12.003.

174. Bonilla, R.R.O. Numerical Simulations of Undrained Granular Media. Dissertation: University of Waterloo, Waterloo, Ontario, Canada, 2004.

175. Hakuno, M. Simulation of the dynamic liquefaction of sand. In Ishihara, editor, Earthquake Geotechnical Engineering. Rotterdam, Balkema 1995, 857–862.

176. Jing, L.; Ma, Y.; Fang, Z. Modeling of fluid flow and solid deformation for fractured rocks with discontinuous deformation analysis (DDA) method. International Journal of Rock Mechanics and Mining Sciences 2001, 38(3), 343–355, DOI: 10.1016/S1365-1609(01)00005-3.

177. Tong, A.-T.; Catalano, E.; Chareyre, B. Pore-scale flow simulations: Model predictions compared with experiments on bi-dispersed granular assemblies. Oil & Gas Science and Technology – Revue d'IFP Energies nouvelles 2012, 67(5), 743–752, DOI: 10.2516/ogst/2012032.

178. Kharaghani, A.; Mahmood, H.T.; Tsotsas, E. Three-dimensional visualization and modelling of capillary liquid rings observed during drying of random particle packings. Chemical Engineering Science (submitted).

179. Kozicki, J.; Donzé, F.V. A new open-source software developed for numerical simulations using discrete modeling methods. Computer Methods in Applied Mechanics and Engineering 2008, 197(49-50), 4429–4443, DOI: 10.1016/j.cma.2008.05.023.

180. Yuan, C.; Chareyre, B. A pore-scale method for hydromechanical coupling in deformable granular media. Computer Methods in Applied Mechanics and Engineering 2017, 318, 1066–1079, DOI: 10.1016/j.cma.2017.02.024.

181. Mayer, R.P.; Stowe, R.A. Mercury porosimetry—breakthrough pressure for penetration between packed spheres. Journal of Colloid Science 1965, 20(8), 893–911, DOI: 10.1016/0095-8522(65)90061-9.

182. Princen, H.M. Capillary phenomena in assemblies of parallel cylinders. Journal of colloid and interface science 1969, 30(3), 359–371, DOI: 10.1016/0021-9797(69)90403-2.

183. Ma, S.; Mason, G.; Morrow, N.R. Effect of contact angle on drainage and imbibition in regular polygonal tubes. Colloids and Surfaces A: Physicochemical and Engineering Aspects 1996, 117(3), 273–291, DOI: 10.1016/0927-7757(96)03702-8.

184. Joekar-Niasar, V.; Prodanović, M.; Wildenschild, D.; Hassanizadeh, S.M. Network model investigation of interfacial area, capillary pressure and saturation relationships in granular porous media. Water Resources Research 2010, 46(6), DOI: 10.1029/2009WR008585.

185. Sweijen, T.; Aslannejad, H.; Hassanizadeh, S.M. Capillary pressure–saturation relationships for porous granular materials: Pore morphology method vs. pore unit assembly method. Advances in Water Resources 2017, 107, 22–31, DOI: 10.1016/j.advwatres.2017.06.001.

186. Sahimi, M. Models of fractures and fractured porous media, in: Flow and Transport in Porous Media and Fractured Rock, Wiley-VCH, Weinheim, 2011, pp. 213-251.

187. Metzger, T.; Irawan, A.; Tsotsas, E. Remarks on the paper "Extension of Hoshen–Kopelman algorithm to non-lattice environments" by A. Al-Futaisi and T.W. Patzek, Physica A 321 (2003) 665–678. Physica A: Statistical Mechanics and its Applications 2006, 363(2), 558–560, DOI: 10.1016/j.physa.2005.08.026.

188. Laurindo, J.B.; Prat, M. Numerical and experimental network study of evaporation in capillary porous media: Phase distributions. Chemical Engineering Science 1996, 51(23), 5171–5185, DOI: 10.1016/S0009-2509(96)00341-7.

189. White, S.M.; Tien, C.L. Analysis of flow channeling near the wall in packed beds. Wärme- und Stoffübertragung 1987, 21(5), 291–296, DOI: 10.1007/BF01009290.

190. Vortmeyer, D.; Schuster, J. Evaluation of steady flow profiles in rectangular and circular packed beds by a variational method. Chemical Engineering Science 1983, 38(10), 1691–1699, DOI: 10.1016/0009-2509(83)85026-X.

191. Mohammadian, S.; Geistlinger, H.; Vogel, H.-J. Quantification of gas-phase trapping within the capillary fringe using computed microtomography. Vadose Zone Journal 2015, 14(5), vzj2014.06.0063, DOI: 10.2136/vzj2014.06.0063.

192. Papachristos, E.; Scholtès, L.; Donzé, F.V.; Chareyre, B. Intensity and volumetric characterizations of hydraulically driven fractures by hydro-mechanical simulations. International Journal of Rock Mechanics and Mining Sciences 2017, 93, 163–178, DOI: 10.1016/j.ijrmms.2017.01.011.

193. Tsotsas, E. Packed beds with fluid flow. In HEDH Multimedia; Begellhouse, 2014, DOI: 10.1615/hedhme.a.000201.

194. Tsotsas, E.; Schlünder, E.-U. Measurements of mass transfer between particles and gas in packed tubes at very low tube to particle diameter ratios. Wärme- und Stoffübertragung 1990, 25(4), 245–256, DOI: 10.1007/BF01785411.

195. Tsotsas, E. M7 Heat and Mass Transfer in Packed Beds with Fluid Flow. In VDI Heat Atlas; Springer Berlin Heidelberg: Berlin, Heidelberg, 2010; 1327–1342, DOI: 10.1007/978-3-540-77877-6_100.

196. Sonntag, G. Einfluß des Lückenvolumens auf den Druckverlust in gasdurchströmten Füllkörpersäulen. Chemie Ingenieur Technik 1960, 32(5), 317–329, DOI: 10.1002/cite.330320502.

197. Jeschar, R. Druckverlust in Mehrkornschüttungen aus Kugeln. Archiv für das Eisenhüttenwesen 1964, 35(2), 91–108, DOI: 10.1002/srin.196402300.

198. Schlünder, E.U.; Tsotsas, E. Wärmeübertragung in Festbetten, durchmischten Schüttgütern und Wirbelschichten; Georg Thieme Verlag: Stuttgart– New York, 1988.

199. Tsotsas, E. Eine einfache empirische Gleichung zur Vorausberechnung der Porosität polydisperser Kugelschüttungen. Chemie Ingenieur Technik 1991, 63(5), 495–496, DOI: 10.1002/cite.330630513.

200. Wärmeleitung und Dispersion in durchströmten Schüttungen, VDI-Wärmeatlas, 12. Auflage, Springer Verlag, Berlin, 2018, DOI: 10.1007/978-3-662-52991-1_102-1.

201. Tsotsas, E.; Schluender, E.-U. Numerical calculation of the thermal conductivity of two regular bidispersed beds of spherical particles. Computers & Chemical Engineering 1990, 14(9), 1031–1038, DOI: 10.1016/0098-1354(90)87059-X.

202. Sufian, A.; Knight, C.; O'Sullivan, C.; van Wachem, B.; Dini, D. Ability of a pore network model to predict fluid flow and drag in saturated granular materials. Computers and Geotechnics 2019, 110, 344–366, DOI: 10.1016/j.compgeo.2019.02.007.

203. Kralchevsky, P.A.; Nagayama, K. Capillary forces between colloidal particles. Langmuir 1994, 10(1), 23–36, DOI: 10.1021/la00013a004.

204. Louati, H.; Oulahna, D.; Ryck, A. de. Effect of the particle size and the liquid content on the shear behaviour of wet granular material. Powder Technology 2017, 315, 398–409, DOI: 10.1016/j.powtec.2017.04.030.

205. Bourrier, F.; Kneib, F.; Chareyre, B.; Fourcaud, T. Discrete modeling of granular soils reinforcement by plant roots. Ecological Engineering 2013, 61, 646–657, DOI: 10.1016/j.ecoleng.2013.05.002.

206. Aboul Hosn, R.; Sibille, L.; Benahmed, N.; Chareyre, B. Discrete numerical modeling of loose soil with spherical particles and interparticle rolling friction. Granular Matter 2017, 19(1), DOI: 10.1007/s10035-016-0687-0.

Publications and presentations

Own publications and presentations related to this thesis in national and international journals and conferences are listed in the following.

1. Son Thai Pham, Bruno Chareyre, Evangelos Tsotsas, Abdolreza Kharaghani. **A pore-scale study on the drying kinetics and mechanical behaviour of particle aggregates,** Interpore 10th Annual Meeting and Jubilee Conference, May 14-17, 2018, New Orleans, USA.

2. Son Thai Pham, Bruno Chareyre, Evangelos Tsotsas, Abdolreza Kharaghani. **Drying characteristics of polydisperse particle aggregates in the capillary-dominated regime**, 21st International Drying Symposium, September 11-14, 2018, Valencia, Spain, DOI: http://dx.doi.org/10.4995/ids2018.2018.7388. (peer-reviewed)

3. Son Thai Pham, Bruno Chareyre, Evangelos Tsotsas, Abdolreza Kharaghani. **Mechanical behavior of particle aggregates during drying**, International Congress on Particle Technology (PARTEC 2019), April 09-11, 2019, Nuremberg, Germany (**Oral presentation**). (peer-reviewed)

4. Son Thai Pham, Bruno Chareyre, Evangelos Tsotsas, Abdolreza Kharaghani**. Fluid-solid interaction during particle aggregates drying**, Interpore 11th Annual Meeting and Jubilee Conference, May 6-10, 2019 Valencia, Spain.

5. Son Thai Pham, Bruno Chareyre, Evangelos Tsotsas, Abdolreza Kharaghani**. Three-dimensional triangulation pore network model: Drying kinetics and capillary force evolution**, Drying Technology (To be submitted).